University of Southampton Research Repository

Thesis: Mirko Trisolini (2018) "Space System Design for Demise and Survival", University of Southampton, Faculty of Engineering and the Environment, Department of Astronautics, PhD Thesis

Data: Mirko Trisolini (2018) Space System Design for Demise and Survival Dataset

UNIVERSITY OF SOUTHAMPTON

FACULTY OF ENGINEERING AND THE ENVIRONMENT

Aeronautics, Astronautics and Computational Engineering

Space system design for demise and survival

by

Mirko Trisolini

ORCID ID 0000-0001-9552-3565

A thesis submitted for the degree of
Doctor of Philosophy

September 2018

UNIVERSITY OF SOUTHAMPTON

ABSTRACT

FACULTY OF ENGINEERING AND THE ENVIRONMENT

Aeronautics, Astronautics and Computational Engineering

Thesis for the degree of Doctor of Philosophy

SPACE SYSTEM DESIGN FOR DEMISE AND SURVIVAL

Mirko Trisolini

In the past two decades, the attention towards a more sustainable use of outer space has increased steadily. The major space-faring nations and international committees have proposed a series of debris mitigation measures to ensure the sustainability of the space environment. Among these mitigation measures, the de-orbiting of spacecraft at the end of their operational life is recommended in order to reduce the risk of collisions in orbit. However, re-entering spacecraft can pose a risk to people and property on the ground. A possible way to limit this risk is to use a design-for-demise philosophy, where the spacecraft is designed such that most of its components will not survive the re-entry process. However, a spacecraft designed for demise still must survive the space environment for many years. As a large number of space debris populates the space around the Earth, a spacecraft can suffer impacts from these particles, which can be extremely dangerous. This means that the spacecraft design has also to comply with the requirements arising from the survivability against debris impacts. The demisability and survivability of a spacecraft are both influenced by a set of common design drivers, such as the material of the structure, its shape, dimension, and position inside the spacecraft. It is important to consider such design choices and how they influence the mission's survivability and demisability from the early stages of the mission design process. The thesis addresses these points with an increasingly higher level of detail by a continuous and interlinked development of a demisability and a survivability model, of two criteria to evaluate the level of demisability and survivability, and of a common framework where both models communicate and interact to find optimal solutions. First, the initial versions of the models, which is limited to simple geometrical shapes, uniform materials, and dimensions, is used to study the sensitivity of the demisability and of the survivability indices as a function of typical design-for-demise options. As new features are introduced, such as the capability of considering internal components and sub-component together with their position inside the spacecraft, as well as the type of shielding, also the analyses become more detailed. As the demisability and the survivability of a spacecraft configuration are closely linked, it is important to assess them in a concurrent fashion for which a multi-objective optimisation framework has been developed. Here the survivability and the demisability requirements are considered simultaneously and trade-off solutions of spacecraft configurations can be obtained. The final part of the thesis presents a test case for the application of the framework, targeting one of the most interesting components from both a demisability and a survivability standpoint that are tank assemblies. Finally, a preliminary study concerning the development of a new demisability index is presented.

Table of Contents

Table of Tables

Table of Figures

Table of Figures

Table of Figures

Academic Thesis: Declaration Of Authorship

I, Mirko Trisolini

declare that this thesis and the work presented in it are my own and has been generated by me as the result of my own original research.

Space System Design for Demise and Survival

I confirm that:

1. This work was done wholly or mainly while in candidature for a research degree at this University;
2. Where any part of this thesis has previously been submitted for a degree or any other qualification at this University or any other institution, this has been clearly stated;
3. Where I have consulted the published work of others, this is always clearly attributed;
4. Where I have quoted from the work of others, the source is always given. With the exception of such quotations, this thesis is entirely my own work;
5. I have acknowledged all main sources of help;
6. Where the thesis is based on work done by myself jointly with others, I have made clear exactly what was done by others and what I have contributed myself;
7. Parts of this work have been published as:
   - M. Trisolini, H.G. Lewis, C. Colombo, Demisability and survivability sensitivity to design-for-demise techniques, *Acta Astronautica*, April 2018, Vol. 145, pp. 357-384, DOI: https://doi.org/10.1016/j.actaastro.2018.01.050
   - M. Trisolini, H.G. Lewis, C. Colombo, Demise and survivability criteria for spacecraft design optimisation, *Journal of Space Safety Engineering*, 2016, Vol. 3, Issue 2, pp. 83-93, DOI: 10.1016/S2468-8967(16)30023-4
   - M. Trisolini, H.G. Lewis, C. Colombo, Spacecraft design optimisation for demise and survivability, Aerospace Science and Technology, 2018, Vol. 77, pp. 638-657, DOI: https://doi.org/10.1016/j.ast.2018.04.006
   - M. Trisolini, H.G. Lewis, C. Colombo, Demisability and survivability multi-objective optimisation for preliminary spacecraft, Proceedings of the 68th International Astronautical Congress, 25-29 September 2017, Adelaide, Australia
   - M. Trisolini, H.G. Lewis, C. Colombo, On the demisability and survivability of modern spacecraft, Proceedings of the 8th European Conference on Space Debris, 18-21 April 2017, ESOC, Darmstadt, Germany
   - M. Trisolini, H.G. Lewis, C. Colombo, Multi-objective optimisation for spacecraft design for demise and survivability, Proceedings of the Stardust Final Conference, 31st October – 4th November 2016, ESTEC, Noordwijk, The Netherlands

- M. Trisolini, H.G. Lewis, C. Colombo, Spacecraft design optimisation for demise and survivability, Proceedings of the 67thInternational Astronautical Congress (IAC), 26-30 September 2016, Guadalajara, Mexico
- M. Trisolini, H.G. Lewis, C. Colombo, Demise and survivability criteria for spacecraft design optimisation, Proceedings of the 8th IAASS Conference, 18-20 May 2016, Melbourne, Florida, USA
- M. Trisolini, H.G. Lewis, C. Colombo, Survivability and Demise Criteria for Sustainable Spacecraft Design, Proceedings of the 66th International Astronautical Conference (IAC), 12-16 October 2015, Jerusalem, Israel

Signed: ....

Date: 16/01/2020

Acknowledgements

I would like to acknowledge my supervisors, Dr. Hugh Lewis and Dr. Camilla Colombo for making this work possible. Your support and your experience have been invaluable throughout these years. I would like to thank Hugh for always being a positive and encouraging guide. Thanks for your contribution in shaping this work with your advices, suggestions, and your inquisitive attitude. Thanks for making me a better researcher, always encouraging me to find own voice, and explore my ideas. Thank you Camilla for your continuous support, even when we were in different countries. Thanks for your precious counselling and tireless guidance and, most of all, thanks for believing in my abilities. Your positivity and passion have been of inspiration and have helped me growing as a researcher and as an individual. I am also grateful to each member of the Astronautics Department at the University of Southampton; it has been a pleasure working with you in such a warm, friendly, and stimulating environment.

The PhD in Southampton has been one of the most valuable experiences in my life; it has changed me and strengthened me in more ways than I can think of. I would like to thank all the colleagues and friends from the Astronautics department; thanks for being good companions on every day of this experience. A special thanks to Fede, Otti, Davide, Irene, Michele, and Geane; you have been a second family to me throughout these years. I will never forget our time together, the laughs, the jokes, the trips, and the all the house dinners we shared. Fede, you were the first person I met in the department and we have been friends since then. You are an inspiring person, always open, with a smile and a good word for everyone. Otti, you are such a loving and caring person. Thanks for having a good word for everyone and thank you for taking care of all of us; I know you will be a wonderful mom. Davide, you are one of the smartest and hard-working person I know. Thanks for being a good colleague and a wonderful friend and, of course, thanks for all the times you prepared pizza for all of us. Irene, you are such a strong and resolute person. Thanks for inspiring me through your strength of character and independence. Michele thanks for always having a joke and a smile on everything, and thanks Geane for your kindness and for trying to mitigate Michele's exuberance. A big hug to Ahmed, Francesca, Gennaro, David, Daniele, Stefano, Stefania, Vanessa, Bernat, Gian Luigi, Clemens; thanks for all the moments we shared through this amazing experience.

Finally, the biggest and deepest thank goes to my family. Thank you Mom, Dad, and Dimi for always being there by my side, supporting me, not only through these PhD years but also through all my studies. Thank you for teaching me the importance of doing what I love, of pursuing my dreams and my objectives, and, most importantly, to think with independence of mind. I am grateful for every video call I had with you Mom, they made me feel like I was home even though I was a thousand kilometres away. Thank you, Dad, for your unconditional support. I know you and I are very much alike; we do not talk much and we struggle to share our feelings, but your actions speak for a thousand words. None of what I have achieved would have been possible without all of you.

List of symbols

a	Semi-major axis	km
A	Area	m^2
A_c	Casualty area	m^2
A_c^k	Area of the intersection between the debris cone associated with the *k*-th cell of the vulnerable area subdivision and the target plane	m^2
$A_{c,\,av}^{j,\,i}$	Average available cone area for the *i*-th vector flux element onto the *j*-th vulnerable zone	m^2
$A_{c,\,av}^{k}$	Available cone area	m^2
$A_{c,ref}$	Reference casualty area	m^2
A_{end}	End area of a cylinder	m^2
A_p^i	Particle cross section relative to the *i*-th vector flux element	m^2
AR	Aspect ratio	
A_s	Area of the side of a box in the z direction	m^2
$A_{s,t}^k$	Area of the perspective projection of the *t*-th shielding component onto the target plane with respect to the *k*-th grid cell of the vulnerable zone	m^2
A_{side}	Side area of a cylinder	m^2
a_t	Thermal accommodation coefficient	
A_t	Target cross-section	m^2
$A_{t,\,av}^{j,\,i}$	Average target visible area for the *i*-th vector flux element onto the *j*-th vulnerable zone	m^2
A_{tot}	Total area of an object	m^2
$A_{tot}^{d,eq}$	Total area of an equivalent disk	m^2
A_{tot}^{fp}	Total area of a flat plate	m^2
$A_{v,av}$	Available visible area	m^2
A_{VZ}	Area of the vulnerable zone	m^2
A_w	Wet area	m^2
A_x	Area of the side of a box in the x direction	m^2
A_y	Area of the side of a box in the y direction	m^2
A_z	Area of the side of a box in the z direction	m^2
Az_i	Impact azimuth	rad
B	Ratio of the average heating on the side of an end-on cylinder to the stagnation point heating on a sphere of the same radius	

C	Speed of sound	m/s
C_D	Drag coefficient	
$C_{D,c}$	Drag coefficient in the continuum regime	
$C_{D,fm}$	Drag coefficient in the free-molecular regime	
$C_{D,t}$	Drag coefficient in the transition regime	
CF_{ball}	Correction factor for the mutual shielding in the ballistic regime	
CF_{hyp}	Correction factor for the mutual shielding in the hypervelocity regime	
C_m	Specific heat capacity	J/kg/K
d	Diameter	m
d_c	Critical diameter	m
$d_{c,\,av}^{j,\,i}$	Equivalent available cone diameter for the *i*-th vector flux element onto the *j*-th vulnerable zone	m
d_{ejecta}	Extent of the debris cloud ejecta at the target plane	m
d_p	Debris particle diameter	m
d_p^i	Diameter of the debris particle associated to the *i*-th vector flux element	m
$d_{p,max}$	Maximum particle diameter	m
$d_{t,\,av}^{j,\,i}$	Equivalent target visible diameter for the *i*-th vector flux element onto the *j*-th vulnerable zone	m
d_{target}	Extent of the target component at the target plane	m
$d_{v,eq}$	Equivalent visible diameter	m
d_{vz}	Equivalent diameter of the vulnerable zone	m
e_{imp}	Impact energy of a component on ground	J
E_0	Tolerance on the displacement from the nominal orbit ground track at the equator	m
El_i	Impact elevation	rad
F_D	Drag force	N
F_L	Lift force	N
$\bar{F}_q$	Shape factor	
$\bar{F}_{q,c}^{c}$	Continuum shape factor of a cylinder	
$\bar{F}_{q,c}^{d,eq}$	Continuum shape factor for the equivalent disk	
$\bar{F}_{q,c}^{end}$	Continuum shape factor for the end area of a cylinder	
$\bar{F}_{q,c}^{fp}$	Continuum shape factor of a flat plate	
$\bar{F}_{q,c}^{s}$	Continuum shape factor of a sphere	

$\overline{F}_{q,c}^{side}$	Continuum shape factor for the side area of a cylinder	
$\overline{F}_{q,fm}^{b}$	Free molecular shape factor of a box	
$\overline{F}_{q,fm}^{c}$	Free molecular shape factor of a cylinder	
$\overline{F}_{q,fm}^{end}$	Free molecular shape factor for the end area of a cylinder	
$\overline{F}_{q,fm}^{fp}$	Free molecular shape factor of a flat plate	
$\overline{F}_{q,fm}^{s}$	Free molecular shape factor of a sphere	
$\overline{F}_{q,fm}^{side}$	Free molecular shape factor for the side area of a cylinder	
g_r	Radial component of the gravitational acceleration	m/s^2
g_δ	Tangential component of the gravitational acceleration	m/s^2
HB	Brinell Hardness	
h_d	Demise altitude	km
H_{design}	Nominal value of the momentum for a reaction wheel	Nm
h_f	Heat of fusion	J/kg
h_{fin}	Re-entry final altitude	km
h_{in}	Re-entry initial altitude	km
h_s	Stagnation point enthalpy	J
h_w	Wall enthalpy	J
h_{w300}	Wall enthalpy at 300K	J
I_D	Demisability index	
Isp	Specific impulse	s
K_1	Filling factor correction for the computation of fuel volume	
Kn	Knudsen number	
K_{sf}	Safety factor	
l	Length	m
LMF	Liquid Mass Fraction	
L_{VZ}	Extent of the vulnerable zone	m
m	Mass	kg
m_f	Fuel mass	kg
m_{fin}	Final mass of component after re-entry	kg
m_{in}	Initial mass of component before re-entry	kg
$m_{s/c}$	Spacecraft mass	kg
$\mathbf{n}$	Normal vector to a spacecraft panel	

n_{cell}	Number of grid cell elements subdividing the vulnerable zone	
N_{fluxes}	Number of vector flux elements schematising the space environment	
N_{panels}	Number of panels composing the analysed structure	
n_t	Number of tanks	
p	Pressure	Pa
P_{BLE}	Probability that a particle in the debris ejecta cloud perforates the internal component wall	
$P^{j,\,i}_{BLE}$	Penetration probability of the i-th vector flux element, already impacting on the *j*-th vulnerable zone, on the considered component	
P_{comp}	Probability that a downrange fragment will hit the internal component	
$P^{j,\,i}_{comp}$	Probability that the *i*-th vector flux element, already impacting on the *j*-th vulnerable zone, will hit the considered component	
P_i	Impact probability	
p_{max}	Maximum operating pressure of a tank	MPa
PNP	Probability of no-Penetration	
P_p	Penetration probability	
P_{struct}	Probability of space debris to impact the external structure of a satellite inside the vulnerable zone relative to a component	
$P^{j,\,i}_{struct}$	Probability of impact on the *j*-th vulnerable zone by the *i*-th vector flux element	
q_0	Free-stream dynamic pressure	Pa
$\dot{q}^{\perp}_{fp}$	Heat rate perpendicular to a flat plate	W/m^2
$\dot{q}_{av}$	Average heat rate	W/m^2
$\dot{q}_c$	Heat rate for continuum flow	W/m^2
$\dot{q}_{fm}$	Heat rate for free molecular row	W/m^2
$\dot{q}_{ref}$	Reference heat rate	W/m^2
$\dot{q}_{ss}$	Stagnation-point heat rate over a sphere	W/m^2
$\dot{q}_t$	Heat rate for transitional flow	W/m^2
r	Radius	m
r_n	Nose radius	m
r_t	Tank radius	m
r_t^{int}	Tank internal radius	m
S	Cross section	m^2
$S_j^{\perp}$	Projected area of the *j*-th panel along the impact direction	m^2
$S^{\perp}_{j,\,VZ}$	Projected area of the *j*-th vulnerable zone of the considered component	m^2

SF	Safety factor	
Si	Sobol first-order sensitivity index for the *i*-th variable	
s_j	Stand-off distance between the component and the external wall associated to the j-th vulnerable zone	m
S_{ref}	Reference cross-section	m^2
S_{Ti}	Sobol total sensitivity index for the *i*-th variable	
T_m	Melting temperature	K
t_s	Shield thickness	m
t_t	Tank thickness	m
T_w	Wall temperature of an object	K
$\mathbf{v}$	Velocity vector	m/s
V	Velocity of the spacecraft	m/s
V_0	Free-stream velocity	m/s
V_f	Fuel volume	m^3
v_p	Particle relative velocity with respect to the spacecraft	km/s
V_p	Vulnerability of spacecraft components to debris impacts	
$V_{s/c}$	Orbital velocity of a spacecraft	km/s
w	Width	m
Y	Free-molecular flow ratio of the average heating on the sides of a rotating side-on cylinder to the heating on surfaces perpendicular to the flow	
Z	Free-molecular flow ratio of the heating on surfaces parallel to the flow to the heating on surfaces perpendicular to the flow	
α	Debris cloud ejection angle	rad
α_{max}	Maximum debris cloud ejection angle	rad
γ	Flight path angle	rad
γ_1	Half-cone aperture angle of the normal debris cloud	rad
γ_2	Half-cone aperture angle of the inline debris cloud	rad
δ	Geometrical latitude	rad
Δa_{decay}	Reduction of the semi-major axis due to the drag	km
Δa_{inj}	Semi-major axis error due to injection	km
Δi_{inj}	Inclination error due to injection	deg
Δi_{sec}	Secular variation of the inclination in one year for sun-synchronous orbits	deg
Δt_{decay}	Reduction of the orbital period due to the drag	s
ΔT	Mission lifetime	year

ΔV_{decay}	Delta-V required to compensate for the spacecraft decay due to atmospheric drag	km/s
ΔV_{disp}	Delta-V required for the disposal manoeuvre	km/s
ΔV_{inc}	Delta-V required to compensate for inclination changes	km/s
ΔV_{inj}	Delta-V required for the correction of injection manoeuvres errors	km/s
ΔV_{tot}	Total delta-V required for the maintenance of sun-synchronous orbits	km/s
$\Delta\lambda$	Longitude displacement at equator passage	deg
χ	Azimuth angle	rad
ε	Emissivity	
θ	Impact angle	rad
θ_1	Deflection angle of the normal debris cloud	rad
θ_2	Deflection angle of the inline debris cloud	rad
λ	Geometrical longitude	rad
λ_s	Mean free path	m
v_m	Poisson ratio of a material	
ρ_0	Free-stream air density	kg/m^3
ρ_{atm}	Atmospheric density	kg/m^3
ρ_f	Fuel density	kg/m^3
ρ_m	Material density	kg/m^3
ρ_{ns}	Density of the air after a normal shock	kg/m^3
ρ_p	Particle density	kg/m^3
ρ_s	Shield density	kg/m^3
$\rho_{s/c}$	Spacecraft average density	kg/m^3
ρ_{SL}	Sea-level air density	kg/m^3
σ_u	Ultimate strength	MPa
σ_y	Yield strength	MPa
φ	Debris flux	1/m^2/yr
φ_c	Critical debris flux	1/m^2/yr
φ_{TOT}	Total debris flux for a mission	1/m^2/yr
ϕ	Colatitude	rad
ω_{max}	Maximum rotational speed of a reaction wheel	rad/s

Constants

σ	Stefan-Boltzman constant	$= 5.670367 \times 10^{-8}$ W/m^2/K^4
ρ_{SL}	Sea-level density	= 1.225 km/m^3
γ	Polytrophic constant	= 1.405
T_{SL}	Sea-level temperature	= 288.15 K
R_e	Equatorial radius of the Earth	= 6378.16 km
R^*	Universal gas constant	$= 8.31432\times10^3$ J/kg/mol/K
R	Air gas constant	= 287.0 J/kg/K
p_{SL}	Sea-level pressure	$= 1.013250\times10^5$ Pa
Na	Avogadro's number	$= 6.0220978\times10^{23}$ J/kg/mol
M_{SL}	Sea-level molecular weight	= 28.966
K_{CFRP}	Coefficient for single wall ballistic limit equations for CFRP structures	= 0.52
J_4	Fourth order zonal harmonic coefficient	$= 1.6109876 \times 10^{-7}$
J_3	Third order zonal harmonic coefficient	$= 2.532153 \times 10^{-7}$
J_2	Second order zonal harmonic coefficient	$= 1.08263 \times 10^{-3}$
g_0	Sea-level gravity	= 9.806 m/s^2
μ_e	Earth’s gravitational parameter	$= 3.986004461921757 \times 10^5$ km^3/s^2
ω_e	Earth’s rotational speed	$= 7.2921150 \times10^{-5}$ rad/s

Definitions and Abbreviations

BLE	Ballistic Limit Equations
CFRP	Carbon Fibre Reinforced Plastic
COPV	Composite Overwrapped Pressure Vessel
DAS	Debris Assessment Software
DKR	Detra-Kemp-Riddel
DOF	Degree Of Freedom
DRAMA	Debris Risk Assessment and Mitigation Analysis
ESA	European Space Agency
GA	Genetic Algorithm
HC-SP	Honeycomb Sandwich Panel
IADC	Inter-Agency Space Debris Coordination Committee
ISS	International Space Station
JAXA	Japan Aerospace Exploration Agency
LEO	Low Earth Orbit
LMF	Liquid Mass Fraction
MM/OD	Micrometeoroids / Orbital Debris
NASA	National Aeronautics and Space Administration
ORSAT	Object Re-entry Survival Analysis Tool
PNP	Probability of No-Penetration
RAAN	Right Ascension of the Ascending Node
SAM	Spacecraft Aerothermal Model
SCARAB	Spacecraft Atmospheric Re-entry and Aerothermal Break-up
SESAM	Spacecraft Entry Survival Analysis Module
SRL	Schafer-Ryan-Lambert
ISS	International Space Station

Chapter 1 Introduction

The research presented in this work aims at understanding the role of the demise and of the survivability when they are considered in the design of the spacecraft since the early stages of the mission. With demise (or demisability) we express the ability of a spacecraft to burn during its re-entry in the atmosphere so that only few or even none of the components reach the ground. With survivability we define the capability of a spacecraft to withstand impacts from orbiting space debris and meteoroids during its lifetime. This thesis presents the methodologies developed to assess the demise and survivability and how these requirements can be considered in a concurrent fashion for the optimised preliminary design of spacecraft configurations.

This chapter starts with an overall description of space mitigation measures and of the relevant topics to the work we have carried out, which is necessary to understand the motivations and objectives of the study that are introduced immediately after. Subsequently, a description of the background of the project will be given, with emphasis on spacecraft re-entry, spacecraft protection to debris impacts, and spacecraft design and optimisation. Finally, a summary of the methodologies developed and implemented in this study is provided, together with a list of the contributions made during the PhD in the form of journal publications and conference attendances.

1.1 Space debris mitigation

In the past two decades, the attention towards a more sustainable use of the outer space has increased steadily (European Space Agencfy, 2008, O'Connor, 2008, H. G. Lewis *et al.*, 2017a, Hugh G. Lewis *et al.*, 2012, Innocenti,Soares and Delaval, 2013). Since the beginning of the space era, the space around the Earth and beyond has been the theatre of remarkable achievements but has also suffered from the consequences of the thousands of missions that have flown. Decommissioned satellites, spent upper stages, other mission related objects, and fragments generated by collisions and explosions of spacecraft and upper stages have polluted and still pollute the space environment in the form of space debris (European Space Agency, 2008). Recent studies have shown a constant increase in the population of space debris (Radtke *et al.*, 2017, H. G. Lewis *et al.*, 2017b, H. G. Lewis *et al.*, 2017a, Hugh G. Lewis *et al.*, 2012), and the amount of debris is expected to keep growing. This has raised awareness towards the sustainability of the space environment and of the future space traffic, more so since the recent deployment of mega-constellations, which are going to double or triple the population of active satellites in orbit in a matter of few years. The major space-faring nations and international committees have thus proposed a series of debris mitigation measures (O'Connor, 2008, F Schäfer *et al.*, 2005a) to protect the space environment. Their implementation can help saving it from an uncontrolled raise of the debris population so that it will still be accessible in the future. In fact, the effect of space debris is now recognised as a major risk to space missions as an object of just 1 cm in size can cause the disruption of a satellite (Putzar and Schäfer, 2006, PH Stokes and Swinerd, 2005), and smaller particles can still have enough energy to produce failures on components critical to the mission success. Consequently, measures must be taken in two directions: preserving the space environment from a future uncontrolled pollution and assessing the effects of the present debris on spacecrafts to protect them from being severely damaged.

1.1.1 Mitigation through re-entry

This thesis fits into this context of a robust and regulated implementation of these mitigation strategies since the early stages of the mission design. One of the most effective measure to control the evolution of the space environment and its future access is the disposal of spacecrafts through re-entry at the end of their operational life (European Space Agency, 2008). In fact, the Inter Agency Debris Coordination Committee (IADC) introduced a 25-year rule stating that a satellite in Low Earth Orbit (LEO) must re-enter within 25 years of its decommissioning. In this way we can avoid cluttering the space environment with too many spacecrafts and prevent decommissioned satellites from creating more debris by impacting other objects or particles orbiting the Earth. However, a spacecraft that re-enters in the atmosphere can pose a risk for people and properties on the ground; consequently, specific measures must be taken to ensure their safety. For this purpose, we can simulate the re-entry of spacecrafts, assess the demise of their parts and components, and compute the probability that the surviving fragments have to impact on populated areas. This probability is identified as the *casualty risk on ground*. To limit this risk, international and national agencies have set the limit for the casualty risk on ground to be lower than 10^{-4}.

1.1.2 Controlled and uncontrolled re-entries

When a spacecraft is decommissioned through re-entry, its disposal may be achieved through a *controlled* or an *uncontrolled re-entry*. When the first option is used, spacecraft operators perform a final manoeuvre, in the last part of the re-entry trajectory, to precisely target an area of the Earth that is not populated (usually oceans). In the second case, instead, the spacecraft is left to naturally decay, no manoeuvres are performed, and the re-entry is not guided. Controlled re-entries can thus ensure the safety of people on the ground; however, they require a high cost in terms of propellant, consequently increasing the mass of the spacecraft, and are complex because they must have a very high reliability. Uncontrolled re-entries, on the other hand, cannot be guided to impact the Earth on a safe location and they can thus pose a risk for people on the ground. As of April 2013, and since the decay of Sputnik I, 22142-catalogued objects have re-entered the Earth's atmosphere, accounting for a re-entered mass of about 29000 metric tons. Of the total re-entered mass, the one of uncontrolled re-entered objects has been assessed to be about 11000 metric tons, consisting of nearly 5200 spacecraft and rocket bodies (Pardini and Anselmo, 2013). During the period from 2010 to 2012, nearly 50% of the re-entering mass was uncontrolled, and mainly consisted of rocket bodies and spacecraft with an average mass of around 1850 kg (Pardini and Anselmo, 2013). On average, between 10% and 40% of the mass of a re-entering object survives the re-entry (Peter MB Waswa and Hoffman, 2012). In addition, re-entry predictions uncertainties are large until a few hours before the actual re-entry occurs (National Astronautics and Space Administration, 2012), making it difficult to alert the population in advance in case an impact onto a populated area is possible. Nonetheless, they are a favourable disposal option in terms of reliability and costs (Peter MB Waswa and Hoffman, 2012), provided specific measures are taken to ensure that the limits on the casualty risk are satisfied. To do so, it is possible to use an integrated approach for the design of spacecraft that is compliant with the re-entry safety requirements, which is called *design-for-demise*.

1.2 Design-for-demise

To reduce the risk that can arise from uncontrolled re-entries and comply with the casualty risk regulations, the implementation of design options that can favour the demise of a spacecraft during the re-entry has been proposed (Waswa and Hoffman, 2012, Waswa et al., 2013, Kelley, 2012, Innocenti et al., 2013). The implementation of such design techniques is known as “design-for-demise”. It consists of changes to the configuration of the spacecraft and to the design of components that favour the demise of the satellite during the re-entry, preventing most (if not all) components and fragments from reaching the surface of the Earth. In this way, it is possible to maintain the casualty risk on ground of a spacecraft re-entering in an uncontrolled fashion below the prescribed threshold of 10^{-4} (National Astronautics and Space Administration, 2012, European Space Agency, 2008, Inter-Agency Space Debris Coordination Committee, 2007) by directly exploiting its design. This is an integrated approach, which aims at tackling the requirements arising from a safe disposal of a satellite from the early stages of the mission design (Waswa et al., 2013). Until recently, re-entry disposal issues were only considered in later stages (Waswa et al., 2013). This can result in late changes to the design of components or configurations. When this happens, solutions are more complicated to implement and can cause delays and increase the cost of the mission (Waswa et al., 2013). Therefore, the implementation of design-for-demise options is most effective when developed alongside the initial phases of the mission design.

However, a spacecraft designed for demise still must survive the space environment for many years. As a large number of space debris and meteoroids populates the space around the Earth, a spacecraft can suffer impacts from these particles, which can be extremely dangerous, damaging the spacecraft or even causing the complete loss of the mission (Christiansen et al., 2009, Putzar and Schäfer, 2006, Grassi et al., 2014). Consequently, the spacecraft design has also to comply with the requirements arising from the survivability against debris impacts. The demisability and survivability of a spacecraft are both influenced by a set of design drivers they have in common, such as the structural material, the shape, the dimension, and the position inside the spacecraft of the components. It is thus interesting to understand how the design changes implemented through the design-for-demise techniques affect the debris impact survivability. Will the demisability and survivability exhibit a competing behaviour in front of the design changes introduced? Will they generate configurations that are too vulnerable to be implemented?

1.3 Research motivations and objectives

The implementation of design-for-demise options has been gaining an increased interest as a mean to enhance the demise of a spacecraft upon its re-entry into the atmosphere and limit the risk on the ground for people and infrastructures. Design-for-demise techniques affect the design of spacecraft structures and components; therefore, they can also influence other characteristics and requirements of a mission (Innocenti et al., 2013).

The motivation behind this work is to quantitatively assess the effects of the implementation of design-for-demise techniques in the early stages of the mission design on both the demisability and the survivability of satellites. The question is if increasing the demisability can hinder the survivability of a spacecraft to debris impacts.

This can be achieved through a series of objectives, which are required to build a proper framework for the analysis of the demisability and survivability of spacecraft configurations and for their preliminary optimised design. A first objective is the development of two models for the analysis of the demisability and of the survivability. Such models need to be fast enough to perform a large set of simulations in order to assess many different configurations in an early-stage mission design process. In addition, they must be of comparable complexity and must be able to work with the same set of inputs so that the results can be effectively compared. Moreover, to assess the demisability and the survivability, two separate criteria must be developed. They summarise the output of the simulations from the two models into a single score. Consequently, another objective is to develop the two models and devise the demisability and survivability criteria.

The second objective of the thesis is to identify the different design-for-demise strategies that can be used from the initial design phases and to understand which design parameters need to be changed in order to implement them. Subsequently, we want to find, in the most general way, which among these parameters are the most influential in affecting the demisability and the survivability. In this way, it is possible to understand which parameters can be prioritised when implementing the design-for-demise principles.

Another objective is the assessment of the trends followed by the demisability and the survivability when implementing the design-for-demise solutions and, in particular, if they have a competing behaviour. In addition, we want to quantify how the demisability and the survivability vary when changing the design parameters associated with the design-for-demise techniques, focusing on the most critical components in terms of demisability such as tanks, pressure vessels, reaction wheels, batteries, etc.

The final objective of the thesis is to develop a comprehensive framework that is able to analyse the demisability and survivability of a preliminary spacecraft design and to propose optimised solutions that consider the requirements arising from the demisability and the survivability. The framework exploits constrained multi-objective optimisation, combined with the developed models to explore many different configurations with different level of demisability and survivability. This is particularly useful in the early stages of the mission design where large number of different configurations must be examined. In this way, the design of a mission implementing design-for-demise options can be much more integrated.

1.4 Background

This section will cover a literature review of the re-entry of satellites, their survivability to debris impact, the design for demise techniques, and the multi-objective optimisation.

1.4.1 Re-entry hazard

Upon re-entry, spacecrafts experience a very high heat load due to their aero-thermodynamic interaction with the Earth's atmosphere (Regan and Anandakrishnan, 1993). This heat load is responsible for the melting of most of the spacecraft parts before they reach the ground. However, not all components demise, and some of them do reach the surface of the Earth, constituting a risk for people and properties on the ground. According to the regulations of the major space-faring nations, the re-entry of a spacecraft should not pose a risk for people on the ground (Inter-Agency Space Debris Coordination Committee, 2007) and the expected *casualty risk* must be below the specified threshold of 10^{-4}.

The main contribution comes from large structures, tanks, and all those parts made with high melting point materials (National Astronautics and Space Administration, 1997, National Astronautics and Space Administration, 2001, National Astronautics and Space Administration, 2011). Several cases of re-entering objects reaching the ground have been documented. For example, in 1991 the re-entry of the USSR's Salyut 7/Kosmos space station (with mass over 36700 kg) occurred over a populated region of Argentina (The Aerospace Corporation, 2016). A similar re-entry occurred in 1979 when the U.S. Skylab re-entered the atmosphere. Other notable re-entries were the 1997 Delta II second stage, the 2000 Delta II second stage, and the 2001 Delta II third stage. In the first case, the thrust chamber, the stainless steel cylindrical tank and a 30 kg pressurant titanium tank were recovered (Ailor et al., 2005, National Astronautics and Space Administration, 1997). In the second case, three objects were recovered in South Africa: a stainless steel propellant tank (about 260 kg), a titanium pressurant spherical tank (33 kg), and a tapered cylinder (30 kg) (National Astronautics and Space

Administration, 2001). In the last case, the Delta third stage tank made of Ti-6Al-4V was recovered in the Saudi Arabia desert (National Astronautics and Space Administration, 2001, Ailor et al., 2005). In addition, flight data has been gathered from the uncontrolled re-entry of the ATV-1 (Snively et al., 2011, Löhle et al., 2011, Blasco et al., 2011) and third stages of launch rockets, which can be used for the validation of the software for the destructive re-entry analysis.

Given the growth of the space traffic in the future and the consequent increase in the frequency of re-entries, more of these objects will reach the ground. If a piece of a medium-to-large spacecraft such as the ones reported above falls onto a densely populated area, this could cause several casualties and related injuries. In addition, houses and industrial buildings could be damaged. However, it is possible to control and prevent these hazards associated with the re-entry of satellites if the spacecraft configuration is carefully designed so that most of it will demise before reaching ground. To do so, the re-entry and demise of spacecrafts must be analysed using specific software packages that evaluate the likely demise of the spacecraft and its components.

1.4.2 Re-entry analysis

In order to assess the compliancy of a spacecraft with the casualty risk threshold, re-entry simulation software is used to analyse the atmospheric re-entry phase of a missions. In general, two types of analyses are performed. At first, a more simplified analysis, with a lower fidelity model and a simpler representation of the spacecraft is carried out. After this first analysis, if the mission is not compliant with the regulations, a more refined, and detailed analysis is performed. The Debris Assessment Software (DAS) (National Astronautics and Space Administration, 2015) and Object Re-entry Survival Analysis Tool (ORSAT) (National Astronautics and Space Administration, 2009) are respectively the low-fidelity and high-fidelity software in use at NASA. The Debris Risk Assessment and Mitigation Analysis (DRAMA) (Martin et al., 2005a) and the Spacecraft Atmospheric Re-entry and Aerothermal Break-Up (SCARAB) (Fritsche and Koppenwallner, 2001, Lips et al., 2004, Koppenwallner et al., 2005, Fritsche et al., 1997, Fritsche et al., 2000) are their analogues in use at ESA. However, the interest in the field of destructive re-entry is growing, and together with it, new software is being developed. For example, the Centre National d’Etudes Spatiales (CNES) is developing the software DEBRISK (Omaly and Spel, 2012) and PAMPERO (Annaloro et al., 2015, Annaloro et al., 2017) to perform independent demise analyses. Another example is represented by the Spacecraft Aerothermal Model (SAM) (Beck et al., 2015b, Beck and Merrifield, 2015) code developed by Belstead Research (Beck and Holbrough, 2014). Alongside destructive re-entry codes, which are mainly used for uncontrolled re-entries, other tools can be used for the assessment of controlled re-entries, especially the ones of manned missions. In this context the tools are used with the opposite objective with respect to destructive re-entry analyses. They have to ensure the survival of the spacecraft and its content. In these cases, the analyses performed have a higher fidelity and the aerothermal loads are precisely computed to assess the resistance of the thermal protection system.

In general, software for the analysis of destructive re-entries shares a similar architecture: the object is geometrically modelled, the re-entry trajectory is simulated given the initial conditions, the aerodynamic and aerothermal loads are computed, the break-up is simulated, the demise of the objects is determined, and the casualty area of the surviving fragments is evaluated. Destructive re-entry codes are usually classified into two categories: object-oriented codes and the spacecraft oriented codes (Lips and Fritsche, 2005).

1.4.2.1 Object-oriented codes

In object-oriented codes, the spacecraft is schematised as a set of individual parts that represent the spacecraft structure, components, and subsystems; for each of these parts an individual re-entry analysis is performed. The spacecraft configuration is modelled using a hierarchical structure with the external structure being the first level and the internal components and sub-components belonging to the following levels. This kind of software usually assumes a fixed break-up altitude in the range 75 to 85 km and a predefined attitude motion of the components (Minisci, 2015a, Lips and Fritsche, 2005). Object oriented codes rely on attitude averaged drag coefficients and heat rates for tumbling objects, together with a correction factor that considers the shape of the object considered. The components are modelled with simple shapes (e.g. sphere, cylinder, and parallelepiped) and are assigned with basic information about materials, size, and mass. Therefore, object-oriented codes are not able to fully describe the spacecraft structure but provide a conservative analysis at a much lower computational cost. Examples of object-oriented codes are NASA’s DAS and ORSAT, and ESA’s DRAMA, which are routinely used to verify the compliance of space missions with the ground safety requirements (Battie et al., 2012, Rochelle et al., 2004).

1.4.2.2 Spacecraft-oriented codes

On the other hand, spacecraft-oriented codes, model the complete spacecraft as close to reality as possible using a triangular mesh schematisation of the spacecraft structure and components. Aerodynamics and aerothermodynamics are analysed for the effective spacecraft geometry. Break-up events and fragmentations are computed using thermal and mechanical load computations. Up to now the only completely spacecraft-oriented code is Spacecraft Atmospheric Re-entry and Aerothermal Break-up (SCARAB), developed by HTG since 1995. In SCARAB, the geometry of the spacecraft is modelled as a panelised structure; each panel has geometrical and mechanical properties attached to it. The material database includes temperature dependent properties. The re-entry trajectory is analysed with a complete six degree-of-freedom computation, thus also considering the attitude motion of the spacecraft. Fragmentation events and separation of the spacecraft into multiple parts are also considered. The aerodynamics and aerothermodynamics are based on local inclination methods where the pressure distribution and the heat rates are functions of the local surface inclination with respect to the external flux. The thermal analysis is based on a twodimensional heat conduction model but heat radiation between each part of the spacecraft is also considered.

1.4.3 Design-for-demise

Emerging from the previous sections it is clear that, during the design of a mission, it is necessary to consider the effects of the disposal through re-entry. Whether this is through a controlled or an uncontrolled re-entry, the safety of people and infrastructure on the ground must be assured within the prescribed limits. Controlled re-entries can ensure the safe landing of the fragments surviving a re-entry by targeting non-populated areas; however, they also have a larger impact on the mission performance compared with uncontrolled re-entries (Waswa and Hoffman, 2012). They require specific attitude determination and control modes for performing the disposal manoeuvres and a bigger launcher may be required given the increased amount of propellant needed and the heavier propulsion subsystem used. In addition, they require a higher level of reliability because a failure of the disposal manoeuvre can endanger people on the ground. Uncontrolled re-entries can thus be advantageous, given their operational simplicity and lower costs, provided that the casualty risk requirements are still met.

In these cases, the compliancy of the mission can only be assured through its design, adopting a so-called *design-for-demise philosophy*. The design-for-demise philosophy aims at reducing the ground casualty risk posed by re-entering spacecraft by favouring the satellite demise during its re-entry. Such a result can be obtained through a series of design choices and solutions to be adopted from the early stages of the mission planning to enhance the demisability of a spacecraft (Waswa and Hoffman, 2012, Kelley, 2012). The general idea is to generate structures and components that require a lower amount of energy to be demised. Among the specific methods employed in designing spacecraft parts to demise, the following can be identified:

- Use of a different material: re-designing a spacecraft using a more demisable material;
- Use of multiple materials: replacing a single non-demisable material with different demisable materials while still maintaining structural integrity;
- Changing the shape: changing the shape of an object can modify its area-to-mass ratio and enhance the demisability;
- Changing the size: changes into the dimensions of a component modify its area-to-mass ratio;
- Changing the thickness results in a change of the mass of the object thus altering the area-to-mass ratio;
- Changing the component location: locating a component close to the exterior structure of the spacecraft can expose the object to the ablative environment earlier than a component located in the inner part of the spacecraft;

- Containment: group objects into one container that survives the re-entry. In this way, the release of many fragments reaching the ground is avoided and thus the casualty area is reduced because it is only the one associated with the container box;
- Enhancing early break-up of components: the early break-up could produce a more prolonged exposure to the re-entry heat load thus promoting the demise of a component.

Alongside these techniques, which are more dedicated to the preliminary design of a spacecraft, it is possible to enhance the demisability of a configuration intervening on the way structure and components are assembled. For example, it is possible to change the design of joints to favour an earlier break-up of the spacecraft.

Currently, NASA considers the demisability only in the later stages of the mission design with a loose integration throughout the project. This often leads to the selection of a controlled re-entry strategy, instead of going through a demisable re-design of the spacecraft in order to comply with casualty risk limitations (Waswa et al., 2013). However, a more integrated approach, where the design-for-demise principles are followed phase-by-phase in the mission life cycle would be more effective and have less impact on the mission costs and timing (Kelley, 2012, Waswa et al., 2013). In general, the implementation of the previously listed strategies is most effective when considered in the early stages of the mission design.

The design-for-demise strategies are only applied to components that are found to be critical in terms of their demisability. Critical parts can be identified in two ways: from prior knowledge of previous re-entry missions where the object taken into account did not demise, or from re-entry analysis with destructive re-entry software (Waswa and Hoffman, 2012). After critical parts are identified, possible methods and design considerations can be adopted to enhance their demisability. Examples of critical parts that usually survive re-entry are propellant tanks and pressure vessels, which are made of high melting point materials such as titanium alloys, stainless steel alloys, or carbon fibre composites. Other critical parts are represented by reaction and momentum wheel assemblies, magneto-torquers, thruster nozzles, telescope lenses, etc.

1.4.4 Debris impact hazard

As introduced in Section 1.1, the threat posed by space debris is recognised by the major national and international agencies, which have proposed regulations and mitigation standards in order to tackle the issue. Nevertheless, the danger posed by possible impacts of space debris on spacecraft structures and components has to be addressed and regarded as a mission design driver because a single impact can compromise an entire mission (Grassi et al., 2014, Stokes et al., 2012, Christiansen et al., 2009). In fact, the number of space debris is increasing, and appears to have rapid growth (Lewis et al., 2017a, Lewis et al., 2017b, Radtke et al., 2017, Lewis et al., 2012) at certain altitudes, especially high-inclination orbits, which are the most densely populated (Liou and Johnson, 2006).

The space debris population accounts for about 29000 objects larger than 10 cm, 750000 objects between 1 cm to 10 cm, and 166 million objects from 1 mm to 1 cm (Space Debris Office, 2017). In Low Earth Orbit (LEO) orbits, only particles larger than 10 cm can be tracked (Schaub et al., 2015). Consequently, only for such particles can a spacecraft perform collision avoidance manoeuvres. However, even particles below this threshold can damage a spacecraft. In particular, particles between 1 cm and 10 cm can still cause the break-up of a spacecraft, and particles below 1 cm can still be extremely dangerous for spacecraft parts and components (Schaub et al., 2015, Stokes et al., 2012). As even untraceable debris can be dangerous for the mission survival, it is necessary to adopt specific measures to ensure the mission success. It is necessary to assess the amount of damage caused be space debris, what are the most vulnerable parts of the spacecraft, and to devise solution to enhance the protection of the spacecraft.

1.4.5 Space debris environment modelling

The knowledge of the debris and meteoroid environment surrounding the Earth is of fundamental importance to predict the damage that these particles can cause to a spacecraft. The number of particles, their density, velocity, size, and distribution are all required to compute the frequency and assess the effect of debris impacts on spacecraft structures and components. All this information can be accessed through space environmental models, which provide information in the form of flux distributions used to predict impacts on the spacecraft geometry.

The two main software tools today available are ESA's Meteoroid and Space Debris Terrestrial Environment Reference (MASTER-2009) (Flegel, 2011) and NASA's Orbital Debris Engineering Model (ORDEM) (Stansbery, 2014). As the two codes are very similar, for the purpose of this project it was decided to use the ESA tool. Consequently, the following description only concerns the MASTER-2009 characteristics. "*The purpose of MASTER is the characterisation of the natural and the man-made particulate environment of the Earth*" (Flegel, 2011). For the man-made space debris, the model adopted by MASTER is semi-deterministic in the sense that its analysis starts from a reference population of all the major sources of space debris. The debris sources considered include spent payloads and upper stages, fragmentations from explosions and collisions, dust and slag from solid rocket motors firing, sodium-potassium coolant droplets from the RORSAT (Rossi et al., 1997) satellite, surface degradation particles, and multi-layer insulation. For each of these sources, MASTER uses a corresponding model to generate mass and diameter distributions, and velocities and directional spreading; then a perturbation model is used to propagate the orbits of all objects. For the meteoroid environment MASTER uses the Divine-Staubach model (Flegel, 2011) for the back-ground component. The seasonal meteoroid streams are also available through the Cour-Palais (Flegel, 2011) or Jenniskens-McBride (Flegel, 2011) models. In a MASTER-2009 simulation, the target orbit is specified through its orbital elements and the start and end epochs of the simulation have to be defined. Moreover, a mitigation scenario among *business as usual*, *intermediate* *mitigation* and *full mitigation* can be selected to assess the spacecraft survivability in different future debris environments. The output provided by MASTER is in the form of debris flux distributions as a function of several parameters (e.g. particle dimeter, impact angles, etc), which are used in debris impact analysis software packages to predict the damage on spacecraft caused by space debris.

1.4.6 Debris impact analysis

The procedures and methods that must be followed when performing a survivability analysis can be found in the NASA Handbook for Designing MMOD Protection (Christiansen *et al.*, 2009) and in the IADC Protection Manual (F. Schäfer *et al.*, 2005b). Following these two documents, it is possible to extrapolate an overall methodology for the assessment of damage caused by debris impact. This methodology first involves the knowledge of the micrometeoroids and orbital debris environment and of the geometrical characteristics of the spacecraft. Then the high velocity impacts hazard has to be assessed for each exposed component using the Ballistic Limit Equations (BLE) (FK Schäfer *et al.*, 2008, Shannon Ryan and Christiansen, 2010, S Ryan and Christiansen, 2011), and the failure criteria for equation used has to be defined. Information from the debris environmental model, the spacecraft geometry, and the critical diameter computed with ballistic limit equations are then used to perform a probabilistic analysis of the entire spacecraft structure and compute the probability-of-no-failure for the entire mission. This computation is carried out using Poisson statistics (Welty *et al.*, 2013), considering that the impacts from debris particles are statistically independent from each other. The result of this analysis must be compared with the requirements of the mission. If the computed probability of failure is greater than the established one, the design of the spacecraft must be iteratively revised to meet them. The survivability analysis can be carried out with different level of detail, depending on the design stage of the mission. Two different procedures can be identified (British Standards, 2014), one referred to as *simple impact risk analysis* and the other one as *detailed impact risk analysis*. The former is indicated to perform a preliminary assessment of how possible impact induced failures can compromise the successful post mission disposal of a spacecraft. If this analysis shows a significant probability of failure, a more detailed analysis must be performed. In this case, a complete modelling of the satellite geometry is required, and an impact analysis on a component-based level must be performed considering the complete properties of the debris flux environment (flux directionality, velocity, and size distributions of the particles, etc.).

1.4.6.1 Software packages for vulnerability assessment

The debris impact assessment of a mission is performed using specific software packages. In general, these codes have a common structure. The satellite is modelled through a geometric representation (which can be more or less detailed) and is then “flown” into the space environment. The nature and frequency of the impacts on the structure and components of the spacecraft is evaluated and the damage associated with them is computed using semi-empirical relationships. Finally, the software packages provide the results of the analysis in the form of number of impacts, number of penetrations, impact probability, and penetration probability for the overall configuration and for the single components.

Today, a few software packages are used by the major space agencies to perform impact survivability analyses. BUMPER (Bjorkman et al., 2014) is used by NASA and JAXA, ESABASE2/DEBRIS (Gäde and Miller, 2013) is used by ESA, and SHIELD (Stokes et al., 2000, Stokes and Swinerd, 2005) was used to support the relevant activities of the British National Space Centre (BNSC). All of these software codes perform the risk analysis with the possibility to define complex spacecraft geometries, considering different materials and shielding options, as well as mutual shielding between components. The geometrical schematisation is usually achieved by modelling the spacecraft structure with a set of panels. To the panels are assigned the properties and characteristics required for the impact analysis (Grassi et al., 2014, Gäde and Miller, 2013, Stokes et al., 2000, Welty et al., 2013), such as the material, the shielding configuration, the thickness, and the geometry of the shield itself.

1.4.6.2 Type of impacts and Ballistic Limit Equations

When a particle impacts the satellite, the type of impact and its effects need to be assessed. The primary way in which the impact is assessed is by using BLEs Ryan and Christiansen (2011), (Ryan and Christiansen, 2010). They represent a set of analytical expressions that allow the computation of the critical diameter of particle that will produce a failure of a spacecraft system/component as a function of the impact speed, angle, projectile density, and target characteristics. The ballistic limit equations have expressions changing as functions of the type of shield and of the type of impact. In general, three different velocity regimes are considered for an impact: ballistic, hypervelocity and shatter regime (Shannon and Christiansen, 2009, Ryan and Christiansen, 2010, Ryan and Christiansen, 2011), for which the shield has different behaviour after the impact. An impact belongs to a specific regime based on its relative impact velocity with the considered structure. The ballistic limit equations are further divided by the shielding type: single wall, double wall, triple wall, and advanced shielding concepts have been developed. Single wall BLEs are subdivided according to the material of the shield, from classical metallic materials such as aluminium, titanium, and stainless steel, to Carbon Fibre Reinforced Plastics (CFRP), fiberglass, glass, and polycarbonate. Dual wall shields are instead subdivided into two categories: the standard metallic Whipple shield (Ryan and Christiansen, 2010), and the Honeycomb Sandwich Panels (HC-SP). Inside the dual wall BLEs, the material and geometrical properties of the front and rear wall of the shield are taken into consideration. The triple wall equation is similar to the dual wall configuration in the sense that allows the user to define the material and geometrical characteristics of all the three faces of the shielding configuration. The triple wall BLE is usually referred as the Schaefer-Ryan-Lambert (SRL) equation (Schäfer et al., 2008, Ryan et al., 2008); it is a very versatile equation that can be adapted to the computation of even dual and single wall structures. The SRL BLE is, in fact, the most commonly used ballistic limit equation in the vulnerability analysis of spacecraft (Putzar and Schäfer, 2006, Grassi et al., 2014, Welty et al., 2013). It allows computation of the critical diameter for equipment placed inside the main structure of the satellite by considering the last plate of the triple wall configuration to be the face of the equipment considered. In general, if a particle has a diameter greater than the critical diameter computed with the BLE, a penetration is considered to occur.

1.4.6.3 Impact assessment methodology

To use the ballistic limit equations, we need to know the impact direction and velocity of the debris particles. As a general approach, a space environmental model (Section 1.4.5) is used to generate a set of debris flux distributions that describe the environment surrounding the spacecraft at a certain orbit and for a certain mission time. However, the impact velocity and direction cannot be directly obtained from the fluxes data. A common procedure to process this data, that is at the very base of software like ESABASE/DEBRIS (Gäde and Miller, 2013) and SHIELD (Stokes et al., 2000), is to perform a random sampling of the distributions to generate a large number of impacting particles having a defined diameter, velocity, and direction. Consequently, a representative population of the debris environment can be generated, and the particles obtained with this procedure can be "shot" towards the satellite structure and the survivability analysis can be performed. This kind of procedure should be repeated several times in a Monte Carlo fashion in order to have a meaningful and robust representation of the actual debris environment Stokes et al. (2000).

A different methodology that can be used and that is the main inspiration of the present work can be found in Welty et al. (2013). Here the full Monte Carlo approach of generating random particles is substituted with a semi-deterministic approach in which the discretised output of a debris fluxes model is directly assessed, eliminating the need to generate and sample secondary distributions. The debris flux model is used to predict the directional particle fluxes encountered by the spacecraft and then the individual particle fluxes are evaluated deterministically. The areas of the satellite structure and components that are susceptible to debris impact are determined, projecting the areas perpendicularly to the velocity vector of the particles. In this way, the exposed area of the components is calculated depending on the individual direction of the particles impacting the satellite.

Regardless of the methodology used, the final output of a survivability analysis is the probability of the spacecraft to suffer a damage from space debris given its characteristics, its orbit, and the mission lifetime. Some software packages directly correlate the probability of penetration to the damage probability (Gäde and Miller, 2013), other instead try also to account for the fact that a penetration does not necessarily translates into damage (Stokes et al., 2000, Stokes and Swinerd, 2005).

1.4.7 Spacecraft protection

When looking at the survivability of a spacecraft there are some measures that can be taken in order to improve the protection of a spacecraft. Such measures involve changing the shielding configuration, selecting different and more resistant materials, modifying the geometry in order, for example, to increase the thickness and reduce the area susceptible to particle impacts, and to adapt the position of the components inside the satellite to protect the most critical ones. Some examples of survivability studies and effects of design adjustments on reference missions can be found in Bunte et al. (2009), Stokes and Swinerd (2005), Reimerdes and Wohlers (2001), Kuiper et al. (2010), and Stokes et al. (2012).

1.4.8 Spacecraft design and multi-objective optimisation

As described in the previous sections, the foundations of this project lie in the fields of spacecraft re-entry, design-for-demise, and debris impact protection. All of these aspects are influenced by common parameters and design choices. However, the demisability and the survivability can be influenced differently and in a possibly contrasting fashion. Using a multi-objective optimisation framework enables trade-off solutions to be found that consider both of these requirements. The outcome from these trade-offs will be a large set of possible preliminary solutions that consider the demisability and the survivability from the earliest stage of the mission development.

In the context of multi-objective optimisation, it is not possible to find the optimum solution in the same way as it is defined for single objective optimisation problems (Deb, 2001). The concept of *dominance* needs to be used in this case. In fact, in multi-objective optimisation, a solution is said to dominate another solution if it is better in all of the objective functions, or if it is strictly better than the other solution in at least one objective. In a set of solutions, all of the individuals that are not dominated by any other member of the set are called non-dominated individuals. These non-dominated solutions constitute the so-called *Pareto front* that is the set of *Pareto-optimal solution*. Any two points on the *Pareto front* are such that a gain in one objective can only happen if there is a sacrifice in another objective. This process in the end generates a set of trade-off solutions from which it is possible to choose using higher-level information (Sanchez et al., 2009).

In order to solve multi-objective optimisation problems, it is possible to adopt gradient-based methods. Such methods, however, require the objective functions to be continuous. Therefore, for the case in question, such an option is not viable because the problem contains a mix of continuous (i.e. dimensions) and discrete variables (i.e. types of materials). In case a classical gradient-based method cannot be used, it is possible to rely on different approaches such as search algorithms or heuristic algorithms. As presented in Reimerdes and Wohlers (2001), search algorithms explore the parameter space according to a specified method for a direction (i.e. gradient) or a point where an improvement is obtained. This kind of algorithm are generally very good to find local optima, but they also tend not to move away from such local optima once they have found it, therefore neglecting the global optimum. For that reason, a priori knowledge of the proximity of the global optimum is usually necessary. Heuristic algorithms such as genetic algorithms or simulated annealing make use of natural principles to select optimal solutions. Genetic algorithms (Deb, 2001, Mitchell, 1995) apply the principles of natural evolution. They have a set of starting points (a population of individuals) in the search space and they evaluate the fitness at these points. Then, using a set of genetic operators such as crossover, mutation and selection (Deb et al., 2002, Deb, 2001) they find a new population, which constitutes the next generation of solutions. After each generation, the individuals are evaluated according to the objective functions of the problem and they are ranked based on their fitness. The probability of an individual to survive to the next generation depends on its fitness level and on chance. As the genetic operators have a certain amount of randomness, the algorithm is capable of leaving local optima and searching the space for global optimum.

Although many types of heuristic algorithm exist, the current work has focused on using genetic algorithms in order to solve the survivability-demisability problem. Such a decision arises from the fact that genetic algorithms are widely used and are supported by extensive documentation and test cases (Mitchell, 1995, Deb et al., 2002, Reimerdes and Wohlers, 2001). They have already been used in the aerospace sector to solve problems such as spacecraft trajectory design (Deb, 2001, Colombo et al., 2015, Vasile and Colombo, 2008, Sanchez et al., 2009). In addition, problems similar to the one posed in this work, which involves mixed variable types (continuous and discrete), have been tackled using genetic algorithms. In Reimerdes and Wohlers (2001) they were used to optimise the shielding thickness of a sample cubic spacecraft against the impact from meteoroids. In Stokes et al. (2000), Stokes and Swinerd (2005) a genetic algorithm was used to optimise an entire debris protection layout for satellites, from the thickness of the shielding to the position of the components inside the spacecraft. Applications of genetic algorithms in optimising the preliminary configuration of a spacecraft during the conceptual design phase have also been reported (Mosher, 1999, Minisci, 2015b).

1.5 Methodologies developed and implemented

The present research focuses on the problem of the implementation of design-for-demise options and their consequent effect on the survivability of a spacecraft to debris impacts. The strategy adopted in the present thesis has focused first on a general understanding of the design-for-demise problem and its effects on the demisability and survivability of spacecraft components and structures. Subsequently, the attention of the analysis has shifted towards the development of an integrated framework, whose aim is to provide a tool to explore the space of the possible preliminary spacecraft configurations considering the effects of the design options on the demisability and the survivability. This is a novel approach, which tries to directly integrate the two models to simultaneously perform a concurrent analysis of the demisability and survivability of preliminary spacecraft designs.

1.5.1 Development of the demisability and survivability models

To assess the demisability and the survivability of components, structures, and entire spacecraft configurations it is necessary to use models that are able to perform an atmospheric re-entry simulation and a debris impact assessment simulation respectively. Software packages that perform such assessments already exist. Of these packages, only few are freely available or available on request. For the objectives of the this research, we are looking for demisability and survivability models possessing specific characteristics that allow the assessment of most of the design-for-demise strategies (Section 4.1) with a sufficient level of detail, while still maintaining a general approach suitable for the preliminary design phases of a mission. In addition, the two models have to possess a comparable level of detail and a comparable computational time, as they need to be used together in a multi-objective optimisation framework. It is also desirable for these models to share the same input for the satellite configuration in order to better compare the results obtained from the two different analyses and simplify the setup of the simulations in the multi-objective optimisation framework. As most of the design-for-demise strategies are concerned with changing the component's material, dimensions, and shape, it was decided to use an object-oriented approach for the demisability assessment. This approach is considered to have a sufficient level of detail as it is commonly adopted for the assessment of ESA, NASA, and JAXA missions during the early development stages. As previously introduced, software packages that perform such assessments are available to the public (DAS, DRAMA). However, it is also important to consider the possibility to have an early detachment of the external panels of the spacecraft structures and the possibility to attach components to these panels to have a longer exposure to the harsh aerothermal environment of the re-entry. Attaching the components to the external panels, as is common in the assembly of actual spacecraft can also influence the survivability of the satellite. In fact, components are more or less vulnerable to debris impacts depending on the distance from the shielding panel. In addition, it was considered important to have the ability to specify the type of shielding (single wall, Whipple, honeycomb sandwich panel) for the external panels of the spacecraft structure as they are important in the survivability assessment and could affect the demisability of the satellite. Such characteristics, however, are not currently implemented in the already available re-entry software packages. For the case of the survivability model, it was observed that there is a considerable gap between the more simplified models and the more complex ones. For instance, simplified models like DRAMA MIDAS (Gelhaus et al., 2014, Gelhaus et al., 2013, Martin et al., 2005b) only consider the external structure of the satellite, which can be defined on a panel-by-panel basis. ESABASE2/DEBRIS is instead able to perform highly detailed simulations, allowing the user to define complicated structures through a panelised representation and to specify different types of shielding techniques and impact assessment methodologies. As input to the model, the position, and orientation of each component and/or panel, constituting the satellite assembly is required. However, this is quite a different approach with respect to the available re-entry packages, making them hardly compatible with each other for what concerns the configuration input to be provided. In addition, ESABASE2/DEBRIS is not directly able to assess the survivability of components placed inside the main spacecraft structure. For these components, the user is required to use an alternative and rather complex approach that is to "remove" the external structure of the satellite and only model the internal components. The external structure is then considered by specifying the standoff distance for each of the panels belonging to the internal components. This can be a long and complex approach, especially for the integration inside the multi-objective optimisation framework.

Considering all these aspects, it was decided to develop a demisability and a survivability model. This decision was mainly driven by the lack of features in available models, and the low compatibility between the configuration inputs for the two commercial software tools available. The presented models, on the other hand, have been developed in parallel, with the clear aim of having two compatible and interlinked tools. This introduces a considerable advantage in terms of facility of use, integration, and understanding of the process; in addition, it enables modification of the models and the implementation of new features if needed. The idea is to use two *quasi object-oriented codes*. These codes need to maintain the simplicity of object-oriented codes, especially in the phase of the configuration definition, while adding some elements of complexity. Such elements of complexity are the features that enable the compatibility between the two models. In fact, object-oriented demisability model do not require the characterisation of the external panels of the structure (including their shielding capabilities), and do not consider the attachment of internal components. However, these features are important in the survivability analysis, and had to be considered so that the two models could be used in combination.

1.5.2 Demisability and survivability criteria

The results obtained with the simulations of the demisability and survivability models need to be summarised by indices that integrate the information obtained into single scores that can efficiently represent the effects of design choices onto the demisability and the survivability of preliminary spacecraft configurations. The result has been the definition of two indices.

These indices also represent the objective functions used inside the multi-objective optimisation framework. For the demisability we are not only interested in the casualty risk associated with a re-entry, but we are mostly interested in the consequences on the actual demise of the objects following changes in their design. Consequently, the demisability index represents how much a design is demisable and is not strictly related to the casualty risk on ground. For the survivability index, the objective is to summarise information on the vulnerability of components and spacecraft configurations to debris impacts. In general, this could be expressed through the probability of a failure of the satellite; however, it can be quite complex as redundancies and the probability of having a failure due to an impact are difficult to compute. Consequently, it was decided to use for the survivability index an expression only related to the penetration probability experienced by the spacecraft and its components.

1.5.3 Sensitivity analysis of the demisability and survivability to design-for-demise techniques

The models for the analysis of the survivability and of the demisability have been developed throughout the entire duration of the project. Consequently, some of the analyses have been performed using different versions of the models. The sensitivity analysis on the main preliminary design parameters connected to design-for-demise techniques was performed using a first version of the models as described in Chapter 2 and Chapter 3. The analysis starts with a sensitivity study on the most influential mission related parameters affecting the demisability and the survivability. This first analysis is of importance as it allows the identification of less important parameters that can then be neglected in subsequent analyses, which are the ones related to the design-for-demise. Following this, the identification of the main design parameters related to the design-for-demise methodologies and the sensitivity analysis concerning them for both the demisability and the survivability indices were completed. The sensitivity analyses were performed using the Sobol methodology, which quantitatively assesses the indices sensitivity to the design-for-demise parameters by computing the variance on the output caused by the variation of each parameter considered.

1.5.4 Demisability and survivability design maps

The process of identifying the most influential mission related parameters and the most important design-for-demise parameters for both the demisability and the survivability criteria has also led the foundation for a further methodology proposed in this work. The methodology proposes the creation of a database of maps in order to quickly estimate the demisability and the survivability of simplified spacecraft components as a function of the most important design parameters, which have been identified by the sensitivity analysis study. In addition, the maps can be created for various initial conditions, but only for the most influential initial conditions, which have been again identified in the sensitivity analysis. The idea is to use these maps as a very quick estimation tool in the initial phases of the design of a mission in order to rule out unfit solutions and simplify the analysis in the following steps of the design procedure.

1.5.5 Multi-objective optimisation framework

As previously introduced, the continuous development of the models also translated into a stepwise development of the methodologies implemented in the thesis. With the increased capabilities of the models, it was decided to develop a more integrated framework that could directly exploit the features of the two models for the demisability and survivability analysis of full preliminary spacecraft configurations. A multi-objective optimisation framework that would integrate the two models and the devised demisability and survivability criteria in order to explore the search space of solutions with competing demisability and survivability has been developed. In this way, it is possible to obtain a large variety of preliminary solutions that can be used as a starting point for the next development phases of a mission. The advantage is that these solutions have been generated already considering the requirements arising from the demisability and the survivability. Nowadays, these requirements are only considered in the latest stages of the mission design, which can cause delays and increased costs. Considering them from the beginning of the mission design would be beneficial in both senses. The developed framework is then applied first to a simplified test case that considers tank assemblies of different classes of missions, also considering the requirements arising from constraints relative to specific types of components.

1.5.6 Demisability index development

At this point, it is interesting to explore the definition of the criteria used for part of the thesis. In particular, the work focuses on the demisability index, and, specifically, on the possibility to add additional terms to the index. Such a decision arises from the willingness to include in the demisability index other interesting aspects of the re-entry process such as the casualty area on ground of the surviving fragments and the demisability altitudes of the demised fragments. Consequently, different options for the new index structure have been studied and an expression for the index has been devised. As this new formulation of the index is a combination of three different contributions (residual mass, casualty area, and demise altitude), it was also considered interesting to study how the index changes as the weights of the different terms change. Moreover, the behaviour of the new index with respect to the spacecraft mass has been studied and its results compared with the one obtained from the original index (Liquid Mass Fraction) for the same test case.

1.6 Contributions

The contents of this thesis have been published in three standalone journal papers. The overall body of the thesis, with the exception of a few parts, are contained in the three publications. The first part of the thesis, which includes the description of the first stage of development of the demisability and survivability models and their application to the sensitivity analysis of the design-for-demise options, has been published in Acta Astronautica (Trisolini et al., 2018a). The part concerning the development of the models has also been presented at the 2015 International Astronautical Congress in Jerusalem, Israel (Trisolini et al., 2015). The results associated with the development of the demisability and survivability-combined maps related to spacecraft components and structures has been published in the Journal of Space Safety Engineering (Trisolini et al., 2016b) and presented at the 8th International Association for the Advancement of Space Safety Conference in Melbourne, Florida (Trisolini et al., 2016a). The second part of the thesis, with the description of the updated models, the development of the multi-objective optimisation framework, and its application to a test case has been published in Aerospace Science and Technology (Trisolini et al., 2018b)and presented at the 2016 International Astronautical Congress in Guadalajara, Mexico (Trisolini et al., 2017a).

In addition to these contributions, the development of the multi-objective optimisation containing the implementation of component specific constraints into the optimisation algorithm has been presented as poster at the 8th European Conference on Space Debris in Darmstadt, Germany (Trisolini et al., 2017b). Moreover, a further development of the survivability model, containing a novel methodology for the quantification of the mutual shielding of components against the debris ejecta generated after an impact has been presented at the 2017 International Astronautical Congress in Adelaide, Australia (Trisolini et al., 2016d). This contribution also contains the description of the constraint implementation in the multi-objective optimisation framework, together with a relevant test case. For both the 2016 and 2017 International Astronautical Congress contributions, the papers have been preselected for publication in Acta Astronautica as among the best contributions of the sessions. Two journal articles based on this conference contribution are under preparation. A first one describing the application of component related constraints into the multi-optimisation framework and comparing the results of the constrained optimisation with the unconstrained one for a relevant test case. A second one, which describes the methodology developed for the assessment of the debris impact on internal component and the procedure used to evaluate the mutual shielding between components.

Journal publications

- M. Trisolini, H.G. Lewis, C. Colombo, Demisability and survivability sensitivity to design-for-demise techniques, *Acta Astronautica*, April 2018, Vol. 145, pp. 357-384, DOI: 10.1016/j.actaastro.2018.01.050
- M. Trisolini, H.G. Lewis, C. Colombo, Demise and survivability criteria for spacecraft design optimisation, *Journal of Space Safety Engineering*, 2016, Vol. 3, Issue 2, pp. 83-93, DOI: 10.1016/S2468-8967(16)30023-4
- M. Trisolini, H.G. Lewis, C. Colombo, Spacecraft design optimisation for demise and survivability, Aerospace Science and Technology, 2018, Vol. 77, pp. 638-657, DOI: 10.1016/j.ast.2018.04.006

Conference publications

- M. Trisolini, H.G. Lewis, C. Colombo, Demisability and survivability multi-objective optimisation for preliminary spacecraft, Proceedings of the 68th International Astronautical Congress, 25-29 September 2017, Adelaide, Australia
- M. Trisolini, H.G. Lewis, C. Colombo, On the demisability and survivability of modern spacecraft, Proceedings of the 8th European Conference on Space Debris, 18-21 April 2017, ESOC, Darmstadt, Germany
- M. Trisolini, H.G. Lewis, C. Colombo, Multi-objective optimisation for spacecraft design for demise and survivability, Proceedings of the Stardust Final Conference, 31st October – 4th November 2016, ESTEC, Noordwijk, The Netherlands

- M. Trisolini, H.G. Lewis, C. Colombo, Spacecraft design optimisation for demise and survivability, Proceedings of the 67th International Astronautical Congress (IAC), 26-30 September 2016, Guadalajara, Mexico
- M. Trisolini, H.G. Lewis, C. Colombo, Demise and survivability criteria for spacecraft design optimisation, Proceedings of the 8th IAASS Conference, 18-20 May 2016, Melbourne, Florida, USA
- M. Trisolini, H.G. Lewis, C. Colombo, Survivability and Demise Criteria for Sustainable Spacecraft Design, Proceedings of the 66th International Astronautical Conference (IAC), 12-16 October 2015, Jerusalem, Israel

1.7 Thesis structure

The thesis is organised in eight chapters and its structure follows the development process of the project. Each chapter opens with a brief introduction on the topic, follows the description of the theoretical background and methods adopted. Subsequently, examples and results are presented.

Chapter 2 and Chapter 3 contain the description of the first stage of development of the demisability and survivability models. In Chapter 4, the application of the models to the analysis of the design-for-demise techniques is described. First, the main design-for-demise techniques are identified. Subsequently, a sensitivity analysis on the inputs to the demisability and survivability models is carried out. Finally, a sensitivity analysis on the design-for-demise techniques is performed. Concluding the chapter is a summary of the most influential design-for-demise techniques identified through the sensitivity analysis for both the demisability and the survivability.

Chapter 5 and Chapter 6 contain the description of the second stage of development of the demisability and survivability models respectively.

Chapter 7 describes a methodology developed to consider both the demisability and survivability requirements since the early stage of mission design in a comprehensive way. First, the methodology is presented together with the motivations for its selection. Following this, a first implementation of the methodology on a representative example, which is able to show its main characteristics and features, is presented. The chapter also includes a further analysis on the demisability index and its development into a more refined formulation.

Chapter 8 presents the findings and conclusion of the thesis and gives an insight on the future possible development of this work.

Chapter 2 Demisability model

The developed demisability model can be classified under the category of object-oriented codes (Kelley et al., 2010, Lips and Fritsche, 2005). It can simulate the three degree-of-freedom trajectories for elementary geometrical shapes representative of spacecraft components, i.e., sphere, cylinder, flat plate, box, assuming a predefined random tumbling motion. The ablation is analysed with a lumped mass model; when the melting temperature is reached, the mass is considered to vary as a function of the heat of ablation of the material. All the material properties are temperature independent and have an average value from the ambient temperature up to the melting temperature. Average drag coefficients, shape factors, and correlations needed to describe the aerodynamic and aero-thermodynamic behaviour of the tumbling object were gathered or derived from the literature. The demise is assessed as the ratio between the residual mass of the object after the re-entry and its initial mass.

The model is the result of a major work of unification of the different sources of information for the heat rate correlations, drag coefficients expressions, and material behaviour sparsely found in the literature.

Section 2.1 contains a general description of the architecture of the model. Follows in Section 2.2 the description of the models used to describe the re-entry dynamics, specifically the equations of motions (Section 2.2.1), the Earth's gravity model (Section 2.2.2), the atmosphere model (Section 2.2.2), and the aerodynamic coefficients used (Section 2.2.3). Section 2.3 describes the models adopted for the prediction of the aerothermodynamic loads and for the calculation of the ablation of the objects. Finally, Section 2.4 provides the verification between the developed model and the state of the art destructive re-entry model SAM (Beck et al., 2015a).

Part of the chapter follows the content of the Acta Astronautica journal publication "Demisability and survivability sensitivity to design-for-demise techniques" (Trisolini et al., 2018a).

2.1 Model architecture

This section contains an overall description of the demisability model. Figure 1 is a schematic representation of the computational procedure followed by the model. Before starting a simulation, the user is required to provide a set of inputs. First the geometry of the re-entering object has to be defined in terms of its shape (sphere, cylinder, flat plate, or box), size (the radius and thickness for a sphere for example), and material. Then the initial conditions of the descent orbit need to be specified. These represent the position of the object at a specific atmosphere interface, typically 120 km (Kelley et al., 2010, Lips and Fritsche, 2005, Beck et al., 2015a, Beck et al., 2015b). The initial conditions are provided in terms of starting latitude, longitude, heading angle, relative velocity, flight path angle, altitude, and initial temperature of the object. Finally, the integration options such as the time interval of the integration, the time step, and the tolerances of the integrator have to be provided. Once all the inputs are defined, the trajectory and the geometry of the object are propagated. The geometry changes only if the melting point is reached during the descent. The solver adopted is the Runge-Kutta-Fehlberg adaptive method of order 45 available in the python library *odespy* (Langtangen and Wang, 2015). A default step size of 0.5 seconds is used for the integration. During the simulation, the trajectory is propagated using the equations of motion (Section 2.2.1), providing a step-by-step update of the forces acting on the objects, i.e. gravity and drag. In fact, such contributions depend on the position of the spacecraft (altitude, latitude, and longitude), on its velocity, and on its geometry. Alongside the integration of the trajectory, the heat load on the object is evaluated by computing at every step the shape factors, which depend on the altitude, velocity, and geometry of the object (Section 2.3.1).

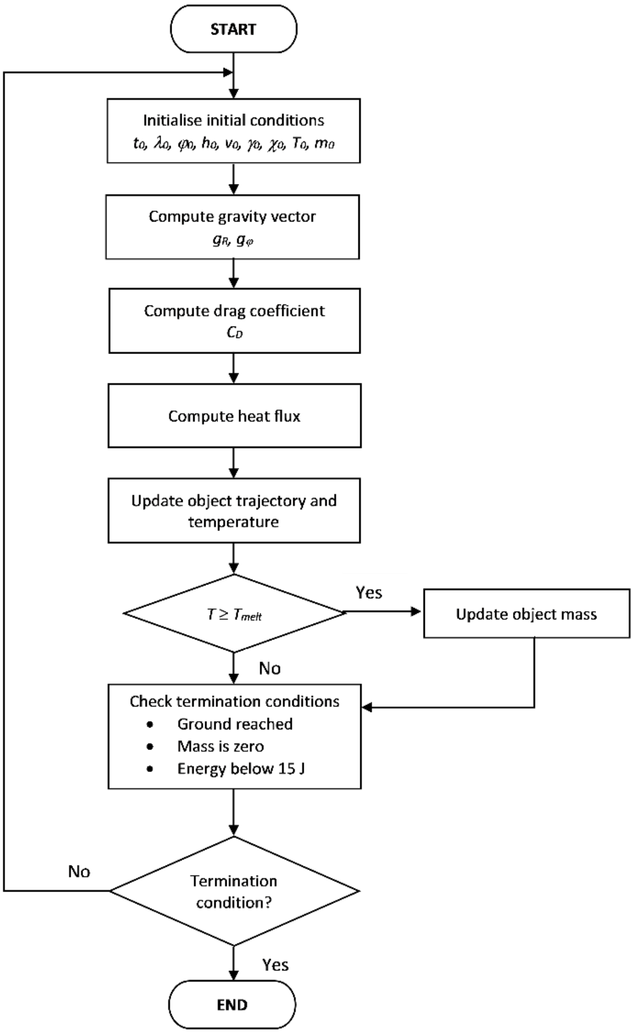

Figure 1: Flow diagram for the procedure used in the integration of the re-entry trajectory.

The simulation continues until one of the termination conditions is met or the integration time limit is reached. The termination conditions correspond to the melting of the object (the mass reaches zero) or to the object reaching the ground (the altitude is zero). The simulation is also terminated when the energy of the object drops below 15 J. The decision is justified by the fact that 15 J has been selected as the threshold below which a re-entering object does not pose risk for people on the ground. After the simulation terminates the output is saved as a text file. The output file includes the time history of the state vector (altitude, velocity, etc.).

2.2 Re-entry dynamics

The present section contains a description of the models used to describe the dynamics of a re-entering object. Specifically, the adopted equations of motion, the description of the Earth's gravity field and atmosphere, and the computation of the aerodynamic forces. The re-entry model implements a three degree-of-freedom model, which describes the evolution of the re-entry trajectory considering the spacecraft as a point mass with a predefined attitude motion. Therefore, the aerodynamic forces acting on the spacecraft (lift and drag) assume an averaged value that is a function of the spacecraft's main shape and of its tumbling attitude motion.

2.2.1 Equations of motion

As the aerodynamic forces on the spacecraft are due to the motion of the spacecraft relative to the atmosphere of the planet, it is convenient to express the equations of motion in a reference frame rotating with the atmosphere. Because a planet's atmosphere rotates with it, it is possible to define a planet-fixed reference frame to express the equations of atmospheric flight. This Earth-fixed Earth-centred reference (*SXYZ*) frame is shown in Figure 2 together with the local horizon reference frame (*oxyz*).

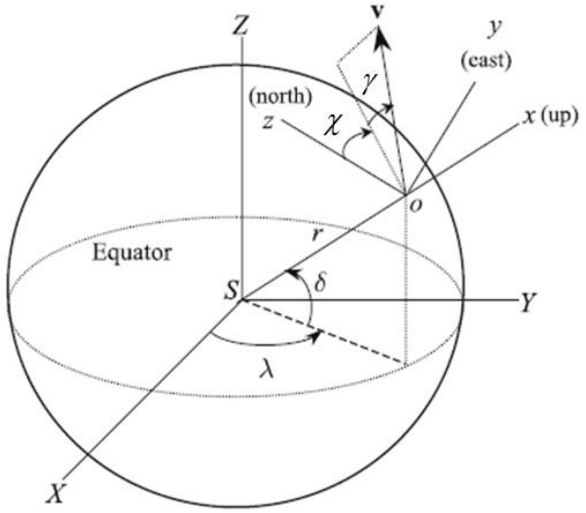

Figure 2: Earth-fixed (*SXYZ*) and local horizon reference frame (*oxyz*) (Tewari, 2007).

The kinematic equations of motion (Tewari, 2007) are

$$\dot{r} = V \cdot \sin\gamma \tag{2.1}$$

$$\dot{\delta} = \frac{V}{r} \cdot \cos\gamma \cdot \cos\chi \tag{2.2}$$

$$\dot{\lambda} = \frac{V \cdot \cos\gamma \cdot \sin\chi}{r \cdot \cos\delta} \tag{2.3}$$

where *V* is the velocity of the spacecraft relative to the atmosphere, γ is the flight path angle, χ is the azimuth angle in the local horizon plane, and δ is the latitude. The dynamic equations of motion can then be written as follows (Tewari, 2007):

$$\begin{gathered}\dot{V} = -\frac{F_D}{m} - g_r \cdot \sin\gamma + g_\delta \cdot \cos\gamma \cdot \cos\chi \\ -\omega_e^2 \cdot r \cdot \cos\delta \cdot (\cos\gamma \cdot \cos\chi \cdot \sin\delta - \sin\gamma \cdot \cos\delta)\end{gathered} \tag{2.4}$$

$$\begin{gathered}V \cdot cos\gamma \cdot \dot{\chi} = \frac{V}{r} \cdot cos^2\gamma \cdot sin\chi \cdot tan\delta - g_\delta \cdot sin\chi + \omega^2 \cdot r \cdot sin\chi \cdot sin\delta \cdot cos\delta \\ -2 \cdot \omega_e \cdot V \cdot (sin\gamma \cdot cos\chi \cdot cos\delta - cos\gamma \cdot sin\delta)\end{gathered} \tag{2.5}$$

$$\begin{gathered}V \cdot \gamma = \left(\frac{V^2}{r} - g_r\right) \cdot \cos\gamma + \frac{F_L}{m} - g_\delta \cdot \sin\gamma \cdot \cos\chi \\ +\omega_e^2 \cdot r \cdot \cos\delta \cdot (\sin\gamma \cdot \cos\chi \cdot \sin\delta + \cos\gamma \cdot \cos\delta) \\ +2 \cdot \omega_e \cdot V \cdot \sin\chi \cdot \cos\delta\end{gathered} \tag{2.6}$$

where ω_e is the angular rotational velocity of the Earth, F_L is the lift force, F_D is the drag force, and g_r and g_δ are the radial and transversal component of the gravitational acceleration, respectively. For the purpose of this work, only uncontrolled re-entries are considered. Consequently, the thrust component in the dynamics equations is neglected and only the aerodynamic and the gravitational forces are considered. In general, for an uncontrolled re-entry, also the lift can be assumed negligible as spacecrafts usually do not have aerodynamic shapes and tend to assume a random attitude during the re-entry. The complete set of governing Eqs. (2.1)-(2.6) can be integrated in time to obtain the position and the velocity of the spacecraft at every time instant along the trajectory.

2.2.2 Re-entry environment

During the descent trajectory, a spacecraft experiences the effects of the surrounding environment in the form of forces and moments acting on it and influencing its motion. The main sources of external forces are the pressure forces (lift and drag) due to the aerodynamic interaction between the spacecraft and the Earth’s atmosphere, and the gravitational forces generated by the effect of the Earth’s gravitational field on the spacecraft.

2.2.2.1 Atmosphere model

The atmospheric model implemented in the model is based on the 1976 U.S. Standard Atmosphere (National Oceanic and Atmospheric Administration, 1976). The Earth's atmosphere is divided into two main zones: the lower atmosphere, which extends from the surface to a geometric altitude of 86 km, and the upper atmosphere, which ranges from 86 km up to 1000 km. Each of the two zones is further divided into layers. Within each layer, the temperature is represented with a predefined function of the altitude. Pressure and density are then derived accordingly as functions of the altitude. A complete description of the atmosphere model is provided in Appendix B.

2.2.2.2 Gravitational model

To compute the gravitational forces contribution present in the equation of motion, a zonal harmonic gravity model up to degree four is adopted. The radial and tangential acceleration components acting on the spacecraft due to gravity can be expressed as (Tewari, 2007)

$$\begin{aligned} g_r = \frac{\mu_e}{r} \cdot \Bigg\{ 1 - \frac{3}{2} \cdot J_2 \cdot \left(\frac{R_e}{r} \right)^2 \cdot \left[3 \cdot \cos^2 \phi - 1 \right] - 2 \cdot J_3 \cdot \left(\frac{R_e}{r} \right)^3 \left[5 \cdot \cos^3 \phi - 3 \cdot \cos \phi \right] \\ - \frac{5}{8} \cdot J_4 \cdot \left(\frac{R_e}{r} \right)^4 \left[35 \cdot \cos^4 \phi - 30 \cdot \cos^2 \phi + 3 \right] \Bigg\} \end{aligned} \tag{2.7}$$

$$\begin{aligned} g_\delta = -\frac{3 \cdot \mu_e}{r^2} \cdot \left(\frac{R_e}{r} \right)^2 \cdot \sin \phi \cdot \cos \phi \cdot \Bigg\{ J_2 + \frac{1}{2} \cdot J_3 \cdot \left(\frac{R_e}{r} \right) \cdot \left[5 \cdot \cos^2 \phi - 1 \right] \\ + \frac{5}{6} \cdot J_4 \cdot \left(\frac{R_e}{r} \right)^2 \cdot \left[7 \cdot \cos^2 \phi - 1 \right] \Bigg\} \end{aligned} \tag{2.8}$$

where μ_e is the gravitational parameter of the Earth, R_e is the Earth's radius, r is the distance between the centre of the Earth and the spacecraft, ϕ is the colatitude, and J_k (k = 1,..,4) are the zonal harmonics coefficients, also known as Jeffery constants.

2.2.3 Aerodynamics

Aerodynamics is a fundamental aspect of the demisability analysis because allow the computation of the forces acting on the spacecraft influencing its trajectory. As an object-oriented approach is followed, a series of motion and geometry averaged coefficients are necessary to describe the aerodynamics of the spacecraft. When a spacecraft enters a planet's atmosphere and moves its way to the ground it passes through different kinds of flows (i.e. sub-sonic, transonic, supersonic, and hypersonic) where the aerodynamics of the spacecraft changes and must be analysed with different methods (Boyd, 1994, Boyd, 1993, Boyd, 1990). However, as the main phenomena influencing the aerodynamic and thermal loads for re-entries happen in the hypersonic regime, only hypersonic aerodynamics is considered (Lips and Fritsche, 2005). Hypersonic flows are extremely complex to analyse given the development of high temperature phenomena such as ionisation and dissociation (Anderson, 2006). Nonetheless, a variety of engineering correlations have been developed to model the aerodynamics forces on simple geometries when exposed to hypersonic regimes, as a function of their trajectory, geometry, and attitude (Zuppardi and Esposito, 2000, Zoby et al., 1981, Perini, 1972, Klett, 1964). In addition, during its descent, a re-entering object travels through the atmosphere, encountering a wide range of density, temperature, and pressure. The spacecraft thus "sees" the flow surrounding it change from very rarefied at high altitudes to continuum at lower altitudes. Three flow regimes are distinguished by using the Knudsen number, which is the ratio between the mean free path travelled by a particle and the characteristic length of the object (Klett, 1964). A common characterisation considers the flow to be *continuum* for values of the Knudsen number below 0.01 and to be *free-molecular* for values above 10. Intermediate values, instead, are associated to a *transitional flow*. In these three regimes, the interaction of the atmosphere with the spacecraft is different and, consequently, the correlations used to model them are different.

The contribution of the aerodynamic forces can be expressed in terms of a non-dimensional coefficient that is the drag coefficient C_D:

$$C_D = \frac{F_D}{q_0 \cdot S_{ref}} \tag{2.9}$$

where $q_0 = 1/2 \cdot \rho_0 \cdot V_0^2$ is the free-stream dynamic pressure, ρ_0 is the free-stream density, V_0 is the free stream velocity, and S_{ref} is the reference cross-sectional area of the object. The free-stream dynamic pressure is referred to the unperturbed flow field surrounding the spacecraft. The drag coefficients used in the model are consider four possible geometrical shapes (i.e., sphere, cylinder, box, and flat plate) and both the free-molecular and continuum flow regimes. The derived expressions for the continuum and free-molecular flux regimes have been developed or derived from the literature and bridging functions are utilised for the description of the aerodynamics in the transitional regime. Table 1 summarises the free molecular and continuum drag coefficients for the specified shapes and the schematics for each shape are summarised in Figure 3.

Table 1: Free molecular drag coefficients for sphere, cylinder, box, and flat plate.

Shape	**Free molecular C_D**	**Continuum CD**	**Reference Area S_{ref}**
Sphere	2.0	0.92	$\pi \cdot r^2$
Cylinder	$1.57 + 0.785 \cdot l/d$	$0.7918 + 0.326 \cdot l/d$	$2 \cdot r \cdot l$
Box	$1.03 \cdot \left(A_x + A_y + A_z\right) / S_{ref}$	$0.46 \cdot \left(A_x + A_y + A_z\right) / S_{ref}$	$\text{Median}(A_x, A_y, A_z)$
Flat Plate	1.03	0.46	$l \cdot w$

The drag coefficient for spheres is set to a constant value (Masson et al., 1960) and the reference area is the cross section of the sphere. For cylinders, the drag coefficient is a function of the ratio between the cylinder diameter *d* and length *l* (Klett, 1964). For flat plates, a constant value is adopted (Hallman and Moody (2005)), with the reference area being the cross section of the plate.

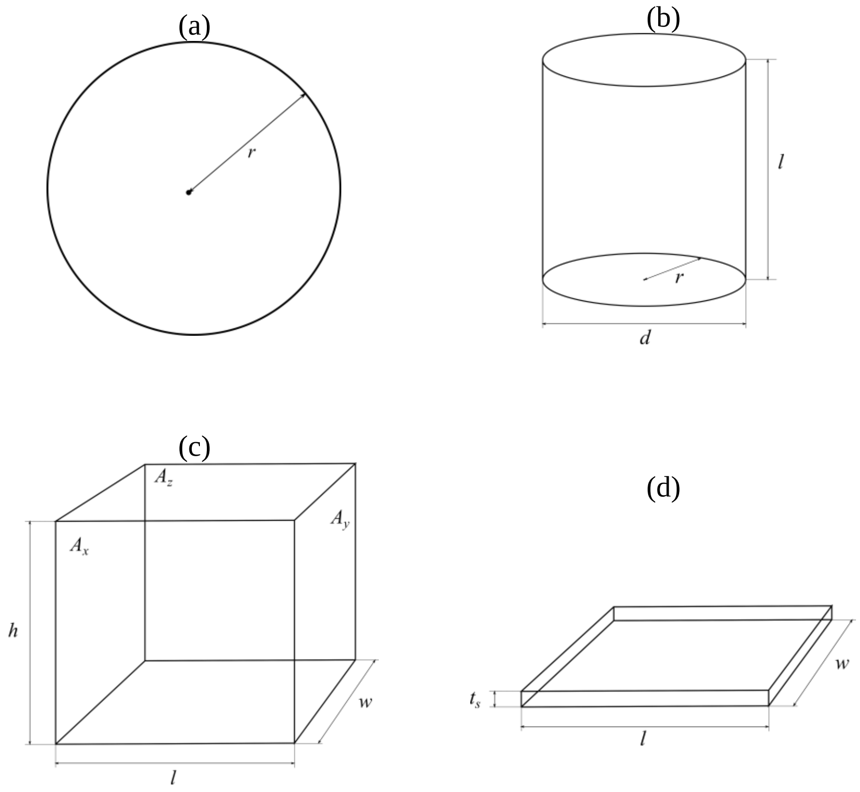

Figure 3: Schematics for the geometry implemented in the model. (a) sphere, (b) cylinder, (c) box, and (d) flat plate.

For box shaped object, the C_D is related to the drag coefficient of a flat plate perpendicular to the free stream by averaging it over the faces of the box. The reference area corresponds to the median value between the areas of each side of the box. In addition to the free molecular and continuum relationships, it is necessary to provide equations for the transitional regime. These equations are referred to as bridging functions. Two bridging functions are implemented in the model as follows:

$$C_{D,t} = C_{D,c} + \left(C_{D,fm} - C_{D,c}\right) \cdot \left\{\sin\left(\pi \cdot (0.5 + 0.25 \cdot \log_{10} Kn)\right)\right\}^3 \tag{2.10}$$

$$C_{D,t} = C_{D,c} + \left(C_{D,fm} - C_{D,c}\right) \cdot \exp\left(-\frac{\rho_{atm} \cdot r}{10 \cdot \rho_S \cdot \lambda_S}\right) \tag{2.11}$$

where $C_{D,fm}$ and $C_{D,c}$ are the free-molecular and the continuum drag coefficients respectively, and Kn is the Knudsen number of the flow surrounding the re-entry object. Eq. (2.10) is the bridging function adopted for spheres (Masson et al., 1960), where r is the radius of the sphere, ρ_{atm} is the atmospheric density, ρ_S is the air density after the normal shock, and λ_S is the mean free path after the normal shock. Eq. (2.11) is the bridging function used for all the remaining shapes (National Astronautics and Space Administration, 2009, Kelley et al., 2010).

2.3 Demise computation

2.3.1 Aerothermodynamics

To analyse the demisability of re-entering objects the heat load acting on them during the descent trajectory needs to be computed. Analogously to the aerodynamics, even the aerothermodynamics in object-oriented codes is modelled through engineering correlations (Zuppardi and Esposito, 2000, Zoby et al., 1981, Perini, 1972, Klett, 1964). As the attitude of the object is predefined, the heat load is computed using averaging factors. The averaging factors, also referred as shape factors ($\bar{F}_q$), provide the relationship between a reference heat load ($\dot{q}_{ref}$) and the average heat rate on the object as a function of its geometrical shape and the attitude motion. In general, the average heat rate on an object can be expressed as

$$\dot{q}_{av} = \bar{F}_q \cdot \dot{q}_{ref} \tag{2.12}$$

where the reference heat load and the shape factor depend on the flux regime considered. Again, both the free-molecular and the continuum regime are considered.

2.3.1.1 Free-molecular flows

The reference heat load for free molecular flows is the heat rate on a flat plate perpendicular to the flow (Klett (1964)) and can be expressed as

$$\dot{q}_{fp}^{\perp} = 11356.6 \cdot \left(\frac{a_t \cdot \rho_0 \cdot V_0^3}{1156}\right) \tag{2.13}$$

where ρ_0 and V_0 are the free-stream density and velocity respectively, and a_t is the thermal accommodation coefficient whose value is assumed to be constant and equal to 0.9 (Owens, 2014). This heat rate refers to a fully catalytic heat flux. Very limited data is available in the literature for shape factors in the free-molecular flow; therefore, some assumptions had to be made. For spheres in free-molecular flow, as no data could be found in the literature, the free-molecular shape factor for a random tumbling disk (Klett, 1964) was adopted. The corresponding value is

$$\bar{F}_{q,fm}^{s} = 0.255 \tag{2.14}$$

For cylinders, the overall shape factor is considered to be weighted average of the free molecular shape factors of the side and end areas of the cylinder, with the weights represented by the side and end areas of the cylinder Klett (1964). The corresponding expressions is as follows

$$\bar{F}_{q,fm}^{c} = \frac{2 \cdot \bar{F}_{q,fm}^{end} \cdot A_{end} + \bar{F}_{q,fm}^{side} \cdot A_{side}}{A_{tot}} \tag{2.15}$$

where $A_{end} = \pi r^2$ and $A_{side} = 2\pi rl$ are the end and side areas of the cylinder respectively, and $A_{tot} = 2A_{end} + A_{side}$ is the total area of the cylinder. $\bar{F}_{q,fm}^{end}$ and $\bar{F}_{q,fm}^{side}$ are the shape coefficients relative to the end and side of the random tumbling cylinder respectively, and can be expressed as

$$\bar{F}_{q,fm}^{end} = 0.255 \tag{2.16}$$

$$\bar{F}_{q,fm}^{side} = 0.785 \cdot Y + 0.500 \cdot Z \tag{2.17}$$

where Y is a curve representing the free-molecular flow ratio of the average heating on the sides of a rotating side-on cylinder to the heating on surfaces perpendicular to the flow. Z instead describes the free-molecular flow ratio of the heating on surfaces parallel to the flow to the heating on surfaces perpendicular to the flow (Appendix C). For box shaped structure the parallelepiped is reduced to an equivalent cylinder and Eq. (2.15) can still be used Hallman and Moody (2005). The equivalence between the box and the cylinder is accomplished in the following way: assuming a box with side lengths equal to l, w, h and following the relationship $l > w > h$, the equivalent length, and the equivalent radius of the cylinder are respectively $l_e = l$ and $r_e = \sqrt{w \cdot h}$. Finally, for flat plates the constant value derived for random tumbling disks (Klett, 1964) is adopted.

$$\bar{F}_{q,fm}^{fp} = 0.255 \tag{2.18}$$

Eq. (2.18) is actually obtained following the theory of Oppenheim (Klett, 1964), which was originally developed for flat plates, and extended by Klett to the disks. Consequently, the extension of such value to flat plates is justified.

2.3.1.2 Continuum flows

For continuum flows, the reference heat rate is the stagnation-point heat rate over a sphere. A large variety of correlations is available in the literature (Perini, 1972, Sreekanth et al., 2003). The developed methodology adopts the Detra-Kemp-Riddel (DKR) (Perini, 1972) correlation.

$$\dot{q}_{ss} = 1.9987 \times 10^8 \cdot \sqrt{\frac{0.3048}{r_n}} \cdot \sqrt{\frac{\rho_0}{\rho_{SL}}} \cdot \left(\frac{V_0}{7924.8}\right)^{3.15} \cdot \frac{h_s - h_w}{h_s - h_{w_{300}}} \tag{2.19}$$

where r_n is the curvature radius at stagnation point, and ρ_{SL} is the air density at sea-level. h_s is the stagnation point enthalpy, h_w is the wall enthalpy and h_{w300} is the wall enthalpy at 300 K. The correlation is based on experiment with fully catalytic heat fluxes. The choice for the Detra-Kemp-Riddel (DKR) correlation was taken considering that it represents a simple engineering correlation that also provides good and meaningful results. It is used in the NASA primary re-entry code ORSAT and is also recommended in Perini (1972) as the correlation to be used to predict laminar, hypersonic, and convective stagnation point heating rates for spherical nose shapes. The actual correlation used in the tool developed in this project is a slight modification of the DKR as suggested by Beck (Beck, 2015).

The continuum shape factor for a random tumbling sphere was derived from an average of shape factors provided in the literature (Merrifield et al., 2014, Beck et al., 2015a), obtaining the value

$$\bar{F}^{s}_{q,c} = 0.234 \tag{2.20}$$

For cylindrical shape, the same principle used for the free molecular flow is adopted again Klett (1964). The corresponding shape factor can be expressed as

$$\bar{F}^{c}_{q,c} = \frac{2 \cdot \bar{F}^{end}_{q,c} \cdot A_{end} + \bar{F}^{side}_{q,c} \cdot A_{side}}{A_{tot}} \tag{2.21}$$

where $\bar{F}^{end}_{q,fm}$ and $\bar{F}^{side}_{q,fm}$ represent the shape factors for the end and the side of a random tumbling cylinder in continuum flow and are expressed as

$$\bar{F}^{side}_{q,c} = 0.179 + 0.333 \cdot B \tag{2.22}$$

$$\bar{F}^{end}_{q,c} = 0.323 \tag{2.23}$$

where B is a curve representing the ratio of the average heating on the side of an end-on cylinder to the stagnation point heating on a sphere of the same radius (Appendix C). For box-shaped structure, an equivalent cylinder is defined in the same way as before and the Eq. (2.21) is used to compute the shape factor. For the flat plate, as no specific results were found in the literature, the shape coefficient for a random tumbling disk has been used. An equivalent disk is defined to compute the shape coefficient for a flat plate with the following procedure. For the heat load on a flat plate

$$\dot{Q}^{fp}_{c} = \bar{F}^{fp}_{q,c} \cdot A^{fp}_{tot} \cdot \dot{q}_{ss} \tag{2.24}$$

where $A^{fp}_{tot}=2\cdot(l\cdot w+l\cdot t+w\cdot t)$ is the total area of the flat plate with length l, width w, and thickness t, and $\bar{F}^{fp}_{q,c}$ is the shape coefficient for a flat plate in continuum flow. To build the equivalent disk, an equivalent radius equal to $r_e = w/2$ is assumed. For a disk the heat load would be

$$\dot{Q}^{fp}_{c} = \bar{F}^{d,eq}_{q,c} \cdot A^{d,eq}_{tot} \cdot \dot{q}_{ss} \tag{2.25}$$

As an equivalent disk has been used, its heat load has to be equivalent to the one of the flat plate. It is thus possible to equate Eq. (2.24) and Eq. (2.25) in order to obtain the shape coefficient for a flat plate as follows:

$$\bar{F}^{fp}_{q,c} = \bar{F}^{d,eq}_{q,c} \cdot \frac{A^{d,eq}_{tot}}{A^{fp}_{tot}} \tag{2.26}$$

where $\bar{F}^{d,eq}_{q,c}$ is the shape coefficient of the equivalent disk that, for a random tumbling disk, is independent on the radius and can be obtained from Klett (1964) where a value of 0.323 is reported.

2.3.1.3 Transition flows

In the same way as for the drag coefficients, a bridging function must be used to obtain the shape factor in the transition regime. The bridging function adopted in the code has the following expression (Minisci, 2015b):

$$\dot{q}_t = \dot{q}_c \Big/ \sqrt{1 + \left(\frac{\dot{q}_c}{\dot{q}_{fm}}\right)} \tag{2.27}$$

During the re-entry, when the Knudsen is below 0.01, we use the heat rate expression for the free-molecular flow (Eq. (2.12) with Eq. (2.13)), when the Knudsen number is above 10 we use the expression for the continuum flow (Eq. (2.12) with Eq. (2.19)), and when in between we use the bridging function of Eq. (2.27).

2.3.2 Ablation model

To describe the mass loss during the demisability analysis of a re-entering object is a lumped mass model is used. In this schematisation, the object is considered to have a certain mass with a uniform temperature. As the heat load increases during the atmospheric descent, the temperature of the object increases until it reaches the melting temperature of the material. The temperature variation during the heating phase can be described with the equation:

$$\frac{dT_w}{dt} = \frac{A_w}{m(t)C_{p,m}}\left(\dot{q}_{av} - \varepsilon \cdot \sigma \cdot T_w^4\right) \tag{2.28}$$

where T_w is the temperature of the object at a certain time instant, considered uniform for the entire object volume. A_w is the wet area, m is the instantaneous mass of the object, $C_{p,m}$ is the specific heat capacity of the material at constant pressure, ε is the emissivity of the material, σ is the Stefan-Boltzmann constant, and $\dot{q}_{av}$ is the heat flux on the object with the shape and attitude dependant averaging factor already taken into account. The model considers the variation with time of the mass of the object and the heat loss due to the re-radiation, but it does not consider oxidation heating.

Once the melting temperature is reached, the object starts melting and loosing mass m at a rate that is proportional to the net heat flux on the object and to the heat of fusion (h_f) of the material as follows:

$$\frac{dm}{dt} = -\frac{A_w}{h_f}\left(\dot{q}_{av} - \varepsilon \cdot \sigma \cdot T_w^4\right) \tag{2.29}$$

It is important to highlight that this model assumes that the conduction inside the object is infinite so that the temperature is uniform everywhere in the volume of the object. This is a good approximation for metallic structure. For non-metallic materials, such as composites, this kind of approach is adapted using an equivalent metal approach and defining equivalent properties for the material under consideration (Costa and Minisci, 2003, Lips et al., 2005a).

2.4 Model verification

This section presents a comparison between the current model and the results obtained by the re-entry code SAM (Beck et al., 2015a, Beck et al., 2015b, Beck and Merrifield, 2015, Beck and Holbrough, 2014) for a variety of standard test cases presented during the First Demise Workshop (R.Tech, 2015). The initial conditions used for all the test cases are summarised in Table 2.

Table 2: Initial conditions for the test cases.

Initial conditions	
Longitude (deg)	0
Latitude (deg)	0
Altitude (km)	120
Velocity (m/s)	7273
Heading (deg)	42.35
Flight Path Angle (deg)	-2.612

The test cases include four different geometrical shapes (sphere, cylinder, box, and flat plate) and two materials (aluminium 7075-T6 and titanium 6Al-4V). The characteristics of the geometrical shapes considered are summarised in Table 3 together with the attitude motion assumed during the re-entry:

Table 3: Geometrical characteristic of the object analysed for re-entry.

Shape	**Dimensions (m)**	**Motion**
Sphere	$r = 0.5$; $t = 0.03$	Random Tumbling
Cylinder	$r = 0.5$; $l = 1.0$; $t = 0.03$	Random Tumbling
Box	$l = 1.0$; $w = 1.0$; $h = 1.0$	Random Tumbling
Flat Plate	$l = 1.0$; $w = 1.0$; $t = 0.03$	Random Tumbling

The first comparison performed is for an aluminium sphere. Figure 4 shows the altitude vs time profile of the descent, which is a function of the drag coefficients used in the model. As can be noted there is a very good agreement between the two models; this is somewhat expected as the drag coefficients between the two models are very close (Beck et al., 2015a) and the atmosphere model is the same, i.e. the 1976 U.S. Standard Atmosphere (National Oceanic and Atmospheric Administration, 1976). Figure 5 instead shows the evolution of the temperature of the object as function of the altitude, which is different for the two models. This is due to the difference between the shape factors used by the two models (0.217 in the SAM model and 0.234 in the current code).

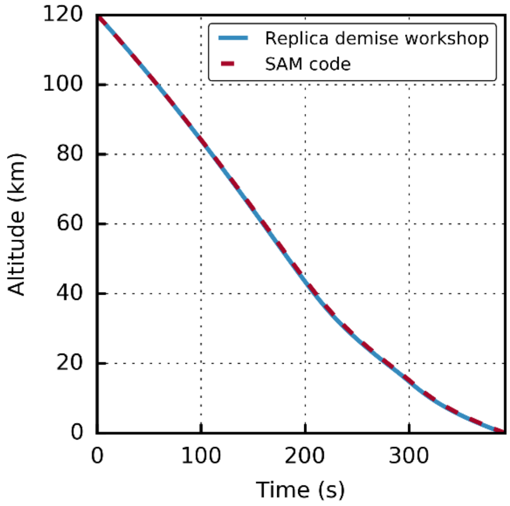

Figure 4: Time-altitude profile for aluminium sphere.

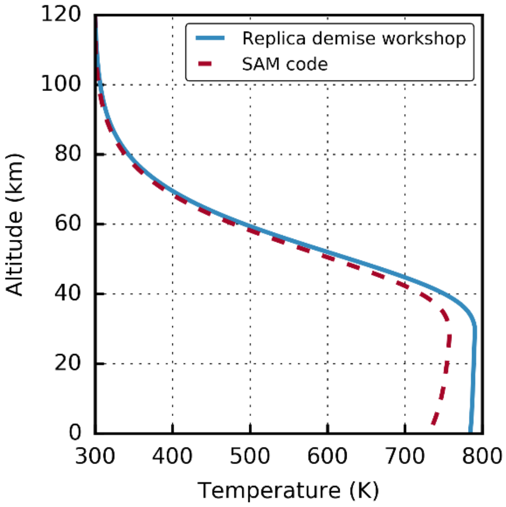

Figure 5: Temperature-altitude profile for aluminium sphere.

Analogous comparisons can be made for all the other shapes and the two materials considered. Of particular relevance is the comparison for the temperature profile of the various objects because they influence the demise.

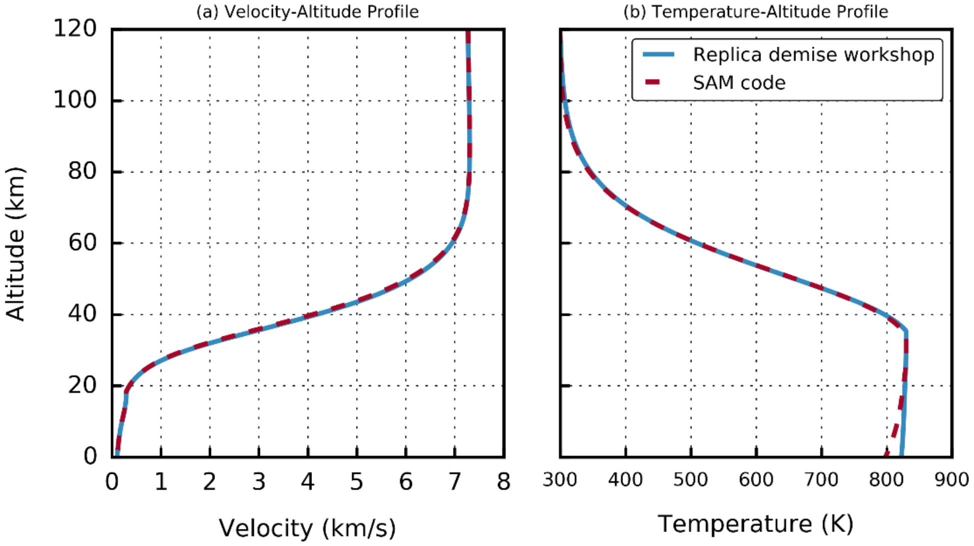

Figure 6: Velocity altitude (a) and temperature-altitude (b) profiles for an aluminium cylinder.

Figure 6, Figure 7, and Figure 8 present the comparisons for the temperature and velocity profiles of a re-entering aluminium cylinder, a titanium box, and an aluminium flat plate respectively. The cylinder case (Figure 6) exhibits a very good agreement with the SAM code; this is due to the fact that the aerodynamics and aerothermodynamics for cylindrical objects is derived from Klett (1964) for both codes. The titanium box case (Figure 7) shows some difference in the temperature profile but they are well within the variability presented by most codes (Merrifield et al., 2015). The last case presented in the paragraph is the re-entry of an aluminium flat plate (Figure 8); this is an interesting case because there is a significant mass loss, with almost 30 kg lost from the initial 83 kg of the flat plate. The model performs well even taking into consideration the mass loss and thus the variation of the ballistic coefficient of the object. Again, the difference in the temperature profile can be explained with a difference in the value of the shape factor for boxes between the presented model and SAM.

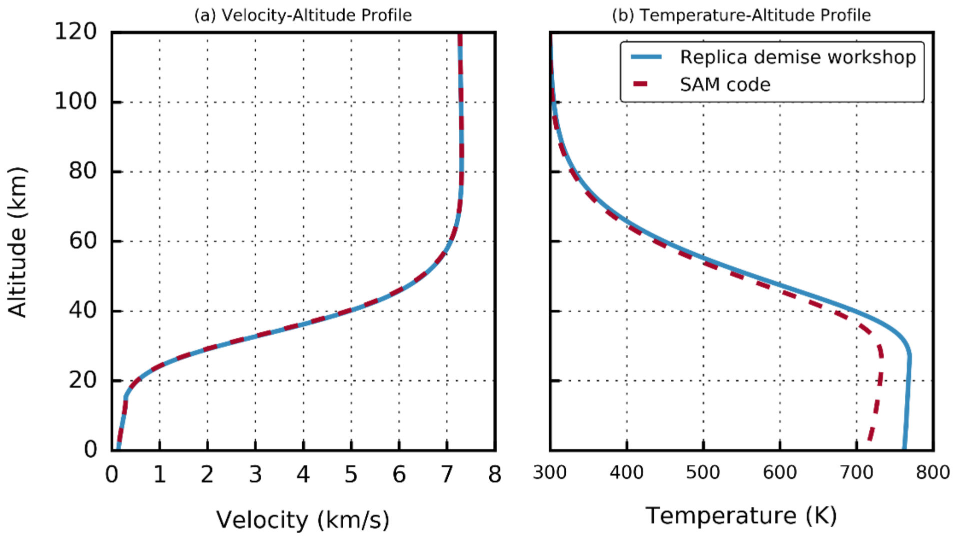

Figure 7: Velocity altitude (a) and temperature-altitude (b) profiles for a titanium box.

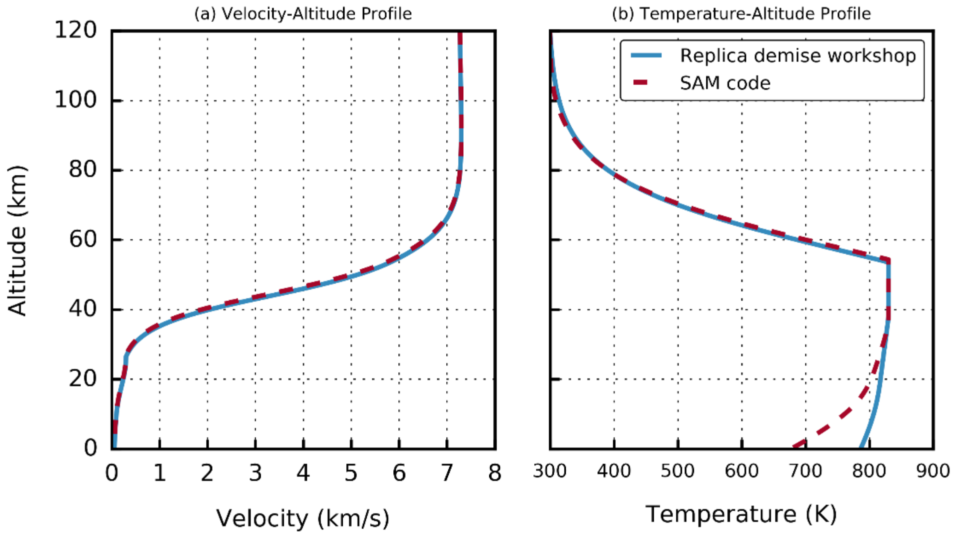

Figure 8: Velocity altitude (a) and temperature-altitude (b) profiles for an aluminium flat plate.

Even the temperature profile is in very good agreement with the SAM code up to the heating and melting phase. A bigger difference is present in the cooling phase. This divergence can be explained with a difference in the model between the two codes when it comes to considering the re-emitted heat load and the effect of the convective cooling in the last part of the trajectory. Unfortunately, no comparison can be made because no knowledge of the model used in SAM is available. This difference in the temperature profile in the cooling phase with respect to the SAM code is common to all the cases and for both materials but is much less evident with respect to the simulation performed by the HTG software SESAM for the same test cases of the Demise Workshop (R.Tech, 2015). Moreover, in a destructive re-entry analysis, the heating phase is by far more important than the cooling phase.

2.5 Demisability criterion

The object oriented destructive re-entry algorithm and code described in Sections 2.1, 2.2, and 2.3 was developed to assess the demisability of spacecraft components and structures as a function of the characteristics of the objects such as the material, the geometry, and the initial conditions at the re-entry. As a measure of the demisability of a component, the fraction of the mass that demises during the re-entry is considered and is referred to as the Liquid Mass Fraction (LMF).

$$LMF = 1 - \frac{m_{fin}}{m_{in}} \tag{2.30}$$

A value of 1.0 of the index corresponds to complete demise, whereas a value of 0 to complete survival. It is also taken into account the 15 J (National Astronautics and Space Administration, 2012, National Astronautics and Space Administration, 2015, National Astronautics and Space Administration, 2009) limit in the index so that when the re-entering object has an impact energy lower than 15 J the index is considered to be equal to 1.0. It is interesting to combine Eq. (2.30) with the integral expression for the mass loss during re-entry of Eq. (2.29). This results in the following expression for the LMF index.

$$LMF = \int_0^t \frac{A_w}{m_{in} \cdot h_f} \cdot \left(q_{av} - \dot{}\,\epsilon\sigma T_w^4\right) dt \tag{2.31}$$

It is clear from this expression the importance of a parameter such as the integral heat load and their contribution to the demise of re-entering components.

The LMF index can give direct and easily interpretable information about the demisability of a component. As the focus of the study is improving the demisability of structure and components, and not on the casualty risk related to them, the LMF index has been considered a suitable choice. The use of the casualty risk has been discarded as it is also related to the population distribution on Earth, which is a variable external to the actual re-entry process. The use of the casualty area has also been excluded, at least in the first stages (Section 7.5). In fact, the contribution of the casualty area varies less gradually with respect to the LMF index and has a more direct relation to the casualty risk rather than to the amount of demise reached by a specific design.

2.6 Summary

This chapter presents the development of the demisability model used in this work. The model adopts an object-oriented approach with six-state re-entry dynamics. All the characteristics of the averaging methods adopted for the evaluation of the aerodynamic and aerothermodynamics are described, together with the lumped mass ablation model. The model is validated against state-of-the-art destructive re-entry software and for standard test cases. Finally, a demisability criterion is devised and presented. In the following chapter, the correspondent survivability model will be presented.

Chapter 3 Survivability model

The second model developed is a survivability model, which assess the vulnerability of a spacecraft to an impact from space debris. As this model is used in combination with the demisability model (Chapter 2), a driving requirement to its development is to maintain characteristics similar to the demisability model, for what concerns both its complexity and computational time. Software such ESABASE/DEBRIS (Gäde and Miller, 2013) and NASA BUMPER (Bjorkman et al., 2014) are already available, however they are complex and they use computationally expensive methodology such as ray tracing methods (Putzar and Schäfer, 2006). The proposed approach, on the other hand, is tailored to be compatible with the object-oriented approach used for the demisability analysis, adopting a new strategy to compute the effects of the debris fluxes on a configuration.

Section 3.1 contains a general description of the architecture of the model. Following this, Section 3.2 presents the model used to schematise the debris environment surrounding the spacecraft. Section 3.3 describes the procedure used to generate the vector flux elements, while Section 3.4 provides the description of the core methodology used to assess the vulnerability of the spacecraft. Finally, Section 3.5 presents the results of the verification of the developed model with ESA DRAMA (Gelhaus et al., 2014).

Part of the chapter follows the content of the Acta Astronautica journal publication "Demisability and survivability sensitivity to design-for-demise techniques" (Trisolini et al., 2018a).

3.1 Model architecture

The block diagram of Figure 9 represents a schema of the algorithm and of the approach followed to compute the spacecraft vulnerability to debris impacts (Gäde and Miller, 2013, Stokes et al., 2000). The model is structured so that the user has to provide the geometry to be analysed, the debris fluxes for the specific orbit considered, and the mission lifetime for which the computation has to be performed. For what concerns the geometry, for this version of the model, the user can specify four types of objects, namely cubes, spheres, cylinders, and flat plates. The user has only to specify the main parameters for each object, e.g. the radius and thickness of a sphere. The model will then proceed to build the proper subdivision into panels used by the algorithm. Alongside the geometrical parameters, the material of the object must be provided together with the failure modality (penetration, detached spall, or incipient spall). The second main input to the model is the data relative to the debris fluxes. The user can either directly provide the path to the MASTER-2009 files needed by the model or provide the parameters of the desired orbit. In this latter case, the model uses a wrapper to MASTER-2009 (Flegel et al., 2009) to first run the MASTER simulation, store the needed distributions, and then perform the survivability analysis. The final input to the model, is the mission lifetime that is the time spent in years by the spacecraft in the specified orbit.

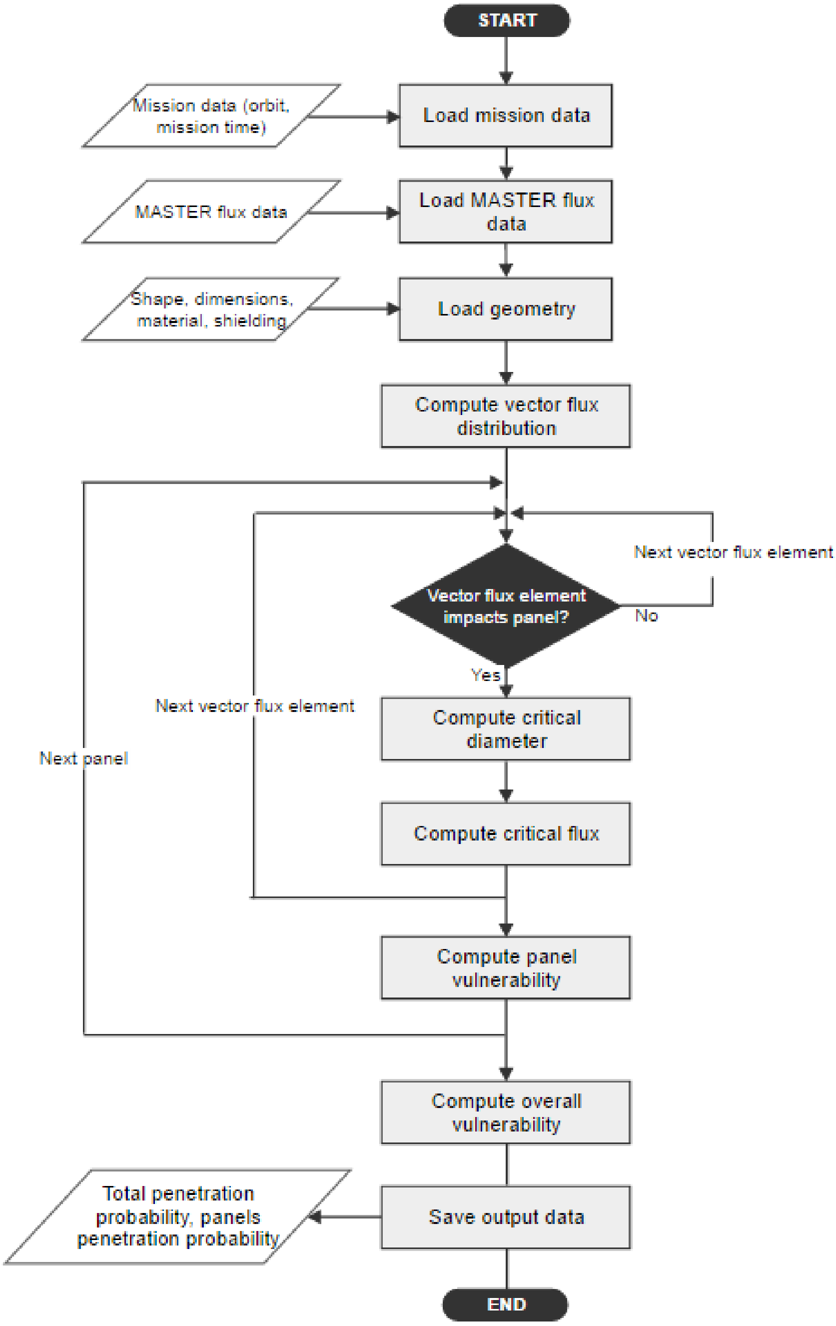

Figure 9: Block diagram schematisation of the survivability model.

For the main part of the vulnerability assessment, first, the flux data from MASTER-2009 are manipulated in order to generate the set of vector flux elements used in the analysis (Section 3.3). This procedure is where the differences with common debris impact assessment software are evident: instead of sampling the distribution obtained from MASTER-2009 in order to generate a set of individual debris particles, a set of vector elements each having a certain velocity and direction associated is generated. For each one of these fluxes, the critical particle diameter corresponding to each panel of the structure is computed using the proper ballistic limit equations (Appendix D) (Ryan and Christiansen, 2011, Ryan and Christiansen, 2010). The type of ballistic limit equation to be used is directly recognised by the model based on the material assigned to the structure. The obtained critical diameter is then used to calculate the critical flux and then obtain the penetration probability on each panel using the standard Poisson probability approach (Section 3.4).

The output provided by the model comprises the impact probability and penetration probability on each panel of the structure and the total impact probability and total penetration probability for the whole structure. In addition, the number of impacts and the number of penetrations is computed.

3.2 Space environment model

The space environment around the Earth is populated by a large amount of man-made debris and is also characterised by the presence of natural particles such as meteoroids. It is thus necessary to have a description as realistic as possible of the natural and man-made particulate environment around the Earth. As the objective of this model is to assess the vulnerability of spacecraft structures to the impact of space debris, it is necessary to have a description of the natural and man-made particulate environment that is as realistic as possible. The ESA software MASTER-2009 (Flegel, 2011) provides the description of the debris environment via flux predictions on user defined target orbits. The fluxes provide the number of particles per unit area and per year that impact the spacecraft. Both 2D and 3D flux distributions are available in MASTER-2009, as a function of many parameters such as the particle diameter, the impact velocity, the impact elevation, etc. All the outputs are provided in a reference frame moving with the spacecraft so that all values obtained are relative to the spacecraft. The inputs to the software are the operational orbit, the starting epoch and the end epoch. The operational orbit has to be defined in terms of the classical orbital parameters: semi-major axis, eccentricity, inclination, argument of perigee and right ascension of the ascending node. MASTER-2009 can provide the impact fluxes down to an impactor diameter of 1 µm and takes into account many different debris sources: on-orbit fragmentation, solid rocket motor firings, etc. In addition, three different scenarios for the evolution of the debris environment can be selected: business as usual, where the launch activities and the implementation of mitigation measures is maintained in line with historical data; intermediate mitigation, where mitigation measures such as passivation and deorbiting within 25 years are partially implemented; and full mitigation, where a complete compliancy with the mitigation guidelines is assumed.

The specific distribution needed for the survivability computation performed in the present work (Gäde and Miller, 2013) are the flux vs particle diameter, flux vs impact elevation, flux vs impact elevation vs impact azimuth, and the flux vs impact velocity vs impact azimuth. This set of distributions is sufficient to compute the vector fluxes needed to perform the spacecraft survivability analysis. An example of the flux distributions given by MASTER can be observed in Figure 10, where the cumulative flux as a function of the particle diameter and the differential flux as function of the impact velocity are presented. Figure 11 and Figure 12 show two three-dimensional distributions: the flux as function of impact azimuth and impact elevation and the flux as function of impact azimuth and impact velocity respectively.

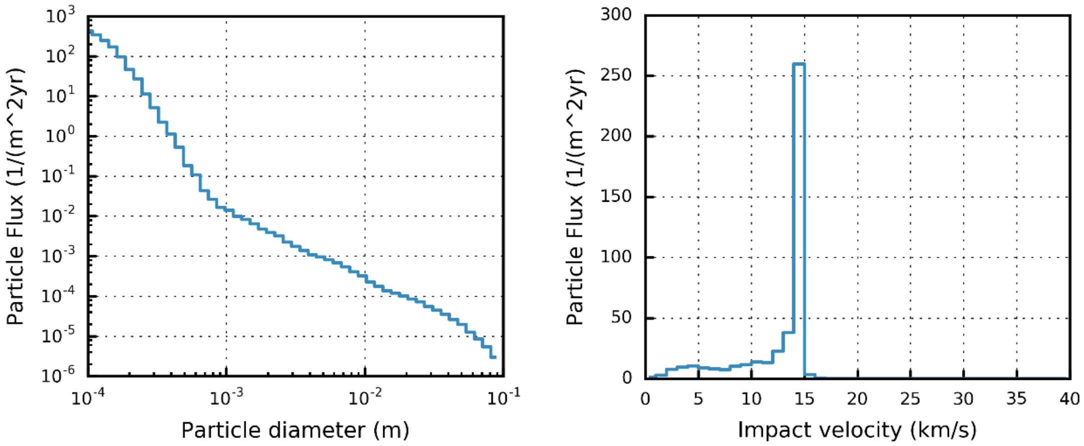

Figure 10: Example of the cumulative flux vs particle diameter distribution (left) and the differential flux vs impact velocity distribution (right).

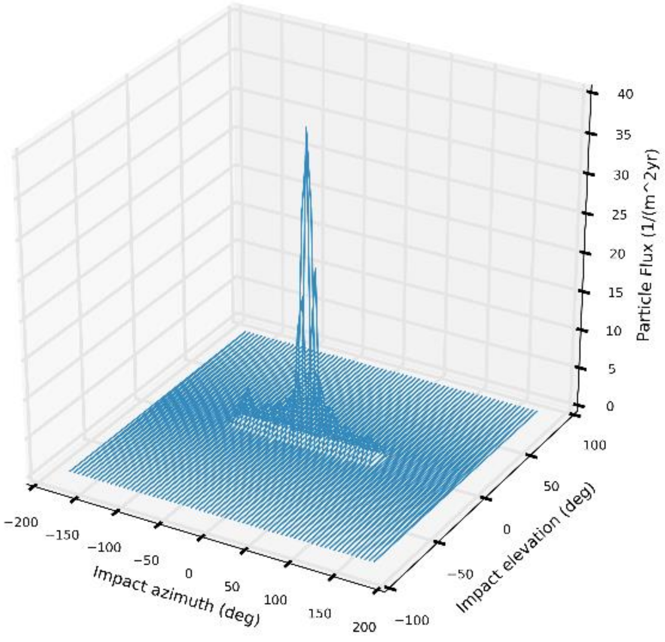

Figure 11: Example of the differential flux vs impact azimuth vs impact elevation distribution.

The user has to provide MASTER-2009 with the ranges and the subdivisions for the specified distributions. Table 4 summarises the ranges and subdivisions used in the present work.

Table 4: Ranges and subdivisions used for the simulations of the present work.

Distribution	**Range**	**Subdivisions**
Flux vs Particle diameter	10^{-4} - 0.1	200
Flux vs Impact elevation	- 90° - 90°	Every 2.5°

Flux vs Impact azimuth	-180° - 180°	Every 2.5°
Flux vs Impact velocity	0 - 40 km/s	Every 0.5 km/s
Flux vs Impact elevation vs Impact azimuth	Same as 2D distribution	Same as 2D distribution
Flux vs Impact azimuth vs Impact velocity	Same as 2D distribution	Same as 2D distribution

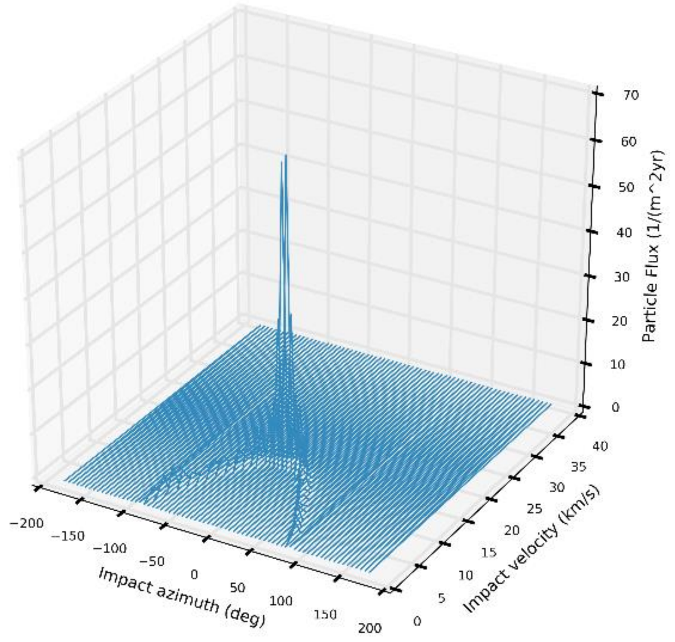

Figure 12: Example of the differential flux vs impact azimuth vs impact velocity distribution.

It is important here to specify the definition of the two angles used to obtain the directionality of the debris fluxes as defined by MASTER-2009, i.e. the impact elevation and azimuth (Flegel, 2011).

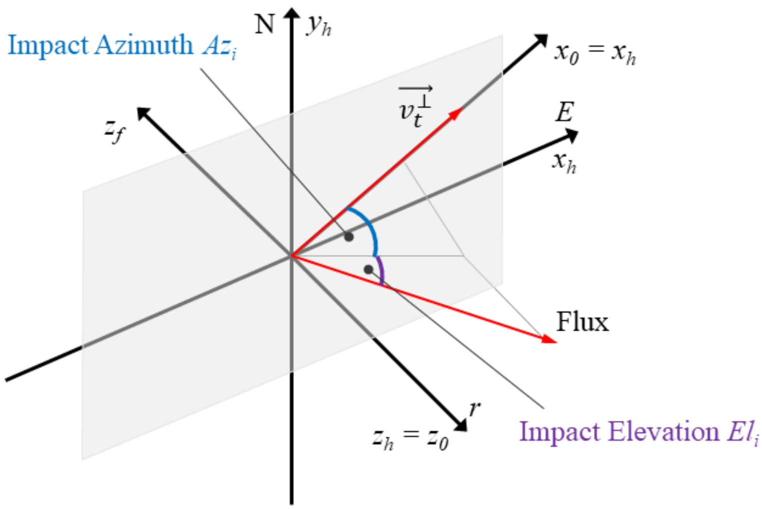

Figure 13: Definition of impact elevation and impact azimuth angle.

The impact azimuth angle is defined as the angle between the orbit velocity vector (the x_0 vector in Figure 13) and the projection of the relative collision velocity vector (the *Flux* vector in Figure 13) in the target object's local horizontal plane (the x_h, y_h, z_h axis in Figure 13). The impact elevation angle is instead defined as the angle between the local horizontal plane (the x_h-y_h plane) and the relative collision velocity vector.

3.3 Vector flux model

In this paragraph the methodology used to represent the debris environment surrounding the spacecraft so that it can be used in the computation of the survivability index is described. The methodology follows a novel approach in order to bypass the use of computationally expensive methods such as ray tracing, and at the same time have a sufficiently accurate description of the debris environment. The compromise is achieved characterising the debris fluxes with *vector flux elements*. Vector flux elements are entities used to reduce the debris flux data associated to a specific space sector around the spacecraft, generated by MASTER-2009, to a single vector element. To each vector element is associated a value of the particle flux, of the velocity, and a direction. This in turn corresponds to the association of an entire set of particles to a specific value of the velocity, flux, and impact angle.

The procedure starts with the subdivision of the space around the spacecraft into a set of angular sectors. The contribution to the particle flux inside each angular sector is summed together in order to generate the flux relative to the specific angular sector. The velocity and the impact direction are extracted from the velocity, impact elevation, and impact azimuth distributions. In order to have a clearer understanding of the procedure, a simplified is used to present the procedure adopted:

- Impact elevation: -5°, 0°, 5°.
- Impact azimuth: -90°, -75°, -60°, -45°, -30°, -15°, 0°, 15°, 30°, 45°, 60°, 75°, 90°.

Once the subdivision is decided, first the distribution of flux vs impact elevation is considered and subdivided in correspondence of the user specified subdivisions (Figure 14). After the subdivision is performed, a value for the elevation angle for each of the elevation interval specified must be selected. Two options are possible: a *most probable value* or a *weighted average value.* The most probable elevation corresponds to the value of the impact elevation angle that has the highest flux in the interval specified. The weighted average elevation is instead given averaging the impact elevation values with weights given by the corresponding value of particle flux. When the subdivision is equal to the minimum possible width the middle value is selected. At this point, the impact elevation associated to the vector flux element is determined.

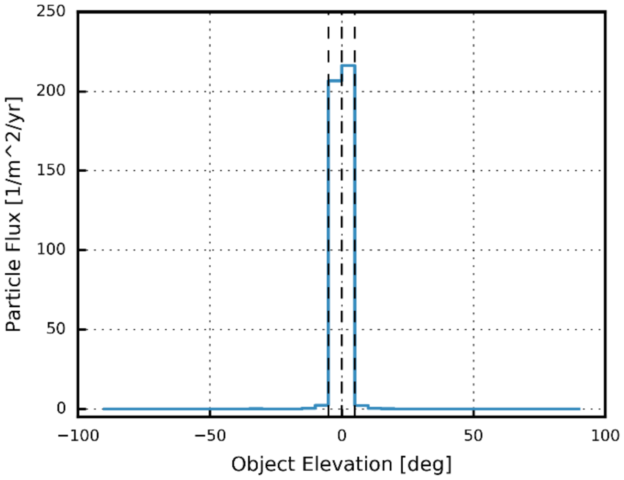

Figure 14: Differential flux vs impact elevation with distribution subdivisions (dashed line) and most probable values of the elevation selected for each interval of the subdivision.

The following step in the procedure allows the computation of the impact azimuth of the vector flux element. To do so, the 3D distribution of flux vs azimuth vs elevation is considered. First, the distribution is subdivided according to the elevation subdivisions. Each one of these subdivisions can contain multiple flux vs azimuth distributions generated by MASTER-2009. Such distributions are thus collapsed to produce one flux vs azimuth distribution for each elevation subdivision. These azimuth distributions are then subdivided following the user defined set of subdivisions (Figure 15). The value of the azimuth associated to each interval is then computed. Following the same procedure used for the elevation distribution, there is the possibility to select between the *most probable* and *weighted average* value.

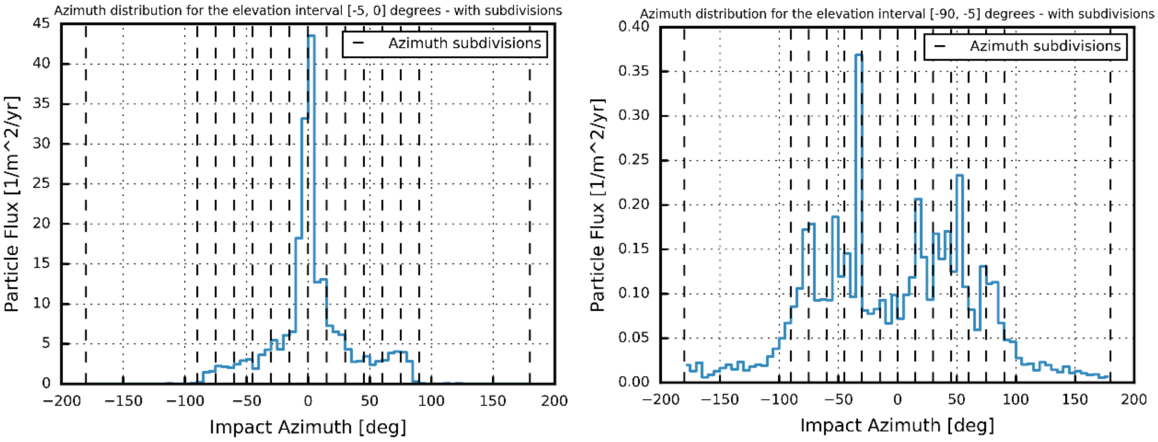

Figure 15: Differential flux distributions vs impact azimuth for the impact elevation interval defined by the user.

At this point, the debris environment surrounding the spacecraft has been subdivided into a set of angular sector and to each angular sector is associated a value of the impact elevation and of the impact azimuth that will serve to compute the direction of the vector flux linked to the correspondent angular sector. For the subdivision considered, there are a total of 14 x 4 = 56 vector fluxes.

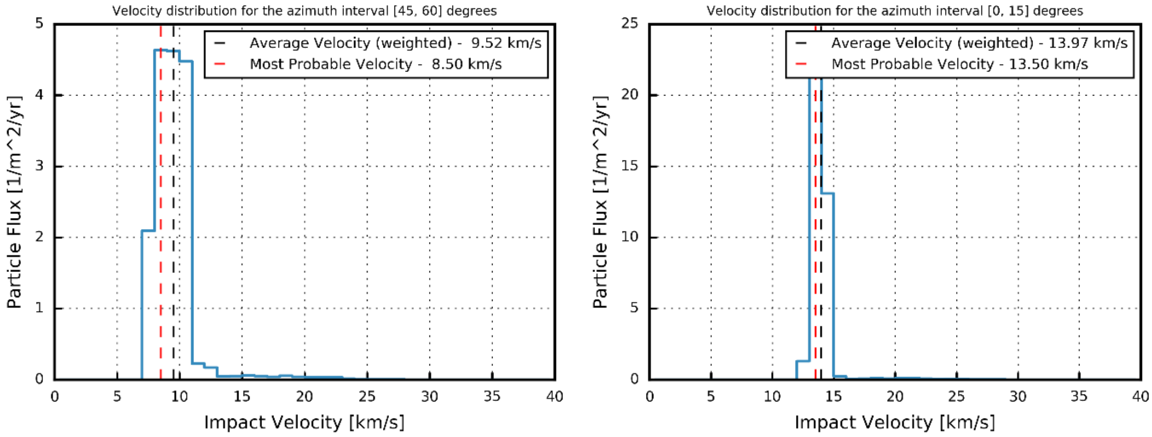

Figure 16: Examples for flux distributions vs impact velocity for the azimuth subdivisions defined by the user.

To complete the definition of the vector fluxes it is necessary to associate them a velocity magnitude. The process is analogous to the one followed for the impact azimuth and impact elevation but in this case the 3D distribution of flux vs azimuth vs velocity is considered. A set of flux vs velocity distributions is obtained. The number of distributions is again the same as the number of azimuth subdivisions (14 in this case). From each distribution, the magnitude of the velocity vector is extracted with possible choices again between the *most probable velocity* and the *weighted average velocity* Figure 16).

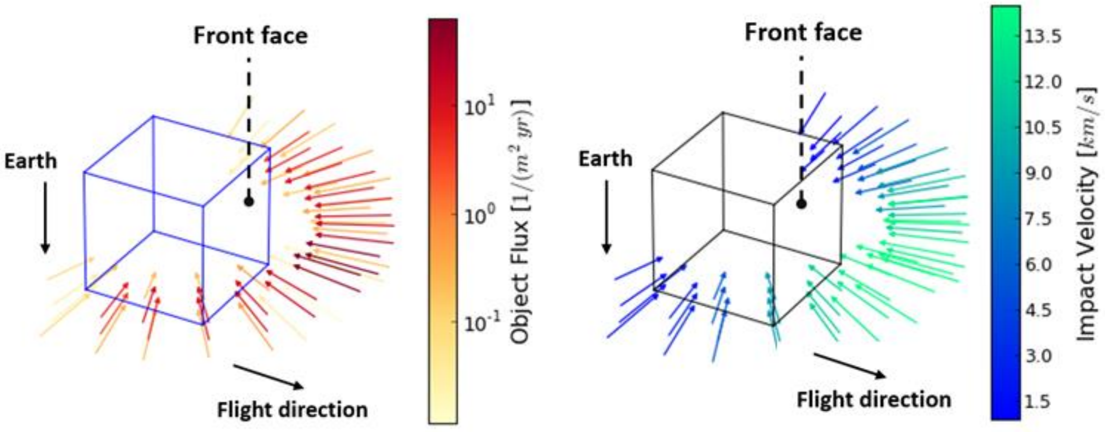

Figure 17: Vector flux representation for the example subdivision. On the left, the colour map represents the flux magnitude; on the right, the colour map represents the velocity magnitude of the vector flux elements.

With this kind of procedure two types of simplifications have been introduced. First, it is considered that the velocity has a higher variability with respect to the impact azimuth rather than the impact elevation that is the reason why the distribution of flux vs azimuth vs velocity is used to compute the velocity magnitude of the vector fluxes. Second, using a unique value for the velocity, whether it is the most probable or the average, we are assuming that all the particles coming from a specific direction (angular sector) possess the same velocity. Finally, the set of vector fluxes with associated flux, velocity, and direction in the form of impact azimuth and elevation can be represented in a visual way as in Figure 17.

3.4 Spacecraft vulnerability

This section presents the methodology developed to compute the vulnerability of spacecraft structures to the impact of space debris. Such a methodology relies on a probabilistic approach where the impact probability (P_i) and the penetration probability (P_p) on a surface is evaluated as a function of the particle flux, velocity, diameter, the projected area of the surface considered, and the mission duration in years. The present methodology is inspired by the procedure described in Welty et al. (2013). The procedure is represented in the flow diagram of Figure 18. First, the vector flux elements describing the debris particle fluxes encountered by the spacecraft during its operational life as a function of the orbit and attitude are computed, following the procedure described in Section 3.3.

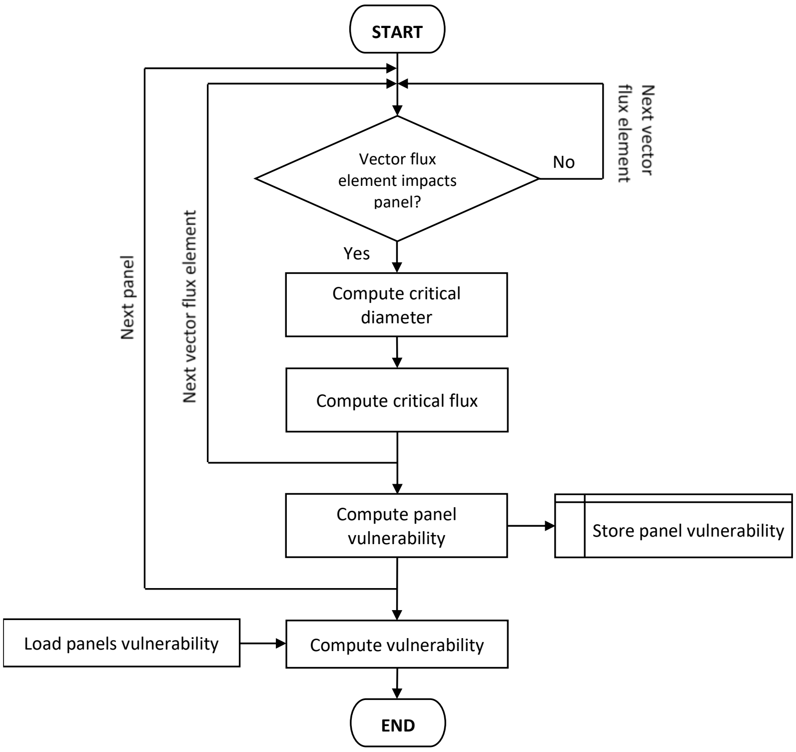

Figure 18: Flow diagram for the vulnerability computation of the external structure.

Then, the areas of the spacecraft that are subject to particle impacts are determined using a simple visibility rule: considering the object to be represented by a set *F* of faces and a vector flux element with associated a velocity vector $\mathbf{v_i}$. To verify if the particles represented by that vector flux element can impact one of the panels in the set *F*, the velocity vector $\mathbf{v_i}$ is checked with respect to the panel normal $\mathbf{n_j}$ with the following rule:

$$v_i \cdot n_j < 0 \tag{3.1}$$

The algorithm applies this visibility rule to a set of debris vector fluxes, extracted from the debris environment model as described in Section 3.3, against the panelised structure of the spacecraft. In the current stage of the model, no shadowing effects due to external components such as solar panels or antennas are considered.

3.4.1 Impact probability

After verifying whether a particular vector flux element hits a panel, it is necessary to compute the probability of the impact to occur. Assuming that debris impact events are independent, it is possible to use a Poisson distribution in Eq. (3.2) to evaluate the probability of encountering a debris particle.

$$p(y) = \frac{\mu^y}{y!} \cdot e^{-\mu} \tag{3.2}$$

where *P(y)* is the probability of having *y* impacts, and μ is the expected number of impacts. Using the Poisson distribution, it is possible to compute the impact probability, which is the complement of no particle impact (i.e., $y = 0$). Considering the expected number of impacts on the *j*-th face due to the *i*-th flux can be expressed as follows:

$$\mu = \varphi_i \cdot S_j^{\perp} \cdot \Delta T \tag{3.3}$$

where φ_i is the *i*-th vector flux element, $S_j^{\perp}$is the projected area of the *j*-th face on the direction of the vector flux element, and ΔT is the mission time in years. Consequently, the impact probability of the *i*-th vector flux element onto the *j*-th face is given by

$$P_i = 1 - e^{-\varphi_i \cdot S_j^{\perp} \cdot \Delta T} \tag{3.4}$$

3.4.2 Penetration probability

The next step in the process is to compute the penetration probability. To do so the classic approach using the ballistic limit equations (Bunte et al., 2009, Grassi et al., 2014, Kuiper et al., 2010, Reimerdes and Wohlers, 2001, Stokes et al., 2012, Stokes et al., 2000, Stokes and Swinerd, 2005, Welty et al., 2013) is adopted. BLEs (Appendix D) allow the computation of the critical diameter at which a particular damage to a component occurs as a function of the material, the velocity, and direction of the debris particle, and the geometric characteristics of the target such as the wall thickness. In this model, the velocity and direction associated with the vector flux element are passed to the relevant BLE and the critical diameter (d_c) is computed. As the direction of the vector flux is given as impact azimuth and impact elevation, it is necessary to convert them into the impact angle θ using the equation

$$\theta_{j,\, i} = \pi - \arccos\left(\frac{v_i \cdot n_j}{\|v_i \cdot n_j\|}\right) \tag{3.5}$$

where $\theta_{j,i}$ is the impact angle of the i-th debris flux element on the j-th panel, and $\mathbf{v_i}$ is the velocity vector associated to the i-th vector flux element. $\mathbf{v_i}$ can be expressed as a function of the impact azimuth Az_i and impact elevation El_i angles as follows:

$$v_i = v \cdot \begin{pmatrix} \cos(El_i) \cdot \cos(Az_i) \\ \cos(El_i) \cdot \sin(Az_i) \\ \sin(Az_i) \end{pmatrix} \tag{3.6}$$

After the computation of the critical diameter, it is possible to calculate the penetration probability $P_p^{j,\,i}$ of the i-th vector flux onto the j-th panel as follows

$$P_p^{j,\,i} = 1 - e^{-\varphi_{c,\,i} \cdot S_j^{\perp} \cdot \Delta T} \tag{3.7}$$

where $\varphi_{c,i}$ is the critical flux that is the particle flux corresponding to diameters bigger than the critical diameter.

The penetration probability on the overall structure is then computed iterating over the entire set of vector flux elements and over all the panels as follows:

$$P_p = 1 - \prod_{j=1}^{N_{panels}} \left(1 - \prod_{i=1}^{N_{fluxes}} \left(1 - P_p^{j,\,i}\right)\right) \tag{3.8}$$

where N_{fluxes} is the total number of vector flux elements and N_{panels} is the total number of panels composing the structure considered.

3.4.2.1 Definition and computation of the critical flux

The procedure to compute the critical flux is as follows: using the MASTER-2009 distribution of the cumulative flux vs particle diameter, the critical flux corresponding to the critical diameter is extracted. In Figure 19, the procedure described above is represented. For the case in the figure, the value taken for the critical flux is the one corresponding directly to the stepwise distribution. In the algorithm, it is also possible to pick a value coming from the linear interpolation of the values assumed by the distribution at the extreme of the interval containing the critical diameter. It is important here to underline a simplification that it must be introduced with this procedure. As the global distribution of cumulative flux vs diameter is adopted, the flux extracted is the overall flux for the entire range of azimuth and elevation angles. This flux cannot be directly used to compute the penetration probability relative to one of the vector flux elements. To each vector flux, in fact, is associated a value of the particle flux that is dependent upon the directionality, i.e. specific impact elevation and impact azimuth. As a simplified model is being developed, the assumption that the distribution of the particles’ diameter is uniform with respect to the impact direction is hereby made. With this assumption, the critical flux associated to a vector flux element is considered a fraction of the overall critical flux.

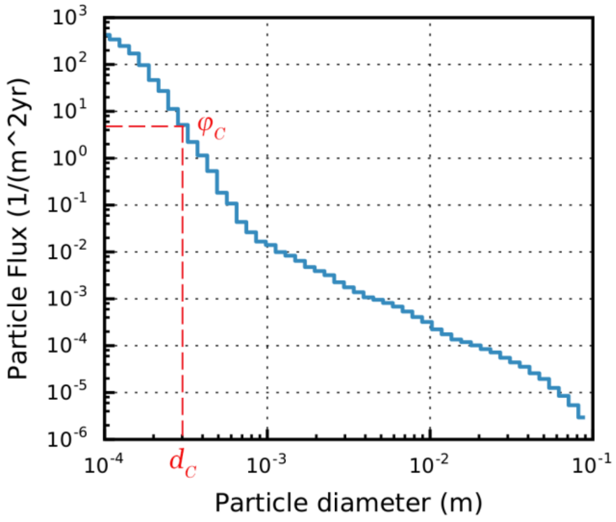

Figure 19: Critical flux computation methodology.

If φ_{TOT} is the total debris flux and φ_C is the overall critical flux computed (see Figure 19), the critical flux relative to the considered vector flux element can be expressed as

$$\varphi_{c,\,i} = \varphi_i \cdot \frac{\varphi_c}{\varphi_{TOT}} \tag{3.9}$$

The value computed with Eq. (3.9) is substituted in Eq. (3.7) to obtain the penetration probability due to the *i*-th vector flux element onto the *j*-th panel.

3.5 Model verification

The model developed in this thesis has been compared with the MIDAS module of the ESA software suite DRAMA (Gelhaus et al., 2014). MIDAS can perform a vulnerability analysis on oriented surfaces using debris fluxes extracted from ESA MASTER-2009. The user must specify the start and ending epoch of the simulation, the orbital elements of the operational orbit, and the thickness and density of the material of the panels. To compare the two codes a cubic shaped structure was chosen with characteristics summarised in Table 5. In order to accurately compare the two codes, the same BLE has been used, corresponding to the Cour-Palais single wall damage equation Gelhaus et al. (2014).

Table 5: Characteristics of the test structure.

Shape	**Cube**
Dimensions	1 × 1 × 1 m
Thickness	2 mm
Material	Aluminium 6061-T6
Damage equation	Cour-Palais single wall

Two mission scenarios are selected for the comparison. Their characteristics are summarised in Table 6. The first scenario is a one-year mission in a typical sun-synchronous orbit that is an orbit in which the spacecraft passes over any given point of the planet's surface at the same local mean solar time. The second scenario is a one-year mission in the International Space Station (ISS) orbit. The scenarios are standard test cases used for the testing of space debris impact assessment software (Christiansen et al., 2009) and have thus been used to test the developed model. The first orbit is characterised by very high debris fluxes, with high impact velocities, especially focused on the leading face of the structure. The second orbit, instead, is characterised by lower fluxes, with lower velocity impacts. The impacts are also more evenly distributed between the lead, left, and right faces of the structure.

Table 6: Mission scenarios characteristics.

Orbit Type	Altitude	Inclination	e	Start epoch	End epoch
SSO	802 km	98.6°	0.001	01/01/2016	01/01/2017
ISS	400 km	51.64°	0.001	01/01/2016	01/01/2017

Table 7 shows the results for the sun-synchronous orbit test case. The number of impact and number of penetrations for each face of the structure are compared for the two codes. The totals are also summarised at the bottom of the table. The results show a very good agreement for both the total number of impact and the total number of penetrations, with only a very small difference between the two models. The face-by-face comparison also shows a very good agreement.

Table 7: Comparison with DRAMA for a sample Sun-Synchronous orbit (SSO).

Test SSO	Number of impacts		Number of penetrations	
Face orientation	**MIDAS**	**Model**	**MIDAS**	**Model**
Lead	69.473	69.473	2.88E-01	2.77E-01
Space	0.48114	1.07841	1.71E-05	2.12E-05
Trail	0.032326	0.032676	7.60E-11	1.03E-06
Earth	0.54294	1.25968	1.73E-05	1.99E-05
Right	19.196	19.179	1.03E-02	6.75E-03
Left	21.953	21.975	1.00E-02	7.64E-03
Total	111.678406	112.997951	0.309034	0.291390

Two differences that are more noticeable can be spotted in the number of impacts for the Space and Earth faces and in the number of penetrations for the Trail face. The first difference can be explained with the approach followed by the described survivability model, where a discretised representation of the debris fluxes is used, with weighted average values for the direction and velocity of the vector flux elements. For the second difference, it can be explained remembering the procedure used to compute the critical flux (Section 3.4). In the case of the trailing face, the velocity and fluxes are very low, thus generating large values for the critical diameters. If the critical diameter is greater than the upper limit for the distribution extracted from MASTER-2009 (0.01 m), the value of the flux corresponding to this upper limit is taken. However, the order of magnitude of the five times lower than the number of penetrations of the leading face, and thus has a negligible influence on the result.

Table 8 summarises the same comparison for an ISS-like orbit. Even in this case the two models compare well, with the results closely following each other. In this case, the difference in the number of impacts for the Space and Earth faces are smaller, and all the other faces compares very well, up to two decimals. For the number of penetrations, the results are still comparable, but the agreement is reduced. Again, this is probably due to the way the vector flux elements are generated. In fact, the fluxes characteristics of ISS-like orbits have a less directional behaviour than the one in SSO orbits that is the fluxes and the velocities are more evenly distributed over the impact directions. The sampling methodology used to generate the vector flux elements is less capable of capturing this behaviour.

Table 8: Comparison with DRAMA for the ISS orbit.

Test ISS	**Number of impacts**		**Number of penetrations**	
Face orientation	**MIDAS**	**Survivability model**	**MIDAS**	**Survivability model**
Lead	1.5241	1.5282	1.21E-02	8.03E-03
Space	0.088823	0.11512	2.62E-06	1.20E-05
Trail	0.04817	0.04799	5.69E-06	5.74E-06
Earth	0.092399	0.116111	9.85E-06	1.21E-05
Right	1.638	1.635	3.69E-03	4.85E-03
Left	1.125	1.128	2.74E-03	3.01E-03
Total	4.516492	4.570212	0.015184	0.015923

3.6 Survivability criterion

To evaluate and compare each solution using the developed survivability model, a survivability criterion is introduced. The criterion used is defined as the probability of no-penetration (*PNP*), which can be expressed as

$$PNP = 1 - P_p \tag{3.8}$$

where P_p is the penetration probability as computed with Eq. (3.8). A value of 0 of the *PNP* index corresponds to a completely vulnerable structure, whose probability to be penetrated by a debris during the mission lifetime considered and given its characteristics is 100%. A value of 1 instead correspond to a fully protected configuration.

3.7 Summary

This chapter has presented the first stage of development of the survivability model, describing the procedure and methodologies used to predict the impact of space debris onto simplified spacecraft structure. The main characteristic of this methodology is the introduction of the concept of vector flux element, through which the entire space debris environment surrounding the spacecraft can be schematised. Subsequently, the computation of the penetration probability related to the debris impact is presented and the model is validated against state-of-the-art software packages. Finally, a survivability criterion is presented. The following chapter will focus on the application of the two models presented in Chapter 2 and Chapter 3 through an extensive sensitivity analysis on the different design-for-demise techniques and through the development of simplified design maps for both the demisability and the survivability.

Chapter 4 Demisability and survivability sensitivity analysis of spacecraft components

This chapter introduces an analysis of the effect of the most commonly used design-for-demise options on the demisability and on the survivability. The analysis is directed towards understanding, in the most general way, which are the parameters involved in the design-for-demise process that mostly affect the demisability and survivability criteria proposed. In addition, we aim at understanding how the two criteria are influenced and if trends can be identified. The analysis relies on the models described in Chapter 2 and Chapter 3. It thus considers basic spacecraft structures, schematised with elementary shapes. Nonetheless, it is important to have a preliminary yet general idea on the contribution of the design-for-demise options not just of the demisability of spacecraft components but also on their survivability.

The first part (Section 4.1) of the chapter analyses the sensitivity of the main design variables linked to the design-for-demise options. The aim is to rank the variables based on their sensitivity on both the demisability and survivability, especially identifying the ones that mostly affect both criteria at the same time. The second part (Section 4.2) focuses on providing contour maps for a quick estimation of the demisability and survivability of simplified objects. The aim is to show the possibility to build a catalogue of maps that can facilitate the detection of more critical components for the demisability and the survivability in the earliest stage of the design process.

The content of Section 4.1 and Section 4.2 follows the Acta Astronautica journal publication “Demisability and survivability sensitivity to design-for-demise techniques” (Trisolini et al., 2018a). Part of Section 4.2 is also derived from the journal publication on the Journal of Space Safety Engineering “Demise and survivability criteria for spacecraft design optimization” (Trisolini et al., 2016b).

4.1 Sensitivity analysis of design-for-demise solutions

Design-for-demise options should be selected since the early stage of the mission design, to achieve the compliance of a spacecraft with the casualty risk regulations without relying on controlled re-entry disposal strategies. As it was described in Section 1.4.3, several design solutions can be implemented to design spacecraft parts to demise (Kelley, 2012, Waswa and Hoffman, 2012). They affect the spacecraft and its components and, in general, they aim at generating structures with an increased area-to-mass ratio, a characteristic that enhance the demisability of an object. As a result, lighter, thinner, and more exposed structures are obtained. These structures, given their new characteristics, may be more vulnerable to the impact from space debris. In the following sections, the introduced design-for-demise solutions, except for the component location, are analysed using the demisability and survivability models of Chapter 2 and Chapter 3.

The problem under examination is extremely complex. Multiple parameters influence both the demisability and the survivability of a spacecraft. Some of these parameters are related to the system design of the spacecraft. The design-for-demise solutions belong to this category as they directly affect the manufacturing of specific parts. In addition, mission related parameters such as the operational orbit of the spacecraft and its disposal strategy can influence the resulting survivability and demisability. Moreover, the dependency of the demisability and the survivability upon these parameters is usually non-linear, thus making it difficult to generalise the results obtained. In fact, the selection of specific design-for-demise options and their consequences on the mission design and requirements is very much mission dependent.

However, it is still possible to study such design options, understanding in which way they influence the demisability and the survivability. Can a specific solution be more effective than others can? Is the implementation of a solution independently affecting the demisability or the survivability or are they influenced at the same time? In this case, have they a competing or a concordant behaviour? In order to study this behaviour and evaluate the design-for-demise options previously described, the single options are analysed independently, keeping constant the other parameters. In this work, the analysis each of the solutions consists in the evaluation of both the demisability and the survivability over a range of initial conditions so that the variability of the indices can also be assessed. In this way for each design solution it is possible to evaluate average effect, measured using the developed indices. Alongside the average effect, also the standard deviation is computed to provide an evaluation of how variable is the effect of the specific design solution as a function of the initial conditions. Before examining the design-for-demise options by considering their average behaviour over a range if initial conditions, it is important to understand which of these conditions is more influential to the problem in exam. A sensitivity analysis has thus been carried out over the initial condition provided to the demisability and the survivability models.

4.1.1 Sensitivity analysis methodology

In sensitivity analysis we study how the different sources of uncertainties in the inputs are influencing the uncertainty of the model output. Specifically, in this work, we want to study how the variation of the design of the spacecraft under the principles of design-for-demise affect both the demisability and the survivability of the spacecraft. Usually, the results of a sensitivity analysis are summaries by a few output scores, which can be referred as sensitivity indices. A sensitivity index indicates in a concise fashion how much the uncertainty in the considered quantity affects the output of the model.

The procedure selected to perform the sensitivity analysis in this work relies on the Sobol method (Sobol, 2001), which is classified among the variance-based sensitivity methods. These methods

(Saltelli et al., 2010, Chan et al., 1997) are global sensitivity analysis procedures, which exploit the decomposition of the variance of the model output into terms depending on the input parameters and their interactions: the variance of the output is decomposed into fractions that can be related to the different inputs. For example, if we have a model with two inputs and one output, we can find that the output variance is caused for 50% by the first input, 30% by the second, and 20% by their interaction. These percentages are directly interpreted as measures of sensitivity.

Considering a general model expressed as $Y = f(\mathbf{X})$, where $\mathbf{X}$ is the vector of d input parameters and Y is the output of the model. The Sobol method decomposes the variance of Y with respect to the variances of the elements of $\mathbf{X}$ so that

$$\mathrm{Var(Y)} = \sum_{i=1}^{d} V_i + \sum_{i<j}^{d} V_{ij} + \cdots + V_{12\dots d} \tag{4.1}$$

where $V_i = \mathrm{Var}_{\mathrm{X_i}}\left(E_{X_{\sim i}}(Y \mid X_i)\right)$ and $V_{ij} = \mathrm{Var}_{\mathrm{X_{ij}}}\left(E_{X_{\sim ij}}(Y \mid X_i, X_j)\right) - V_i - V_j$. Here $X_{\sim i}$ indicates the set of all variables except X_i, and E is the expected value. With this procedure, the variance of the output is decomposed into terms that can be attributed to each input and to their interactions. When summed together, they give the total variance of the output. The Sobol method allows the computation of the first order and total order effects of the input parameters, as well as the mutual interactions between them. The first order effects are expressed by the index

$$S_i = \frac{V_i}{\mathrm{Var(Y)}} \tag{4.2}$$

This index measures the effect that changing a single variable has on the output. This is the contribution to the output variance caused varying a single parameter but averaged over the variations in other input parameters. The value of S_i is always smaller than 1. The total order effects instead measure the contribution to the output variance of a variable, including all variance caused by its interactions, of any order, with any other input variables. It is expressed as

$$S_{T_i} = 1 - \frac{\mathrm{Var}_{\mathrm{X_{\sim i}}}\left(E_{X_i}(Y \mid X_{\sim i})\right)}{\mathrm{Var(Y)}} \tag{4.3}$$

Differently to the first-order effects, the total effects can have a sum greater than 1.

These methods are extremely versatile (Sobol, 2001, Chan et al., 1997) and can be used with many different models. Using a Monte-Carlo based sampling procedure they are suitable to be used with non-linear models and models whose input parameters are not directly correlated (Kucherenko, 2005, Sobol, 2001). For this reason, they have been selected for the analysis in exam. In the present work the Sobol methodology coupled with the Saltelli sampling technique (Saltelli, 2002, Saltelli et al., 1999) have been used. In the Saltelli sampling a number $N = (2k + 2) \cdot n$ simulations must be ran, where *k* is the number of input parameters, and *n* is the sampling size. Throughout the chapter, the number of sample *n* used is equal to 2000.

4.1.2 Demisability and Survivability indices

To perform a sensitivity analysis of the demisability and of the survivability it is necessary to define indices which can summarise the level of demisability and survivability of an object. We define these indices as the demisability index and the survivability index.

For the presented sensitivity analysis, the selected demisability index is the Liquid Mass Fraction (LMF) index defined by Eq. (2.30) in Section 2.5 and the selected survivability index is the Probability of no-Penetration (PNP) as defined by Eq. (3.8) of Section 3.6.

4.1.3 Representative component for the sensitivity analysis

To carry out the sensitivity analysis, it was decided to consider the effects of the design-for-demise options on a reference internal component, as it is not practically possible to perform such an analysis on a large variety of components and structures. This choice must consider both the characteristics of the demisability and the survivability analysis, considering a component whose analysis is interesting for both aspects. Following this consideration, spacecraft tanks were selected as reference components. In fact, they are sensitive components for the demisability as they usually survive re-entry (National Astronautics and Space Administration, 1997, National Astronautics and Space Administration, 2001, Battie et al., 2012). At the same time, it is important to ensure adequate protection and resistance of tanks from debris impact as, being pressurised, they are particularly susceptible to ruptures and leakage (Putzar and Schäfer, 2006). The characteristics of the selected representative tank are summarised in Table 9.

Table 9: Characteristics of the reference tank.

Parameters	**Values**
Mass	15 kg
Shape	Cylinder
Length	0.896 m
Diameter	0.6 m
Material	Steel AISI-316[1]

They were derived from the data available for the MetOp-A mission (European Space Agency, 2012, Airbus Safran Launchers GmbH, 2003b, Readings and Reynolds, 1996). The mission is selected to

---

[1] The original material of the tank is the titanium alloy Ti-6Al-4V. The decision to change the tank material was made in order to have a greater variety of results for the different initial conditions. Titanium alloys, in fact, rarely demise and/or reach the melting temperature.

be representative of medium to large LEO satellites, which are the most interesting to analyse for design-for-demise options. Moreover, the spacecraft belongs to the sun-synchronous region that is the most exploited LEO region, making it a good candidate to be representative of many mission scenarios. Knowing the amount of propellant stored by MetOp-A (316 kg), and the tank manufacturer (Airbus Safran Launchers GmbH, 2003b), a suitable tank was selected, considering a filling factor of 0.4 and knowing that the entire storage system consists of four identical tanks.

The presented analyses have some limitations that are mainly a consequence of the simplified nature of the models used. Using the models described in Chapter 2 and Chapter 3 it is still not possible to model internal components. This allow considering only single simplified components, preventing the analysis from modelling more realistic spacecraft configurations. As such, the break-up of internal components cannot be modelled, as well as the shielding effect of the external structures on the internal components (these aspects will be assessed in Chapter 5 and Chapter 6). This last point affects the absolute value of the survivability index. In fact, with the presence of the external structure, the penetration probability on internal components is greatly reduced in magnitude. However, it was considered that the results obtained with an object directly exposed to the debris fluxes could be extended in relative terms also to internal components. It is in fact reasonable to assume, for example, that changes to a component design that increase its survivability, evaluated when it is directly exposed to the debris fluxes, will still produce an increase of the survivability when it is protected also by the external structure.

4.1.4 Sensitivity to mission characteristics

When considering the demisability and the survivability models as described in Chapter 2 and Chapter 3, it is necessary to provide them some parameters in order to perform the simulations. For the demisability, the initial conditions at re-entry are the initial altitude, relative velocity, flight path angle, longitude, latitude, and heading angle. For the survivability, the operational orbit is provided, which consists of the altitude, and inclination of the orbit. In addition, the mission lifetime in years is specified. These are the main characteristics that influence the re-entry of a spacecraft and its vulnerability to debris impact. Consequently, these are the parameters considered in the sensitivity analysis presented. The reference component is the tank described in Table 9.

4.1.4.1 Demisability sensitivity to re-entry inputs

The sensitivity of the demisability index is analysed varying all the parameters defining the initial conditions at the re-entry interface. The boundaries of the values adopted in the sensitivity analysis are summarised in Table 10. All the variables in Table 10 are uniformly varied inside the specified ranges. Such choice reflects the fact that the demise of components is only studied after the break-up of the main spacecraft body happens. The standard value for the break-up altitude is 78 km (Martin et al., 2005b, Gelhaus et al., 2014); however, this value can vary according to the spacecraft characteristics and the entry scenario. Despite the difficulties in predicting the actual break-up altitude, it is possible to consider its variation in a sensitivity analysis and study its contribution to the demisability. The selected altitude range reflects several possible re-entry scenarios. The longitude, latitude, and heading angle ranges were selected to consider all the possible re-entry locations and orientations. The range of velocity is considerably wide, in order to consider for different re-entry scenarios and characteristics of the spacecraft. In fact, the velocity at break-up is influenced by the slope of the re-entry trajectory, the initial velocity, and the aerodynamics of the spacecraft main body. The range for the flight path angle is representative of uncontrolled re-entry, either from a slowly decaying orbit or from a disposal orbit directly targeting a re-entry.

Table 10: lower and upper bounds for the parameters of the re-entry sensitivity analysis.

Parameters	**Lower bounds**	**Upper bounds**
Longitude	0°	360°
Latitude	-90°	90°
Altitude	60 km	100 km
Entry velocity	7.1 km/s	8.1 km/s
Flight path angle	-5°	0°
Heading angle	-90°	90°

The results of the sensitivity analysis are shown in Figure 20. The most influential parameters are the altitude and the velocity at the break-up. In fact, the influence on the LMF variance is around 55% (first order index) for the altitude and 35% for the velocity. All the other parameters have a considerably lower sensitivity index, with a contribution to the output variance that is lower than 5%. Latitude and longitude have an almost negligible sensitivity index.

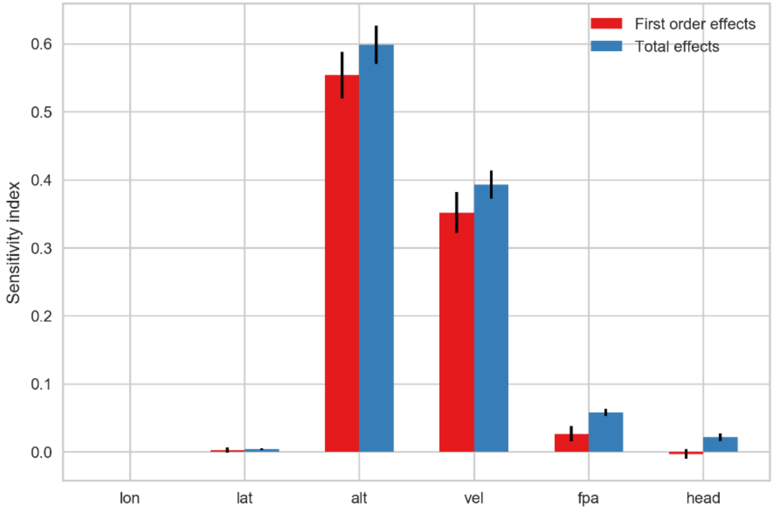

Figure 20: First order and total order effects for the re-entry sensitivity analysis of components. In the x-axis, from left to right, longitude, latitude, altitude, velocity, flight path angle, and heading angle.

It is nonetheless important to mention that latitude and longitude become important in case the casualty risk on ground is considered. In this case, in fact, the variability of the population on Earth as a function of latitude and longitude is important for the computation of the casualty risk. Both the first order and the total order effects are presented in the analysis. It is interesting to observe that the first and total order effects are of comparable magnitude. This means that in the re-entry of a spacecraft component, the value of a parameter directly influences the demisability even with different combinations of the other parameters.

4.1.4.2 Survivability sensitivity to operational conditions

To study the sensitivity of the survivability, the altitude, the inclination, and the mission lifetime have been considered. The values ranges adopted in the sensitivity analysis are summarised in Table 11. The study focuses on the LEO region; as such, the maximum altitude was set to 2000 km. The maximum mission operational lifetime has been set to 15 years as it was considered a reasonable upper value for the duration of a mission. The specified time range only includes values for the operational life of the spacecraft, without considering the disposal time needed by the spacecraft to re-enter into the atmosphere after decommissioning. In this latter case, a larger time span would be needed to include the entire lifetime of the mission. The inclination range instead considers all possible orbit options.

Table 11: Lower and upper bounds for the parameters of the survivability sensitivity analysis.

Parameters	Lower bounds	Upper bounds
Altitude	700 km	2000 km
Inclination	0°	180°
Mission lifetime	1 yr	15 yr

The results of the sensitivity analysis are presented in Figure 21. As expected, the altitude has the highest impact on the survivability analysis, contributing for more than 35% to the first order effects (variance of the PNP index). This is due to the variation of the debris fluxes as a function of the altitude, where the highest concentrations are in correspondence of specific altitude ranges such as the bands between 600 km and 900 km and between 1400 km and 1500 km (Lewis et al., 2017b, Radtke et al., 2017, Flegel et al., 2009). An interesting result is the influence of the orbit inclination, being almost half the sensitivity index of the altitude (about 15% contribution). Orbit inclination can affect the penetration probability on a structure because different flux concentrations can be present at different inclinations and because of the flight direction of the spacecraft with respect to space debris. Retrograde orbits are in general more dangerous than direct orbits as they generate impacts with a larger relative velocity. This is probably because orbit inclination becomes a more important factor only for those orbits with higher debris fluxes (e.g. sun-synchronous orbits). As such, over the wide range of altitude considered, the debris density variation with the altitude becomes a more determinant factor than the inclination. Nonetheless, this contribution is still important and is thus considered for the remaining of the analysis. Finally, the mission lifetime has clearly a strong influence on the survivability. As expected, the longer the mission the higher is the probability of a component being damaged by debris impacts (Figure 21).

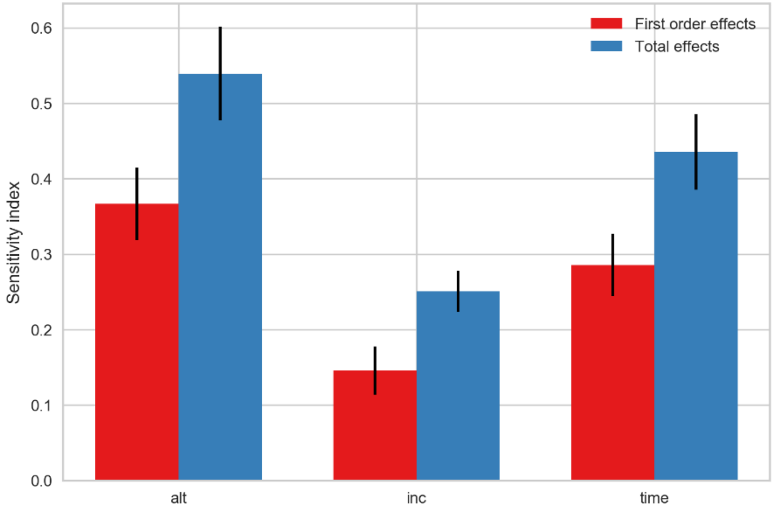

Figure 21: First order and total order effects for the survivability sensitivity analysis of components.

4.1.4.3 Effects of design-for-demise solutions on the demisability and survivability indices

Once the main environmental parameters affecting the demisability and the survivability have been identified, it is possible to focus on the effects that the design-for-demise solutions have, on average, on the demisability and on the survivability. To do so, the identified design-for-demise options are considered singularly, varying them while keeping constant the other parameters. In this way, their effect is isolated from the others. Following the results obtained in Section 4.1.4, the effect of the design-for-demise options is studied varying the three identified most influential initial conditions (i.e. altitude, entry velocity, and flight path angle) for each of the solutions available in the design-for-demise options. For each option, a Monte Carlo simulation was performed varying the initial conditions inside the altitude, velocity, and flight path angle ranges (Table 10) for the demisability, and the altitude, inclination, and mission time ranges for the survivability (Table 11). Again, the Saltelli sampling methodology (Saltelli, 2002, Saltelli et al., 2010) was used with 2000 samples. In this way, it is possible to perform a more general analysis of the impact of the design-for-demise solutions as they are evaluated over the entire range of possible initial conditions.

The obtained plots represent for each solution the average value of the demisability and of the survivability indices over the set of Monte Carlo simulations, together with the standard. In addition, to the plot is added the percentage of solutions above a threshold value of demisability and survivability. For the demisability, the selected threshold is a value of the LMF index equal to 0.9. For the survivability, the equivalent threshold is a value of the PNP index equal to 0.99. This percentage is directly related to the quality of the solutions. A higher percentage corresponds to a solution more likely to generate a more robust design in terms of demisability and survivability over a wide range of initial conditions. In a preliminary design phase, this is an important aspect as many the design can still be modified.

Changing the component material

The first design-for-demise option considered is the change of the material of the component. The materials considered are the aluminium alloys 6061-T6 and 7075-T6, the stainless steels AISI-304 and AISI-316, the Inconel-601 alloy, the titanium alloy 6Al-4V, and the graphite epoxy. Titanium and stainless-steel alloys are common materials used in the manufacturing of spacecraft tanks. Aluminium alloys have been also considered as they can be used to manufacture tanks and they are being studied by ESA Clean Space as demisable substitutes of currently non-demisable titanium tanks (Grassi et al., 2017, Riley et al., 2017). Graphite-epoxy has been selected as representative of composites solutions and is used throughout the thesis to identify CFRP materials. Two options for the graphite-epoxy are considered, as there is a significant discrepancy in the literature on the models used to describe its behaviour. According to the model used in DAS and ORSAT, the graphite-epoxy is extremely demisable as it is considered to char as it reaches its melting temperature. We labelled this model as *Graphite-epoxy 2* and its properties are summarised in Table A-1. However, according to other studies, graphite-epoxy and composites in general are very resistant to the ablation process, usually surviving the re-entry process (Lips et al., 2005b, Lips et al., 2015). This is especially due to the properties of carbon fibres, which are very temperature resistant. We refer to this model as *Graphite-epoxy 1* (Table A-1). Two different cases have been considered: components with a constant thickness (2 mm in this analysis) and components with a variable thickness, coinciding with the minimum allowable thickness sustainable by the tank (which depends on the material). In the first case, together with the thickness, the dimensions are kept constant and correspond to the one specified in Table 9. In the second case, the dimensions are constant, and the thickness is varied in order to maintain the structural integrity. The minimum allowed thickness is computed using Eq. (4.4) (Wertz and Larson, 1999).

$$t_{s,\,\min} = \frac{K_{sf} \cdot p_{\max} \cdot r}{\sigma_u} \tag{4.4}$$

where σ_u is the ultimate strength of the material, r is the radius of the cylinder, p_{max} is the maximum operating pressure (assumed equal to 4 MPa) and K_{sf} is a safety factor (assumed equal to 1.5). This analysis is meant to compare the performance of feasible tanks configuration for the different material considered. It is important to underline the fact that changing the material of tanks can also have a considerable influence on the mass budget of the mission. Table 12 summarises the mass of the tanks for each material option used in the analysis and for both the cases considered.

Table 12: Summary of the mass impact of tank solutions as a function of the material and case considered.

Tank material	Tank mass (kg) Constant thickness	Tank mass (kg) Minimum thickness

Al-6061T6	12.161	26.448
Al-7075T6	12.493	27.169
AISI-304	35.412	39.985
AISI-316	35.981	40.627
Inconel-601	36.117	40.781
Ti-6Al4V	19.889	14.244
Graphite-epoxy-1	7.038	9.551
Graphite-epoxy-2	6.95	9.432

Figure 22 and Figure 23 show the results for both cases and for different materials. In both graphs, the top plot represents the behaviour of the Liquid Mass Fraction, and the bottom graphs represent the probability of no-penetration.

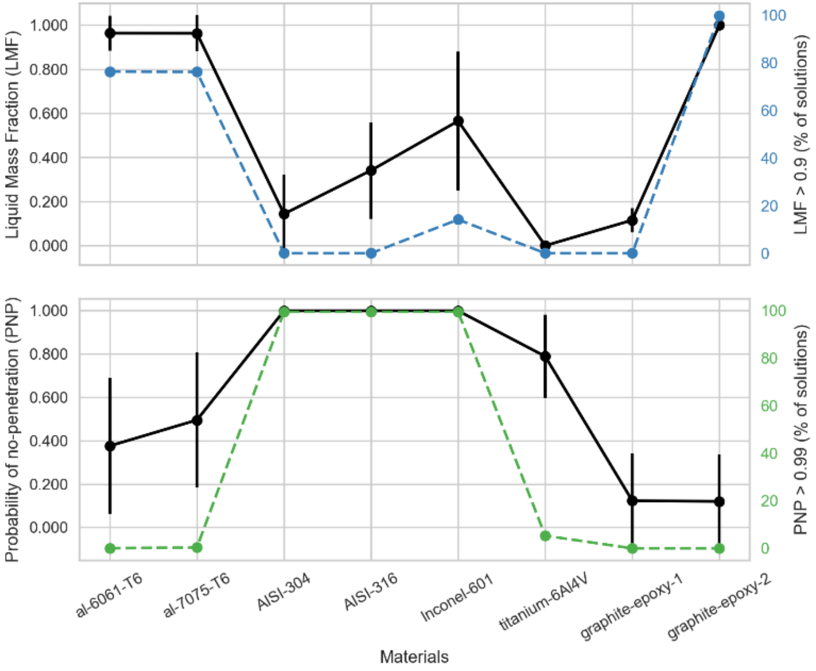

Figure 22: Average value and standard deviation of the LMF and PNP indices for different materials and a constant thickness configuration (black lines). Percentage of solutions over a 0.9 LMF index (blue line) and over a 0.99 PNP index (green line).

The black points and the bars represent the average values and standard deviations of each Monte Carlo simulations. The blue lines show the percentages of solutions for each material case whose LMF index is higher than 0.9. The green lines represent the percentages of solutions for each material case whose PNP index is higher than 0.99. From the presented analysis, it is first possible to observe the considerable difference in both the demisability and survivability index that is obtained when just a change in the material is introduced. Taking a closer look to the demisability, the materials can be ranked based on their LMF index results. Aluminium alloys and the graphite-epoxy-2 have the highest demisability. The results associated to the graphite-epoxy-2 are here presented for completeness; however, they constitute a very optimistic representation of the behaviour of composites material, which has been proved not to be very accurate (Lips et al., 2015). The main destructive re-entry codes, such as SESAM, SCARAB, and SAM use a much more conservative approach that can be best represented by the graphite-epoxy-1 case.

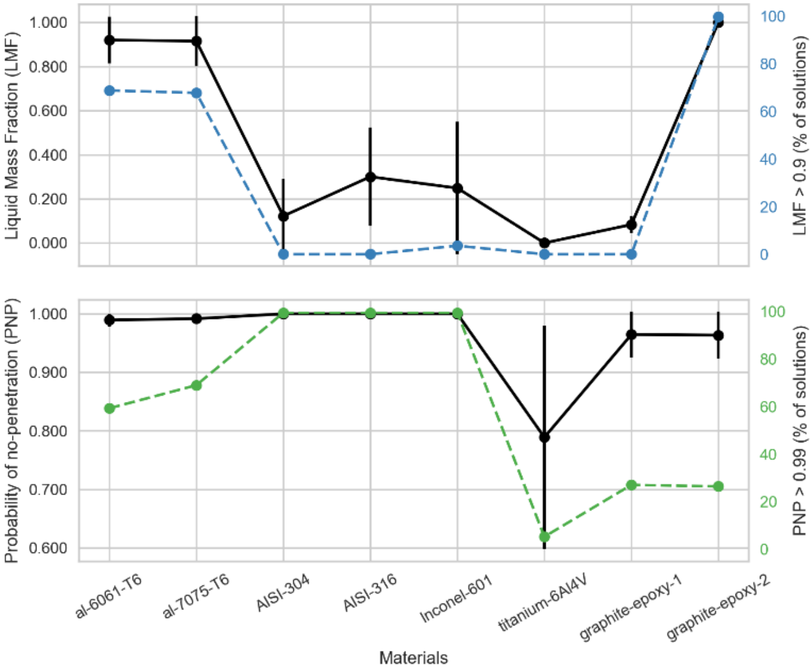

Figure 23: Average value and standard deviation of the LMF and PNP indices for different materials and a minimum allowable thickness configuration (black lines). Percentage of solutions over a 0.9 LMF index (blue line) and over a 0.99 PNP index (green line).

Aluminium alloys, as expected, prove to be very effective in improving the demisability of the analysed components, also resulting in robust design, given the high percentage of solution with an LMF index over 0.9. On the other hand, materials such as titanium and graphite-epoxy-1 are extremely difficult to demise, producing no solutions with a demisability above 0.9. In the middle between these two extreme behaviours, there is the group represented by the stainless steels and the Inconel alloy. Such solutions can reach an LMF index around half the one of aluminium. However, only for the Inconel alloy solutions, the demisability can reach the level of 0.9. As such, among this group of material the Inconel alloy proves to be the most demisable one. Titanium, as expected, generated no demisable solutions in both cases.

Looking at the other side of the problem that is the correspondent change in survivability introduced when changing the material, it is evident that the particular case in exam makes a considerable difference. In Figure 22, where the thickness is kept constant to 2 mm (a typical value for spacecraft component (Bunte et al., 2009) the PNP changes significantly between the different materials. The clear favourite in terms of resistance to debris impact are the stainless steels and the Inconel alloys. Follow the aluminium alloys with a PNP index half the one of the stainless steels, to terminate with the graphite epoxy. The behaviour described by Figure 22 can be considered as the absolute scale of value for the survivability of the considered materials as the main characteristics influencing the PNP index (dimensions and thickness) are kept constant.

In Figure 23, the results are more directly applicable to tanks, where the thickness is related to the structural integrity. In this case the aluminium alloys and the graphite-epoxy have a PNP closer to the one reached by the stainless-steel solutions. Still the difference is in one order of magnitude as the PNP for the aluminium alloy solutions is in the order 0.99, whereas the PNP for stainless steel solutions is in the order of 0.999. A behaviour that is more clearly deduced looking at the probability of having solutions with PNP greater than 0.99 (green dashed line). Titanium solutions in this case are much more vulnerable to debris impacts because, given their high ultimate strength (950 MPa), the solutions considered have the lowest thickness (about 1.5 mm), thus making it about 20% more vulnerable. Aluminium solutions, on the other hand, have a thickness of about 4.4 mm whereas the stainless-steel solutions of about 2.1 mm.

From the results in Figure 23, it possible to deduce that, by only changing the material of commonly used tank configuration to an aluminium alloy, it is very likely to achieve a demisable solutions or at least a solution that will only require other minor changes to be completely demisable. Under the constraint of maintaining structural integrity, such solution also proves to have a very good survivability, almost comparable to the one of a stainless-steel solution of similar resistance. However, given the thickness is more than doubled such solution would also be heavier (Table 12). In any case, the necessity to consider more alternatives and perform trade-off anlyses, also considering the other requirement and constraints of a mission is of primary importance.

Changing the component thickness

Another option to affect the demisability of a component is to change its thickness. This solution can be used in combination with other design-for-demise options but can also be useful in all those cases in which other options such as changing the material, or the dimensions of a component are not viable. To present the dependence of the demisability and of the survivability upon the thickness variation, all the characteristics of the reference tank are kept constant, except for the thickness itself. Different materials are taken into account, and the results for the aluminium alloy 7075-T6 and the stainless steel AISI316 are presented in Figure 24 and Figure 25 respectively. The thickness is varied from 0.5 mm to 10 mm in steps of 0.5 mm. The behaviour of the demisability and survivability indices is different with a variation of the thickness. The liquid mass fraction, in fact, varies smoothly, constantly decreasing for the aluminium (Figure 24), and reaching a maximum around 2 mm for the stainless steel (Figure 25). On the other hand, the probability of no-penetration has a steeper trend, with a considerable variation in a small range of thicknesses and a flattening afterwards. As expected, an increase in the thickness translates in a lower demisability for the aluminium alloys. As the thickness increases, also the standard deviation of the solutions increases indicating a higher dependence of the outcome on the initial conditions for less demisable solutions. In a similar but opposite fashion, the standard deviation of the solutions for the survivability increases with decreasing thickness. In fact, as the vulnerability of the solution increases, the orbit selected becomes more influential.

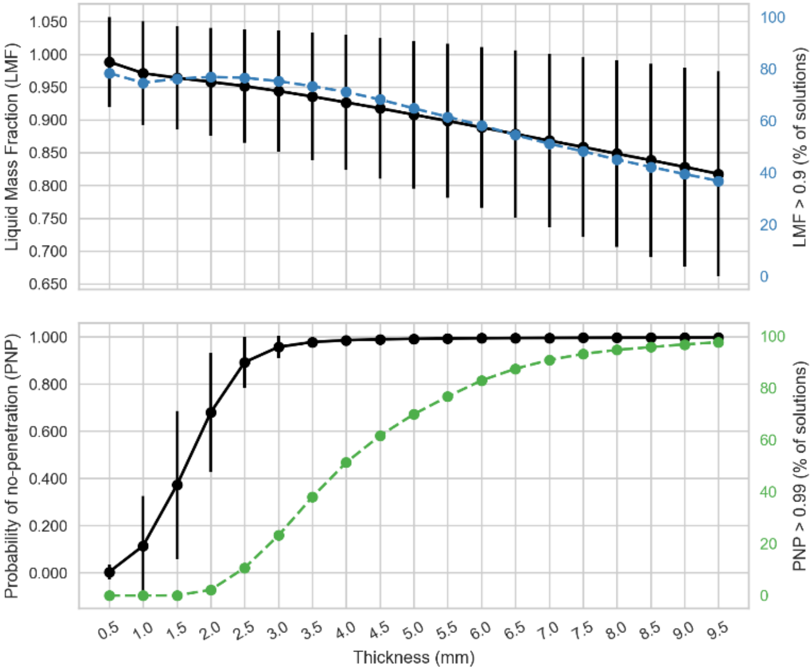

Figure 24: Average value and standard deviation of the LMF and PNP indices for variable thicknesses of aluminium alloy components (black lines). Percentage of solutions over a 0.9 LMF index (blue line) and over a 0.99 PNP index (green line).

In general, it is possible to observe that aluminium alloy solutions are more robust on the demisability side, granting a high LMF index over a wide range of thicknesses. The stainless-steel solutions, on the other hand, are more robust on the survivability side, generating very resistant structure even with small thicknesses. In fact, the percentage of solutions with a PNP index greater than 0.99 is over 90% in all the cases except for the smaller thickness (0.5 mm). From the presented results is possible to deduce that the thickness has a more direct influence on the survivability rather than on the demisability. When the thickness changes, the probability of no-penetration changes considerably (with orders of magnitude of difference). This is strikingly evident for the aluminium alloys but is also true for the stainless-steel case. Moreover, the requirements over the probability of no-penetration are usually very strict, aiming at components with a PNP index below 1%. The influence on the demisability is instead more gradual. For the stainless steel case (Figure 25), despite a 20% change in the LMF index can be obtained varying the thickness, in no case such difference produces solutions with a demisability over 0.9. Consequently, a change in the thickness would need to be coupled with other design-for-demise solutions to achieve a substantial effect. In the aluminium alloy case, instead the LMF index remains always high and with a good percentage of solutions over a 0.9 LMF index. Therefore, a high demisability can be maintained coupling the thickness change with small changes in the other design-for-demise options.

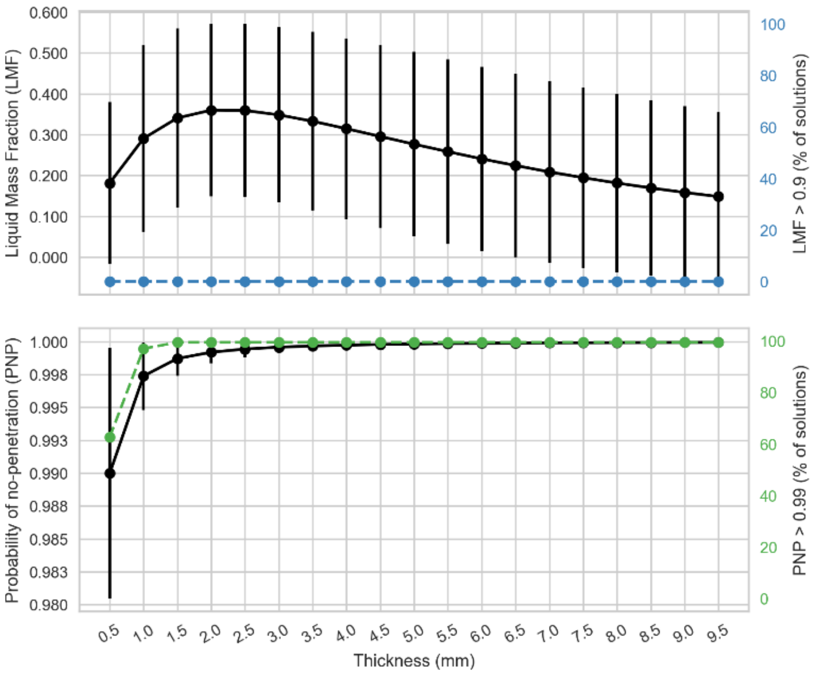

Figure 25: Average value and standard deviation of the LMF and PNP indices for variable thicknesses of stainless-steel components (black lines). Percentage of solutions over a 0.9 LMF index (blue line) and over a 0.99 PNP index (green line).

Changing the component dimensions

Changing the component dimensions is an option that can be implemented in order to change the area-to-mass ratio of the component, trying to increase its demisability. Nonetheless, when the dimensions change, also the survivability of the component changes and these effects need to be considered. For example, larger components have a greater exposed area to the debris fluxes, which results in a higher vulnerability of the component itself. It can also result in the subdivision of a large component into smaller parts. For example, a large battery assembly can be subdivided into more than one box, making it more demisable. The same procedure can be carried out with tanks, dividing the amount of propellant into more vessels. This last case is the one considered here to show the dependence of the demisability and the survivability with respect to changing the dimensions of a component.

Starting from the tank configuration of Table 9, the range of dimensions is varied as if the number of tanks ranges from one to ten vessels. The aspect ratio of the tank is kept constant. The thickness is instead varied according to Eq. (4.4) in order to compare realistic configurations. The corresponding dimensions of the tanks for the different configurations is summarised in Table 13 and Table 14. The corresponding results are presented in Figure 26 and Figure 27 for aluminium alloy and stainless steel tanks respectively. It is evident in both cases that increasing the number of tanks, thus making them smaller and less massive, results into a higher demisability. For both materials, the increase in the Liquid Mass Fraction is considerable and can make the configuration completely demisable.

Table 13: Radius and thickness values for aluminium alloy tank assemblies.

Number of tanks	1	2	3	4	5	6	7	8	9	10
Radius (m)	0.366	0.290	0.254	0.230	0.214	0.201	0.191	0.183	0.176	0.170
Thickness (mm)	6.946	5.513	4.816	4.376	4.062	3.823	3.631	3.473	3.339	3.224

Table 14: Radius and thickness values for stainless steel tank assemblies.

Number of tanks	1	2	3	4	5	6	7	8	9	10
Radius (m)	0.366	0.290	0.254	0.230	0.214	0.201	0.191	0.183	0.176	0.170
Thickness (mm)	3.589	2.848	2.488	2.261	2.099	1.975	1.876	1.794	1.725	1.666

In the stainless-steel case, it is possible to pass from configurations where none of the solutions have a demisability higher than 0.9 to having almost 40% of the solutions above this limit. This is a considerable increase in demisability. An interesting aspect is also represented by the fact that for the configurations with lower number of tanks (1 to 3), just changing the material from stainless steel to aluminium alloy would not make the configuration completely demisable on average. Therefore, a further increasing in the number of tanks would be needed, or an integration of other design-for-demise solutions in order to increase the demisability.

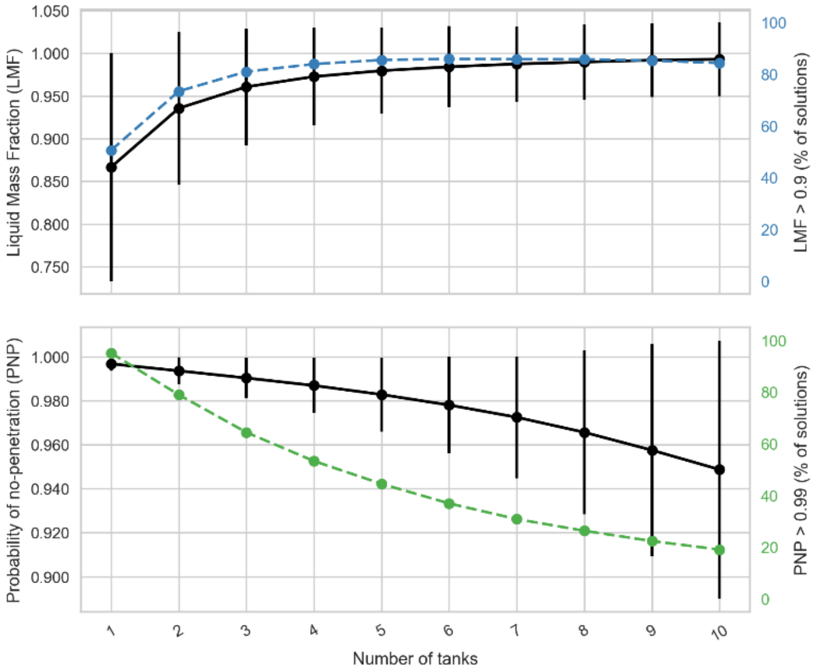

Figure 26: Average value and standard deviation of the LMF and PNP indices for variable dimensions of aluminium alloy components (black lines). Percentage of solutions over a 0.9 LMF index (blue line) and over a 0.99 PNP index (green line).

For what concerns the survivability, it is evident that increasing the number of components reduces the probability of no-penetration, at the cost, however, of increasing the configuration weight. Despite a higher number of elements produces smaller components, these components are also thinner and thus more vulnerable to the debris impact. In addition, more components, even smaller in dimensions, have in total a larger exposed area. For these reasons a contrasting behaviour between the two indices when changing the dimensions can be observed. It is also important to observe the difference between the change in survivability produced for the aluminium alloy and for the stainless steel. In the first case, the reduction in the PNP index is about 5%, whereas in the second case is about 0.2%.

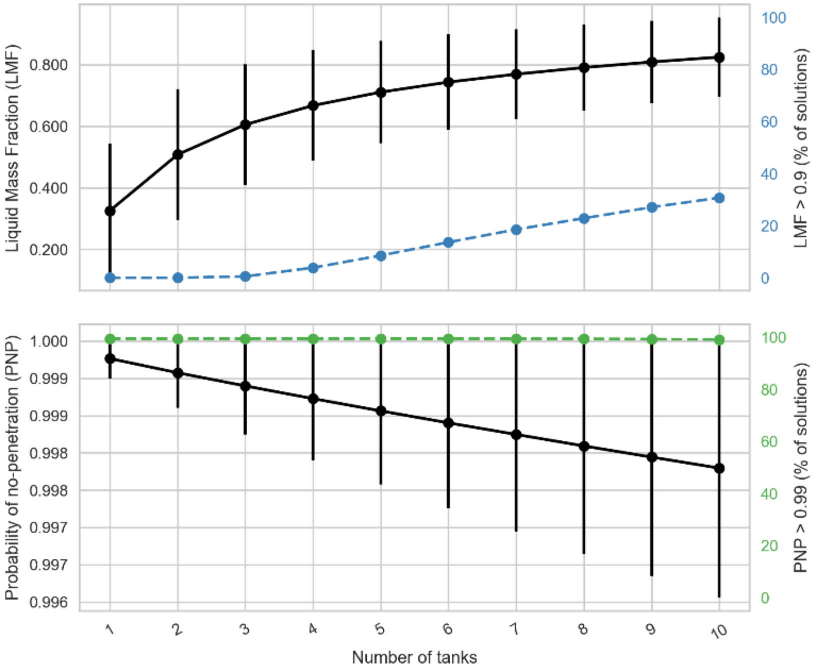

Figure 27: Average value and standard deviation of the LMF and PNP indices for variable dimensions of stainless-steel components (black lines). Percentage of solutions over a 0.9 LMF index (blue line) and over a 0.99 PNP index (green line).

There is thus one order of magnitude difference in the effects for the two materials. As such, changing the number of components for more vulnerable materials (such as aluminium alloys) is more influential on the overall probability of no-penetration than for a more resistant material. Another aspect is the robustness of the solution. In the aluminium alloy case, the percentage of solution with a PNP index over 0.99 drops quickly with increasing number of tanks, down to 20% for a ten tanks configuration.

Changing the component shape

A change in the component shape can be reflected into changes into the demisability and the survivability of a component. The demisability is influenced because of the different area-to-mass ratio and the different shape factors (Sections 2.2.3 and 2.3.1). In the same way, also the survivability is influenced by a change in the area-to-mass ratio and in the thickness of the component. As the reference component is a tank, the two shapes considered for the comparison here are a sphere and a cylinder. In Table 15 and Table 16, the results for the two shapes are presented for two material, the aluminium alloy 7075-T6 and the stainless steel AISI-316. For the simulation, the internal volume of the component is kept constant as well as the average cross-sectional area. The thickness varies according to Eq. (4.4) for the cylinder and Eq. (4.5) for the sphere.

$$t_{s,\ \mathrm{min}} = \frac{K_{sf} \cdot p_{\mathrm{max}} \cdot r}{2 \cdot \sigma_u} \tag{4.5}$$

Both the demisability and the survivability indices are higher for cylindrical tanks than for spherical ones. The LMF index is more significantly influenced by a change in the shape. For the aluminium case, it increases by 0.237, and 0.339 for the stainless-steel case. The change obtained is definitely not negligible. However, while the percentage of solutions with an LMF index above 0.9 significantly increase for the aluminium solutions, the same cannot be observed for the stainless-steel solutions where no solution could achieve such a level of demisability. On the other hand, the survivability is less influenced by the shape change, with a 0.015 variation in the *PNP* index for the aluminium alloy and a 0.001 variation for the stainless-steel case.

Table 15: Variation of the average value of the LMF and PNP indices with changing shape for aluminium alloy tanks. Percentage of solutions over a 0.9 LMF index and over a 0.99 PNP index.

	Sphere	**Cylinder**
LMF (average)	0.709	0.946
PNP (average)	0.932	0.947
LMF > 0.9 (%)	26.4	75.8
PNP > 0.99 (%)	14.6	19.3

Table 16: Variation of the average value of the LMF and PNP indices with changing shape for stainless steel tanks. Percentage of solutions over a 0.9 LMF index and over a 0.99 PNP index.

	Sphere	**Cylinder**
LMF (average)	0.0002	0.339
PNP (average)	0.998	0.999
LMF > 0.9 (%)	0	0
PNP > 0.99 (%)	97.46	99.45

It can be concluded that a change of the shape in a sensitive component such as spacecraft tanks can produce, on average, significantly more demisable solutions for low-melting point alloys such as aluminium alloys. Table 15 clearly shows that the average LMF index substantially increase and, more importantly, the percentage of solutions with a high value of the LMF index increases, thus ensuring a higher probability of having a fully demisable configuration. On the other hand, it is also showed that the variation of the shape has little effect on the demisability of high-melting point alloys such as stainless steel. As such, changing the shape of high-melting point alloys can only be used as a complementary design-for-demise solution, with other, more effective, options to be considered as main way of action.

Changing the component aspect ratio

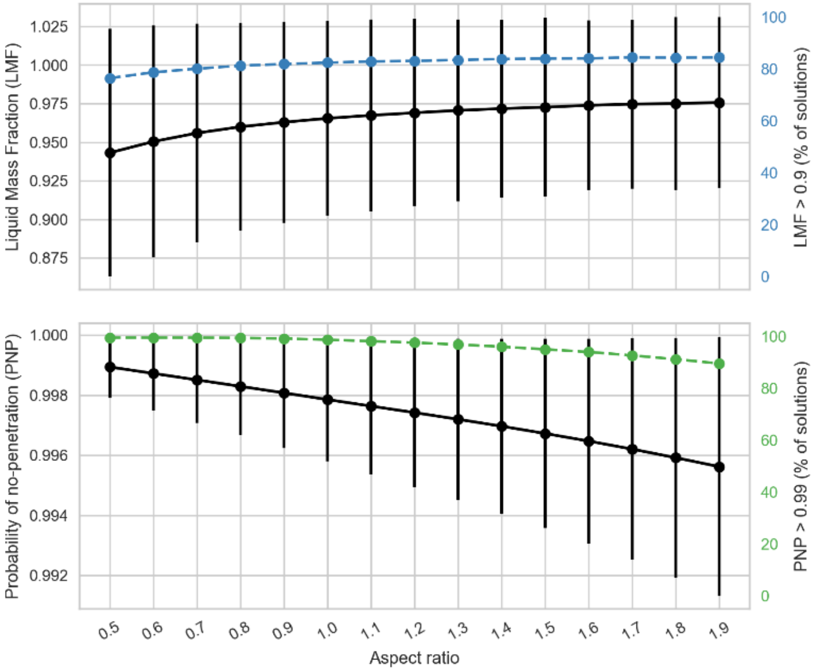

Figure 28: Average value and standard deviation of the LMF and PNP indices with changing aspect ratio for aluminium alloy components (black lines). Percentage of solutions over a 0.9 LMF index (blue line) and over a 0.99 PNP index (green lines).

Another possible strategy to act on the demisability of a component is to modify its aspect ratio. To compare different solutions, the baseline tank of Table 9 is adopted. Starting from this geometry, the aspect ratio is varied so that the internal volume of the tank is kept constant. The range of aspect ratios considered goes from a minimum of 0.5 to a maximum of 2.0. In addition, the thickness of the component is kept constant and equal to 2 mm. Figure 28 shows the effect of changing the aspect ratio for an aluminium alloy tank. The average variations result quite small, in particular if compared with the influence of design options such as changing the material or the dimensions of the component. In general, however, increasing the aspect ratio will slightly increase the demisability while at the same time slightly decreasing the survivability of a component as it is expected. Such design option can thus only be used as a complement to other, more effective, design solution as it cannot determine by itself a major variation of either of the two indices.

4.1.5 Sensitivity of the demisability and survivability indices to the design-for-demise solutions

Similarly, to the sensitivity analysis carried out in Section 4.1.4, and complementing the analysis of the previous sections, this section presents the sensitivity analysis of the demisability and survivability indices as a function of all the design-for-demise options taken into account. Again, the Saltelli method is adopted with 2000 samples (equivalent to 24000 simulations) for both the demisability and the survivability analyses. The ranges and values of the parameters considered in the sensitivity analysis are summarised in Table 17.

Table 17: Ranges and values for the sensitivity analysis on the design-for-demise parameters.

Parameters	**Ranges / Values**	
Material	Al-6061-T6, Al-7075-T6, AISI-304, AISI-316, Graphite epoxy 1, Titanium 6Al4V	
Shape	Sphere, Cylinder	
Dimensions	1 to 10 components	
Thickness	0.0005 mm	0.01 mm
Aspect ratio	0.5	2.0

Figure 29 shows the sensitivity of the demisability index to the design-for-demise options for a reference initial condition. The initial condition has an altitude of 80 km, a flight path angle of -1° and a relative velocity of 7.3 km/s. The conditions well represent an average uncontrolled re-entry from the LEO region with a break-up happening at an 80 km altitude. The most important parameter in determining the demisability of a component is the material. However, it is not always possible to change the material of a component. Therefore, it is also important to consider the other parameters that play a role when adopting a design-for-demise approach. Among the other parameters, the most important are the dimensions (width and radius) and the thickness. This could also be deduced by the results discussed for the effects of changing the thickness and the dimensions (Section 4.1.4.3), where the influence of changing the dimensions and the thickness was quantified for a reference component.

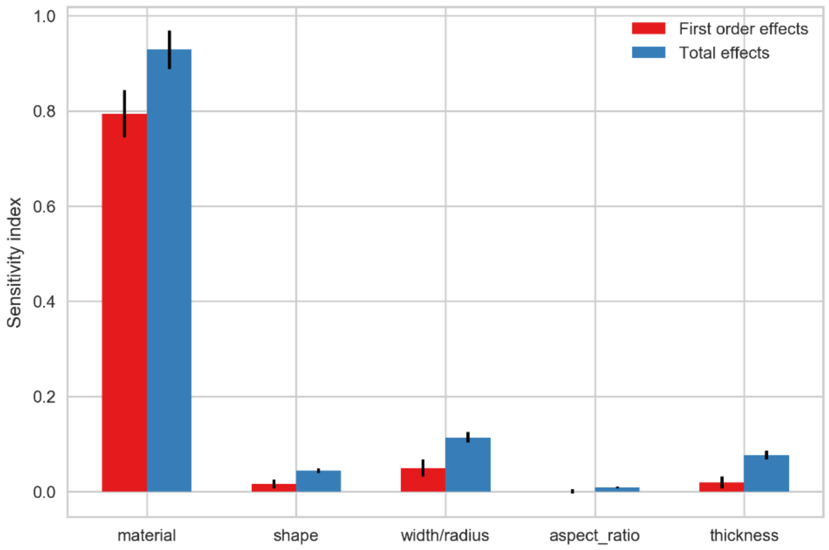

Figure 29: Sensitivity analysis of the demisability index with respect to the design-for-demise solutions.

Another interesting observation concerns the non-negligible difference between the first order effects and the total order effects, for the three main parameters (material, width/radius, and thickness). In fact, they greatly affect the ballistic coefficients of a re-entering component, which in turn affects the evolution of the re-entry trajectory. As such, not just their single contribution is important, but their combination.

Figure 30 shows the corresponding sensitivity analysis for the survivability index. In this case, the most influential parameters are the thickness and the material, with a comparable sensitivity index. The dimensions have an average sensitivity on the survivability index, whereas the shape and the aspect ratio have a negligible influence on the output. Another feature that can be observed is the difference between the first order and total order effects of the sensitivity. The total order effects are clearly higher than the first order effects. Therefore, the contributions of the design parameters to the probability of no-penetration are coupled between each other. This can be observed in a quantitative way in the previous analysis. For example, the variation of the PNP index with the thickness (Figure 24 and Figure 25) has a clear difference in its variation when considering the aluminium alloys rather than the stainless steel, meaning that the effect of the change in thickness is also coupled to the change in the material.

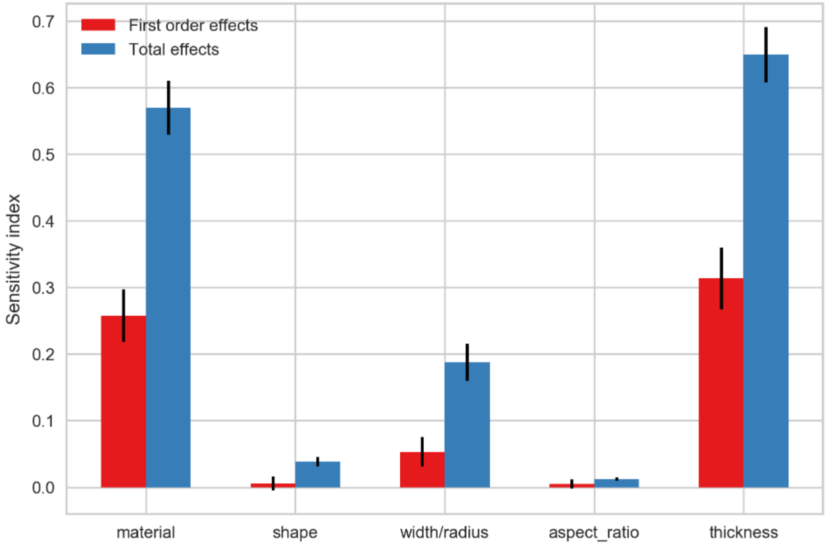

Figure 30: Sensitivity analysis of the survivability index with respect to the design-for-demise solutions.

4.1.6 Results

The presented analyses show the contribution of each design-for-demise option to the demisability and the survivability to spacecraft components. In addition, the sensitivity associated to each solution is evaluated for both the demisability and the survivability. Despite the results were obtained using a reference component they are useful to determine the more important parameters to be considered when changing the design of a component following the design-for-demise principles.

The most relevant design parameters are the material, the dimension, and the thickness of a component. As these parameters are important in influencing the demisability, they should be considered before the others when changing the design of a component. However, they are also the most influential for the survivability. As such, a design has also to be verified against the survivability requirements when the design-for-demise options are implemented. This means that trade-off solutions should be searched for where the different design options generate different levels of demisability and survivability. In a later stage, the most promising among these solutions are analysed in more detail and compared with the requirements and constraints of the mission design.

Alongside the identification of the most important design parameters, the quantitative influence of the single design options on the survivability and demisability indices was investigated. Many of the design options, except for some changes in material, affect the demisability and the survivability in a contrasting way that is while one of the two indices increases the other decreases. The different magnitude of this influence can also be observed, with the change of material and thickness being the most influential.

4.2 Demisability and survivability maps for spacecraft components

The results of Section 4.1.5 show that the survivability and the demisability are mostly influenced by a subset of the design-for-demise options. Following this consideration, a set of maps are presented for both the demisability and the survivability to better highlight the mutual dependency between these parameters. The maps show the variation of the LMF and PNP indices with the dimension and thickness for different shapes and materials. It is possible to generate such maps for the most common materials used in spacecraft design, for the main basic shapes and for a set of common initial conditions for the re-entry and most exploited orbits for the survivability. Such generated “booklet” of maps can be used as a useful tool to quickly assess the level of demisability and survivability that can be expected from a component, considering its dimension, thickness, and material, and to compare it with other design options. In fact, we can locate on the maps the geometry considered and estimate its level of demisability and survivability. Then, moving on the maps the effect of changing the dimensions and the thickness can be observed. Going to another map, with the same geometry is instead possible to evaluate the effect of a change of material or shape.

4.2.1 Demisability maps

Examples of the demisability maps are presented in Figure 32 and Figure 34. Three commonly used materials are considered that are an aluminium alloy (Al-7075-T6), a stainless steel (AISI-316), and a titanium alloy (Ti-6Al-V), and three different shapes (Sphere, Cylinder, Box). In addition, a set of six different orbit (Table 18) is used to present the difference between the maps when considering different initial condition for the re-entry.

Table 18: Initial re-entry conditions examined.

Orbit ID	**Altitude**	**Relative velocity**	**Flight path angle**	**Longitude**	**Latitude**	**Heading angle**
1	100 km	7.3 km/s	0°	0°	0°	45°
2	100 km	7.3 km/s	-1.5°	0°	0°	45°
3	100 km	7.3 km/s	-3°	0°	0°	45°
4	80 km	7.1 km/s	-1°	0°	0°	45°
5	80 km	7.1 km/s	-2°	0°	0°	45°
6	80 km	7.1 km/s	-3°	0°	0°	45°

Figure 31 to Figure 34 show how the LMF index varies when changing the radius and the thickness of a spherical component.

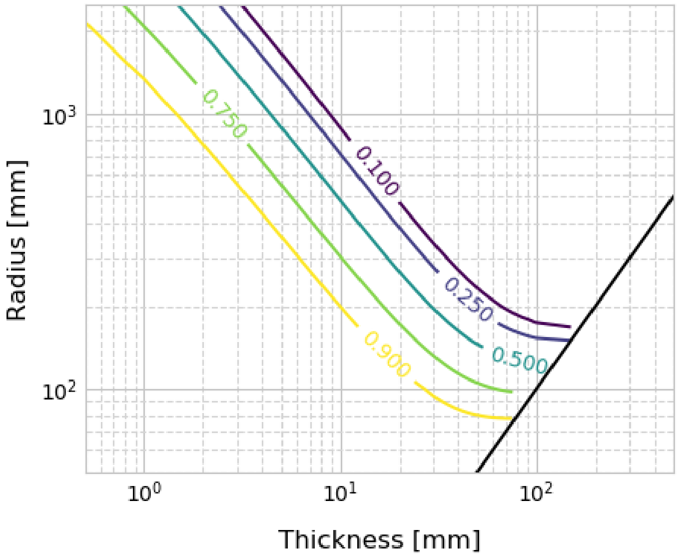

Figure 31: Demisability contour maps for aluminium alloy spheres. Case 3.

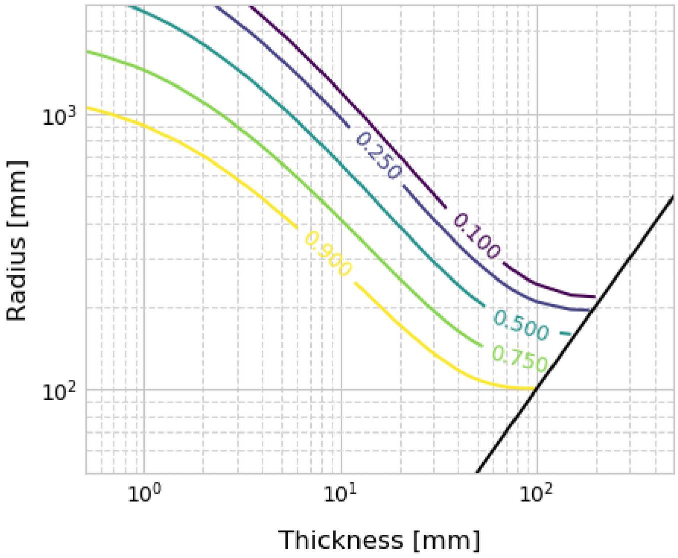

Figure 32: Demisability contour maps for aluminium alloy spheres. Case 6.

The map on the left correspond to the orbit case 3 of Table 18, and the map on the right to the orbit case 6. The radius ranges from 50 to 2500 mm while the thickness varies from 0.5 to 500 mm. The bottom right corner of the plots represents a region of non-physical combinations of radius and thickness, i.e., the thickness is greater than the radius.

It is possible to observe from Figure 31 and Figure 32 that quite a big portion of the maps correspond to very demisable geometries, with a LMF index greater than 0.9. A regular pattern is also recognisable as the demisability reduces going towards the upper right portion of the map. The two plots differ from each other for the initial altitude and velocity. In Figure 32, given the lower initial altitude and velocity, the demisability reduces. A considerable difference can be observed between the aluminium spheres plot (Figure 32) and the equivalent plot for stainless steel spheres (Figure 34). The latter has an evidently smaller demisable region due to the higher melting temperature and heat capacity of the stainless steel with respect to the aluminium alloy, but also because of the larger mass of a steel sphere having the same dimension of an aluminium sphere.

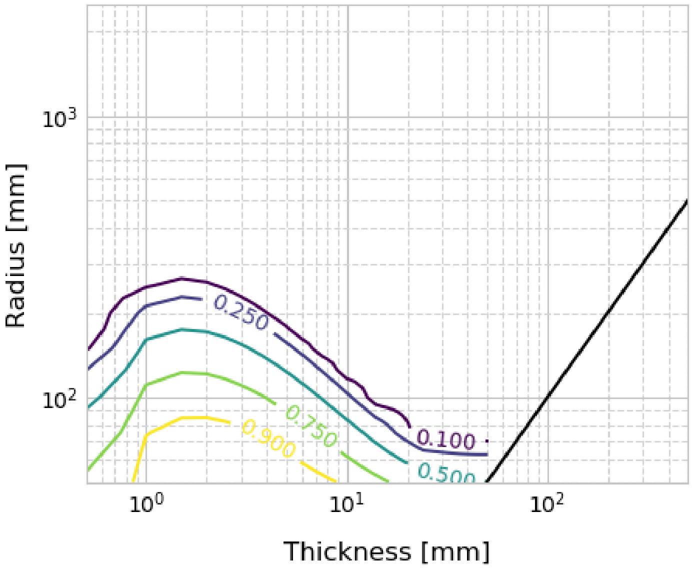

Figure 33: Demisability contour map for stainless steel spheres. Case 3.

The presented maps can be a powerful and easy-to-use tool to evaluate the demisability level of spacecraft components in the early stages of the mission design. In fact, it is easy to locate the component on a map given its geometry and its material and evaluate its demisability.

Figure 35 shows a possible variation of the aforementioned maps, where the comparison between three common materials is presented, with a simultaneous representation of the contour lines of the LMF for each material. For sake of clarity, only three contours for each material are represented, showing the combination of radius and thickness where a 30%, 60%, and 90% of the object mass demises during the re-entry.

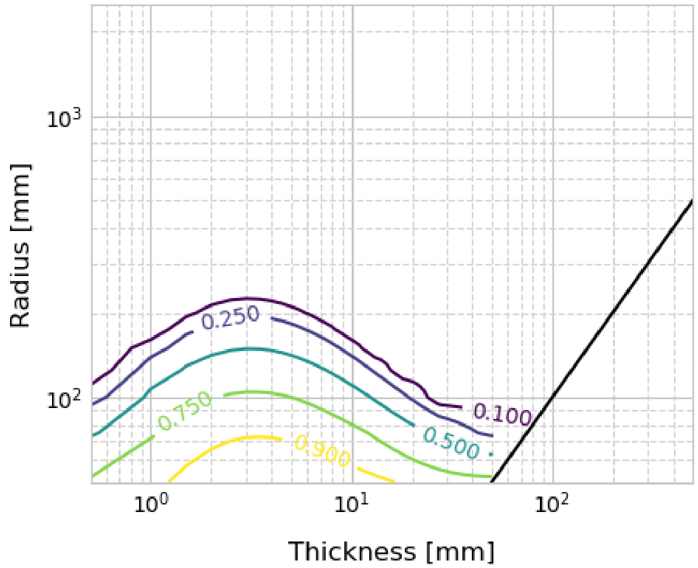

Figure 34: Demisability contour map for stainless steel spheres. Case 6.

The difference between the three materials is clear from the graph, with titanium being by far the less demisable of the materials, only granting a partial demise even for the smallest components. Stainless steel and the aluminium alloy follow with increasing demisability. Using these kinds of maps, it is even more convenient for a fast comparison between different materials.

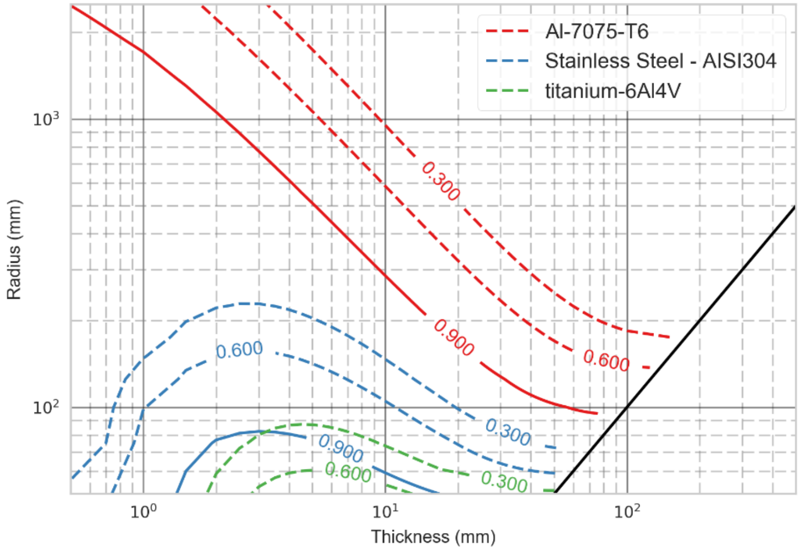

Figure 35: Comparison between the Liquid Mass Fraction of spheres made of aluminium 7075-T6, stainless steel, and titanium 6Al-4V for the orbit case 1.

Figure 36 and Figure 37 show equivalent diagrams for the other two shapes considered, the cylinder, and the box. Figure 36 shows the same contours for a right cylinder, and Figure 37 represents the contours for a cubic shape. As mentioned at the beginning of the section, these types of maps can be readily used to estimate the demisability of a solution based on its dimensions, thickness, material, and shape. The maps can be either generated for different initial conditions, for example a range of initial velocities and break-up altitudes or a reference trajectory could be selected end evaluate the different options with respect to the results obtained with it. In this latter case, only one set of maps has to be generated as function of the initial conditions. This last scenario is the one adopted at the ESA Clean Space office to compare different design-for-demise options.

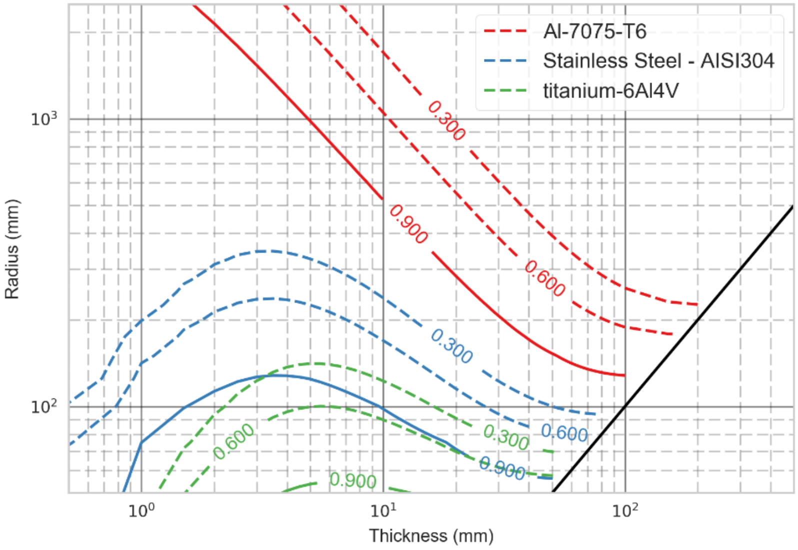

Figure 36: Comparison between the Liquid Mass Fraction of right cylinders made of aluminium 7075-T6, stainless steel, and titanium 6Al-4V for the orbit case 1.

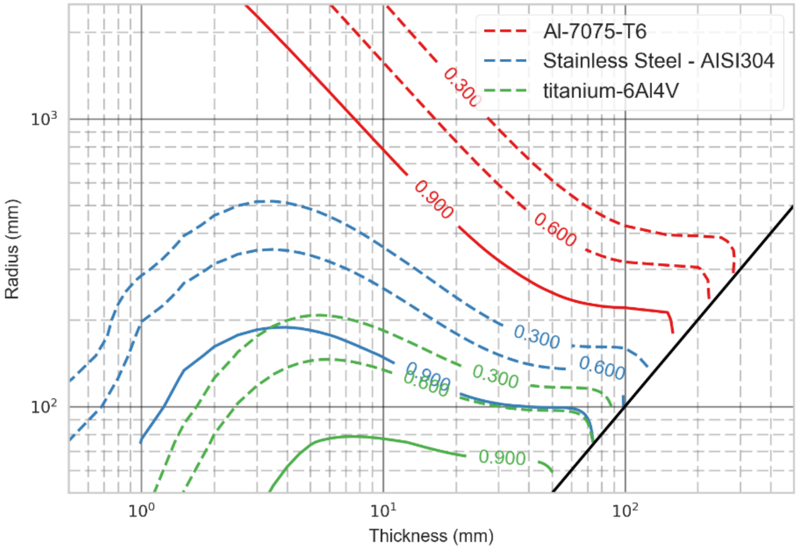

Figure 37: Comparison between the Liquid Mass Fraction of cubes made of aluminium 7075-T6, stainless steel, and titanium 6Al-4V for the orbit case 1.

4.2.2 Survivability Maps

Analogous maps can be generated for the survivability of components as a function of their dimensions, thickness, material, and geometry. In this case, three different orbits have been considered (Table 19), to show the variation in inclination and altitude for orbits in the sun-synchronous region that is one of the most exploited altitude range.

Table 19: Characteristics of the orbits considered in the analyses.

Parameter	Orbit 1	Orbit 2	Orbit 3
Altitude	800 km	700 km	700 km
Eccentricity	0.001	0.001	0.001
Inclination	98°	30°	60°
Mission time	1 yr	1 yr	1 yr

The maps of Figure 38 and Figure 39 represent the penetration probability variation with changing dimensions and thickness for a cubic structure made of aluminium for the orbit cases 1 and 3 respectively. In the same way, Figure 40 and Figure 41 show the penetration probability on a stainless steel cube for the orbit case 1 and 3.

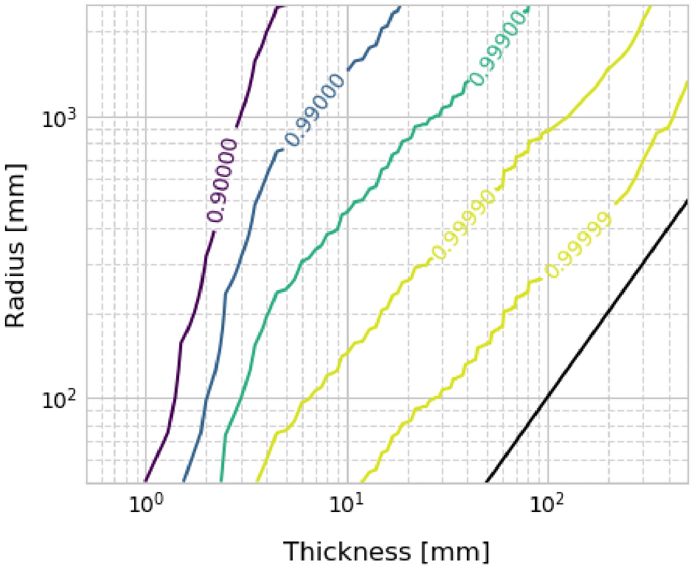

Figure 38: Survivability contour maps for aluminium alloy cubes. Orbit 1.

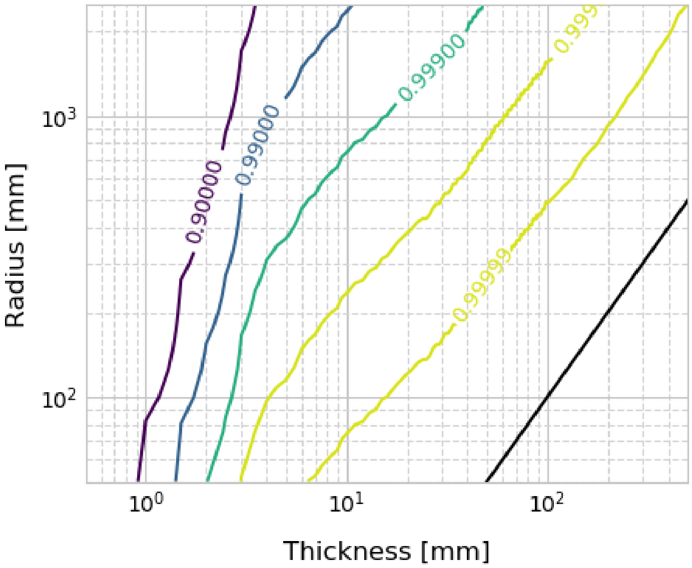

Figure 39: Survivability contour maps for aluminium alloy cubes. Orbit 3.

The plots have the same basic structure of the demisability contour maps with logarithmic scale on the axes, the same ranges of thickness and side length, and the non-physical zone in the bottom right corner of the plot. The contours of the map on the other hand are not linear anymore but they are represented in logarithmic scale ranging from 1 to 0, one being a 100% probability of no-penetration that is the structure provides full shielding. Figure 38 to Figure 41 show an expected behaviour, with the probability of no-penetration decreasing with decreasing thickness and dimension. Figure 40 and Figure 41 shows a flattening of the contour lines after a certain value of the side length, corresponding to a constant probability of no-penetration even with varying thickness. Examining Eq. (3.7) and considering a constant side length, the value of the area at risk remains constant and so does the mission duration when the mission is specified. Consequently, the only element changing is the critical flux whose value depends on the size of the critical diameter and on the shape of the particle flux distribution as a function of the diameter. Now, as the thickness increases, the critical diameter becomes bigger and can exceed the upper limit specified for the MASTER-2009 distributions. If this is the case, the critical flux is the one associated with the upper limit and is thus constant for all the thicknesses leading to a critical diameter greater than the limit one.

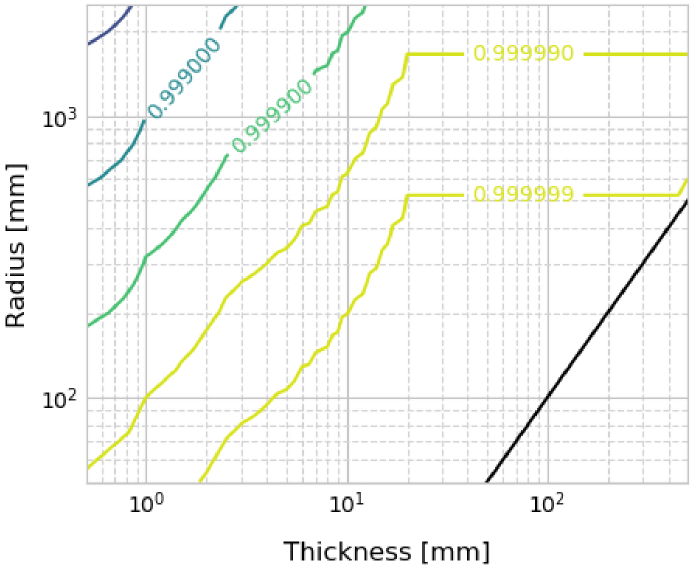

Figure 40: Survivability contour maps for stainless steel cubes. Orbit 1.

Considering the plots of Figure 38 and Figure 39, the difference between two operational orbits can be observed. The plot on the left represent an 800 km altitude orbit inclined by 98 degrees and the plot on the left a 700 km orbit with a 60 degrees inclination. The right plot appears shifted towards the upper left corner with respect to the left plot. Consequently, the areas with a lower probability of no-penetration are reduced in dimension, meaning that the orbit case 3 is less dangerous than the orbit case 1 for the same configuration. Comparing Figure 38 and Figure 39 to Figure 40 and Figure 41, the differences and the similarities between the maps of the two different materials (aluminium alloy and stainless steel) can be observed. Stainless steel structures are more resistant than aluminium structures having the same geometry by at least two orders of magnitude. The two graphs, however, have a similar behaviour with almost linear contour lines that shifts from the bottom right corner to the upper left and vice versa according to the resistance of the material. The same happens when changing the orbit characteristics. This is a considerably different behaviour from the demisability where the shapes of the maps are clearly influenced by the type of material. It is important to know and consider such trends when comparing different solutions and changing the characteristics of the components.

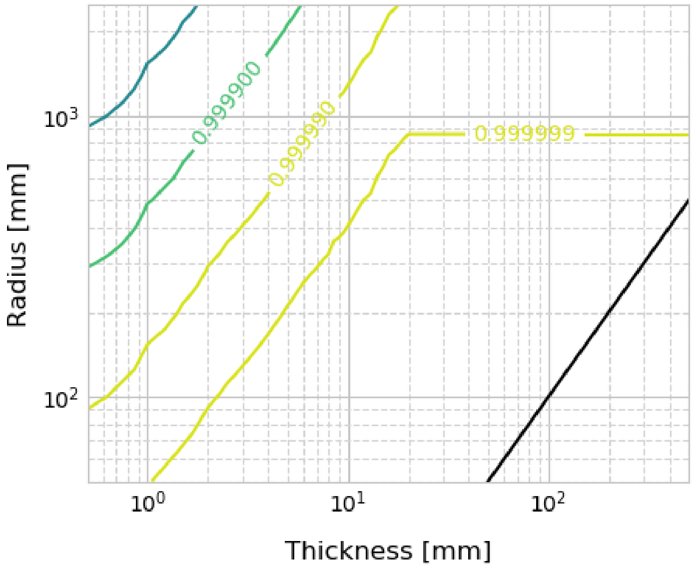

Figure 41: Survivability contour maps for stainless steel cubes. Orbit 3.

Similarly, a comprehensive demisability map showing a comparison between the materials considered can be observed in Figure 42. For the sake of clarity, only two contours for each material are represented, showing the combination of side length and thickness where a 0.9 and a 0.999 PNP is achieved for the considered orbit and mission duration. Only the 0.999 line is present for the stainless-steel case, meaning that such an option provides a very high shielding capability even at very low values of thickness. These kinds of maps, alongside the previously presented demisability maps, can be generated for the different geometrical shapes considered and for the most exploited orbital regions, such as the sun-synchronous region (between 600 and 900 km altitude) and the constellation region (between 1200 and 1500 km of altitude).

The presented maps can be used easily and effectively for a quick assessment and comparison of components design options, comparing preliminary designs by just looking at their position inside the maps. It is in fact possible to generate a set of maps covering the most common initial conditions for the re-entry, the most exploited orbital regions for the survivability, and do it for the different shapes, and a baseline set of materials. Once the maps are available, it is possible to locate on them the component considered and have a fast evaluation of both its demisability and survivability. In the same way, it is possible to compare different solutions and already select the most promising that will undergo a more detailed analysis in later stages of the mission design.

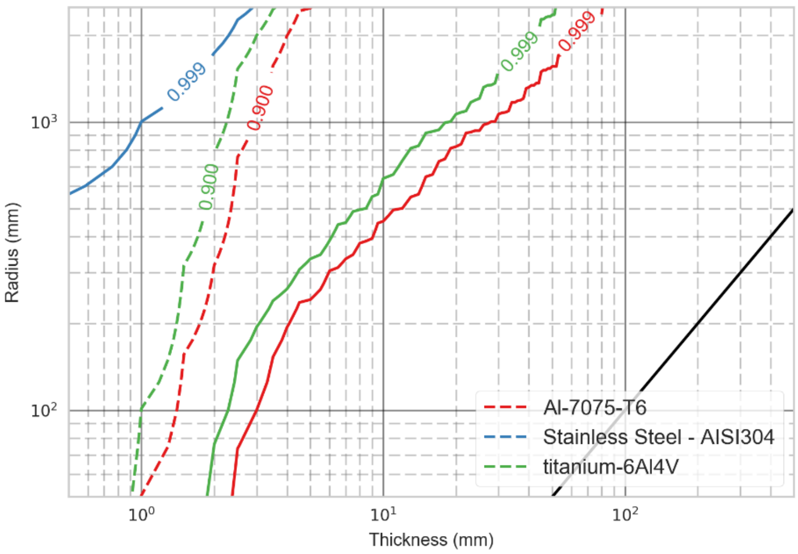

Figure 42: Comparison between the probability of no-penetration of cubes made of aluminium 7075-T6, stainless steel, and titanium 6Al-4V for the orbit case 2.

4.2.3 Combined maps

A way to immediately capture the demisability and the survivability of an object given its characteristics, is to combine the previously presented maps. This paragraph shows some examples of these combined maps where the contour lines of both the demisability index (red lines) and the survivability index (blue lines) are presented. The shaded areas identify the dimensions ranges of some common spacecraft components, which are summarised in Table 20, together with their ranges of thickness and size. The ranges of thickness and size have been derived from data available of Earth observation and remote sensing missions (Estes and Moore, 2007, Fritsche et al., 2007, Waswa and Hoffman, 2012, VECTRONIC Aerospace, 2014, Rockwell Collins, 2016, EaglePicher Technologies, 2016). In this way, it is possible to locate where inside a map typical component belong. In all the maps, the survivability part of the plots refers to a 700 km altitude and 98 degrees inclination orbit with a mission lifetime of three years. The demisability analysis refers to an initial altitude of 120 km and an initial velocity of 7.3 km/s with an initial flight path angle of 0 degrees.

Table 20: Size ranges used in the article for typical spacecraft structures and components.

S/C Component	Thickness range (mm)	Size range (mm)
Tanks	0.5 – 15	150 – 500 (radius)
EOS payloads	2 – 20	500 – 1200 (side length)
Typical structures	1 – 10	100 - 2000 (side length)
Reaction wheels	0.5 – 3	70 - 150 (radius)
Battery cells	0.5 - 1	55 – 85 (radius)

Figure 43 (a)-(b)-(c), show the combined maps highlighting the demisability and survivability of common spacecraft tanks, which are identified by the grey-shaded region. The three combined demisability and survivability maps, shows the results for aluminium alloy Al-7075-T6, stainless steel AISI304, and titanium alloy Ti-6Al4V respectively. The shaded area that represents the region of typical spacecraft tanks is quite extended as it covers many different options for tank designs. Most spacecraft tanks are manufactured with stainless steel or titanium; usually these tanks have thicknesses of the order of millimetres (Estes and Moore, 2007, Fritsche et al., 2007, Waswa and Hoffman, 2012). However, a sub-millimetre portion is also represented in the graph in order to consider tank liners. Liners constitute the inner part of Composite Overwrapped Pressure Vessels (COPV) and are usually under one millimetre in size (Waswa and Hoffman, 2012, Estes and Moore, 2007). The selection of the upper limit was driven by the composite part of the COPV tanks, which is made of graphite epoxy or equivalent composite materials (which are not shown here).

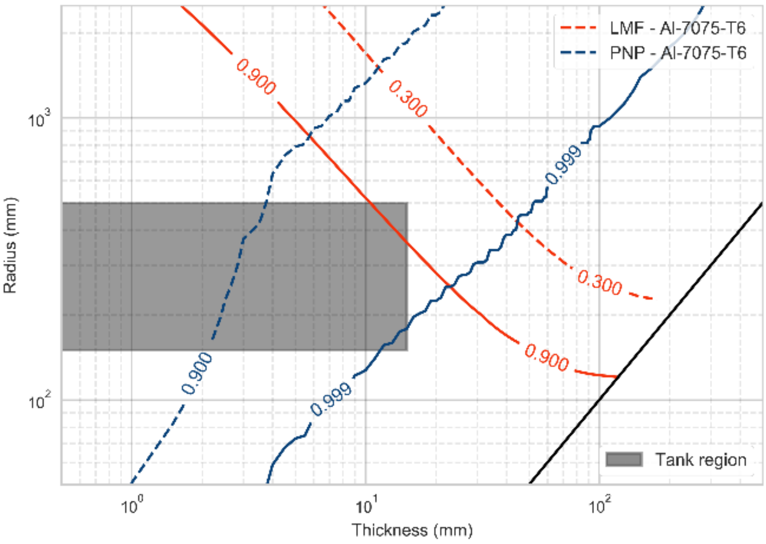

(a)

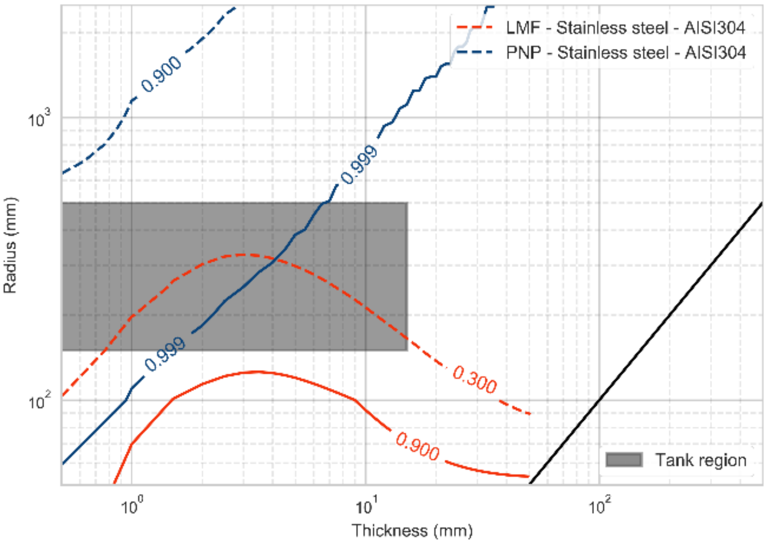

(b)

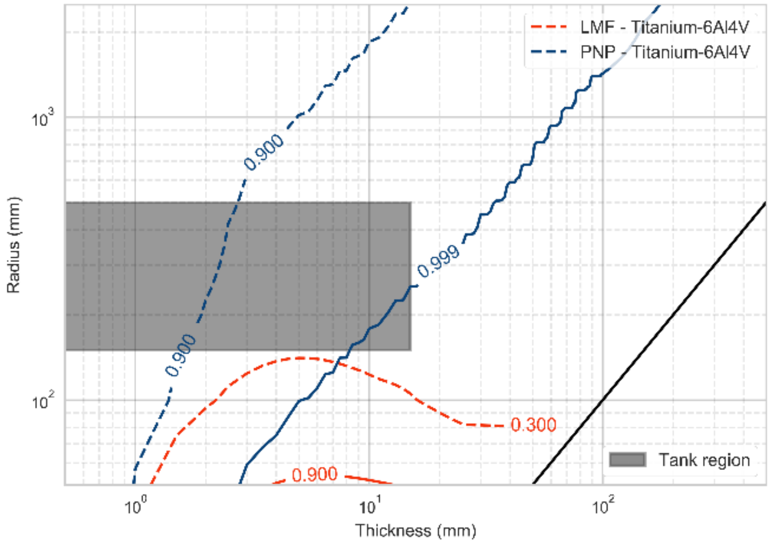

(c)

Figure 43: Demisability and survivability map for aluminium alloy, stainless steel, and titanium alloy cylinders with tank region highlight.

An analogous set of maps, which highlight regions with a combination of radius and thickness typical of battery cells and reaction wheels are presented in the Figure 44. Both objects are schematised with right cylinders (i.e. height equals the diameter) and their regions are presented together in the map.

These regions were estimated following an investigation of catalogues of battery cells (EaglePicher Technologies, 2016) and reaction wheels (VECTRONIC Aerospace, 2014, Rockwell Collins, 2016) from manufacturers and using preliminary design sizing relationships (Wertz and Larson, 1999). The decision to consider these two components arose from the fact that they can usually survive the re-entry, thus posing a risk for people on the ground (Kelley, 2012, Owens, 2014, R.Tech, 2015).

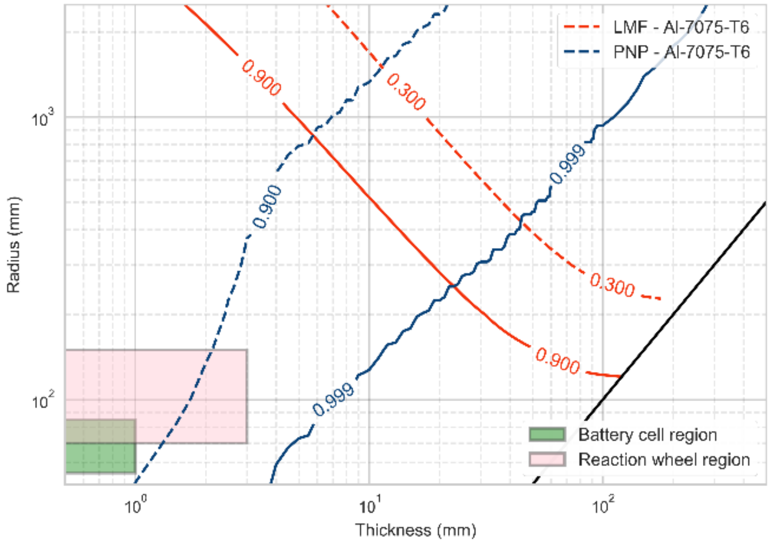

(a)

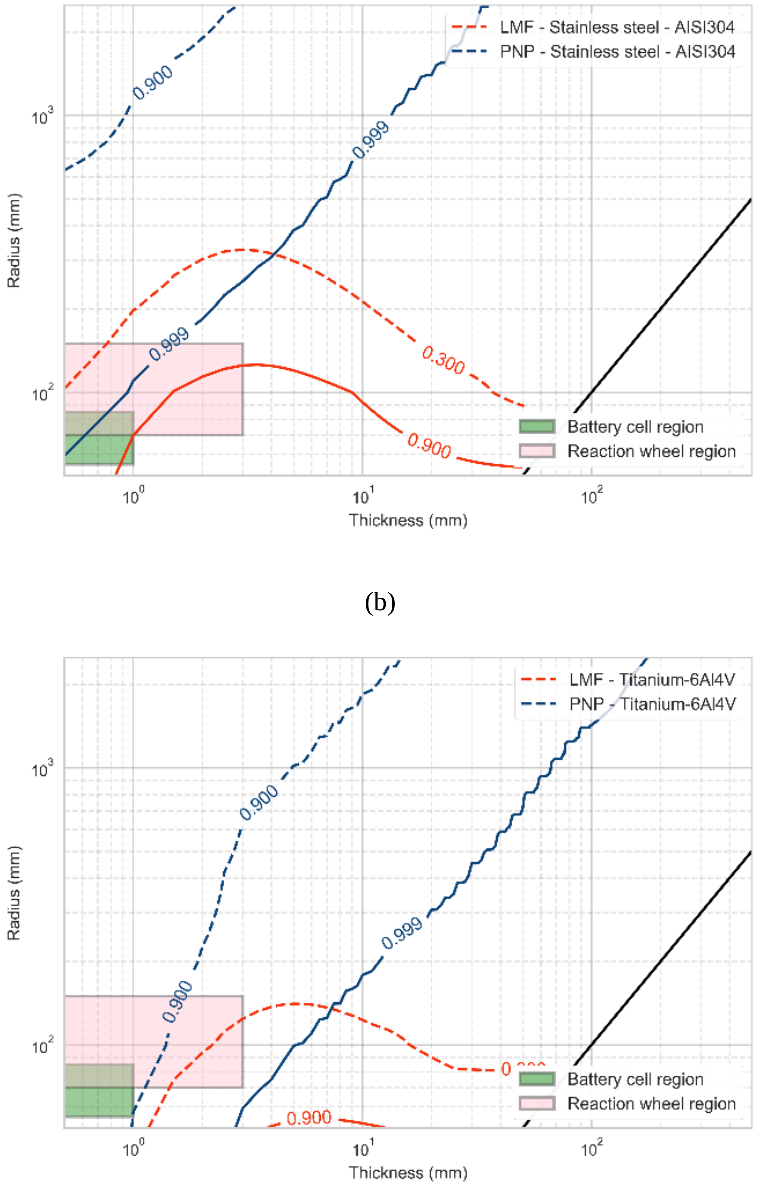

(b)

(c)

Figure 44: Demisability and survivability map for aluminium alloy, stainless steel, and titanium alloy cylinders with reaction wheels and battery cells regions highlight.

Both reaction wheels and battery cells are usually made of titanium and stainless steel. It can be observed from Figure 44 (b) and (c) that these two materials produce non-demisable solutions. As seen in Section 4.1.4.3, one of the most effective methods to achieve the demisability is to change the component material. Changing the material from steel to aluminium would make both components demise upon re-entry. For battery cells, it is possible to consider Li-ion batteries instead of NiH and NiCd. The latter, in fact, are manufactured with stainless steel vessels whereas the former are usually made of aluminium (Waswa and Hoffman, 2012).

This change, of course, has to come at a price in terms of survivability: a more demisable aluminium battery cell will be more vulnerable to debris impacts. The same situation applies to reaction wheels.

In addition, moving from titanium to aluminium reaction wheels also implies larger reaction wheels for the same amount of angular momentum, as aluminium is less dense than titanium. This will further enhance their vulnerability to debris impact as their surface will be larger.

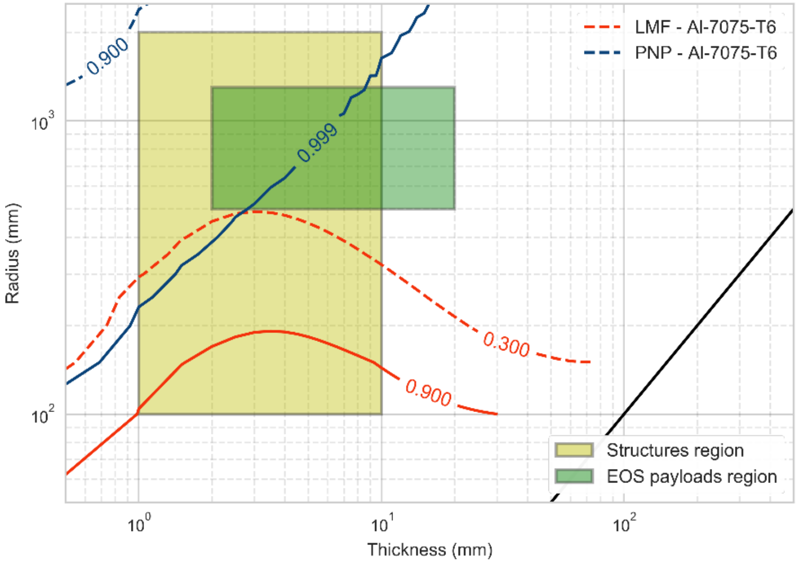

Figure 45: Survivability and demisability map for aluminium alloy and stainless steel with typical S/C structure and EOS payload region highlighted.

Finally, Figure 45 shows the areas of the dimensions ranges for common spacecraft components and for Earth Observing System (EOS) payloads. In this case, the maps represent a cubic-shaped structure as this better schematise the shape of common spacecraft structures and components such as electronic boxes and power units. The limits for the typical spacecraft structure were taken form (Fritsche et al., 2007), whereas the limits for the EO payloads have been deduced from the data available for actual payloads used into NASA Earth Observing Systems Missions (Platnick, 2016). Their dimensions were traced back to a cubic shape with equivalent volume and range of thicknesses. Most spacecraft structures and component casings are manufactured with aluminium. It is possible to observe that aluminium produces configurations that usually demise. Considering this, in most situations a configuration could be optimised by changing the geometry and the thickness of components rather than the material itself unless specific needs for demise or survivability arise. On the payload side, the situation is much more variable as there is usually a wide variety of instruments and sensors. Their requirements and integration with the spacecraft are also less flexible and a change of material or geometry may be possible but not in every situation.

4.3 Summary

This chapter has first presented a thorough sensitivity analysis concerning the main design-for-demise options and their effects on both the demisability and the survivability. First, each option has been analysed separately showing that most of the design options affect the demisability and the survivability in a contrasting way. Then a complete sensitivity analysis comparing all the options has been carried out, and the most relevant design parameters have been identified (i.e. the material, the dimension, and the thickness of components). Finally, using the information acquired from the sensitivity analysis, a set of simplified design maps has been obtained, for a quick comparison and assessment of the demisability and survivability of spacecraft components.

In the following chapters (Chapter 5 Chapter 6), the extension of the demisability and survivability models will be described. As a natural development of the two models, the extensions include a large work dedicated to implementing the possibility to analyse the demisability and survivability of both external structures and internal components, while maintaining an object-oriented approach and a general simplicity of use.

Chapter 5 Extension of the demisability model for the analysis of complete spacecraft configurations

The demise model described in Chapter 2 allows the simulation of the re-entry trajectory and the demise of a single object. Although in this way the re-entry of objects as a function of their shape, material, dimensions, and the re-entry trajectory can be studied, such a model is still limiting. Spacecrafts are in fact composed of several components and subsystems. When a spacecraft re-enters, the high aerodynamic and thermal loads of the descent will lead to a break-up of its main structure, causing its internal components to be released. Consequently, for a proper evaluation of the demisability of a spacecraft, we need to be able to simulate its trajectory and assess the demise of its main structure and internal components. In this chapter, this point is addressed and the required improvements with respect to the model of Chapter 2 are described. The developed model both simulates the re-entry trajectory of the spacecraft and its components and computes their demise. In fact, the evaluation of the demise requires the information on the evolution of the trajectory as it depends upon the speed of the spacecraft and the exposure time to high heat loads. Many of the characteristics of the algorithm of Chapter 2 have been retained: the object-oriented approach, the use of elementary shapes, and the aerodynamics and aerothermodynamics modelling of each shape. The added features allow the definition of a more complex spacecraft architecture, defining the external structure and the internal components, and the simulation of their trajectory and demise, for a more complete destructive re-entry analysis.

The content of the chapter is partially derived from the journal publication on Aerospace Science and Technology, “Spacecraft design optimisation for demise and survivability” (Trisolini et al., 2018b) and from the conference proceedings of the Final Stardust Conference “Multi-objective optimisation for spacecraft design for demise and survivability” (Trisolini et al., 2016c).

5.1 Model characteristics

The characteristics of the updated version of the demisability model include many additional aspects with respect to the initial version of Chapter 2. First, the trajectory of the full spacecraft configuration and of the demise of the internal components can be analysed. Another additional aspect is the possibility to define separately the panels composing the external structure of the spacecraft. This feature increases the interconnection between the demisability and the survivability model as both are dependent upon the positioning of the components inside the spacecraft. When these panels are specified, their detachment from the main structure is computed separately from the main break-up altitude and depends on the melting temperature of the panel itself. The internal components can be positioned inside the spacecraft structure or attached to the external panels. In case they are attached, their release altitude is the same of the panels they are attached to. Internal components can also contain sub-components, which will be released in case the components demise before reaching the ground. The described features make the developed model an evolution of object-oriented codes. In fact, it is not normally possible in these codes to specify the position of the components inside the spacecraft, nor it is possible to define separately the characteristics of the external structure. We thus retain the main features of object-oriented codes and their simplicity of operation, but we go beyond them through this novel implementation. This is also connected to the necessity to link the demisability model with the survivability one, as we need a single framework to perform a combined demisability and survivability analysis. It is no more necessary to use two different software packages, which require different inputs and perform analyses on different level of detail. Instead, a single input is used, and a more coherent, more consistent analysis is carried out. The main structure of the code schematising all these features is represented in Figure 46.

5.1.1 Initial conditions of the simulations

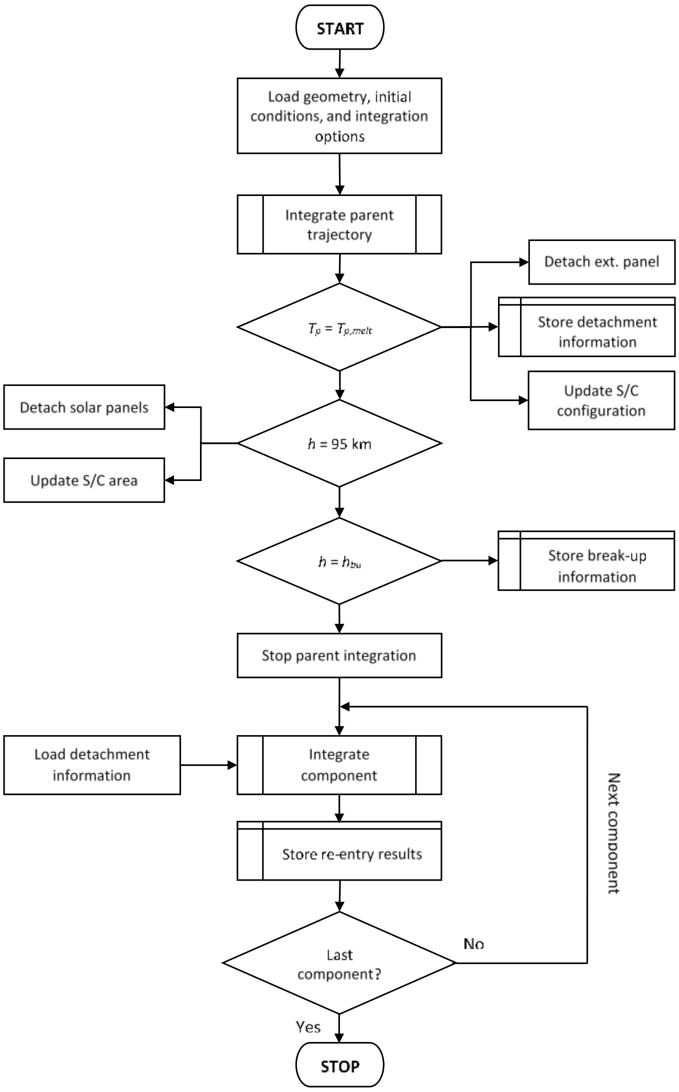

Figure 46: Flow diagram of the main structure of the re-entry model.

Even in this version of the model, first the initial conditions of the re-entry must be provided. The initial conditions can still be provided in the form of longitude, latitude, altitude, relative velocity, flight path angle, and heading angle. In addition, is possible to provide the initial conditions using the classical orbital elements (semi-major axis, eccentricity, inclination, right ascension of the ascending node, argument of perigee, and true anomaly).

5.1.2 Spacecraft configuration

The fundamental difference with respect to the previous model is the possibility to define a full spacecraft configuration, which includes internal components. This aspect is considered by defining the different parts of the spacecraft in a hierarchical fashion. The first level is constituted by the main spacecraft structure (commonly referred as the *parent object*). Here the overall spacecraft mass and dimensions are defined. In addition, the solar panels can be defined and schematised as flat plates. The re-entry of the solar panels is not performed, and they are assumed to demise. However, their area is considered in the computation of the aerodynamic cross-section of the spacecraft. The second hierarchical level defines the external panels of the main structure. This gives the opportunity to specify different characteristics for the external panels, such as the material, the thickness, and the type of panel (e.g. single wall, double wall, and honeycomb sandwich panel). The third level defines the main internal components such as tanks and reaction wheels. The internal components can be attached to the external panels of the main structure by providing the ID of the parent panel that is the panel to which the component is going to be attached. An additional level can also be used for the definition of sub-components like battery cells. An example of the input configuration is shown in Table 21. The quantity of an object can be directly provided, without having to define the same components multiple times if several instances of the same object need to be simulated.

Table 21: Example of spacecraft configuration required by the survivability model.

ID	Name	Parent	Shape	Mass (kg)	Length (m)	Radius (m)	Width (m)	Height (m)	Quantity
0	Spacecraft	n/a	Box	2000	3.5	n/a	1.5	1.5	1
1	Tank	0	Sphere	15	n/a	0.55	n/a	n/a	1
2	BattBox	0	Box	5	0.6	n/a	0.5	0.4	1
3	BattCell	2	Box	1	0.1	n/a	0.05	0.05	20
…	…	…	…	…	…	…	…	…	…

5.1.3 Simulation procedure

After the initialisation is complete, the trajectory of the parent object is simulated. This first part of the simulation carries on until the main break-up altitude is reached and only the parent structure can interact with the external heat flux. The internal components do not experience any heat load during this phase. The break-up altitude is user-defined but the default value is set to 78 km, which is the standard value used in most destructive re-entry software (Minisci, 2015b).

During this first phase of the simulation, the methodology considers the occurrence of specific events. Specifically, the detachment of the solar panels and the detachment of the external panels of the main structure. The solar panels are considered to detach from the main spacecraft body at a predefined altitude. A standard value of 95 km is usually adopted for this altitude by the main object-oriented destructive re-entry codes. Analogously to the standard 78 km break-up altitude, this value comes from a series of observations of re-entries and represents an average detachment altitude of the solar panels (Gelhaus et al., 2014, Martin et al., 2005b). In case the characteristics of the spacecraft or its re-entry trajectory suggest that this standard value is not adequate, the user can define the detachment altitude of the solar panels. The only constraint is that the solar panel detachment altitude must by greater than the break-up altitude of the spacecraft. When this altitude is reached, the solar panels are simply removed from the simulation, with the consequent change in the aerodynamics of the main body, as the area of the solar panels is not considered anymore in the contribution to the average cross-section of the spacecraft.

The detachment of the external panels of the structure is instead triggered by the temperature of the panels themselves. Once the temperature reaches the melting temperature of the panel material, the panel is considered to detach (Koppenwallner et al., 2005). This is a conservative approach as the panels may detach earlier because of the melting of the bolts or adhesive, which are usually used to mount them. If an internal component is attached to the panel, even the component is detached from the main structure. The detachment conditions for each panel and component are used as the initial conditions for the second part of the propagation, when each component is considered separately. When a component is detached, the mass of the spacecraft is updated accordingly.

The first part of the simulation ends with the main spacecraft reaching the break-up altitude. At this point, the break-up state will be used as the initial condition for all the internal components released at break-up. Both the internal objects and the remaining external panels are detached from the main structure and released. At this point, the trajectory is simulated separately for each component. In addition, the panels that have detached before the break-up altitude are analysed: the trajectory information previously stored is used now to propagate their trajectory from the detachment point. The simulation of each one of the released components follows the same procedure outlined in Section 2.1. Finally, we store the final mass, cross-section, landing location and impact energy of each surviving object, and the demise altitude of each demised object.

5.1.4 Demisability criterion

As a measure of the demisability of a spacecraft configuration, the fraction of the mass that demises during the re-entry is considered and is referred to as the Liquid Mass Fraction (LMF). The definition of the index is analogous to the one of Section 2.5 but now is considering the presence of multiple components. Only the internal components and sub-components are considered to contribute to the LMF index, while the external structure and the solar arrays are assumed to demise.

$$\begin{cases} LMF = 1 - \dfrac{\sum_{j=1}^{N_c} m_{fin}^{j}}{\sum_{j=1}^{N_c} m_{in}^{j}} & \text{if } e_{imp} > 15\text{J} \\ LMF = 1 & \text{if } e_{imp} \leq 15\text{J} \end{cases} \tag{5.1}$$

where N_c is the number of components. Again, a value of 1.0 of the index corresponds to complete demise, whereas a value of 0 to complete survival. The 15 J (National Astronautics and Space Administration, 2012, National Astronautics and Space Administration, 2015, National Astronautics and Space Administration, 2009) limit is still taken into account so that when the re-entering object has an impact energy lower than 15 J the index is considered to be equal to 1.0.

5.2 Test Case

In this section, a test case is presented to show the features of the upgraded demise model described in the previous sections. The test case shows the simulation of the break-up events and the release of internal components, as well as the possibility to analyse the detachment of the external panels of the main structure.

Table 22 summarises the initial conditions of the re-entry configuration, and Table 23 shows the characteristics of the spacecraft and the components analysed in the simulation.

Table 22: Initial condition for the re-entry test case simulation.

Initial conditions	
Longitude	0°
Latitude	0°
Altitude	122 km
Velocity	7.3 km/s
Flight path angle	0°
Heading angle	45°

The configuration analysed is an example of a generic upper stage. The parent object represents the outer structure, which define the main dimensions of the re-entering object. The other components are contained inside the parent object and represent some typical elements present in upper stages such as the propellant and pressurant tanks, the nozzle, and the thrust chamber.

Table 23: Spacecraft configuration for the re-entry test case simulation.

Part	Shape	Material	Mass (kg)	L (m)	W/D (m)	H (m)
Parent	Cylinder	Aluminium generic	420.3	6.3	1.8	
Nozzle	Cylinder	Graphite epoxy 2	97.8	1.6	1	
Support	Cylinder	Aluminium generic	42.0	0.43	0.3	
Guidance electronics	Box	Aluminium generic	9.9	0.45	0.5	0.1
Propellant tank	Cylinder	Stainless steel	267.3	2.7	1.7	
Thrust chamber	Cylinder	Inconel-600	44.9	0.6	0.44	
Gas tank 1	Sphere	Titanium generic	9.85	0.41		
Gas tank 2	Sphere	Titanium generic	30.9	0.59		

Figure 47 shows the altitude evolution of the trajectory as a function of time for the parent object and for the inner components. The point in which the inner components are separated from the parent object can be seen. From that point on the components follow their own trajectory; all of them except one reach the ground. The nozzle is the only component to completely demise as shown by the cyan line in Figure 47; its demise altitude is around 68 km. The nozzle demises because it is made of graphite-epoxy 2, which has a charring behaviour with a low heat of fusion (Table A-1). The electronic box reaches the ground, however most of it demises during the re-entry, with only 1.6 kg of mass surviving. The other components are made of high melting temperature materials such as stainless steel and titanium, causing them to survive the re-entry as expected. In addition, the support, the other aluminium object, partially demises, halving its mass from 42 kg to about 21 kg.

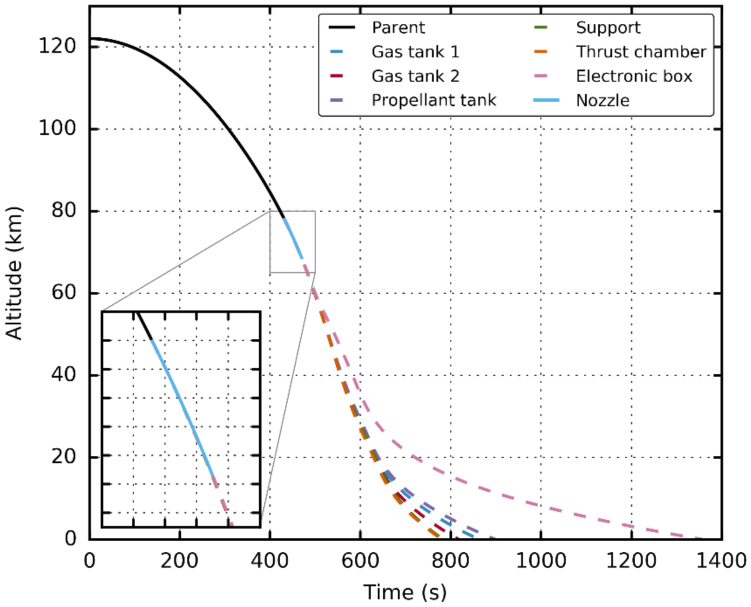

Figure 47: Altitude as a function of time for the parent object and the inner components for the re-entry test case.

Figure 48 presents the 3D trajectory of the spacecraft, showing the altitude evolution as a function of the longitude and the latitude. It is also possible to observe the distinct impact points of the different objects as their aerodynamic characteristics are different and change during the re-entry. It is interesting to see how the electronic box, despite being the component with the longest flight time, turns out to be the one to actually travel the least distance. This is because the electronic box partially demises, causing an increment in the area to mass ratio, which in turn makes the component slow down significantly. As the final portion of the trajectory is almost vertical, the low horizontal velocity causes the object to experience a shorter path.

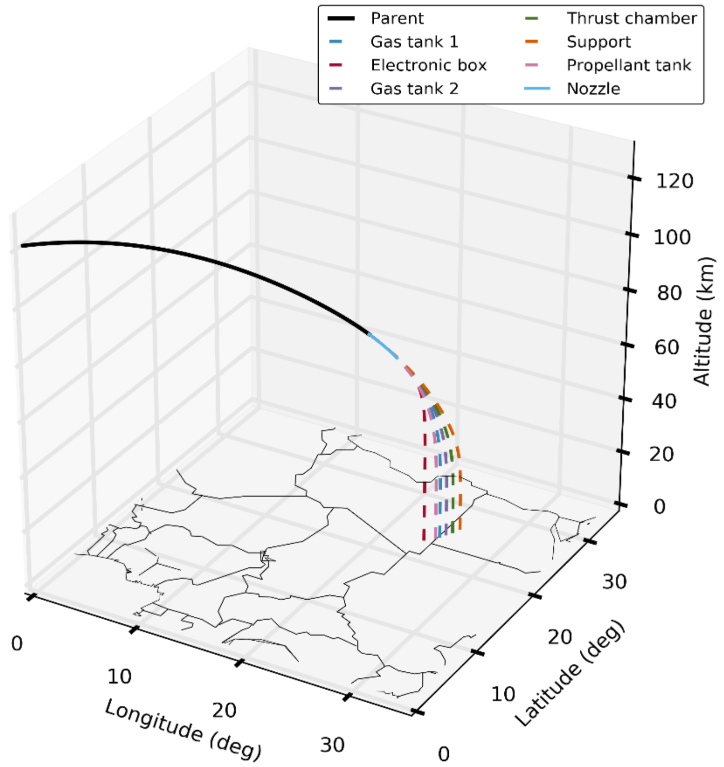

Figure 48: 3D trajectory representation for the re-entry test case.

Finally, Figure 49 shows the temperature profiles of the different components after the break-up and of the parent object during the first part of the trajectory. The heating of the parent object is not considered in this simulation, as is the common practice in many object-oriented codes. The main structure is a container used to carry the inner components up to the break-up points; consequently, its temperature is kept constant at 300 K. The other components instead receive the heat load only after the break-up. Before the break-up, the main structure is treated as a container because its heating is not influential to the re-entry. The main structure as a whole, in fact, will not maintain its shape (a box like or a cylinder like structure) but it will disintegrate into many structural elements and panels. To consider the contribution of the main structure to the casualty risk, such elements, and panels can be modelled as child objects that will be released at the break-up as it happens for the internal components. A higher initial temperature can be given to these components to consider for the heating they experience before the break-up.

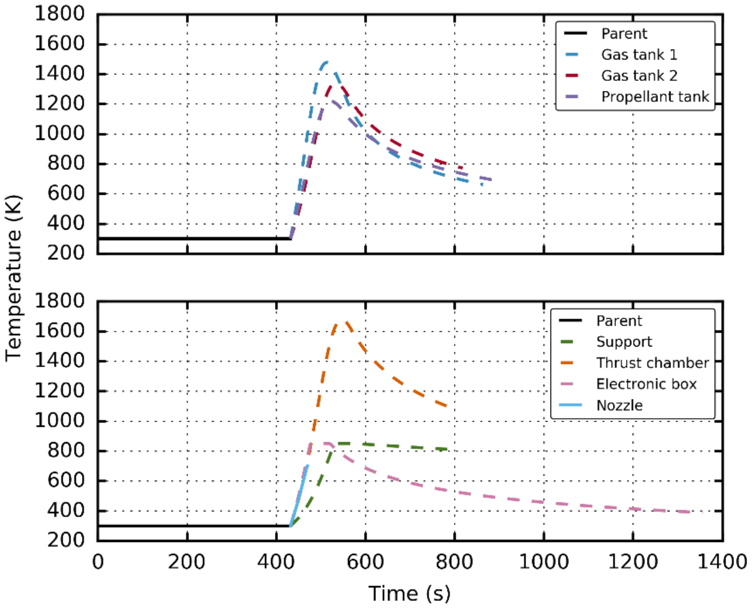

Figure 49: Temperature profiles for the parent object and the inner components for the re-entry test case.

5.3 Summary

This chapter has described the several developments introduced in the demisability model such as the parent/child architecture up to sub-components level, the possibility to position the components inside the spacecraft and attach them to the external panels. The external panels themselves can be defined separately, also including the type of shielding related to them. Bothe the break-up altitude of the solar panels and of the main spacecraft structure can be decided by the user. The model will be combined with the improved survivability model of Chapter 6 into a common framework that will be described in Chapter 7.

Chapter 6 Extension of the survivability model for the impact analysis of complete spacecraft configurations

This chapter contains the description of the extension of the survivability model first introduced in Chapter 3. The fundamental feature added to the model is the possibility to evaluate the vulnerability of components contained inside the main spacecraft structure. In addition, the development of a novel methodology to compute the penetration probability on internal components is presented and compared with state-of-the-art software. The added features have been developed keeping in mind that the demise and the survivability analyses have to be compatible and have to maintain a similar level of complexity. The added capability of assessing the vulnerability of internal components now allows performing a full survivability analysis on preliminary spacecraft configurations.

When considering internal components also the debris clouds that develop inside the spacecraft after the impact (Schonberg, 2001, Depczuk and Schonberg, 2003, Putzar and Schäfer, 2006, Welty et al., 2013) has to be considered. These clouds can in fact hit and damage internal components, resulting in a possible mission failure or loss of performance. A survivability analysis has thus to consider the impact of particles on the outer structure and how the resulting debris clouds propagate inside the spacecraft and interact with internal components. Standard vulnerability analysis software relies on ray tracing methods; such methods are computationally expensive and require many simulations in order to have a statistically meaningful result, as the impact point of each particle is randomly generated. We here describe a novel methodology that uses a probabilistic approach capable of computing the vulnerability of a spacecraft configuration, avoiding ray tracing methods. The method is based on two main tools: the Schaefer-Ryan-Lambert (SRL) ballistic limit equation (Ryan and Christiansen, 2010, Welty et al., 2013) which can take into account impacts on multi-walled structures (up to three layers) and the concept of a vulnerable area (Putzar and Schäfer, 2006). The vulnerable area (Section 6.3) consists of an adjusted projection of an inner component onto the outer spacecraft structure. This area represents the portion of the external structure that, if impacted by a particle, could also lead to the impact on the inner component to which the relevant vulnerable area is associated. The SRL BLE (Appendix D) subsequently allows the direct calculation of the critical diameter associated with the inner components walls. In addition to the computation of the vulnerable areas and the critical diameters for the individual components, it is also necessary to consider the interaction between the different components inside the spacecraft. The vulnerability of individual components is affected by the shielding provided by the other internal components. Moreover, the distance of the object from the external walls is important, as the closer the component is to the wall the more vulnerable it will be to impacts. All these aspects are considered in the methodology developed and are illustrated in the following sections.

The chapter first introduces the architecture of the updated model; subsequently, the modelling of the propagation of the secondary debris ejecta inside the spacecraft and their interaction with internal components is described (Section 6.2). Section 6.3 contains the definition of the concept of vulnerable zone, while Section 6.4 describes the procedure for the evaluation of the vulnerability of internal components. Section 6.5 presents an entirely novel procedure that combined with the concept of vulnerable zones, allows the computation of the effects that mutual shielding between internal components has on the computation of their vulnerability. Finally, Section 6.6 shows the comparison between the developed survivability model and state of the art impact analysis software.

Part of the chapter follows the content of the Aerospace Science and Technology journal publication “Spacecraft design optimisation for demise and survivability” (Trisolini et al., 2018b) and of the conference proceedings “Demisability and survivability multi-objective optimisation for preliminary spacecraft design” presented at the 68th International Astronautical Congress in Adelaide, Australia (Trisolini et al., 2017a).

6.1 Model architecture

The block diagram of Figure 50 represents a visual schematisation of the code architecture, including all the main steps followed for the computation of the vulnerability of a spacecraft configuration to debris impacts using the extended version of the survivability model. First, the model requires a set of inputs that is the mission scenario in the form of orbit altitude, orbit inclination, and mission duration. The second required input is the spacecraft configuration. This is a file describing the characteristics of each component in the configuration. An example of the structure of such file is represented in Table 24.

Table 24: Example of spacecraft configuration to be provided to the model.

ID	Name	Parent	Shape	Mass (kg)	Length (m)	Radius (m)	Width (m)	Height (m)	Position
0	Spacecraft	n/a	Box	2000	3.5	n/a	1.5	1.5	n/a
1	Tank	0	Sphere	15	n/a	0.55	n/a	n/a	(-1,0,0)
2	BattBox	0	Box	5	0.6	n/a	0.5	0.4	(0,1,1)
3	BattCell	2	Box	1	0.1	n/a	0.05	0.05	n/a
…	…	…	…	…	…	…	…	…	…

When the configuration is generated, the main body of the spacecraft is always at the centre of the reference frame of the spacecraft. The x-axis points towards the direction of the orbital velocity (RAM direction), the z-axis points away from the Earth, and the y-axis follows from the right-hand rule. In the current version of the model, the main body has to be box-shaped. A single material and a uniform thickness for the spacecraft structure can be used; alternatively, different materials, thicknesses, and shielding types can be used for each face of the box. In this case, the characteristics of each one of the external panels constituting the main structure have to be specified. Three types of shielding can be used in the current version of the model: single wall shields, Whipple shields, and honeycomb sandwich panels. All of these shielding techniques must use the appropriate parameters in the ballistic limit equations (Appendix D) when the critical diameter is evaluated. The algorithm automatically recognises the equations to adopt based on the inputs in the configuration file. For all the internal components, in addition to the classical geometrical characteristics, the position needs to be specified.

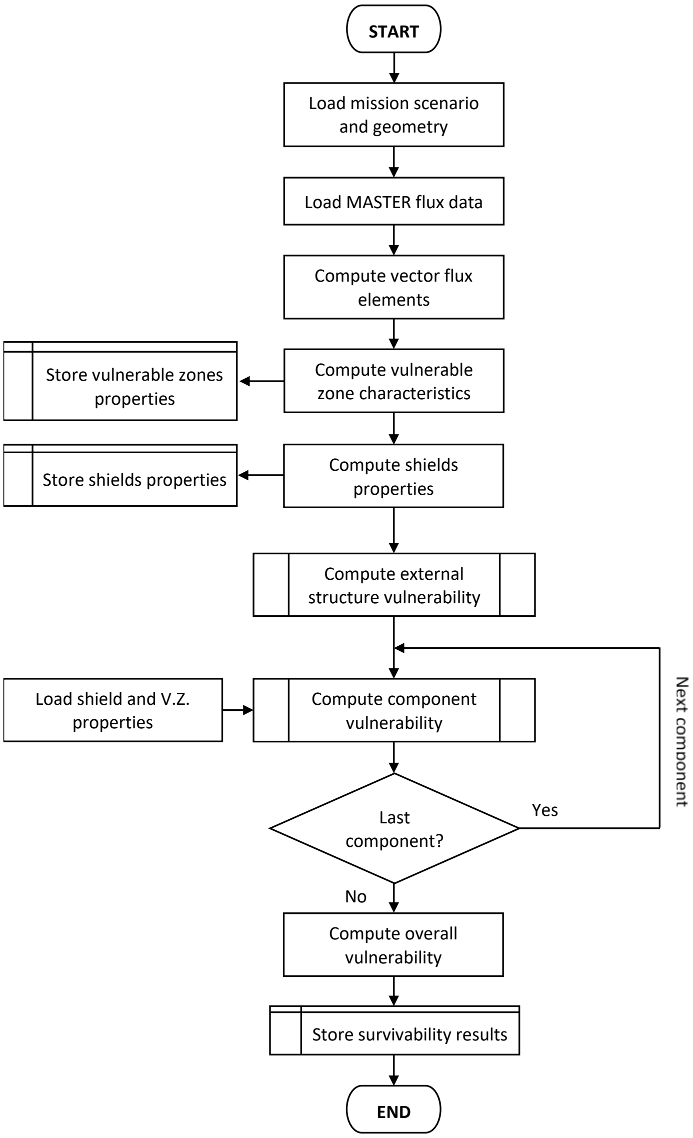

Figure 50: Flow diagram of the main structure of the survivability model.

The components can be free inside the main structure, or they can be attached to the external panels. The position can be assigned in two different ways. For components that are not attached to the external panels, the coordinates with respect to the spacecraft reference frame have to be specified; for attached components, the relative position with respect to the centre of the considered panel has to be provided. The orientation of a component can also be provided (despite it is not represented in

Table 24 for limits of space). As the methodology aims at providing a simplified representation of a spacecraft, it has been decided to allow the orientation to be specified only along the main axes of the spacecraft (*x*, *y*, and *z*). Once the geometry is specified, it is again necessary to generate the vector flux elements. The procedure is analogous to the one described in Section 3.3. However, an additional feature is present in this extension of the model, which consists in the addition to each vector flux elements of a weighted average particle diameter. Similarly, to the procedure used for the velocity, elevation angle, and azimuth angle (Section 3.3), the diameter value is extracted from the fluxes associated to each sector. The flux vs diameter vs azimuth distribution is used, and the weighted average value of the debris particle diameter is extracted for each azimuth sector considered. After all the preliminary analyses are performed, the computational procedure differentiates from the initial model. In order to correctly assess the vulnerability of an internal component using the vulnerable zone concept it is necessary to project the vulnerable zone on each one of the external panels of the external structure. It is thus necessary to know the characteristics of these vulnerable zones, together with the characteristics of the shielding associated with the considered panels. In total, for each internal component, the properties of six vulnerable zones and six shielding configurations are stored. The algorithm precomputes the characteristics of the vulnerable zones and of the shielding associated with each internal component and store the information for a later use. Using this information together with the vector flux elements, and the ballistic limit equations, the model evaluates the vulnerability of each internal component. The vulnerability of the external structure is instead evaluated using the procedure presented in Chapter 3.

6.2 Impact Propagation

In general, when a debris particle impacts the structure of the spacecraft, the impact will be oblique, i.e. the angle between the spacecraft face and the impact velocity is not 90°, resulting in two different debris clouds being produced after the impact (Schonberg, 2001, Depczuk and Schonberg, 2003).

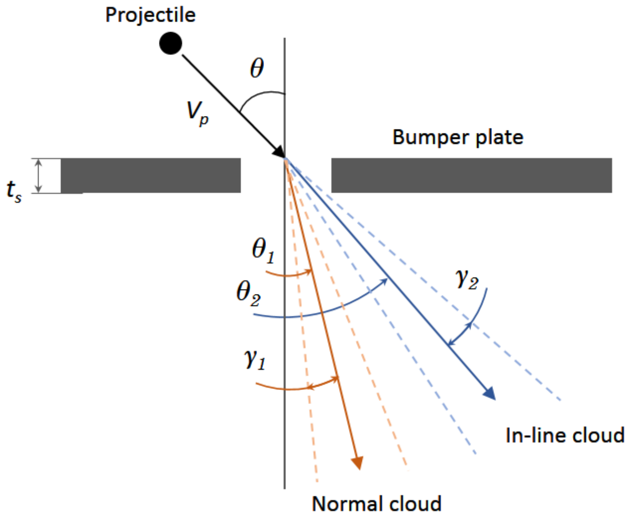

Figure 51: Secondary ejecta clouds characteristics.

One cloud exits almost perpendicularly to the impacted wall, the *normal* debris cloud. The second cloud closely follows the direction of the projectile and is identified as the *inline* debris cloud (Figure 51). The clouds are taken into account assuming that the debris belonging to the clouds are contained inside conic surfaces so that they can be modelled using just the direction of the cone axis and the spread angle of the cone (Figure 51). The geometry of the cones can be expressed as a function of the impact characteristics (impact velocity, impact angle, particle diameter, and wall material) as follows (Depczuk and Schonberg, 2003, Schonberg, 2001):

$$\begin{aligned}
\frac{\theta_1}{\theta} &= 0.471 \cdot \left(\frac{v_p}{C}\right)^{-0.049} \cdot \left(\frac{t_s}{d_p}\right)^{-0.054} \cdot \cos(\theta)^{1.134} \\
\frac{\theta_2}{\theta} &= 0.532 \cdot \left(\frac{v_p}{C}\right)^{-0.086} \cdot \left(\frac{t_s}{d_p}\right)^{-0.478} \cdot \cos(\theta)^{0.586} \\
\tan\gamma_1 &= 1.318 \cdot \left(\frac{v_p}{C}\right)^{0.907} \cdot \left(\frac{t_s}{d_p}\right)^{0.195} \cdot \cos(\theta)^{0.394} \\
\tan\gamma_2 &= 1.556 \cdot \left(\frac{v_p}{C}\right)^{1.096} \cdot \left(\frac{t_s}{d_p}\right)^{0.345} \cdot \cos(\theta)^{0.738}
\end{aligned} \tag{6.1}$$

where θ is the impact angle, θ_1 is the deflection angle of the normal debris cloud, θ_2 is the deflection angle of the inline debris cloud, γ_1 is the half-cone angle of the normal cloud, γ_2 is the half-cone angle of the inline cloud. t_s is the impacted plane thickness, C is the speed of sound of the plate material, d_p is the particle diameter, and v_p is the relative particle impact velocity. These equations have been developed for impacts on Whipple shields and for a range of impact angles between 30 and 75 degrees. However, it is here assumed that the validity of the equations can be extended to the entire range of impact angles and to other shielding configurations such as honeycomb sandwich panels (Putzar and Schäfer, 2006).

6.3 Vulnerable Zone

The vulnerable zone (Putzar and Schäfer, 2006) is defined as the area on the external structure of the spacecraft that, if impacted, can lead to an impact also on the component considered. Any impact of a particle onto this area generate fragments that may hit the component in question, with a probability that depends on the impact parameters, the spacecraft structure, and the stand-off distance of the component from the structure wall. The lateral extent of the vulnerable zone is expressed as:

$$L_{VZ} = 2 \cdot \left(\tan\alpha_{\max} \cdot s + \frac{1}{2} \cdot \left(d_{target} + d_{p,\max} \right) \right) \tag{6.2}$$

where (see Figure 52) L_{VZ} is the lateral extension of the vulnerable zone, s is the spacing between the structure wall and the component face (stand-off distance), d_{target} is the lateral extent of the considered component, $d_{p,max}$ is the maximum projectile diameter, and α_{max} is the maximum ejection angle. The computation of α_{max} requires the simplification of Eqs. (6.1) (Putzar and Schäfer, 2006). It is assumed that the ejection and spread angles are only a function of the impact angle θ and that all the other parameters can be absorbed by a constant factor giving

$$\alpha(\theta) = \theta_2 + \frac{\psi_2}{2} \tag{6.3}$$

and resulting in a maximum ejection angle $\alpha_{max} = 63.15^{\circ}$.

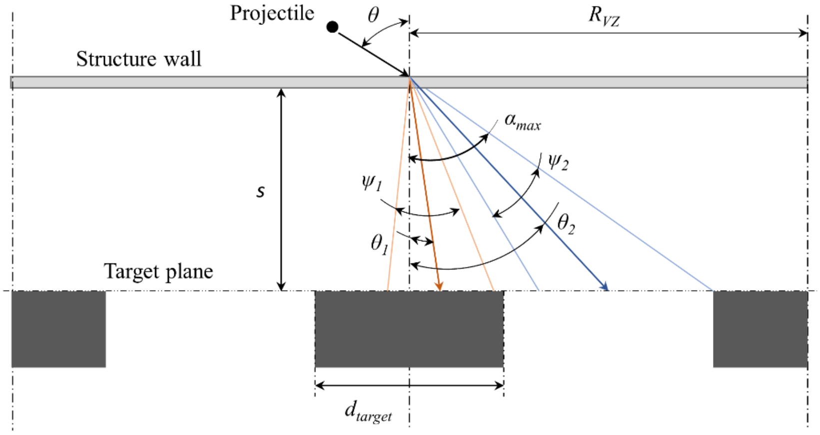

Figure 52: Representation of the extension of the vulnerable zone.

The parameter $d_{p,max}$ instead represents a user defined value of the projectile diameter that takes into account the contribution of the particle to the impact probability. Suggested values for $d_{p.max}$ are 10 mm for vulnerable components and 20 mm for component with higher impact resistance (Putzar and Schäfer, 2006). Figure 53 shows a visual example of vulnerable zones as computed with the described procedure.

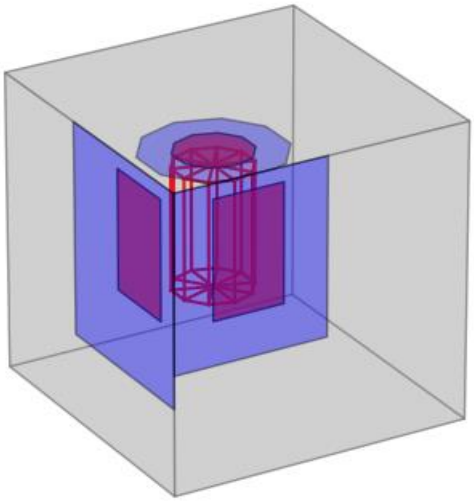

Figure 53: Vulnerable zones of a cylinder projected onto the faces of a cubic structure (only closest faces are shown; the vulnerable zones are projected also on the other panels).

6.4 Vulnerability of internal components

When a debris particle with enough size and velocity hits the outer structure of the spacecraft, a secondary debris cloud is usually generated. Particles belonging to this debris cloud can still impact internal components and damage them. It is thus necessary to evaluate the probability that such secondary debris penetrate the inner components. The vulnerability of an internal component can be evaluated as the product of three different probabilities:

$$V_p = P_{struct} \cdot P_{comp} \cdot P_{BLE} \tag{6.4}$$

where P_{struct} is the probability of space debris impacting the spacecraft external structure inside the vulnerable zone assigned to the specific spacecraft component; P_{comp} is the probability that the downrange fragment cloud will hit the component; and P_{BLE} is the probability that the projectile in this cloud perforates the component wall.

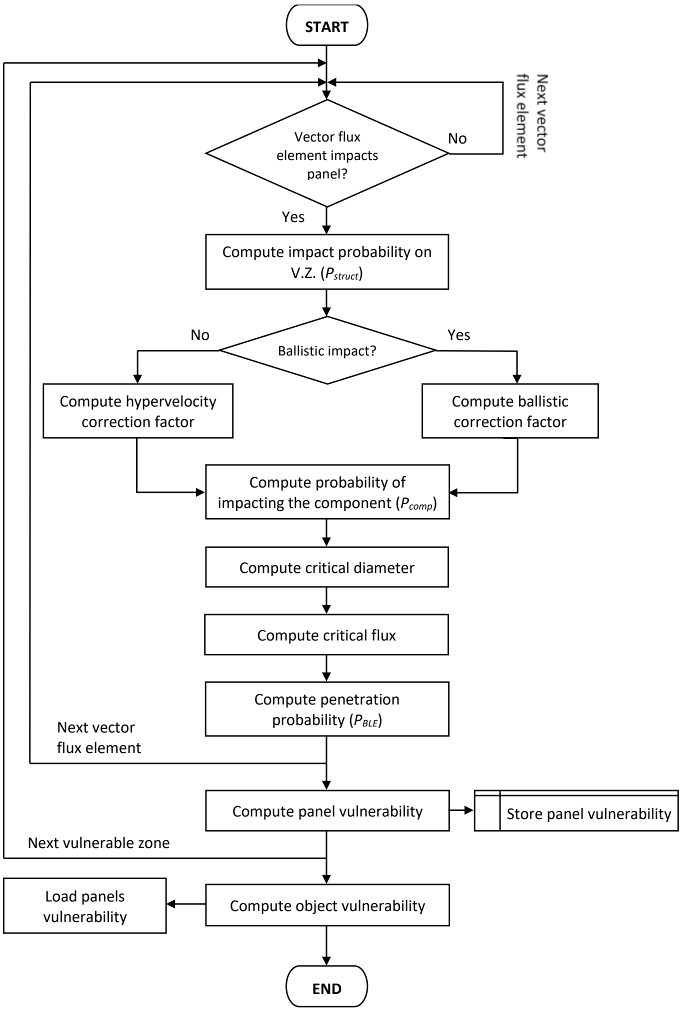

Figure 54: Flow diagram for the vulnerability computation of an internal component.

In this section, the general procedure followed for the computation of each of the three contributions in Eq. (6.4) will be outlined. Figure 54 shows a flow diagram of the general computational procedure.

The first contribution, $P_{struct}^{j,i}$ can be computed following the same procedure of Eq. (3.4); in this case, however, the impacted surface considered is only the one delimited by the vulnerable zone. The resulting expression is

$$P_{struct}^{j,i} = 1 - \exp\left(-\varphi_i \cdot S_{j,VZ}^{\perp} \cdot \Delta T\right) \tag{6.5}$$

where $P_{struct}^{j,i}$ is the probability of an impact on the j-th vulnerable zone by the i-th vector flux element. φ_i is the i-th vector flux element, $S_{j,VZ}^{\perp}$ is the projected area of the j-th vulnerable zone corresponding to the component; and ΔT is the mission time in years.

A particle impacting the vulnerable zone or the resulting debris cloud, will not necessarily impact the inner component associated with it. It is thus necessary to consider the probability that an impact on the vulnerable zone will subsequently cause an impact on the component itself. This is taken into account by the second term on the right end side of Eq. (6.4). This term depends on the type of impact: if the impact occurs in the hypersonic regime, secondary debris clouds will form, whereas if the impact is in the ballistic regime the projectile will pass almost intact through the outer structure. It is thus necessary to distinguish between these two situations. In the hypervelocity regime the probability to impact the component is computed as the ratio between the extent of the ejecta in the component plane and the vulnerable zone of the component (Putzar and Schäfer, 2006) and can be expressed as

$$P_{comp}^{j,i} = \frac{d_{ejecta}}{L_{VZ}^{j}} \tag{6.6}$$

where $P_{comp}^{j,i}$ is the probability that the i-th vector flux element, which has already impacted the j-th vulnerable zone, will hit the component considered, L_{VZ}^{j} is the extent of the j-th vulnerable zone in the target plane, and d_{ejecta} is the extent of the debris ejecta at the target plane (Figure 56), which is expressed as

$$d_{ejecta} = 2 \cdot \left(\tan\alpha\left(\theta^{j,i}\right) \cdot s_j + \frac{1}{2} \cdot d_{target} \right) \tag{6.7}$$

where s_j is the stand-off distance between the component and the external wall to which the j-th vulnerable zone is associated, and $\alpha(\theta^{j,i})$ is the ejection angle associated with the i-th vector flux element impacting on the i-th vulnerable zone, and can be computed with Eq. (6.3). In case of an impact in the ballistic regime, instead, only the size of the projectile needs to be considered, as no fragmentation occurs.

$$P_{comp}^{j,i} = \frac{d_p^{j,i} + d_{target}}{L_{VZ}^{j}} \tag{6.8}$$

where $d_p^{j,\,i}$ is the particle diameter relative to the *i*-th vector flux element impacting on the *j*-th vulnerable zone. This value is associated to each vector flux element and is extracted from the debris flux distributions obtained with MASTER-2009 as the most probable particle diameter for the *i*-th vector flux element. For the scatter regime, a linear interpolation between the ballistic and hypervelocity regime is adopted.

The last contribution in Eq. (6.4) comes from the computation of the penetration probability as follows

$$P_{BLE}^{j,i} = 1 - \exp\left(-\varphi_{c,i} \cdot S_{j,VZ}^{\perp} \cdot \Delta T\right) \tag{6.9}$$

where $P_{BLE}^{j,\,i}$ is the penetration probability for the *j*-th vector flux element on the component associated with the *i*-th vulnerable zone, and $\varphi_{c,i}$ is the critical flux that is the flux associated to the value of the critical diameter computed with ballistic limit equation. The adopted ballistic limit equation is the SRL (Appendix D). The SRL BLE is a triple-wall ballistic limit equation and can be used for both triple-wall and double wall-configurations. The developed model uses this equation in a way that assumes the last wall of the shielding configuration is always the face of the inner component considered, whereas the other walls represent the outer structure.

The overall penetration probability for a component can then be computed as

$$V_p = 1 - \prod_{j=1}^{N_{panels}} \left(\prod_{i=1}^{N_{fluxes}} \left(1 - P_{struct}^{j,i} \cdot P_{comp}^{j,i} \cdot P_{BLE}^{j,i}\right)\right) \tag{6.10}$$

where N_{panels} and N_{fluxes} are the number of panels in which the structure is schematized and the number of vector flux elements, respectively.

6.5 Mutual shielding modelling

The standard vulnerable zone formulation allows the computation of the vulnerability of a component inside the main spacecraft structure. However, it lacks the capability of considering the mutual shielding between components. In fact, Eqs. (6.6) and (6.8) do not take into account the contribution of possible interposing components. However, when a component is placed in front of another, it considerably reduces the amount of damage the target component can receive from space debris impacts. This is especially important considering the directional nature of the space debris fluxes. For example, impacts coming from the RAM direction are considerably more dangerous than from other directions (higher relative velocity). In such case, a component placed in front of another along the RAM direction has a non-negligible shielding effect.

The vulnerable zone approach has its simplicity and speed among its advantages, together with the possibility to avoid a time-consuming Monte Carlo simulation. Therefore, we aim here at extending this approach by integrating a methodology that allows the mutual shielding to be evaluated while still maintaining the advantages of the original approach. By looking at the three contributions used to compute the penetration probability of Eq. (6.4), the second term (associated to the impact probability of the ejecta on the component) is the one related to the mutual shielding. The idea is to consider the interaction between the debris cone developed after the impact and the shielding elements interposed between the outer faces and the target component. Three methodologies are described in the following and will be compared between each other and two state of the art impact assessment software such as DRAMA and ESABASE2/DEBRIS. The three methodologies proposed are all variants of this idea. First, the general approach is described in Section 6.5.1, and then the variants are presented in Section 6.5.2 and 6.5.3.

6.5.1 Impact ejecta methodology

The novel methodology aims at introducing the mutual shielding inside the original formulation of the vulnerable zone. To do so, we first consider the nature of the debris impacts on the spacecraft structure. In the standard approach, a particle can impact anywhere on the vulnerable zone (no impact location is sampled or considered). The lack of a precise impact location results in an issue connected to the mutual shielding. In fact, the shielding capability of a component with respect to the debris ejecta depends on the impact location and on the characteristic of the debris produced after the impact. In case of a hypervelocity impact, a cone of debris is generated. Depending on the different characteristics of the cone (i.e. axis and aperture angle) and impact locations, different parts of the target components may be visible and different portions of the debris cone can be shielded by the interposing components. To overcome this issue, it was decided to subdivide the vulnerable zone using a grid (Figure 55). As there must not be a preferred impact location, for each vector flux element, an impact is simulated assuming the centre of each cell in the grid to represent the impact location. At this point, for each impact location, the resulting debris cone is generated and its interaction with the target and the shielding components is evaluated.

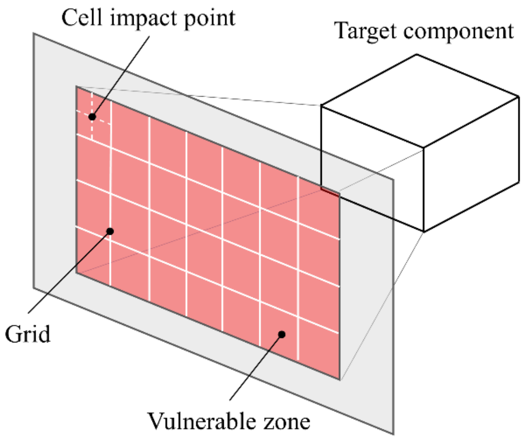

Figure 55: Representation of the vulnerable zone grid and of the cell impact locations.

The overall effect of a vector flux element impacting the considered vulnerable zone is then obtained averaging the contribution of each cell. The procedure is then repeated for each vector flux element and for each vulnerable zone. The procedure is different in case the impact is of ballistic type. In this case, the projectile is considered to pass through along the same direction of the impact vector, with no debris cone produced.

Hypervelocity regime

After a hypervelocity impact, the impacting debris is destroyed together with the area of the panel subject to the impact. Consequently, a cloud of debris is generated, which almost follows a conical shape. In fact, in the standard formulation, the vulnerable zone is defined using a conical shape. It is thus natural to maintain such a shape in our extension, as we want to maintain the main structure of the standard approach. In general, a hypervelocity impact generates two clouds, a normal, and an inline debris cloud. However, in this formulation it is assumed that both clouds are contained inside one single debris cone. The characteristics of such a cone (i.e. its axis and aperture angle) are determined using Eqs. (6.1). The cone half-aperture angle (α) can be computed as follows:

$$\alpha = \frac{1}{2}\cdot\left(\theta_2 - \theta_1\right) + \frac{1}{4}\cdot\left(\gamma_1 + \gamma_2\right) \tag{6.11}$$

The axis of the cone is the bisector of the cone aperture angle considered in the impact plane, which is the plane containing the impact vector flux element and the normal to the impacted face (Figure 56). The cone obtained in such fashion is then used to determine the impact probability on the target component considered. To do so, the interaction of the debris cone with the target object and the shielding components must be evaluated.

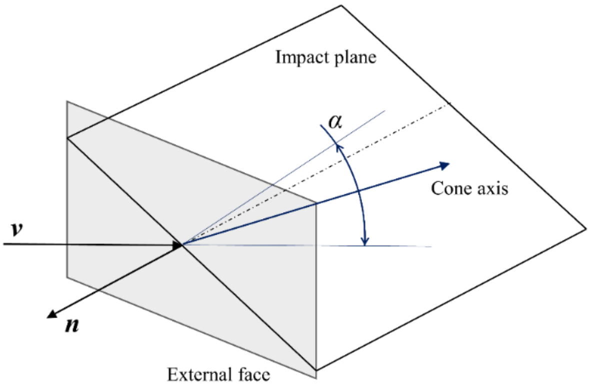

Figure 56: Representation of the cone aperture angle in the impact plane.

The initial approach computes the probability of impact adding the extent of the target section with the extent of the debris cone in the target plane (Eq. (6.6)). The same mechanism is used here. However, to consider the mutual shielding, the contribution of the debris cone and of the target section can be affected by the presence of shielding components. For the debris cone, the effect of the shielding components is taken into account applying them a perspective projection onto the target plane and intersecting such projection with the section of the cone at the target plane (Figure 57).

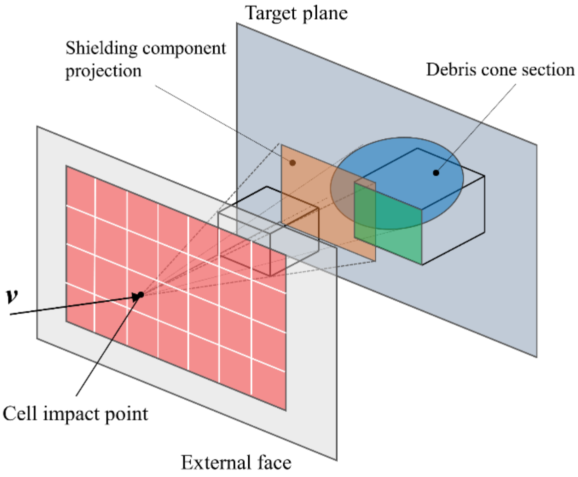

Figure 57: Mutual shielding in the hypervelocity regime (representation of the procedure for a single cell element).

The area used then in the impact probability computation is the remaining area of the cone after the shielding component projections have been subtracted. This area is referred to as the *available cone area* and, for each vector flux element, is evaluated over all the grid cells subdividing the vulnerable zone.

$$A^{k}_{c,av} = A^{k}_{c} \neg \left(A^{k}_{s,1}, \ldots, A^{k}_{s,t}, \ldots, A^{k}_{s,n_s} \right) \tag{6.12}$$

where A^k_c is the intersection ($\neg$) between the k-th debris cone with the target plane, and $A^k_{s,t}$ is the perspective projection of the t-th shielding component onto the target plane with respect to the k-th grid cell. The procedure is then repeated for each grid cell. Subsequently, the *average available cone area* for the i-th vector flux element ($A^{j,i}_{c,av}$) onto the j-th vulnerable zone can be expressed as

$$A^{j,i}_{c,av} = \frac{\sum_{k=1}^{n_{cell}} A^{k}_{c,av}}{n_{cell}} \tag{6.13}$$

The second contribution in the vulnerable zone equation is the target component length. In this extension of the methodology, the *visible target area* is computed by performing a Boolean difference operation between the target section and the perspective projection of the shielding components onto the target plane (Figure 58).

The operation is repeated over each grid cell. Then the average over the grid cell is carried out to evaluate the *average target visible area* ($A^{j,i}_{t,av}$) as follows:

$$A_{t,av}^{j,i} = \frac{\sum_{k=1}^{n_{cell}} \left[A_t \neg \left(A_{s,1}^{k}, \ldots, A_{s,t}^{k}, \ldots, A_{s,n_s}^{k} \right) \right]}{n_{cell}} \tag{6.14}$$

The impact probability associated to the *i*-th vector flux element impacting on the *j*-th vulnerable zone is then obtained with the following equation

$$P_{comp}^{j,i} = \frac{A_{t,av}^{j,i} + A_{c,av}^{j,i}}{A_{VZ}^{j}} \tag{6.15}$$

where A_{VZ}^{j} is the area of the *j*-th vulnerable zone.

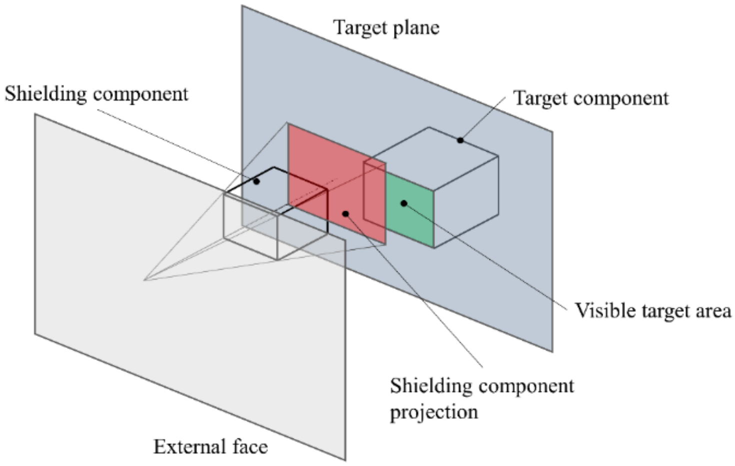

Figure 58: Perspective projection of a shielding component onto the target plane.

Ballistic impacts

In case of a ballistic impact, the projectile passes through the panel without being destroyed. Therefore, no ejecta is produced, and the consequence of the impact cannot be schematised with a debris cone.

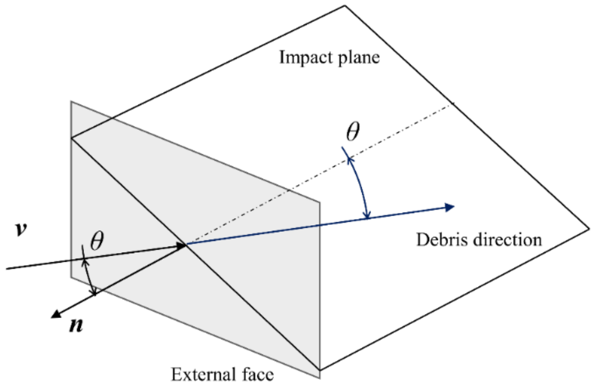

Figure 59: Trajectory of the vector flux elements after a ballistic impact.

Instead, for each vector flux element and impact point on the vulnerable zone grid a line is generated with vertex on the centre of the cell and direction equivalent to the one of the vector flux element (Figure 59). This line represents the trajectory of the debris after the impact. The interaction with this line with the target component and the shielding components is then evaluated. Again, this is to maintain the analogy with the standard formulation. The variables that need to be taken into account are the particle size and the target area. It is assumed that the particle is not affected during the impact and maintains its shape (spherical) and dimensions. The equivalence to the standard formulation is obtained by considering the cross section of the particle that is

$$A_p^i = \frac{1}{4} \cdot \pi \cdot d_{p,i}^2 \tag{6.16}$$

where $d_{p,i}$ is the sample particle diameter associated with the *i*-th vector flux element. For the target section instead, the same procedure used in the hypervelocity case is adopted and the computation is again performed using Eq. (6.14). Finally, the impact probability in the ballistic case is given as

$$P_{comp}^{j,i} = \frac{A_{t,av}^{j,i} + A_p^i}{A_{VZ}^j} \tag{6.17}$$

Eqs. (6.15) and (6.17) can be used inside Eq. (6.10) to compute the impact probability of a component.

6.5.2 Linear impact ejecta methodology

What is defined as the *linear impact ejecta methodology* is a variation of the approach previously described where the impact probability on internal components is no longer computed using areas but using lengths. This variation is introduced as more closely follows the approach used in the original formulation of the vulnerable zone. In this methodology the impact probability in the hypervelocity (Eq. (6.18)) and ballistic (Eq. (6.19)) regimes can be expressed as follows:

$$P_{comp}^{j,i} = \frac{d_{t,av}^{j,i} + d_{c,av}^{j,i}}{d_{Vz}^j} \tag{6.18}$$

$$P_{comp}^{j,i} = \frac{d_{t,av}^{j,i} + d_p^i}{d_{VZ}^j} \tag{6.19}$$

where the different terms maintain the same meaning. The conversions from the areas used in Section 6.5.1 to the equivalent length is carried out using the following relation:

$$d = 2 \cdot \sqrt{A / \pi} \tag{6.20}$$

6.5.3 Correction factor methodology

The previously described methodology is still complex and requires a consistent amount of computational time (around 30 seconds for a configuration with two internal components). A simplified methodology has then been developed, which still considers the mutual shielding, while reducing the large number of expensive geometrical operations needed for the complete procedure. The method used consists in using the standard methodology and applying a correction factor whenever one or more components cover the target component. This approach maintains the simplicity and the short computational time of the standard one while providing a consistent way to account for the reduced impact probability caused by the mutual shielding. Given the different nature of the impacts in the hypervelocity and in the ballistic regime, two correction factors are used. In the case of the hypervelocity regime, the fictional visible area of the target is represented by the area of the vulnerable zone that is the area where an impact can happen and have consequences on the target components. The correction factor in the hypervelocity regime accounts for the portion of the vulnerable zone area that can be covered by the shielding components. The expression for the visible vulnerable zone area for the *j*-th vulnerable zone can be computed as follows:

$$A_{v,av}^{j} = \frac{\sum_{k=1}^{n_{cell}} \left[A_{vz} \neg \left(A_{S,\,1}^{k}, \ldots, A_{S,\,t}^{k}, \ldots, A_{S,\,n_S}^{k} \right) \right]}{n_{cell}} \tag{6.21}$$

where A_{VZ} is the area of the *j*-th vulnerable zone. The expression for the hypervelocity correction factor relative to the *j*-th vulnerable zone is then

$$CF_{hyp}^{j} = \frac{A_{v,av}^{j}}{A_{VZ}} \tag{6.22}$$

The correction factor considers the projection of the extent of each shielding component onto the target plane (Figure 60). If the correction factor is 1, no shielding is present, if is 0 the target component is not *visible* by the impactor.

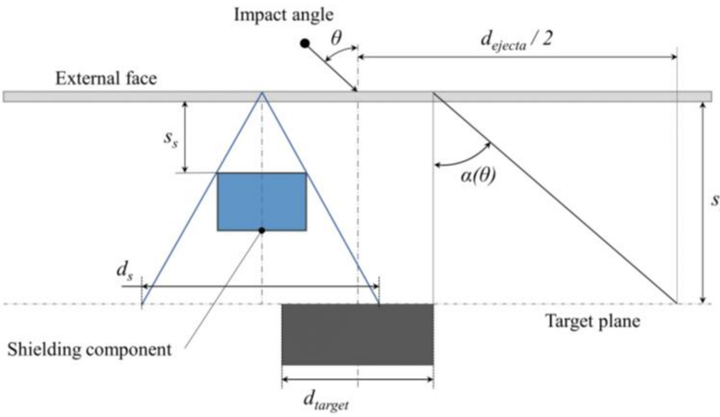

Figure 60: Representation of shielding component contribution to the correction factor.

It is possible to observe that the correction factor depends on the impact characteristics (i.e. impact angle); therefore, it must be computed for each vector flux element impacting the considered vulnerable zone, in case the impact is of hypervelocity nature.

In the case of the ballistic regime, the same approach cannot be used, as there is no ejecta generation. Looking at Eq. (6.8), the impact probability in the ballistic regime depends only on the size of the particle and on the extent of the target object. As the dimension of the particle cannot change, only the extent of the target can be changed in order to correct the impact probability. In the case of a ballistic impact, a corrected target extent is used, which can be referred to as the *visible target extent*. Using an approach similar to the hypervelocity case, the section of the shielding components is projected onto the target plane (Figure 60). At this point, if the projections of the shielding components intersect the target component, they are subtracted from the target components using Boolean operations (difference between sections). The procedure is repeated over each grid cell and averaged as follows:

$$A_{v,av} = \frac{\sum_{k=1}^{n_{cell}} \left[A_t \neg \left(A_{s,1}^k, \ldots, A_{s,t}^k, \ldots, A_{s,n_s}^k \right) \right]}{n_{cell}} \tag{6.22}$$

where $A_{v,av}$ is the average visible area of the target associated to the *j*-th vulnerable zone, A_t is the target component section, and $A_{s,t}^k$ is the perspective projection of the *t*-th shielding component onto the target plane with respect to the *k*-th grid cell. However, as lengths are used in the computation of the impact probability, it is necessary to convert the visible area into a visible equivalent length. The equivalent visible length ($d_{v,eq}$) is computed as follows:

$$d_{v,eq} = 2 \cdot \sqrt{A_{v,av} / \pi} \tag{6.23}$$

The ballistic correction factor can then be expressed as

$$CF_{ball}^{j} = \frac{d_{v,eq}}{d_{target}} \tag{6.24}$$

Finally, the hypervelocity and the ballistic correction factors can be applied to the computation of the impact probabilities as follows:

$$P_{comp}^{j,i} = \frac{d_{ejecta}}{L_{VZ}^{j}} \cdot CF_{hyp}^{j} \tag{6.25}$$

$$P_{comp}^{j,i} = \frac{d_p^{j,i} + CF_{ball}^{j} \cdot d_{target}}{L_{VZ}^{j}} \tag{6.26}$$

6.6 Comparison with DRAMA and ESABASE2/Debris

To verify the validity of the approach followed for the survivability computation the comparison with two software, ESA DRAMA and ESABASE2/DEBRIS is presented. The software suite MIDAS contained in DRAMA can perform simplified vulnerability analysis on outer structure but not on internal components. The user can select the orientation, area, density, and type of shielding of the panels. For the debris population DRAMA uses the fluxes of MASTER-2009. ESABASE2/DEBRIS instead is a more complex software, which allows the user to build arbitrarily complex structure. The methodology used by ESABASE2 is based on a ray tracing method. No debris-cloud propagation is considered. Internal components can be analysed; however, an expedient must be used: the outer structure needs to be removed and the user must provide manually the type of shielding and the standoff distance for each panel of the internal structure. The developed model, on the other hand, automatically detects the characteristics of the outer structure and assigns the proper standoff distance and shielding configuration.

First, we compared the codes for a box shaped object made of aluminium 6061-T6 with a 1m side length, and a 2 mm thickness. The characteristics of the material are summarised in Table A-1. The mission profile considered is a 1-year mission in a sun-synchronous orbit with altitude equal to 802 km and inclination of 98.6 degrees. The ballistic limit equation used is the Cour-Palais thin wall. The resulting comparison for the number of impacts and penetration is summarised in Table 25 and Table 26 respectively.

Table 25: Comparison between the numbers of impacts.

Face	**DRAMA**	**ESABASE**	**Survivability model**
Lead	69.473	80.58	69.47
Space	0.48114	2.176	1.078
Trail	0.032326	0.0222	0.032
Earth	0.54294	2.517	1.259
Right	19.196	21.78	19.17
Left	21.953	27.96	21.975
Total	111.678406	135.0352	112.998

Table 26: Comparison between the numbers of penetrations.

Face	**DRAMA**	**ESABASE**	**Survivability model**
Lead	0.2887	0.2868	0.276
Space	1.71E-05	5.65E-05	2.12E-05
Trail	7.60E-11	5.26E-08	1.03E-06

Earth	1.73E-05	5.05E-05	1.99E-05
Right	0.01027	0.0164	0.0067
Left	0.01	0.0203	0.0076
Total	0.3090	0.3235	0.2913

It is possible to observe a good agreement between the models, especially with DRAMA, whose results are almost identical to the one provided by the presented code. When looking at ESABASE result it is possible to observe a higher number of impacts with respect to the other two codes. This difference can be possibly explained with a different use of the MASTER-2009 files by ESABASE and is common to all the simulations performed. The higher number of impacts for ESABASE can be explained with the higher number of impacts.

To assess the validity of the model also for internal components, a comparison with ESABASE has been performed, given that DRAMA is not able to perform such computations. To perform the comparison, a box shaped parent object made of aluminium 6061-T6 with a 1 m side length and a 1 mm thickness has been selected. This parent object contains another box of the same material, with a side length of 40 cm and a thickness of 1 mm. The mission scenario is the same as of the previous test case. The ballistic limit equation used is the ESABASE Double Wall (Gäde and Miller, 2013). The results for the ESABASE and for the presented code with three four different options are presented in Figure 61.

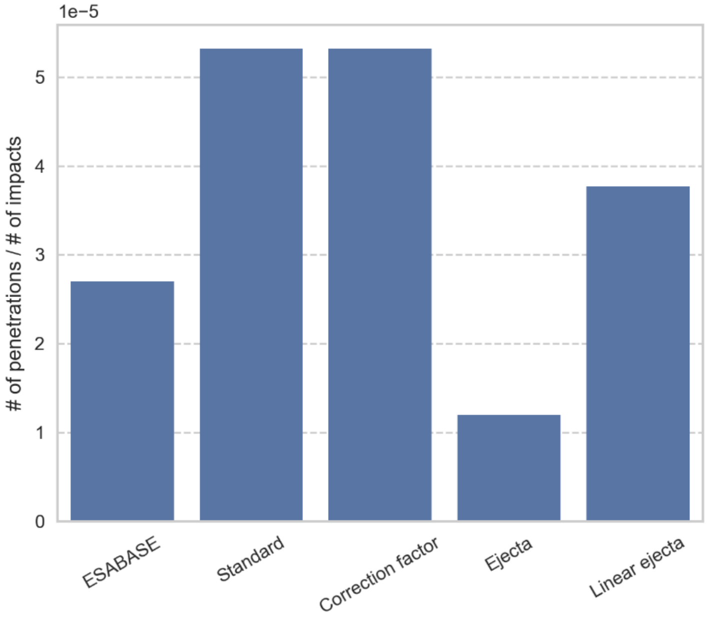

Figure 61: Comparison for one internal component.

The options considered are the standard vulnerable zone methodology, the correction factor methodology, and the impact ejecta methodology in both its versions. Given the difference between the impacts given by the presented code and ESABASE, a comparison of the ratio between the number of penetrations and the number of impacts on the outer structure is here presented. First, it is possible to observe that the models give results in the same order of magnitude. The model predicting the highest number of penetrations is the standard one. This is expected, as the vulnerable zone formulation is conservative. It is important to remember that ESABASE uses a ray tracing method and does not consider the formation of debris clouds. It is natural to assume that when a debris cloud is formed, the probability of having impacts would be higher. As the vulnerable zone methodology considers the debris clouds it is natural to expect a higher number of penetrations. As expected, the correction factor method gives the same results of the standard, as no shielding components are present in the test case. For the ejecta model, the first one using the ratio between the areas gives lower results. The linearized version, which is more similar to the standard vulnerable zone, instead is more conservative, giving a slightly higher number of penetrations. The difference between the linearized and the non-linearized ejecta model is considerable but is also expected. Both models rely on the same computational procedure to evaluate the interactions between the debris ejecta and the shielding components. However, the *linearization* process clearly increases the computed value of P_{comp} as the ratio between the areas will always be considerably lower than the ratio between the equivalent lengths.

For the final comparison, a parent structure with two internal components. The parent structure is a 2x1x1 m aluminium 6061-T6 box with a 1 mm thickness. The two internal components are identical to the one described before. The first box (child 1) is in the centre of the parent structure. The second box (child 2), however, is positioned in front of the first one along the RAM direction at a distance of 0.2 m from the outer face. This comparison is used to demonstrate the capability of the code to deal with shielding components. As such, as a term of comparison is presented in Figure 62 the ratio between the penetration on the lead face of the first child component and the penetrations on the lead face of the second child. As the first child is shielded by the second child, the ratio should be lower than zero. It is possible to observe from Figure 62 that for ESABASE the ratio is about 0.6. The standard model gives a very different result, where the first child has even more penetration than the second does. In fact, in this case, no shielding is considered, and the two internal components are treated separately. The other three methodologies instead show their capability to compute the shielding between the two components. Similarly, to Figure 61, the correction factor model is the most conservative. The linearized ejecta model instead is the closest to ESABASE results. A novel methodology to compute the vulnerability of a spacecraft configuration has been presented, an alternative to the common ray tracing methods. The advantage of this methodology resides in the probabilistic approach, only using vector fluxes, without sampling physical particles to be shot to the spacecraft. This prevents the need to run many simulations to have a sufficiently representative sample. In addition, this methodology considers the contribution of the debris clouds generated after the impacts, unlike ESABASE2/DEBRIS, which only simulates the particle along its impact ray. Three different variations of the methodology have been presented and compared with the standard formulation and with ESABASE. The developed methodologies proved to be able to effectively consider mutual shielding between components and the results obtained are comparable with the one of state-of-the-art software like DRAMA and ESABASE2/DEBRIS.

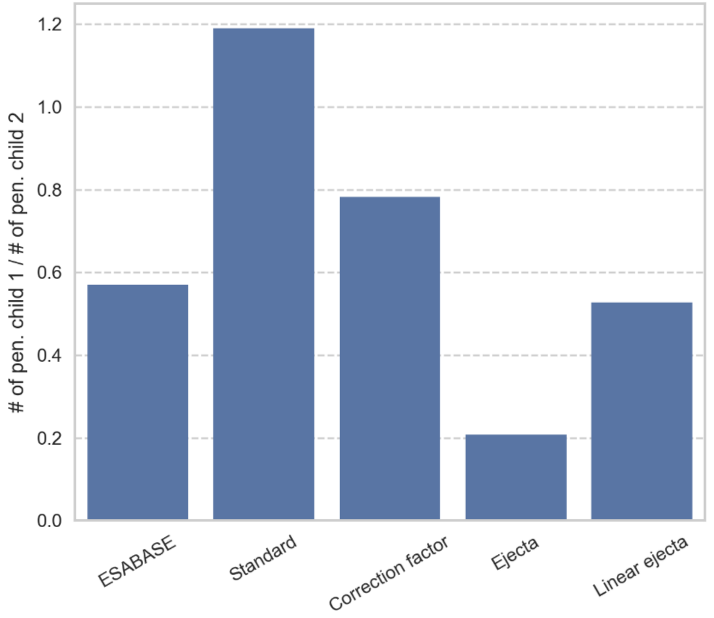

Figure 62: Comparison for two internal components.

6.7 Summary

This chapter has presented the development of a novel methodology for assessing the damage on external and internal structure of spacecraft configurations. The methodology exploits the concept of vulnerable zone and adopts a purely geometrical procedure to assess the mutual shielding between components. Finally, the model is tested against state-of-the-art software. The following chapter will include all the characteristics of the models developed in Chapter 5 and Chapter 6 into a comprehensive framework to evaluate the demisability and the survivability in a concurrent fashion for preliminary spacecraft designs.

Chapter 7 Multi-objective optimisation for the assessment of demisability and survivability of preliminary spacecraft designs

This chapter describes the multi-objective optimisation framework developed to study trade-off solutions as a function of the demisability and of the survivability of specific spacecraft configurations, and presents the results obtained through the application of such framework to relevant test cases. The idea behind this novel approach is to provide a tool that is able to evaluate a wide range of possible preliminary solutions against the demisability and the survivability, testing the search space using multi-objective optimisation, and then providing a family of optimised solutions. These solutions can be the starting point of more refined analyses by the mission design team; however, they will already represent a much more integrated design. Currently, the demisability and survivability requirements are only considered in the latest stages of the mission design and usually imply the modification or the re-design of components. This is not an optimised procedure and can lead to delays or increased costs. The proposed approach tries to reduce these limitations from the initial stages of the mission design. The chapter presents the development of the framework together with an application to a relevant test case in order to demonstrate its capabilities and applicability. In addition, a study on the demisability index is performed and a new formulation is proposed and tested, comparing it to the original expression of the Liquid Mass Fraction (Section 2.5).

Part of the chapter follows the content of the Aerospace Science and Technology journal publication "Spacecraft design optimisation for demise and survivability" (Trisolini et al., 2018b), of the conference proceedings "Demisability and survivability multi-objective optimisation for preliminary spacecraft design" presented at the 68th International Astronautical Congress in Adelaide, Australia (Trisolini et al., 2017a), and of the conference proceedings "On the demisability and survivability of modern spacecraft" presented at the 7th European Conference on Space Debris in Darmstadt, Germany.

7.1 Multi-objective optimisation

Multi-objective optimisation has been selected as the channel of communication between the demisability and the survivability models presented in Chapter 5 and Chapter 6. In fact, as it was possible to observe in Chapter 4, the demisability and the survivability usually exhibit a competing behaviour so that when one improves the other worsen. As we are considering two distinct aspects of the design of a spacecraft, we decided to use multi-objective optimisation. With this methodology, we can assign a score to the demisability and one to the survivability through the devise of specific criteria. With multi-objective optimisation we have the immediate representation of the trade-off between the demisability and survivability of the spacecraft configuration.

In its general formulation, a multi-objective optimisation problem can be described in mathematical terms as

$$\begin{aligned} \text{Min/Max } & f_m(x), \quad m = 1,2,...,M; \\ \text{Subject to } & g_j(x) \le 0, \quad j = 1,2,...,J; \\ & h_k(x) = 0, \quad k = 1,2,...,K; \\ & x_i^L \le x_i \le x_i^U, \quad i = 1,2,...,n \end{aligned} \tag{7.1}$$

where x is the solution vector. $f_m(x)$ are the set of m objective functions, $g_j(x)$ and $h_k(x)$ represent constraints on the problem in the form of inequalities and equalities respectively, and x^L and x^U are the lower and upper boundaries, respectively. In this work, dimension limitations, mass, volume upper limits, and structural resistance of the components represent the constraints. The problem can equally be a minimum or a maximum problem. In multi-objective optimisation, there is not usually a solution that minimises/maximises simultaneously all the objective functions; therefore, there is not a unique optimal solution.

Therefore, the concept of Pareto optimality can be introduced. A Pareto optimal solution is a solution that cannot be improved in any of the objective functions without producing degradation in at least one other objective (Deb, 2001). Expressed in mathematical terms, a solution x_1 is said to Pareto dominate a second solution x_2 if

$$\begin{aligned} & f_i(x_1) \le f_i(x_2) \, \forall \, i \in \{1,2,...,M\} \\ & f_j(x_1) < f_j(x_2) \, | \, \exists \, j \in \{1,2,...,M\} \end{aligned} \tag{7.2}$$

A Pareto optimal solution is a solution that is not dominated by any other solution. The set of Pareto optimal solution is referred as to the Pareto front. They are used to represent the mutual dependency of the demisability and survivability from the design of the configuration. In Pareto fronts, only the solutions which improves at least one of the objectives is kept through the optimisation process. Consequently, at the end of the optimisation, the result is the representation of all the solutions with the best pair of demisability and survivability, given the characteristics of the spacecraft configuration they are associated to. This is a powerful tool when competing objectives are considered that is when improving one, requires compromising the other in some way. As this is the case for the optimisation of the design of a spacecraft for the demisability and the survivability, multi-objective optimisation and Pareto fronts where considered a proper choice for the analysis in exam.

Both the demisability and the survivability of a spacecraft configuration are influenced by a large set of parameters as they are related to the design of the spacecraft structure and all the components present in the configuration. These considerations led to the decision of using multi-objective optimisation for the analysis and identification of trade-off solutions (Minisci et al., 2008, D'Angelo and Minisci, 2007, Vasile and Zuiani, 2011, Zotes and Peñas, 2012) related to the demisability and the survivability requirements.

7.2 Genetic Algorithm

This analysis takes into consideration very diversified parameters, such as the shape of the object (sphere, box, and cylinder), its dimensions, material, and position. These parameters are a mix of discrete variables such as the material and the shape, and continuous variables like the size and thickness of the component. Considering all these aspects, it was decided to use genetic algorithm for the multi-objective optimisation framework. They were selected because of their extended documentation and their relative simplicity of implementation. Moreover, they are suitable for complex problems with a combination of continuous and discrete variables such as the preliminary design of a spacecraft configuration (Mosher, 1999). Figure 63 shows the basic structure of a genetic algorithm.

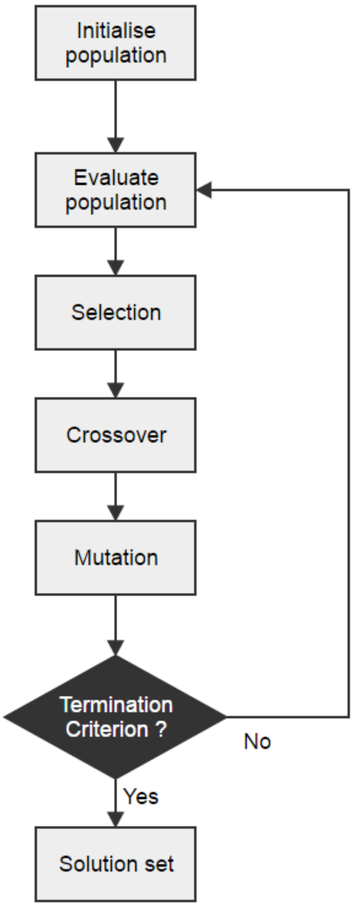

Figure 63: Generic genetic algorithm block diagram.

7.2.1 Algorithm outline

7.2.1.1 Population initialisation

First, the population is initialised, generating the desired number of individuals. Often, the initial population is generated randomly inside the search space defined by the user. Each individual in the population is coded as a finite length vector of variables in terms of an alphabet of choice. Common choices for the encoding alphabet of the individual are the binary alphabet, the hexadecimal alphabet, or the real-value encoding (Deb, 2001). Maintaining the genetic analogy, the individuals represent the chromosomes whereas the variables represent the genes. For example, considering the shape optimisation of a cylinder, the variables defining its shape are the length (l_i), the radius (r_i) and the thickness (t_i) (the genes in this case). Assuming a real-valued encoding, each individual in the population (a cylinder with a defined shape) can thus be represented with a three components vector (the chromosome).

$$I_i = \left[l_i, r_i, t_i \right] \tag{7.3}$$

where I_i is the generic i-th individual in the population, and l_i, r_i, and t_i are the variable describing it. Each variable is initialised as a random generated number inside the search space defined by the user. Table 27 shows an example of randomly generated individuals for the example considered. As this is meant to be an explicative example, the boundaries for the variables have been constrained to a small search space: $l_i \in [1, 2]$, $r_i \in [0.5, 1]$, $t_i \in [0.001, 0.015]$.

Table 27: Examples of individuals made of three variables in a population.

Individual #	Random sample
Individual 1	[1.525, 0.621, 0.0025]
Individual 2	[1.127, 0.896, 0.0106]
Individual 3	[1.945, 0.511, 0.0047]

After the initial population is generated, each individual has to be evaluated so that a fitness score is assigned to each solution. The aim of the genetic algorithm is then to use selective “breeding” of the solutions to produce fitter “offspring”. Highly fit solutions are given more opportunities to reproduce, so that offspring inherit the best characteristics from the parent population. The breeding of the parent population is obtained replicating the natural mechanisms of crossover and mutation.

7.2.1.2 Crossover and mutation

In the crossover mechanism, two individuals from the parent population are selected and their genetic material is mixed to produce one or two child individuals. Several methods of crossover are available (Deb, 2001) such as the single-point, two-point, cut-and-splice, etc. For example, in the single-point crossover (see Figure 64), one point in the chromosome is selected and the parent individuals have their genetic material split into two parts. Then the genetic material is mixed to obtain the offspring.

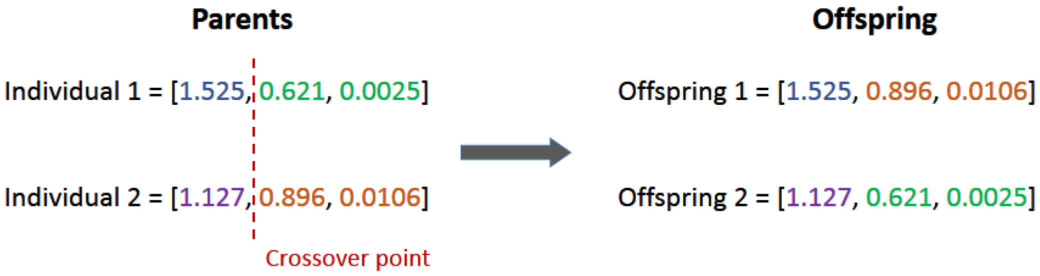

Figure 64: Example of single-point crossover.

To the crossover operator is also associated a probability that is decided by the user, the so-called *crossover rat*e. When two individuals from the parent population are selected, a random number between zero and one is generated with uniform probability and compared to the *crossover rate*. If the random number is higher than the *crossover rate*, no crossover occurs and both parents are kept unchanged. If the random number is lower than or equal to the *crossover rate*, the crossover operator is applied. Usually the crossover rate is high, greater than 0.8. After the application of the crossover operator, another operator is usually adopted that is the mutation operator. It acts on an individual chromosome and changes the single variables (genes) (Figure 65). Even in this case, the process is related to the generation of a random number and to the definition by the user of a *mutation rate*. The mutation is usually related to a specific criterion, for example, for real-valued genes the variable is usually slightly modified inside an interval centred in the variable itself, whereas for binary-encoded genes, they are flipped from zero to one or vice versa. *Mutation rates* are typically very small.

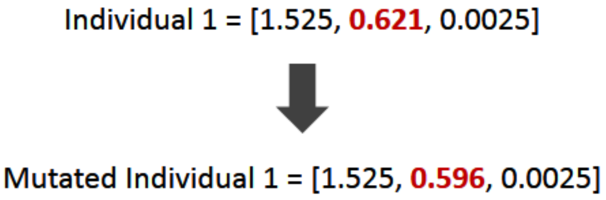

Figure 65: Example of mutation.

7.2.1.3 Individual selection

After the processes of crossover and mutation, a new population is obtained made by the offspring of the parent population. At this point, it is necessary to select the individuals that will be passed to the successor population. Several selection strategies are available for genetic algorithms (Deb, 2001), however is not the purpose of this work to describe all of them. In the following section (Section 7.2.2); the utilised selection strategy will be described in detail. Once the new population is formed, the algorithm checks if the termination condition has been met. If this is the case, the algorithm stops and outputs the solution. If the condition is not met, the process starts again with the new population used as the parent population, which will go through the previously described steps (selection, crossover, and mutation) to produce another generation.

7.2.2 Non-dominated Sorting Genetic Algorithm (NSGA) II

For the purpose of this work, the Non-dominated Sorting Genetic Algorithm (NSGAII) algorithm was selected. This choice was made because of the good documentation available for the NSGAII algorithm, because it is directly available in a Python library and because it has proved to be a fast algorithm that also provides a very good solution variability (Deb et al., 2002). In this section are described the main characteristics of the NSGAII algorithm.

7.2.2.1 Non-dominated sorting

This is the procedure (Deb, 2001) of sorting the individuals in a population to emphasise the best solutions in the population. A schematisation of the procedure is given in Figure 66.

```
fast-non-dominated-sort($P$):
for each $p \in P$
    $S_p = \varnothing$
    $n_p = 0$
    for each $q \in P$
        if $(p \prec q)$ then                 if $p$ dominates $q$
            $S_p = S_p \cup \{q\}$           add $q$ to the set of solutions dominated by $p$
        else if $(q \prec p)$ then
            $n_p = n_p + 1$                  increase the domination counter of $p$
        if $n_p = 0$ then                    $p$ belongs to the first front
            $p_{rank} = 1$
            $F_1 = F_1 \cup \{p\}$
$i = 1$                                      initialise the front counter
while $F_i \neq 0$
    $Q = \varnothing$                        used to store the members of the next front
    for each $p \in F_i$
        for each $q \in S_p$
            $n_q = n_q - 1$
            if $n_q = 0$ then                $q$ belongs to the next front
                $q_{rank} = i + 1$
                $Q = Q \cup \{q\}$
    $i = i + 1$
    $F_i = Q$
```

Figure 66: Description of the Fast non-dominated sort algorithm (Deb et al., 2002).

In its simplest form, the algorithm first compares each solution with every other solution in the population to find if it is dominated or not. A solution is non-dominated if none of the objective functions can be improved without degrading some of the other objectives. After this process is terminated, the first non-dominated front of the population is obtained. In order to find the individuals belonging to the next non-dominated front, the solutions of the first front are removed from the population and the remaining individuals go through the same procedure described before. This procedure is repeated until all the individuals in the population are assigned to a non-domination level.

7.2.2.2 Diversity preservation

The preservation of a diverse set of solution is important in genetic algorithms because favours a better scan of the search space. For this, the NSGAII algorithm uses an approach based on the definition of a crowded-comparison operator (Deb, 2001). This is based on the idea to associate a *distance metric* to each solution in a population that describes how far each solution is from the others in the population. This is done in the objective function space. The distance metric is computed as follows: for each solution, the distance between the two points on either side of the it is computed. This distance is computed for every objective function. Then, for each solution, all the associated distances are summed together to obtain the crowding-distance value. It is important to observe that the objective functions are normalised before calculating the crowding-distance. The crowded-comparison operator then guides the selection process at the various stages of the algorithm towards a uniformly distributed Pareto-optimal front. Throughout the algorithm, when the solutions need to be selected, priority will be given first to solution with a lower non-domination level, and then the crowding-distance operator is used, selecting solutions with a bigger crowding-distance. In this, solutions located in less crowded regions are preferred.

7.2.2.3 Main loop

In the NSGAII algorithm (Deb et al., 2002), first a random parent population P_0 of size N is generated; the population is then sorted based on non-domination. Each solution is assigned a rank equal to its non-domination level. Then the genetic operators of tournament selection[2], mutation, and crossover are used to generate the first offspring population Q_0 of size N. At this point *elitism*[3] is introduced by comparing the current offspring population with the original parent population and selecting the best non-dominated individuals. After the first generation, the procedure is slightly different. The description for a generic *t*-th generation (see Figure 67) is followed here. First, a combined population

---

[2] Tournament selection is a method of genetic algorithms used to select an individual from a population. The procedure first involves the random selection of few individuals from the population. Then a series of "tournaments" are carried out among these selected individuals. The winner of each tournament (the one with the best fitness) is selected for crossover.

[3] Elitism is the practice of maintaining the best individual from one population to the next one.

$R_t = P_t \cup Q_t$ is formed from the parent population (P_t) and the offspring population (Q_t), both of size N. The obtained population R_t is of size $2N$. Then, R_t is sorted according to non-domination.

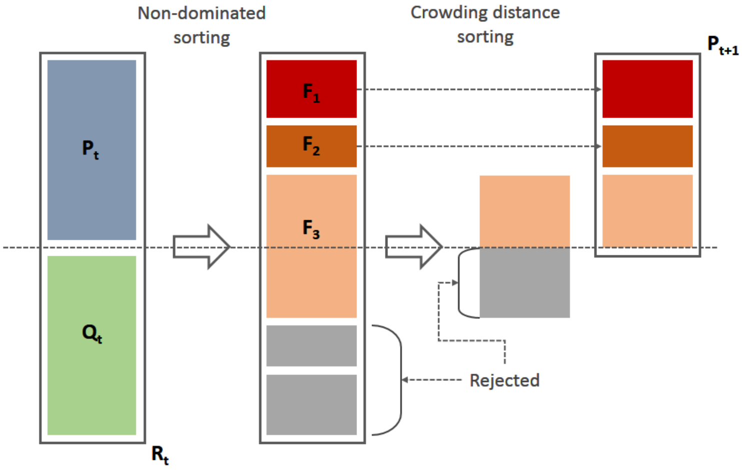

Figure 67: NSGAII procedure (Deb et al., 2002).

The new population P_{t+1} is formed following the non-domination level of the solution that is first the individuals belonging to the best non-dominated front F_1 are all selected first and moved to the P_{t+1} population. The remaining individuals of the P_{t+1} population are chosen from the subsequent non-dominated fronts in order of their rank. This procedure continues until no more sets can be accommodated. It is reasonable to think that the last set, say F_l, will not be completely accommodated inside the population of P_{t+1} (which is limited to N individuals). The individuals belonging to this "last" set are then sorted according to the crowding distance operator, and the best solutions are selected until the population is filled. The diversity among non-dominated solution is then introduced by using a crowding comparison procedure as previously described. A more formal outline of the entire procedure is given in Figure 68:

```
$R_t = P_t \cup Q_t$                                        Combine parent and offspring population
$F = \text{fast-non-dominated-sort}(R_t)$                   $F = (F_1, F_2, .)$, all non-dominated fronts of $R_t$
$P_{t+1} = 0$ and $i = 1$                                   Until the parent population is filled
Until $P_{t+1} + F_i <= N$                                  Calculate crowding-distance in $F_i$
  $\text{Crowding-distance-assignment}(F_i)$                Add $i$-th non-dominated front in parent pop.
  $P_{t+1} = P_{t+1} \cup F_i$                              Check the next front for inclusion
  $i = i + 1$                                               Sort in descending order using $\prec_n$
Sort $(F_i, p_n)$                                           Chose first $(N - |P_{t+1}|)$ elements of $F_i$
$P_{t+1} = P_{t+1} \cup F_i[1:(N - P_{t+1})]$               Use selection, crossover and mutation to create
                                                            a new population $Q_{t+1}$
$Q_{t+1} = \text{make-new-population}(P_{t+1})$             Increment the generation counter

$t = t + 1$
```

Figure 68: NSGAII main Loop description (Deb et al., 2002).

7.3 Optimisation problem setting

This section contains the description of the baseline features of the multi-objective optimisation framework as applied to the demisability and survivability problem. The description of the characteristics of the individuals is presented, together with the procedure followed for their generation and the subsequent conversion into a spacecraft configuration. In addition, the section contains the description of the procedure followed to handle the constraints, with particular importance given to some relevant spacecraft components such as tanks and reaction wheels. Finally, also the handling of position errors is considered. If the position of a component is optimised, not all the random generated positions will generate a feasible configuration, consequently, there we must take into account the wrong position of components inside the spacecraft. The evaluation functions used in the optimisation framework are the ones introduced in the previous chapters; specifically the Liquid Mass Fraction (Section 5.1.4) for the demisability and the Probability of no-Penetration (Section 6.4) for the survivability.

7.3.1 Individual Generation

During the optimisation, each spacecraft configuration is represented by an individual. Among the possible representation for the individual, a real valued representation has been selected. With this, each gene directly represents the variable to be optimised. The variables can be both integer and floating-point numbers. For continues variables such as the thickness, the floating representation is used, whereas for discrete variables such as the material, the integer representation is adopted. Table 28 summarises all the possible variables that can be optimised in the developed framework, together with their representation in the individual.

Table 28: Summary of optimisation variables for the present problem.

Variable	Variable type
Component quantity	Integer
Component material	Integer
Component shape	Integer
Component thickness	Real
Component parent	Integer
Component position	Real
Component size	Real
Component orientation	Integer
Component catalogue	Integer
External panel material	Integer
External panel shielding	Integer
External panel thickness	Real

The *quantity* variable represents the number of a certain component in a configuration. The *component parent* variable represents the ID of anther object to which the component is connected. This connection can be a containment if the ID refers to another internal component or an attachment if it identifies one of the external panels. The *orientation* is represented with an integer as only predefined orientations along the main axis of the spacecraft can be considered. The *component catalogue* variable can be used when a component is taken from a catalogued option as, for example, battery cells. The *external panel shielding* variable considers the possibility to have external panels made of a single panel sheet or by honeycomb sandwich panels. For each component to be optimised in the spacecraft configuration, the user can specify which variables will be optimised. For each optimisation variable is also necessary to specify the lower and upper bounds from which the optimiser can sample during the generation of the population. The shape variable, for example, can be selected among the available shapes that are the Box, Sphere, Cylinder, Flat Plate, and Sandwich Panel. The material can be selected from an available database, where each material is has a different integer identifier. The size, thickness, and position variables can be component and mission dependent and can be set separately for each component in the optimisation.

7.3.1.1 Baseline configuration

When performing the setup of the optimisation, a baseline configuration needs to be provided with its main characteristics. This configuration serves as a blueprint to specify the components to be optimised: by specifying the ID of the component we can identify it and then specify the variables we want to optimise. The parent spacecraft dimensions, and mass must be provided, together with the dimensions and mass of the solar panels. In addition, a layout of the external panels and of the internal components must be specified. As an example, in Table 29 is represented a simplified version of a spacecraft configuration.

Table 29: Simplified baseline configuration definition.

ID	Name	Shape	ts (mm)	Mass (kg)	…
0	Parent	Box	n/a	2000	…
1	SolarPanel	FlatPlate	0.05	100	…
…	…	…		…	…
9	Tank	Sphere	0.003	12	
10	Battery	Box	0.002	45	…

Once the baseline configuration is specified, the optimisation variables for each component can be specified. For example, in case the tank with ID 9 has to be optimised we can specify its ID and then all the optimisation variables with the relative boundaries (Table 30).

Table 30: Example of optimisation variable definition.

ID	Opt. variable	Bound low	Bound up
9	Thickness	0.0005 mm	0.005 mm

7.3.2 Constraints handling and components requirements

Specific constraints need to be satisfied for a realistic spacecraft configuration to be feasible. For example, reaction wheels need to be perpendicular to one another or the tank must sustain a specific internal pressure. These types of constraints need to be set additionally with respect to the provided boundaries for the optimisation variables. In fact, it is possible that combinations of the sampled optimisation variables are not feasible, despite belonging to the defined sampling boundaries. The developed optimisation framework handles such constraints on a component basis that is the user can set different constraint checking functions for different types of components. When the feasibility is checked, two possibilities are available; the individual either is rejected or is repaired, making it feasible. For each component is also possible to specify limits on the possible materials and shapes used, if such limitations are needed. In addition, also the parent of the component can be limited. For example, the attachment of components could be forced on specific panels.

In the current implementation of the framework, the constraints handling procedure is implemented for tanks and reaction wheels. The focus on these components arises from the fact that they are critical components when both considering the demisability and the survivability requirements.

7.3.2.1 Tank assembly constraints

When considering the feasibility of a tank assembly it is necessary to consider the following parameters: the propellant mass, the storage pressure, the number of tanks, their shape, their thickness, and their material. Starting from the amount of propellant required by the mission and from the propellant used, the propellant volume is computed as

$$V_f = K_1 \cdot \frac{m_f}{\rho_f} \tag{7.4}$$

where m_f is the mass of the fuel, ρ_f is the density of the fuel, and K_1 is a factor that considers the additional volume needed for the pressurant gas (the filling factor). Given the propellant volume, the shape, and the number of tanks the internal radius of the vessel can be computed. For spherical tanks, the radius corresponds to

$$r_t^{int} = \sqrt[3]{\frac{3 \cdot V_f}{4 \cdot \pi \cdot n_t}} \tag{7.5}$$

whereas for cylindrical tanks we have:

$$r_t^{int} = \sqrt[3]{\frac{V_f}{2 \cdot \pi \cdot AR \cdot n_t}} \tag{7.6}$$

Here, r_t^{int} is the internal radius of the tank, n_t is the number of tanks in the configuration, and AR is the aspect ratio for a cylindrical tank. Finally, to evaluate the feasibility of a solution, the ultimate strength acting on the walls of a tank has to be computed. For cylindrical tanks, the ultimate strength can be expressed as follows:

$$\sigma_u^{wall} = \frac{SF \cdot p \cdot r_t^{int}}{t_t} \tag{7.7}$$

whereas for spherical tanks the equivalent expression is

$$\sigma_u^{wall} = \frac{SF \cdot p \cdot r_t^{int}}{2 \cdot t_t} \tag{7.8}$$

where t_t is the thickness of the tank wall, p is the operating pressure, and SF a safety factor. For a solution to be feasible, the ultimate strength on the walls of the tank has to be below the ultimate strength of the material of the tank.

$$\sigma_u^{wall} < \sigma_u^{material} \tag{7.9}$$

The implementation of the constraint inside the multi-objective optimisation algorithm is in the form of a *death penalty* (Coello, 2002), where unfeasible solutions are directly discarded.

When initialising the optimisation problem some data needs to be provided for the feasibility check. Specifically, the propellant mass, the storage pressure, the fuel density, the safety factor, and the filling factor are needed. In addition, the aspect ratio of the tank can be provided or optimised. However, the sensitivity of the demisability and survivability indices to the aspect ratio is low with respect to the other parameters considered.

7.3.2.2 Reaction wheels constraints

For the reaction wheels, two checks need to be performed. First, the amount of angular momentum provided by the reaction will must be greater than the minimum requirements. Second, the structural integrity of the reaction wheel needs to be satisfied.

The minimum required radius for the reaction wheel to satisfy the angular momentum requirements can be computed as follows

$$r_{min} = \left(\frac{H_{design}}{\pi \cdot \rho_m \cdot \omega_{max} \cdot AR} \right)^{1/5} \tag{7.10}$$

where H_{design} is the design angular momentum of the wheel, ρ_m is the material density, ω_{max} is the maximum rotation speed of the wheel, and AR is the aspect ratio of the wheel.

The structural integrity of the reaction wheel is then checked as follows

$$\sigma_y \geq SF \cdot \left(3 + \nu_m\right) \cdot \rho_m \cdot \omega_{max}^2 \cdot r^2 \tag{7.11}$$

where σ_y is the yield strength of the material, SF is a safety factor, r is the radius of the wheel, and ν_m is the Poisson ratio of the material.

If the radius of the reaction wheel does not satisfy the requirements, it is repaired and the radius is set equal to the minimum possible value, if such value is inside the initially specified boundaries. On the other hand, if the structural integrity test fails, the solution is discarded.

7.3.2.3 Position errors handling

When the position of the components can be optimised, it is possible that after the random generation of the individual, some of the components intersect each other. As this is a rather common event, we decided not to discard these solutions, but to repair them, moving the components until they no longer intersect each other.

The procedure relies on the generation of a 3D grid inside the parent object of points available for the positioning of the components. At the beginning, all the grid points are flagged with a 0, meaning that all points are available. When a component is added to the grid, the grid points occupied by the component switch to 1, and that they are no longer available (Figure 69).

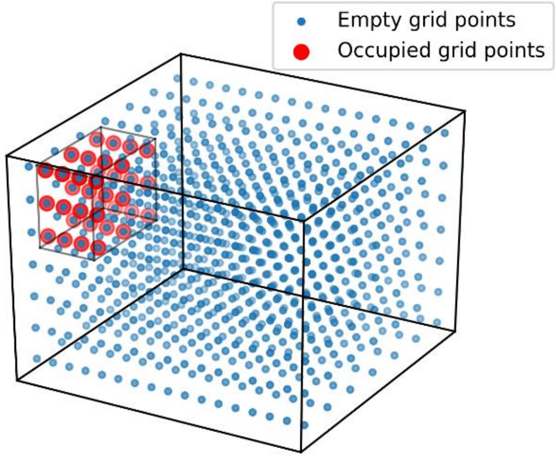

Figure 69: Position grid representation with occupied points.

The repairing procedure consists of the following steps:

- Finding the intersecting components;
- Select one of these components to be repaired;

- Add all the other components to the grid:
- Sort all the available grid points with respect to the distance from the original component position;
- Position the component in the closest available grid points;
- Repeat the procedure until all intersecting components are repaired.

The available grid points are sorted with respect to the distance from the original position of the component to maintain the highest similarity with the randomly generated individual.

7.4 Tank assembly test case

For this test case we are considering the optimisation of tank assemblies for Earth observation and remote sensing missions (Wertz and Larson, 1999, Platnick, 2016). Tanks were selected because they are interesting for both the survivability and the demisability. They represent critical components in the demisability analysis as they usually survive the atmospheric re-entry. They are also components that need protection from the impact against space debris because it can cause leaking or ruptures, which can compromise the mission success. Earth observation and remote sensing missions frequently exploit sun-synchronous orbits and that is the reason why the current work focuses on these orbits. A sun-synchronous orbit is a Low Earth Orbit (LEO) that combines altitude and inclination in order for the spacecraft to pass over any given point of the Earth’s surface at the same local solar time, granting the spacecraft a view of the Earth’s surface at nearly the same illumination angle and sunlight input.

Different configurations have been analysed as a function of the characteristics of the tank assembly and of the mission itself, such as the mission duration and the mass class of the spacecraft. In particular, it was decided to relate the total volume of the tankage to the size of the spacecraft, to its orbit, and to the mission duration by computing the delta-V budget required for sun-synchronous missions.

7.4.1 Propellant budget for sun-synchronous missions

To estimate the size of the tank assembly it is necessary to compute the amount of propellant needed for the mission through a delta-V budget. As sun-synchronous orbits are influenced by atmospheric drag and by the non-uniformity of the Earth’s gravitational field, they require regular orbit correction manoeuvres. They also need, as for most spacecraft, additional manoeuvres to correct orbit injection errors and to perform disposal manoeuvres. To estimate the tankage volume, it is necessary to compute the amount of propellant needed by the spacecraft as a function of the mission characteristics. The three main elements that contribute to the ΔV budget for the required mission lifetime are the orbit maintenance, the launch injection errors, and the disposal manoeuvres.

Orbit maintenance manoeuvres are used to keep the sun-synchronism of the orbit and to control the accuracy of the ground track. To do so, the orbital height and inclination need to be maintained within admissible ranges. In LEO, atmospheric drag results in orbital decay, causing the semi-major axis and the orbit period to decrease. The reduction in the semi-major axis δa and in the orbital period $\delta\tau$ for one orbit can be computed as (Colombo and Swinerd, 2013)

$$\delta a = -2 \cdot \pi \cdot \rho_{atm} \cdot \frac{S \cdot C_D}{m_{s/c}} \cdot a_0^2 \tag{7.12}$$

$$\delta\tau = \frac{3 \cdot \pi}{V_{s/c}} \cdot \delta a \tag{7.13}$$

where ρ_{atm} is the atmospheric density, S is the average cross section of the spacecraft, C_D is the drag coefficient, $m_{s/c}$ is the mass of the spacecraft, a_0 is the nominal orbit semi-major axis, and $V_{s/c}$ is the orbital velocity of the spacecraft. The changes in the orbital height and period lead to changes in the ground track. Such variations can be controlled by imposing a tolerance on the nominal ground track. When the spacecraft's ground track reaches the prescribed tolerance, a correction manoeuvre needs to be executed. To do so, the time difference from the nominal time at the equator passage Δt_0 needs to be computed:

$$\Delta t_0 = \frac{\Delta\lambda}{\omega_e} \tag{7.14}$$

where ω_e is the angular speed of the Earth and $\Delta\lambda$ is the longitude displacement at equator passage and can be expressed as:

$$\Delta\lambda = \frac{2 \cdot E_0}{R_e} \tag{7.15}$$

R_e is the radius of the Earth, and E_0 is the imposed tolerance on the displacement from the nominal orbit ground track at the equator (equal to 0.7 km for this study). Using Eqs. (7.14) and (7.15) It is possible to compute the number of orbits after which the equator crossing displacement reaches the prescribed limit as follows:

$$k = \sqrt{\frac{2 \cdot \Delta t_0}{\delta\tau}} \tag{7.16}$$

To control the ground track, the manoeuvre must be executed every 2k orbits, leading to a variation in the orbit semi-major axis (Δa_{decay}) and orbital period (Δt_{decay}) of:

$$\Delta a_{decay} = 2 \cdot k \cdot |\delta a| \tag{7.17}$$

$$\Delta t_{decay} = 2 \cdot k \cdot |\delta\tau|$$

Δt_{decay} is also the time between the necessary orbit correction manoeuvres. The correction manoeuvre can be computed with a Hohmann transfer:

$$\Delta V_{decay,\, i} = \sqrt{\frac{\mu_e}{r_1}}\left(\sqrt{\frac{2 \cdot r_2}{r_1+r_2}} - 1\right) + \sqrt{\frac{\mu_e}{r_2}}\left(1 - \sqrt{\frac{2 \cdot r_1}{r_1+r_2}}\right) \tag{7.18}$$

where μ_e is the gravitational parameter of the Earth, $r_1 = a_0 - \Delta a_{decay}$ is the radius of the initial circular orbit, and $r_2 = a_0$ is the radius of the final orbit after the manoeuvre. The total ΔV_{decay} due to the orbital height correction manoeuvres for the entire mission lifetime is the sum of the contribution of Eq. (7.18) every Δt_{decay} so that

$$\Delta V_{decay} = \left\lfloor \frac{\Delta t}{\Delta t_{decay}} \right\rfloor \cdot \Delta V_{decay,\, i} \tag{7.19}$$

where Δt is the mission lifetime. In addition, the orbit inclination needs to be controlled during the lifetime of a sun-synchronous spacecraft. The variation of the orbital inclination in fact causes the drifting of the line of the nodes and affects ground track repetition. The total ΔV_{inc} needed to compensate for the inclination variation can be computed as

$$\Delta V_{inc} = 2 \cdot sin\left(\frac{\Delta i_{sec}}{2}\right) \cdot \Delta t \tag{7.20}$$

where Δi_{sec} is the secular variation of the inclination in one year that can be assumed equal to 0.05 deg/year. To compute the ΔV_{inj} needed to compensate for injection errors, that the maximum errors in the orbital parameters after launch are:

$$\begin{aligned} \Delta a_{inj} &= \pm 35\ km \\ \Delta i_{inj} &= \pm 0.2\ deg \end{aligned} \tag{7.21}$$

The ΔV_{inj} due to the injection errors can then be computed using a Hohmann transfer with plane change where the initial and final orbits have a radius of $r_1 = a_0 - \Delta a_{inj}$ and $r_2 = a_0$ respectively, and the inclination change is equal to Δi_{inj}. Finally, the ΔV_{disp} to ensure the end-of-life disposal of the spacecraft can be computed as follows. It is possible to consider as a disposal manoeuvre a Hohmann transfer from the nominal orbit to a 600 km orbit, assuming that the 600 km altitude will allow a spacecraft to decay naturally within 25 years,

The sum of the previously computed delta-V values is the total ΔV_{tot} budget of a sun-synchronous mission, which depends on the nominal orbit of the spacecraft, the mission duration, and the characteristics of the spacecraft (mass, cross-section, drag coefficient).

$$\Delta V_{tot} = \Delta V_{decay} + \Delta V_{inc} + \Delta V_{inj} + \Delta V_{disp} \tag{7.22}$$

It is assumed that a monopropellant hydrazine propulsion system is adequate for all the orbit correction manoeuvres previously described. The specific impulse of hydrazine is set to 200 s (Airbus Safran Launchers GmbH, 2003a). The propellant mass needed by the spacecraft during its entire lifetime can be computed using the Tsiolkowsky equation (Wertz and Larson, 1999)

$$m_f = m_{s/c}^{in} \cdot \left(1 - exp\left(-\frac{\Delta V_{tot}}{g_0 \cdot Isp}\right)\right) \tag{7.23}$$

where m_f is the propellant mass needed to perform the total velocity change ΔV_{tot}, $m_{s/c}^{in}$ is the initial spacecraft mass, g_0 is the gravitational acceleration at sea level (equal to 9.81 m/s^2), and I_{sp} is the specific impulse of the fuel used. Once the propellant mass is calculated, the tankage volume can be estimated using Eq. (7.4)

As an example, let us consider the MetOp mission (European Space Agency, 2012). MetOp is a sun-synchronous spacecraft with a mass of 4085 kg, and an average cross section S = 18 m^2. The operational orbit of the mission is 817 km in altitude with an inclination of 98.7 degrees. The mission design life is 5 years. Computing the mass of propellant with Eq. (7.23) returns a value of 332 kg of propellant, which is very close to the one of the actual mission of 320 kg. As another example, Cryo-Sat2 (European Space Agency, 2016) is a 3 years mission with a spacecraft mass of 720 kg, an average cross section of 8.8 m^2, and an orbital altitude of 717 km. The resulting propellant mass is 43 kg that is in good agreement with the value of 38 kg of the actual mission.

7.4.2 Optimisation setup

The setup of the optimisation requires the specification of a baseline spacecraft configuration and of some basic information about the mission. From the configuration, the optimiser will then generate the random individuals used in the genetic algorithm. The mission related information is instead used for feasibility checking and constraints handling of the different components. In addition, both the demisability and the survivability analysis cannot be carried out without knowing the characteristics of the main spacecraft structure, i.e. the overall size and mass of the spacecraft, the material, the thickness, and the type of shielding.

7.4.2.1 Mission scenario

The mission scenario needs to specify both the characteristics of the re-entry trajectory adopted and of the operational orbit used for the survivability analysis. For the demisability simulation, the initial re-entry conditions are provided by the altitude, the flight path angle, the velocity, the longitude, the latitude, and the heading angle. Standard values for these parameters (Beck et al., 2015a, Fritsche et al., 2007) were selected and are presented in Table 31.

Table 31: Initial conditions for the re-entry simulations.

Parameter	Symbol	Value
Altitude	h_{in}	120 km
Flight path angle	γ_{in}	0 deg
Velocity	v_{in}	7.3 km/s
Longitude	λ_{in}	0 deg
Latitude	φ_{in}	0 deg
Heading	χ_{in}	-8 deg

For the survivability, the mission scenario is defined by the operational orbit of the spacecraft. Sun-synchronous missions are considered. As such, the orbit selected has an inclination of 98.6 degrees and an altitude of 802 km, which are typical values for sun-synchronous missions. In addition, four different mission durations were selected: 3, 5, 7, and 10 years.

7.4.2.2 Spacecraft external configuration

As the optimisation presented in the paper focuses on internal components (i.e. tanks), the external configuration of the spacecraft needs to be defined. A cubic shaped spacecraft is used to keep the analysis as general as possible. The dimensions of the cubic structure (i.e. its side length) can be computed tacking into account the mass of the spacecraft ($m_{s/c}$) and assuming an average density for it ($\rho_{s/c}$) as follows (Wertz and Larson, 1999).

$$l = \sqrt[3]{\frac{m_{s/c}}{\rho_{s/c}}} \tag{7.24}$$

where the average density of the spacecraft is 100 kg/m^3, which is a value that can be used in preliminary design computations (Wertz and Larson, 1999). Four classes of spacecrafts were considered in the analysis. The classes were defined according to the mass of the spacecraft: 500 kg, 1000 kg, 2000 kg, and 4000 kg. This is done because the demisability is influenced by the size of the spacecraft as more massive components will be less likely to demise. The classes and the corresponding spacecraft sizes are summarised in Table 32. In addition to the size and mass of the spacecraft, the thickness and material of the external wall also need to be defined. For the purpose of this work, and in order to maintain the same conditions for all the simulations, it was decided to use a single wall configuration with a 3 mm wall thickness made of Aluminium alloy 6061-T6.

Table 32: Mission classes analysed with respective size of the spacecraft.

Class	Side length
500 kg	1.7 m
1000 kg	2.15 m
2000 kg	2.7 m
4000 kg	3.4 m

7.4.2.3 Optimisation variables

For the tank assembly, the shape (sphere or cylinder), material, thickness, and the number of vessels were optimised. Table 33 summarised the variables considered and their boundaries.

Table 33: Optimisation variables for the tank assembly.

Variable	Bounds / Options
Material	Al-6061-T6, AISI-316, Ti-6Al4V
Thickness	0.0005 – 0.005 mm
Shape	Sphere, Cylinder
# of vessels	1 - 6

For this simplified test case, two aspects of the tank configuration have not been directly considered in the optimisation variables, which are the size and positions of the tanks. It was decided to relate the size of the tanks, i.e. the radius, to the total volume required to store the propellant (Section 7.4.1) and to the number of tanks in order to have a realistic mission scenario. Delta-V budgets are in fact one of the main constraints on the mission design process and the amount of propellant, which is related to the size of the tanks, needs to be sufficient for the mission requirements. Instead, the position of the centre of mass of the tanks was fixed and the tanks evenly distributed around it as a function of their number (Figure 70). The centre of mass for the test case simulation has been set to coincide with the centre of the external structure.

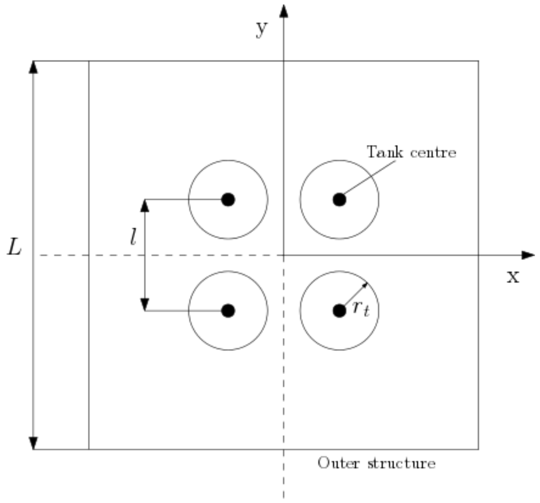

Figure 70: Example of a tank configuration with four tanks equally spaced with respect to the centre of mass.

As described previously, the tanks need to satisfy strength requirements. Consequently, parameters such as the storage pressure, the safety factor, and the filling factor need to be provided (see Eqs. (7.7) and (7.8)). For this specific test case, the storage pressure of the tank was set to 4 MPa (Wertz and Larson, 1999), the safety factor of the tanks to 1.5 (Wertz and Larson, 1999), and the filling factor to 1.4 (average value from (Airbus Safran Launchers GmbH, 2003a)).

7.4.3 Results and discussion

The problem in exam of considering a combined demisability-survivability analysis is very much mission dependent. In fact, the mission time influences the amount of debris impacts on the spacecraft and consequently its probability of no-penetration. The size and mass of the spacecraft and its components strongly influence the demisability. The geometry, the quantity, and the material of the components affect both the demisability and the survivability. For these reasons, it was decided to perform the optimisation for different spacecraft masses and mission lifetimes.

The general characteristics of the Pareto front are analysed. Figure 71 represents the Pareto fronts for a 2000 kg spacecraft with a mission lifetime of 10 years with a maximum allowed number of tanks equal to three. In the Pareto front, the different solutions are distinguished as follows: the colours indicate the three materials; the marker shape indicates the configuration of the tank assembly, i.e. the number of tanks. The difference between cylindrical and spherical tanks is highlighted filled or unfilled markers. Figure 71 shows several features of the optimisation results. First, the expected competing behaviour between the demisability and the survivability is clearly represented by the shape of the Pareto front with high demisability solutions having a relative low probability of no-penetration and vice versa. Second, the ranges for the two indices are considerably different. This is indeed expected, given the very different domains described by the two models. In particular, the survivability has a naturally narrow range of values, considering that a PNP index of 95%-98% is typical for many missions (obtained as the sum of the contribution of every component in the spacecraft). As such, even small variations at component level can be significant, especially when these components are critical to the mission success. For example, the overall probability of no-penetration for the MetOp SVM spacecraft evaluated with the software SHIELD (Putzar and Schäfer, 2006), is 97.26%, and the tank assembly (four tanks in total) probability of no-penetration is 99.78%, which is comparable with the value obtained in the presented optimisation.

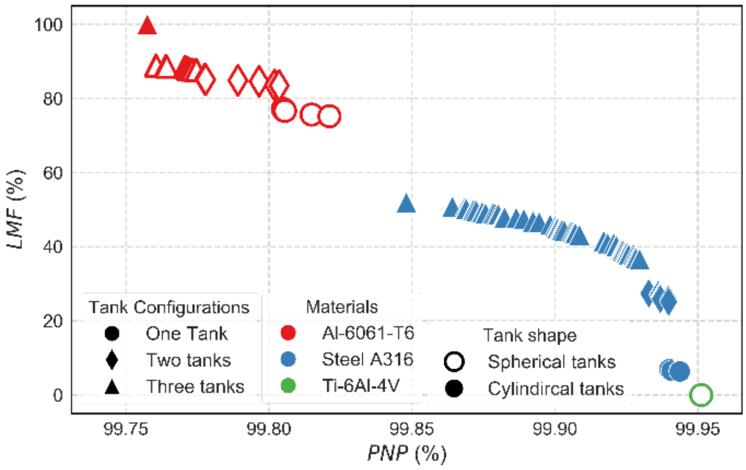

Figure 71: Pareto front for a 2000 kg spacecraft, 10 years mission lifetime, and 3 maximum tanks.

Looking more closely at the solutions obtained, it is first recognisable that there is a separation between the three materials considered. The aluminium solutions are identified by the greatest demisability and lowest survivability, whereas the stainless-steel solutions with higher survivability and lower demisability. Only one titanium alloy solution has been identified and is the one with the greatest survivability. In fact, titanium solutions are always dominated by other solutions in terms of the demisability, given their high temperature resistance. However, among the low demisability solutions, they are more resistant to debris impacts than the stainless-steel equivalents.

Another recognisable trend is the presence in both the aluminium and stainless-steel groups of solutions corresponding to configurations with one, two, and three tanks. As the number of tanks increases, the demisability improves and the survivability deteriorates. However, the reduction of the survivability index because of the increased number of vessels does not prevent these solutions from dominating configurations with a lower number of tanks. From this behaviour, it can be inferred that adopting a design strategy that substitutes physically large components with a higher number of smaller components has a greater impact on the demisability of a configuration with respect to the survivability.

Another evident feature of the Pareto front is the distribution of the spherical tank solutions. All aluminium alloy solutions except for one are spherical, whereas no stainless-steel solution is. The important difference between spherical and cylindrical tanks is their ultimate strength, as spherical solutions have twice the ultimate strength of cylindrical tanks with the same radius and thickness. As the aluminium alloy has a lower ultimate strength than the stainless steel, the shape of the vessel has a considerable impact on the optimisation output, as many cylindrical solutions are unfeasible. However, it is possible to observe that the solution having a 100% LMF index has cylindrical tanks because they guarantee a better demisability even with larger thicknesses. On the other hand, for the stainless-steel case, both the spherical and the cylindrical solutions are sufficiently resistant. Therefore, the optimiser favours cylindrical solutions, as they are more demisable. All the solutions presented in the Pareto front of Figure 71 are viable design solutions. As such, they can all be considered in a preliminary design phase. Then according to the mission requirements and other mission constraints, a more detailed analysis will follow for some of them. For example, the optimiser has identified one fully demisable solution, which consists of three cylindrical aluminium tanks. However, other high demisability solutions may be worth further investigation, because they could be demisable when a more refined analysis is carried out

7.4.3.1 Varying the maximum allowed number of tanks

Varying the number of vessels in which to split the propellant is an effective strategy to improve the demisability (Section 4.1.4.3). A larger number of smaller tanks are in fact more easily demisable than a single very large tank.

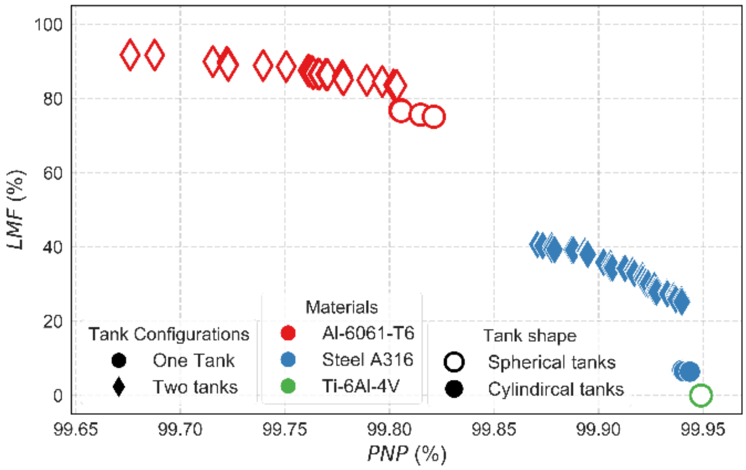

Figure 72: Pareto front for a 2000 kg spacecraft, 10 years mission lifetime, and 2 maximum tanks.

However, increasing the number of components also increases the exposure of the spacecraft to space damaging debris impacts. Figure 72 and Figure 73 represent the Pareto fronts for the same mission profile of Figure 71 with the only difference being the maximum number of tanks allowed by the optimiser. In these cases, this amount was set to two and six respectively. It can be noticed from examining both graphs, that it is the tendency of the optimiser to select solutions with the maximum possible number of tanks. Another observable trend is the increasing ratio between stainless steel and aluminium alloy solutions as the number of tanks allowed increases. As stainless-steel solutions become more demisable, given the possibility of using smaller vessels, they tend to dominate more aluminium solutions thanks to their better performances with respect to the survivability. Another interesting aspect can be observed in Figure 72, where no solution is fully demisable.

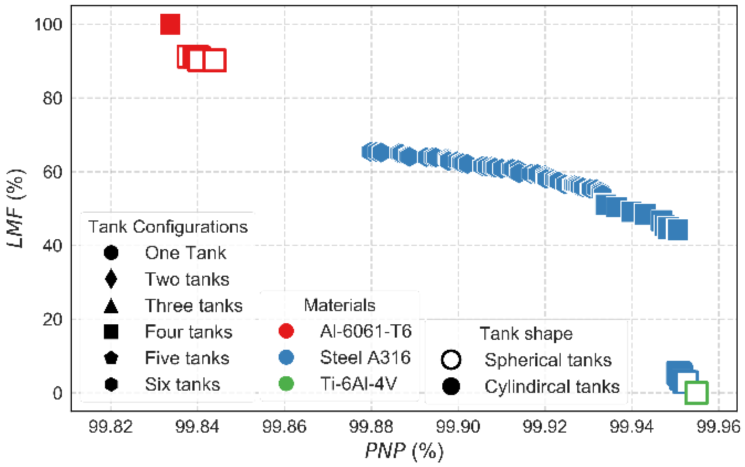

Figure 73: Pareto front for a 2000 kg spacecraft, 10 years mission lifetime, and 6 maximum tanks.

Even the aluminium alloy cases are not completely demisable as the minimum thickness required to be feasible is not small enough to guarantee the demise. This underlines the importance, from a design-for-demise standpoint, of the subdivision of large components into smaller parts. This could lead to a requirement definition for spacecraft tanks, even on medium sized spacecrafts.

7.4.3.2 Varying the mission lifetime

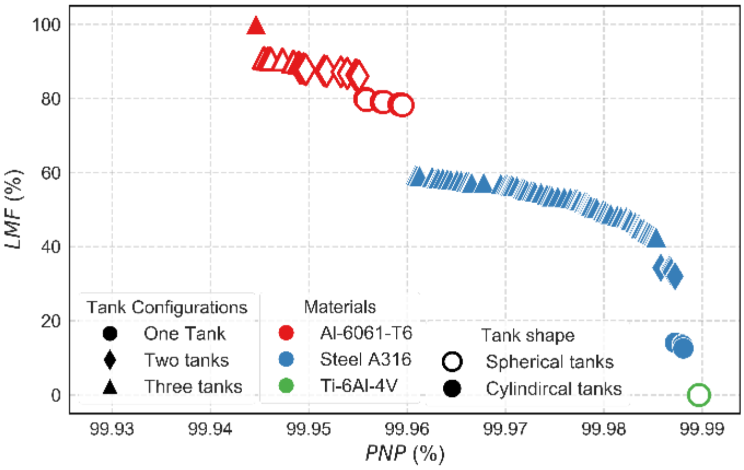

Figure 74: Pareto front for a 2000 kg spacecraft, 3 years mission lifetime, and 3 maximum tanks.

As shown in Figure 74, varying the mission lifetime mainly influences the extent of the *PNP* index range. As expected, lower mission lifetimes generate narrower ranges, and, they reduce the lower limit for the probability of no-penetration. This is an expected yet important behaviour. In fact, it is possible that, for some mission profiles, implementing design-for-demise solutions do not result in a significant deterioration of the survivability of the spacecraft.

7.4.3.3 Varying the mission mass

Another important aspect discriminating the mission typology is the mission mass. In fact, the mission mass can be related to the size of the spacecraft and to the propellant requirements of the mission (thus changing the size of the tanks). Figure 75 and Figure 76 show the Pareto front for the same mission scenario of Figure 71 but for a 1000 kg and a 4000 kg mission respectively. A clear trend is the increase in the number of aluminium alloy solutions as the mass of the mission increases.

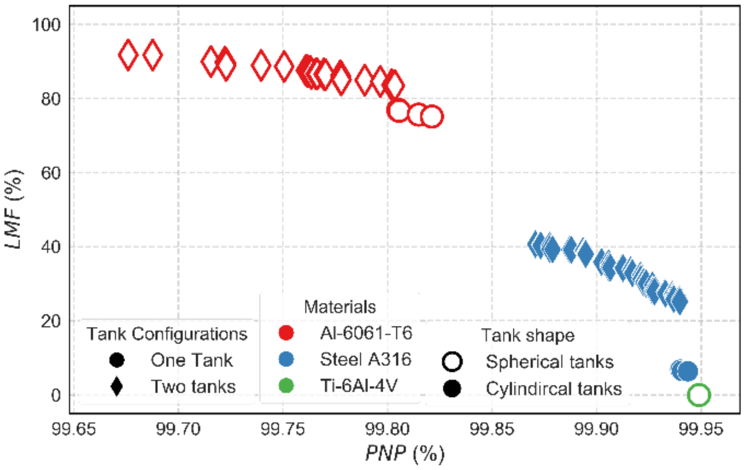

Figure 75: Pareto front for a 1000 kg spacecraft, 10 years mission lifetime, and 3 maximum tanks.

Missions that are more massive require larger tanks; therefore, more aluminium solutions start to dominate stainless steel solutions given their higher demisability. Additionally, the difference in the demisability between the aluminium and the stainless-steel solutions increases as the mass increases, more clearly discriminating between solution with high demisability and with high survivability. This indicates that, when considering tank assemblies, an increasing mass amplifies the dichotomy between demisable and survivable solutions, giving more importance also to other design parameters such as the external shielding of the spacecraft, which is not considered in this study. This is even more important when other types of components are considered in a more complete architecture of the spacecraft.

Another interesting feature derived from Figure 76 is that no solution is fully demisable. Therefore, a 3-tank configuration is not enough for the 4000 kg spacecraft analysed to obtain fully demisable solutions. This highlights how the design-for-demise solutions are coupled not just with the mission scenario but also with the main characteristics of the spacecraft.

In all the provided test cases, it is possible to observe that the influence of the configuration design on the demisability is more significant than for the survivability, so that the PNP index plays a reduced role in the optimisation process with respect to the LMF index. Nonetheless, it is important to point out that the scale of change of the PNP index is different from the LMF index. In fact, a change of just 1% in the value of the PNP index is to be considered significant in terms of the reliability of a mission. In addition, in this example a configuration with only few components has been considered. With more complex configurations, the relative weight of the two indices may considerably change, having the PNP index playing a more relevant role in the optimisation.

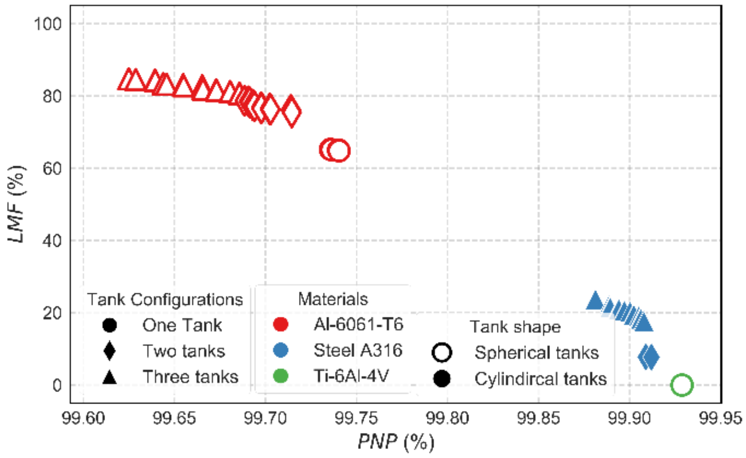

Figure 76: Pareto front for a 4000 kg spacecraft, 10 years mission lifetime, and 3 maximum tanks.

7.5 Extension of the demisability index

Up to this point, the focus of the thesis has been the general understanding of the effects of the implementation of design-for-demise options on the survivability of a spacecraft since the early stages of the mission design. As the focus of this work is the evaluation of the demisability of components and structures, and not the risk on ground related to the re-entry, it was decided to adopt a metric that would reflect only the consequences of the design choices on the actual demisability of components, i.e. the mass loss during the re-entry process. As discussed at length in the previous sections, the prediction capabilities of current destructive re-entry codes have limitations, which do not allow for definite conclusions about the casualty risk computation related to the re-entry of a specific configuration. Consequently, it was decided not to consider the casualty risk as a possible option for the demisability index. In fact, the casualty risk is not able to capture the effects of the design changes in a satisfactory fashion for the purpose of this work. Therefore, it was decided to use a mass-based index definition, which led to the definition of the Liquid Mass Fraction (LMF). Such index has proved to be a suitable choice for effectively discriminate between different design solutions in terms of their demisability level. In addition, the definition of the LMF index is elegant and of simple implementation as it does not rely on any external data for its computations as opposed to the casualty risk, which requires the knowledge of the yearly world population distribution. Nonetheless, we thought that it could be of interest to develop an index that includes also more insight on the re-entry process (not just the residual mass), while maintaining the simplicity of the LMF. These considerations led to an effort directed towards the development of an updated version of the demisability index.

7.5.1 Requirements of the new index

The new index should include two additional pieces of information related to the re-entry of spacecraft configurations: a part relative to the effect on the ground and a part relative to the uncertainty of the demise prediction inherent with the use of destructive re-entry codes. For the first part, the casualty risk contribution has been neglected again. Instead, a term related to the casualty area of the surviving components has been introduced. In fact, the casualty area contribution retains information on the effects of the re-entry on the ground without relying on external data. For the second part, a method to give an estimate of the uncertainty of the demisability prediction is to compute the demise altitude of the component. As the demise computation of all destructive re-entry, codes do not have a 100% confidence level, it interesting to introduce a parameter that can carry some information on the *quality* of the prediction. Because the aim of this study is to maintain the simplicity of the index, it was decided to use the demisability altitude to account for such uncertainties. In fact, in case the demise of a component happens in at high altitude we can be confident about the demise prediction. On the other hand, if the predicted demise altitude is low, the confidence level of the prediction can be considered lower (R.Tech, 2015, Beck et al., 2015a).

In the following section, the details of the procedure and thought process followed for the development of the new index will be described and discussed. Several options for the new index structure will be considered and their quality evaluated. A final structure for the index will be selected and its behaviour when applied to different classes of missions will be studied and discussed. Finally, a comparison between the new formulation and the LMF index will be performed using as test ground the tank optimisation of Section 7.4.

7.5.2 A new formulation of the demisability index

This paragraph focuses on the different contributions to the index and in which way they can be combined into a single score. In addition, a set of desirable characteristics for the index will be specified, and which are the criteria used for the evaluation of the *quality* of a specific index formulation.

The general structure of the new index can be formulated in the following way:

$$I_D = A \cdot f_1\left(\frac{m_{fin}}{m_{in}}\right)^{\alpha} \circ B \cdot f_2\left(\frac{h_d}{h_{in}}\right)^{\beta} \circ C \cdot f_3\left(\frac{A_c}{A_{c,ref}}\right)^{\gamma} \tag{7.25}$$

where f_1 identifies the contribution related to the relative mass loss of the components, f_2 the contribution related to the demise altitude, and f_3 the one related to the casualty area. In addition, it is also necessary to consider that the different contributions can be combined together with different weights, which are represented in Eq. (7.25) by the multiplicative coefficients *A*, *B*, and *C*, and by the exponents α, β, and γ. The symbol ○ represents a generic operator. In general, finding the optimal combination of the three functions and of the three coefficients is a very complex problem. It was thus decided to define a set of expressions for the index, which involve different versions of the functions f_1, f_2, and f_3, and different combinations between the functions themselves and the coefficients. In general, the new expression of the index should not have singularities and should capture as well as possible the variability in the demisability of several spacecraft configurations, avoiding ambiguity between them, even if only small changes in the configurations are present. Moreover, we decided to have an index that, just like the Liquid Mass Fraction (LMF) used up until now, increases with increasing demisability.

7.5.2.1 Proposed index formulations

We propose four different expressions for the new index formulation.

$$I_D = \exp\left\{\alpha \cdot \left(1 - \sum_{j=1}^{N_c} \frac{m_{fin}^j}{m_{in}^j}\right) + \beta \cdot \left(\sum_{j=1}^{N_c} \frac{h_d^j}{h_{in}^j}\right) - \gamma \cdot \left(\sum_{j=1}^{N_c} \frac{A_c^j}{A_c^{ref}}\right)\right\} \tag{7.26}$$

$$I_D = \frac{\left(1+\sum_{j=1}^{N_c}\frac{h_{d,j}}{h_{in,j}}\right)^{\beta}}{\left(1+\sum_{j=1}^{N_c}\frac{m_{fin,j}}{m_{in,j}}\right)^{\alpha}\cdot\left(1+\sum_{j=1}^{N_c}\frac{A_{c,j}}{A_{c,ref}}\right)^{\gamma}} \tag{7.27}$$

$$I_D = \left(1-\sum_{j=1}^{N_c}\frac{m_{fin,j}}{m_{in,j}}\right)^{\alpha}\cdot\left(\sum_{j=1}^{N_c}\frac{h_{d,j}}{h_{in,j}}\right)^{\beta}\cdot\left(1-\sum_{j=1}^{N_c}\frac{A_{c,j}}{A_{c,\max}}\right)^{\gamma} \tag{7.28}$$

$$I_D = \alpha\cdot\left(1-\sum_{j=1}^{N_c}\frac{m_{fin,j}}{m_{in,j}}\right)+\beta\cdot\left(\sum_{j=1}^{N_c}\frac{h_{d,j}}{h_{in,j}}\right)+\gamma\cdot\left(1-\sum_{j=1}^{N_c}\frac{A_{c,j}}{A_{c,\max}}\right) \tag{7.29}$$

In Eq. (7.26), the functions f_1, f_2, and f_3 are exponential functions, which can then be combined into a single exponential whose arguments depends on the coefficients and on the three contributions previously introduced. As the demisability of a configuration increases the final mass of the components and the overall casualty area decrease, whereas the demise altitude increases. The different contributions are arranged in the index formulation so that the value if I_D increases with increasing demisability as it was previously discussed. In the mass contribution and in the demise altitude contribution the normalisation is performed using the initial values of the respective term that is the initial mass of each components and their release altitude. For the casualty area term, the normalisation is instead obtained using a reference value of the casualty area (this is also used in the second option of Eq. (7.27)). Such a reference value is assumed to be 8 m^2. This value is used in NASA DAS (National Astronautics and Space Administration, 2015, Lips and Fritsche, 2005) as a warning limit over which, usually, the value of the casualty risk will probably exceed the 10^{-4} limit.

The procedure behind the remaining three indices presented is analogous but with different combinations of the functions f_1, f_2, and f_3, with the use of different operators, and different weightings between the three terms using the coefficients. In addition, for Eqs. (7.28) and (7.29), the reference value of the casualty area is the maximum possible value of the casualty area considering all the possible combinations of configurations. The other main difference between the four formulations resides in the lower and upper limits that the indices can reach. The worst demisability corresponds to all the components surviving intact and landing on ground, whereas the best demisability corresponds to all the components demising at the highest altitude possible. For Eq. (7.26), this translates into f_1 and f_2 tending to 0 and f_3 tending to $A_{c,tot}/A_{c,ref}$ for the worst demisability case so that we have a lower bound of $\exp(-\gamma\cdot A_{c,tot}/A_{c,ref})$. On the other hand, when the demisability is highest, f_1 and f_2 tend to 1, and f_3 tends to 0, for an upper bound given by $\exp(\alpha+\beta)$. In the same way, for Eq. (7.27), the lower and upper bounds are given respectively by $2^{-\alpha}\cdot(1+A_{c,tot}/A_{c,ref})^{-\gamma}$ and 2^{β}. The expression of Eq. (7.28) is instead bounded between 0 and 1. Finally, Eq. (7.29) has a lower bound equal to 0 and an upper bound equal to $(\alpha+\beta+\gamma)$. Consequently, the presented formulations follow the guidelines previously described; moreover, they maintain a good level of simplicity and an elegant structure to the index, which is as easy to evaluate as the initial index defined by the Liquid Mass Fraction. The *simplicity* of the index formulation is considered a relevant aspect as the index is going to be used as a tool to assess the outcome of a re-entry simulation into a single score, which can then be used in immediate comparisons of different configurations, whether is in an optimisation context or in a preliminary mission design situation. In general, for each of the terms involved, the overall contribution of all the components in the configuration is considered (by summing over all the components) and the term is normalised with respect to a correspondent value computed before the demise process.

7.5.2.2 Ranking the index formulations

However, it is not known a priori which one of these expressions is the most appropriate to describe the variation of the demisability of a spacecraft from a numerical point of view. In addition, all these expressions depend on the weighting factors α, β, and γ. Consequently, it is necessary to introduce some metrics that allow the evaluation of the *quality* of each of the formulations with varying coefficients, and a procedure must be devised in order to measure such *quality*. The effectiveness of the demisability of a specific spacecraft configuration can be measured in terms of the final mass reaching the ground (which measures the actual increase in the demisability of a component), the demise altitude of the fragments (which reflects the amount of uncertainty related to the demisability of a component), and the casualty area (which is related to the effects of the re-entry process). As the index can reflect all these contributions and as the importance of these contributions can be changed using the weighting factors, it seemed natural to consider three different evaluation functions. The three evaluation functions have been selected so that they give information on the monotonicity of the index with respect to the three main contributions considered, i.e. the residual mass, the demise altitude and, and the casualty area. For example, let us consider the residual mass contribution; in this case, it is desirable that the index increases as the residual mass decreases. If this correspondence is perfect, it results in a reverse monotonic relation between the index and the residual mass. Consequently, for each of the formulations considered, there will be combinations of the three coefficients α, β, and γ that improve the monotonicity of the index with respect to the residual mass. The same line of reasoning can be followed for the other two main parts of the index, which are the demise altitude and the casualty area. In this way, for each of the index formulations of Eqs. (7.26)-(7.29), their fitness can be evaluated as a function of the three weighting coefficients. The monotonicity of the index is evaluated using the Spearman's rank, which is defined as

$$\rho_s = 1 - \frac{6 \cdot \sum_i D_i^2}{N \cdot \left(N^2 - 1\right)} \tag{7.30}$$

where, $D_i = r_i - s_i$ is the difference between the ranks, being r_i and s_i the ranks of the first and second variable for the *i*-th observation respectively, and N is the total number of observations. For the case in exam, the second variable is always the value of the index, whereas the first variables are the values of the residual mass, the demise altitude, and the casualty area respectively. Therefore, there are three evaluations functions, namely ρ_m, ρ_{Ac}, and ρ_{hd}, which return the *quality* of the demisability index with respect to the residual mass, the casualty area, and the demise altitude as a function of three different coefficients. The expressions for the three evaluations functions are as follows:

$$\rho_m = 1 - \frac{6 \cdot \sum_i \left(r_i \left(m_{fin} \right) - s_i \left(I_D \right) \right)^2}{N \cdot \left(N^2 - 1 \right)} \tag{7.31}$$

$$\rho_{h_d} = 1 - \frac{6 \cdot \sum_i \left(r_i \left(\bar{h}_d \right) - s_i \left(I_D \right) \right)^2}{N \cdot \left(N^2 - 1 \right)} \tag{7.32}$$

$$\rho_m = 1 - \frac{6 \cdot \sum_i \left(r_i \left(A_{c,tot} \right) - s_i \left(I_D \right) \right)^2}{N \cdot \left(N^2 - 1 \right)} \tag{7.33}$$

where $r_i\,(m_{fin})$ is the rank of the *i*-th observation related to the overall final mass, $r_i\,(\overline{h_d})$ is the rank of the *i*-th observation relative to the average demise altitude of the fragments, and $r_i\,(A_{c,tot})$ is the rank of the *i*-th observation relative to the total casualty area. $s_i\,(I_D)$ is the rank if the *i*-th observation relative to the demisability index. All the Spearman's rank values lie between -1 and 1. A value of -1 correspond to a reverse monotonic relation and a value of 1 to a direct monotonic relation. If the rank is 0, there is no monotonic relations between the two datasets. For the case in exam, ρ_m has a reverse monotonic relation, as well as ρ_{Ac}. Instead, ρ_{hd} has a direct monotonic relation.

These three evaluation functions are used to compare different configuration options for a specific mission scenario. In fact, it is interesting to qualify the different indices expressions for how well they can discriminate between the demisability of different design options for a specific mission as a function of the weighting factors introduced to balance the three main terms of the index formulation.

7.5.3 Selecting the new demisability index expression

At this point, it is important to specify how to actually compare the *quality* of the different formulations of the index introduced in Section 7.5.2, and how to use the evaluation functions defined through the Spearman's rank. In order to perform such evaluation, it is necessary to have a set of *observations* for which the monotonicity is then evaluated. To obtain these observations, we consider a baseline mission scenario in which we specify the re-entry condition of a spacecraft (Table 34).

Table 34: Initial conditions for the generation of the observation’s samples.

Parameter	**Value**
Altitude	120 km
Flight path angle	0 deg
Velocity	7.3 km/s
Longitude	0 deg
Latitude	0 deg
Heading	90 deg
Break-up altitude	78 km

In addition, a set of randomised spacecraft configurations is generated: starting from a general outline of a spacecraft (Table 35), the framework described in Section 7.3 is used to generate a set of feasible yet random configurations. For this specific case, 1000 samples have been generated.

Table 35: Outline of the spacecraft configuration used to generate the random samples.

Id	**Name**	**Parent**	**Shape**	**Material**	**Mass**	**Length**	**Radius**	**Width**	**Height**	**ts**
0	Parent	0	Box	al-6061-T6	0	3	0	2	2	0.003
1	SolarPanel	0	FlatPlate	al-generic	57	7	0	2	0	0
2	RW	0	Cylinder	al-6061-T6	0	0.06	0.15	0	0	0.03
3	Tank	0	Cylinder	ss-AISI316	0	0.6	0.3	0	0	0.005
4	BattBox	0	Box	al-6061-T6	0	0.6	0	0.4	0.4	0.003
5	Batt	4	Cylinder	al-6061-T6	0	0.2	0.05	0	0	0.001
6	Thrst	0	Cylinder	Inconel-625	0.3	0.17	0.015	0	0	0
7	MgnTrq	0	Cylinder	ss-generic	4	0.578	0.022	0	0	0

The spacecraft in exam is a reference 2000 kg spacecraft with the following characteristics:

Table 36: Spacecraft characteristics for the generation of the random samples.

Spacecraft design characteristics	
Propellant mass	167 kg
Required angular momentum	60 Nms
Power	1400 W
Eclipse time	35 minutes
Maximum number of tank vessels	4

This information is used to properly size the different components of the spacecraft that are considered in the presented analysis. Using the configuration of Table 35 and specifying the variables to be changed, together with their boundaries, it is possible to obtain a set of randomised yet feasible spacecraft configurations. Appendix E contains a more detailed description of the sizing procedure adopted for each component considered.

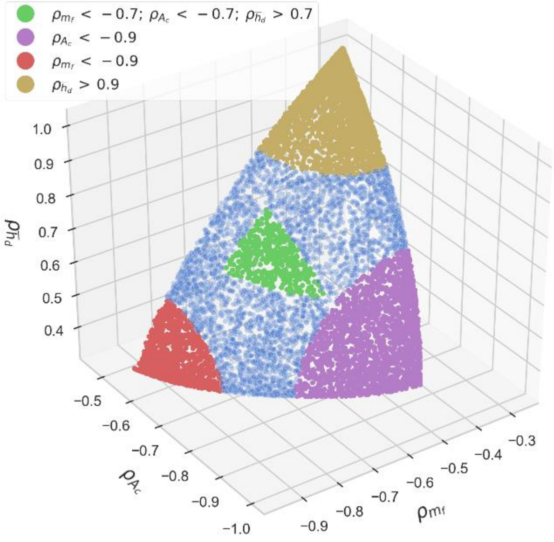

Figure 77: Pareto front for index of Eq. (7.26).

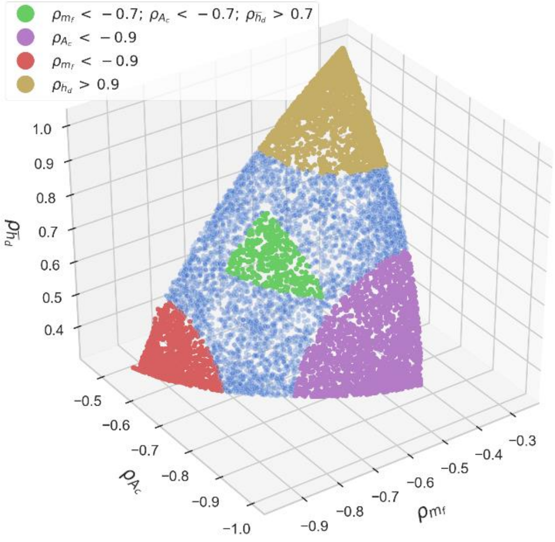

Figure 78: Pareto front for index of Eq. (7.27).

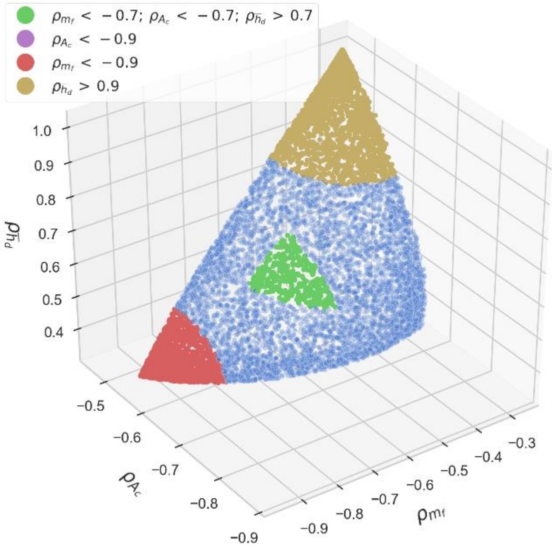

Figure 79: Pareto front for index of Eq. (7.28).

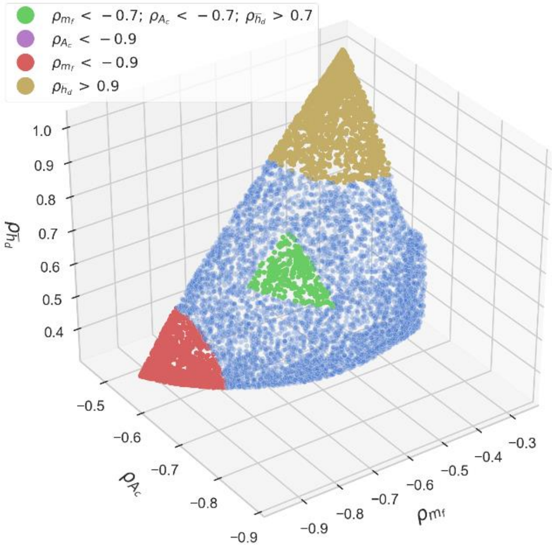

Figure 80: Pareto front for index of Eq. (7.29).

Once the samples are generated, they are used together with the initial re-entry conditions to perform a set of 1000 re-entry simulations. For each simulation, the relevant data for the index computation are stored. At this point, a multi-objective optimisation is performed in order to find the optimal combinations of the coefficients α, β, and γ. A single value of the re-entry conditions was used, but many different configurations because the true aim of the index, for the way it is defined, is to compare many possible configurations for the same mission scenario. This ultimately means that, in a simplified scenario, it is possible to consider a single re-entry conditions if the variability of the index with respect to the configurations is to be studied.

The input to the optimisation is the result of the re-entry simulations; the evaluation functions are the previously defined Spearman's ranks. Using again a genetic algorithm, a Pareto front of coefficients is obtained. In the optimisation, a population of 400 individuals and 150 generations were used; moreover, a crossover probability of 0.95 and a mutation probability of 0.05 were used. The boundaries of the search space for the three coefficients α, β, and γ are 0 for the lower bound and 10 for the upper bound. The variation of the coefficients produces different levels of monotonicity of the index with respect to the residual mass, the demise altitude, and the casualty area of the configuration for each one of the formulations considered. The index, in fact, can be tuned using α, β, and γ to more closely follow one of the desired terms, or to find the best compromise between two of the terms, or even all three of them. In the end, according to the values obtained for the evaluation functions for each one of the formulations, and considering the shape of the Pareto front, it is possible to evaluate the different expressions proposed and to select the one that is considered the most effective for our purposes.

The Pareto fronts of Figure 77 to Figure 80 show the behaviour in terms of the three fitness functions for the four proposed variations of the demisability index. Some areas of the Pareto fronts are highlighted with different colours in order to indicate the coefficients corresponding to specific values of the fitness functions. The red solutions have a value of the mass Spearman's rank (ρ_m) below -0.9 (almost fully inversely monotonic). In the same way, purple points have a ρ_{Ac} lower than -0.9, and bronze points have ρ_{hd} values greater than 0.9. The green areas instead show the region with the best compromise between the three fitness functions, i.e. where all the Spearman ranks of the solutions are better than 70% of the best possible value (-0.7 for both ρ_m and $\rho_{Ac},$ and 0.7 for ρ_{hd}). The first observation that can be drawn is that both the formulations of Eqs. (7.28) and (7.29), are not able to provide solutions with a casualty area related Spearman's rank better than -0.9. Consequently, these two cases are considered worse than the other two expressions (Eqs. (7.26) and (7.27)). These latter formulations have almost identical Pareto fronts. Table 37 shows the main characteristics of the four Pareto fronts that are the maximum, minimum, and average values of the fitness functions for each one of the fitness functions considered. From the summary table is clearer that the last two expressions cannot provide the same *quality* for the solution with respect to the casualty risk fitness function. The first two options instead have almost identical results. In light of these results, it was decided to proceed with a more in depth analysis only for the index formulation of Eq. (7.26).

Table 37: Summary of the Pareto front characteristics for the four index expressions considered.

Index	**Max ρ_m**	**Min ρ_m**	**Avg ρ_m**	**Max ρ_{Ac}**	**Min ρ_{Ac}**	**Avg ρ_{Ac}**	**Max ρ_{hd}**	**Min ρ_{hd}**	**Avg ρ_{hd}**
Eq.(7.26)	-0.2696	-0.9580	-0.6431	-0.4615	-1.0000	-0.7458	0.9999	0.3476	0.7263
Eq.(7.27)	-0.2696	-0.9580	-0.6449	-0.4623	-1.0000	-0.7420	0.9999	0.3463	0.7194
Eq.(7.28)	-0.2698	-0.9580	-0.6565	-0.4617	-0.8807	-0.6907	0.9999	0.3464	0.7288
Eq.(7.29)	-0.2703	-0.9580	-0.6349	-0.4618	-0.8816	-0.6841	0.9999	0.3464	0.7538

7.5.4 Analysis of the behaviour of the new demisability index with the spacecraft class

At this point, a final version of the new index is selected. It is now interesting to perform a more refined analysis on the possible coefficients' combinations relative to the demisability index, which generate different behaviours in evaluate the level of demisability of a configuration, according to the different weight assigned to the three parts of the index. Specifically, it is interesting to verify if the selection of different coefficients α, β, and γ can be related to the objective functions (ρ_m, ρ_{Ac}, ρ_{hd}) in a way that can also be related to specific spacecraft characteristics. It is interesting to investigate how the coefficients changes when the mass of the spacecraft changes, being the total mass of the spacecraft one of the most important drivers in predicting the amount of mass reaching the ground after re-entry. In order to check this behaviour, the procedure described in Section 7.5.3 is repeated for different spacecraft classes: 500 kg, 1000 kg, 1500 kg, 2000 kg, 2500 kg, 3000 kg, 3500 kg, 4000 kg, 5000 kg, and 6000 kg. For each spacecraft class, a set of 1000 random configurations are generated: each component design is scaled with the spacecraft mass according to preliminary design relations (Appendix E). Alongside the multiple spacecraft classes, it was decided to consider three different initial conditions, which are summarised in Table 38.

Table 38: Initial conditions characteristics used in the demisability index study.

Parameter	Orbit Equatorial	Orbit Communication	Orbit Sun-synchronous
Altitude	120 km	120 km	120 km
Flight path angle	0 deg	0 deg	0 deg
Velocity	7.3 km/s	7.6 km/s	7.8 km/s
Longitude	0 deg	0 deg	0 deg
Latitude	0 deg	0 deg	0 deg
Heading	90 deg	45 deg	-8 deg
Break-up altitude	78 km	78 km	78 km

These additional orbits have been considered in order to consider the variations introduced in the demisability of a configuration due to the varying initial conditions of the re-entry. For each class, a set of 1000 simulations have been performed for each of the three initial conditions provided, resulting in a total of 3000 re-entry simulations per class. The output data from these simulations is then used as the input to the multi-objective optimisation related to the weighting coefficients. A set of Pareto front, one for each spacecraft class, has then been generated and is presented in Figure 81 to Figure 86. Each point in the Pareto fronts corresponds to a different index expression with different values of the coefficients α, β, and γ. The Pareto fronts shows that varying the coefficients, the three fitness functions show a competing behaviour and that it is not possible to obtain at the same time a high monotonicity of the index with respect to all the three terms considered. It is thus not possible, with the formulations considered, to have an index that can perfectly capture the mass loss, the surviving casualty area, and the demise altitude variations of spacecraft configurations.

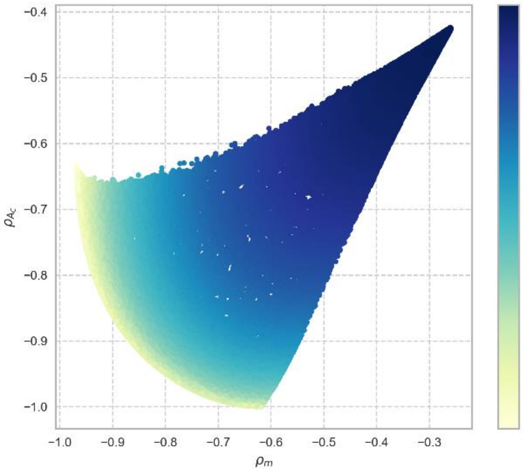

Figure 81: Pareto front for a 1000 kg spacecraft.

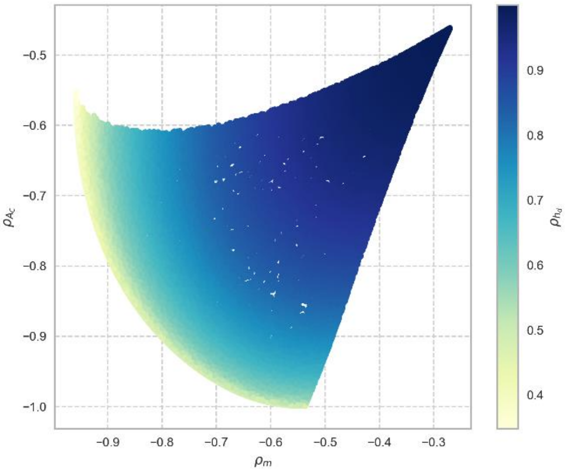

Figure 82: Pareto front for a 2000 kg spacecraft.

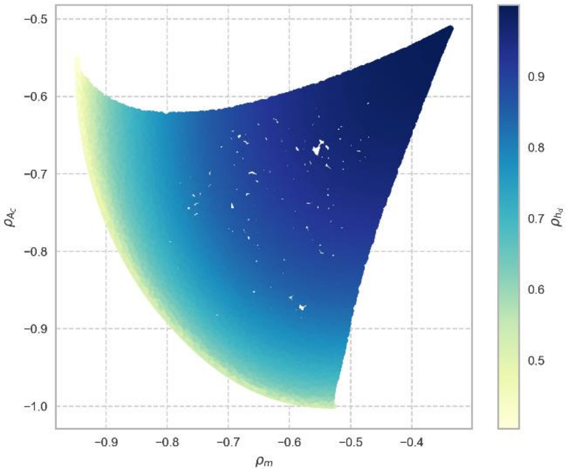

Figure 83: Pareto front for a 3000 kg spacecraft.

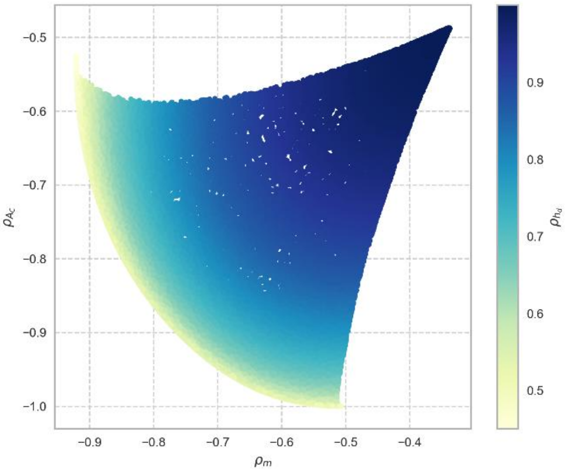

Figure 84: Pareto front for a 4000 kg spacecraft.

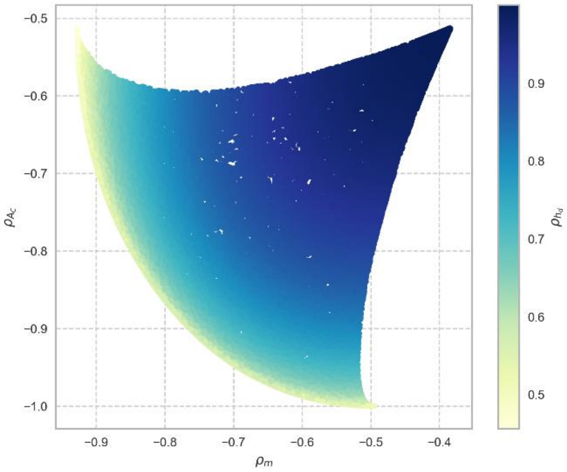

Figure 85: Pareto front for a 5000 kg spacecraft.

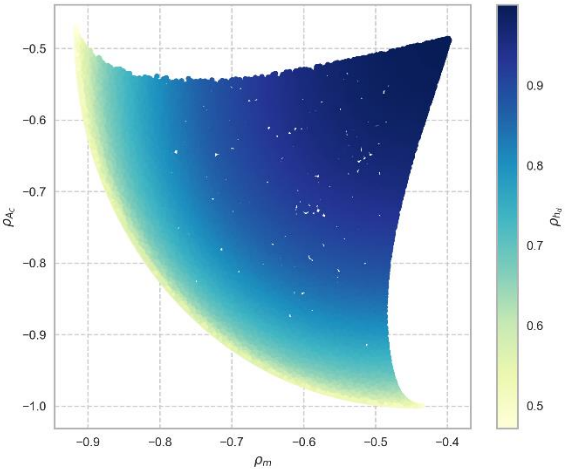

Figure 86: Pareto front for a 6000 kg spacecraft.

However, it is possible to tune the coefficients α, β, and γ to better focus on one or two of these contributions according to the desired outcome. From Figure 81 to Figure 86, it is possible to observe that the Pareto fronts have all a similar shape; however, they also tend to get wider as the spacecraft mass increases. In addition, the curved line delimiting the fronts on the left tends to move towards the right as the mass increases. This behaviour translates into a worsening of the best possible combination between ρ_m and ρ_{Ac}. In fact, for example for a 1000 kg spacecraft, best value of ρ_{Ac} corresponding to a value of ρ_m of -0.9 is about -0.85. This same value lowers to about -0.73 for a 6000 kg spacecraft configuration. Nonetheless, given the similarities between the Pareto fronts and the presence of a regular behaviour with the spacecraft mass, it is interesting to further search for a trend in the selection of the coefficients α, β, and γ as a function of the desired combination of fitness functions (ρ_m, ρ_{Ac}, ρ_{hd}) and spacecraft mass.

As during the optimisation no constraint were imposed on the coefficient selection except from the boundaries themselves, it is possible that not all the obtained solutions in the Pareto fronts are good enough. In fact, despite the combination of the coefficients provide a viable value of the fitness functions; we are also concerned with the capabilities of the resulting index expression to sufficiently discriminate between different solutions. In other terms, it is also requested to the index to provide a wide spectrum of values when computed for a large variety of spacecraft configurations. To check these characteristics, the value of the index for each of the coefficients in the Pareto fronts has been computed for each one of the random configurations used as inputs to the optimisation. In this way, for each one of the index expressions (corresponding to a point in the Pareto front) we have the value of the index for each of the 3000 random configurations generated. This set of values is then normalised. Finally, the difference between the maximum and the minimum value of the obtained distribution is computed. Such value is comprised between 0 and 1 and measures how the indices values are distributed when computed for a very diversified population of spacecraft configuration. A value of the metric close to 1 refers to a more spread distribution of the index values, while a value close to 0 refers to a distribution where all the values are concentrated into a narrow interval. We refer to this metric as to a *dispersion coefficient*. Consequently, it was decided to prune the original population obtained through the optimisation by using this metric. Specifically, all the combinations of coefficients leading to indices expressions with a dispersion coefficient below 0.95 were discarded. The resulting Pareto fronts for some of the spacecraft classes are shown in Figure 87 to Figure 92. The new Pareto fronts are similar to the initial ones; however, as expected, there are less dense of points and some parts are now missing. Specifically, all the fronts except the one related to 6000 kg spacecraft (Figure 92) have lost their bottom parts.

At this point, it is also interesting to analyse the possible relations between the triplets of coefficients α, β, and γ and the three fitness functions ρ_m, ρ_{Ac}, ρ_{hd}. Figure 93, Figure 94, and Figure 95 show the variation of the three fitness functions for a 2000 kg spacecraft as a function of the coefficients. The x-axis refers to the value of α, the y-axis to the ratio between β and α and the z-axis to the ratio between γ and α.

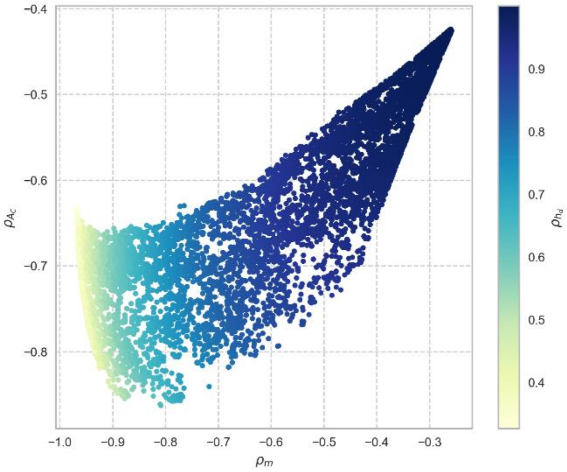

Figure 87: Pruned Pareto front for 1000 kg spacecraft.

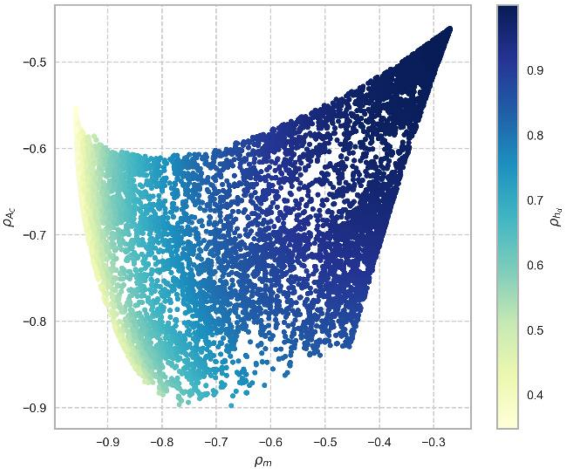

Figure 88: Pruned Pareto front for 2000 kg spacecraft.

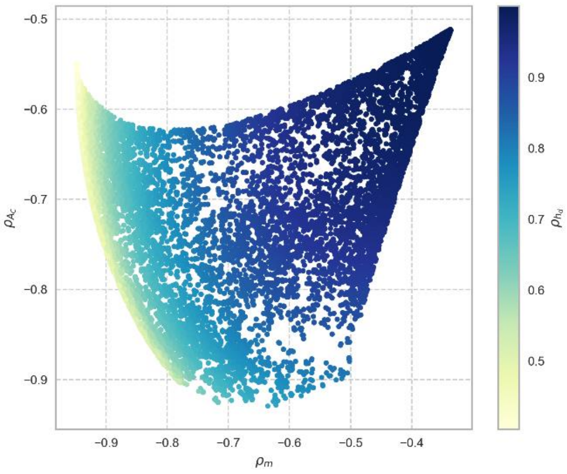

Figure 89: Pruned Pareto front for 3000 kg spacecraft.

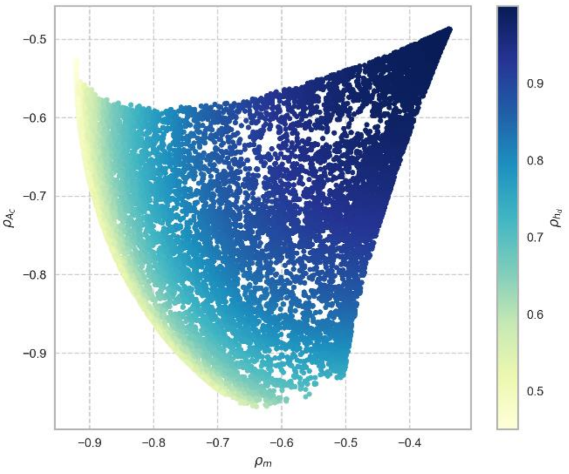

Figure 90: Pruned Pareto front for 4000 kg spacecraft.

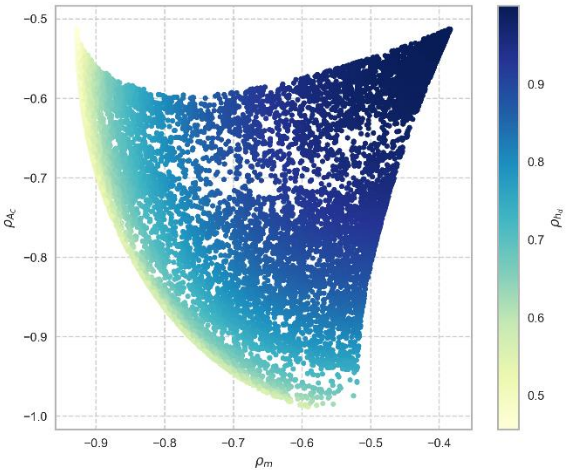

Figure 91: Pruned Pareto front for 5000 kg spacecraft.

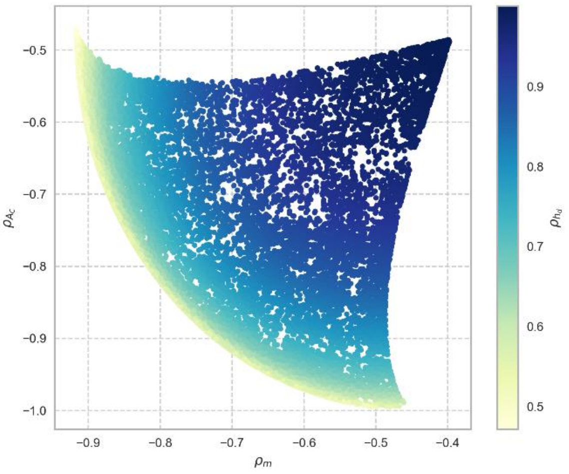

Figure 92: Pruned Pareto front for 6000 kg spacecraft.

The colour-map refers to the variation of the fitness functions. For the case of ρ_m, ρ_{Ac} the closer to -1 the better, whereas for ρ_{hd} the closer to 1 the better. It is possible to observe that trends are recognisable in the plots, which link the selection of the coefficients to the value of the fitness functions obtained by a specific formulation of the index. The same trends are present also in Figure 96, Figure 97, and Figure 98, which refer to a 4000 kg spacecraft. Therefore, it is natural to ask ourselves if it is possible to extrapolate some trends, not just between the coefficients and the evaluation functions for a single spacecraft class, but also among the different classes. Ultimately, it is of interest to investigate if the variation of the spacecraft class has an influence in the selection of the weighting coefficients that is if the three terms of the index must be weighted differently as the spacecraft mass changes.

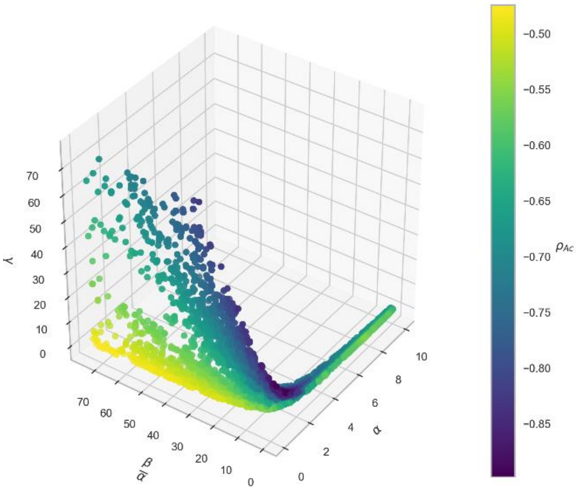

Figure 93: Variation of ρ_{Ac} with α, β, and γ for a 2000 kg spacecraft.

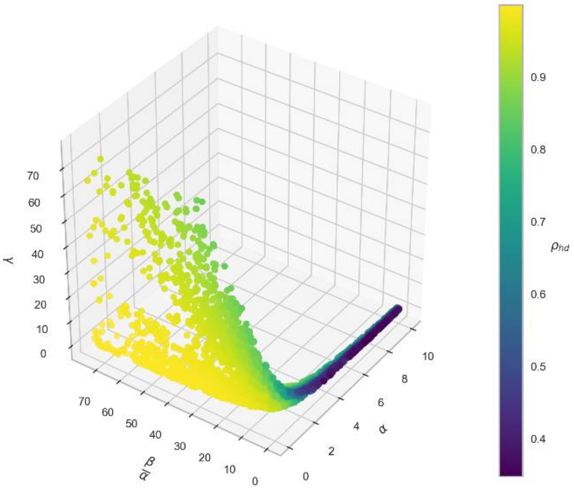

Figure 94: Variation of ρ_{hd} with α, β, and γ for a 2000 kg spacecraft.

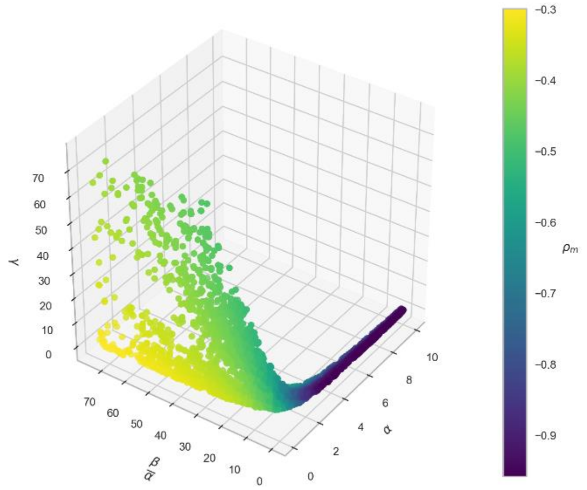

Figure 95: Variation of ρ_m with α, β, and γ for a 2000 kg spacecraft.

In order to search for this trend, it was first necessary to simplify the Pareto fronts. Therefore, a grid was built, subdividing the ranges of the evaluation functions (from -1 to 1) into steps of 0.025. The result is a 3D grid with cubes of 0.025 side length. To simplify the entire set of scattered points, an average of the values of the coefficients α, β, and γ for each one of the grid parts. In this way, to each one of the triples of values in the Pareto front (ρ_m, ρ_{Ac}, ρ_{hd}), are associated average values of the coefficients α, β, and γ. This procedure is repeated for each one of the spacecraft classes considered.

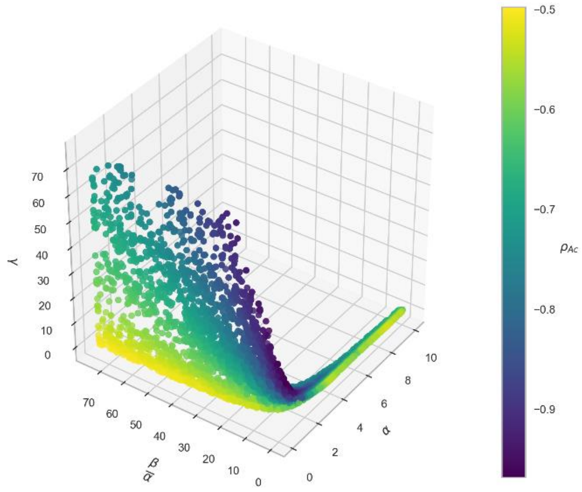

Figure 96: Variation of ρ_{Ac} with α, β, and γ for a 2000 kg spacecraft.

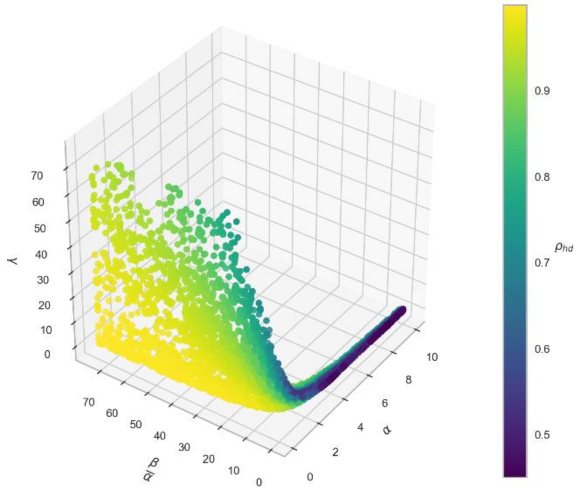

Figure 97: Variation of ρ_{hd} with α, β, and γ for a 2000 kg spacecraft.

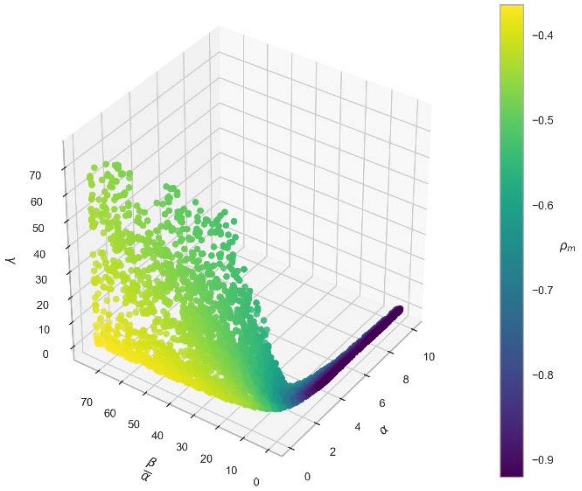

Figure 98: Variation of ρ_m with α, β, and γ for a 2000 kg spacecraft.

At this point, using the obtained sets of averaged coefficients, a linear regression analysis is performed using the spacecraft mass as the independent value. The linear regression analysis has been performed through a least-square methodology using the built-in *python* function *polyfit*, available in the *numpy* library. The linear regression analysis is performed for each one of the cells of the grid that was previously described: the averaged values of the coefficients α, β, and γ for each corresponding grid cell of different spacecraft classes are used in the linear regression analysis. From each linear regression analysis, the values of the intercept, the slope, and the residuals are obtained. The results are a set of maps giving the characteristics of the linear interpolation as a function of the coefficients α, β, and γ and the evaluation functions (Figure 99 to Figure 104).

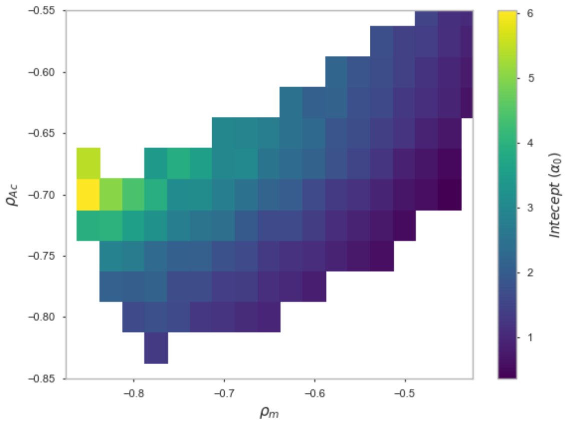

Figure 99: Linear regression intercepts for the coefficient α.

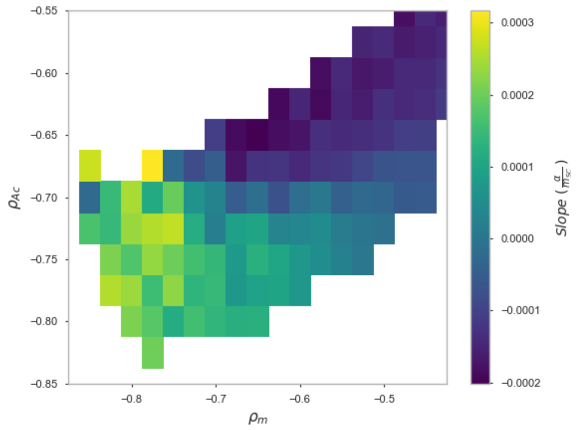

Figure 100: Linear regression slopes for the coefficient α.

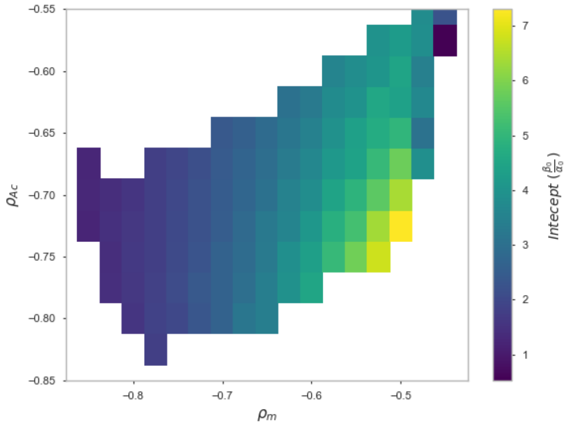

Figure 101: Linear regression intercepts for the ratio β/α.

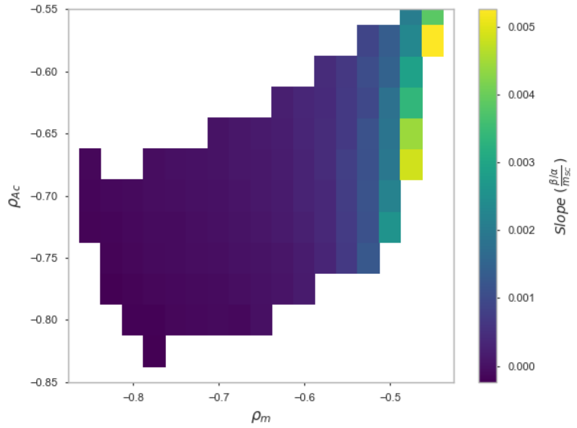

Figure 102: Linear regression slopes for the ratio β/α.

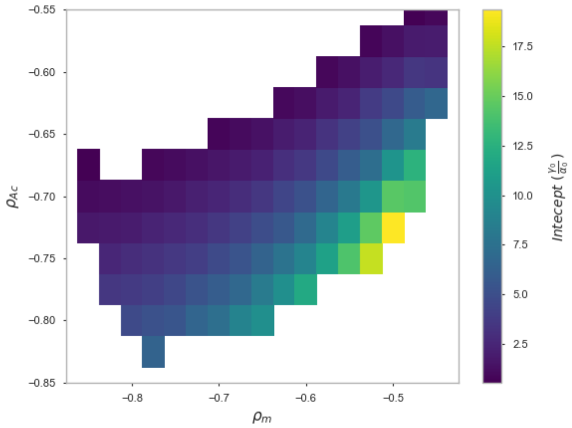

Figure 103: Linear regression intercepts for the ratio γ/α.

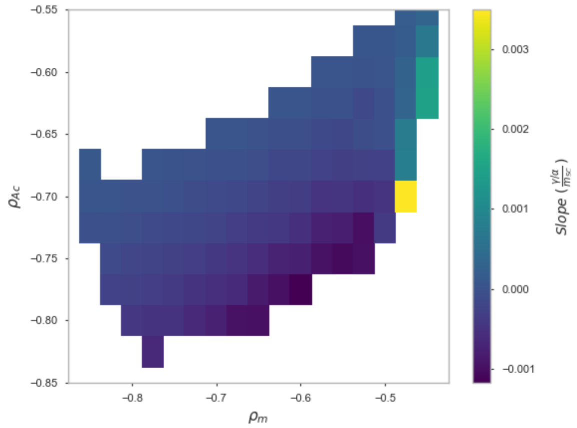

Figure 104: Linear regression slopes for the ratio γ/α.

The figures show the variation of the intercepts and the slopes for the coefficient α (Figure 99 and Figure 100), and for the ratio between β and α (Figure 101 and Figure 102), and the ratio between γ

and α (Figure 103 and Figure 104). The maps are only represented as a function of ρ_m and ρ_{Ac} as there is a one to one correspondence between the couple ρ_m, ρ_{Ac} and the value of ρ_{hd}. From the linear regression analysis, it is possible to notice some clear trends in the values of the intercept for α (Figure 99), β/α (Figure 101), and γ/α (Figure 103). Only some discrepancies are present at the boarder of the Pareto front. A similar regular behaviour is observable for the slopes of the ratios β/α (Figure 100) and γ/α (Figure 102). In the case of the slope associated to the coefficient α (Figure 104), a trend is still recognisable but is less clear and less smooth with respect to the other two. However, it is also possible to notice that the value of the slopes for the coefficient α is one order of magnitude lower than the slopes of the ratios β/α and γ/α. It is also necessary to look at the quality of the linear regression analysis performed; to do so it is interesting to look at the residual obtained.

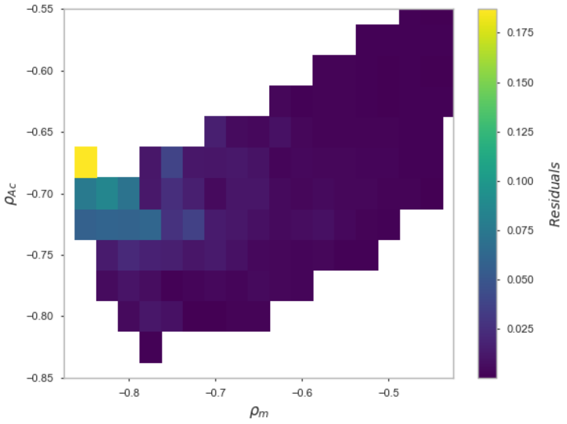

Figure 105: Linear regression residuals for the coefficient α.

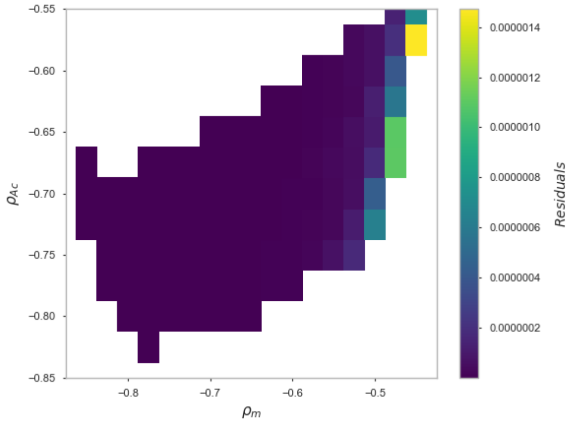

Figure 106: Linear regression residuals for the ratio β/α.

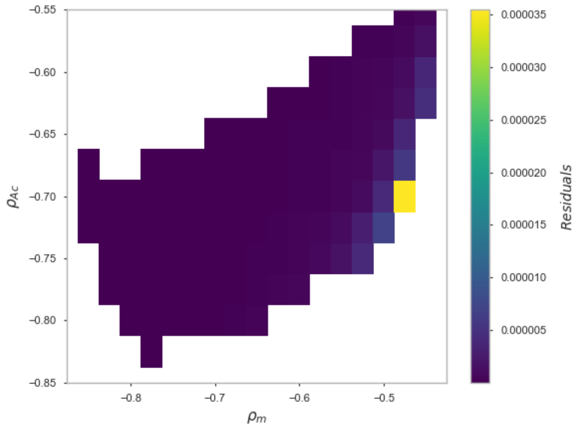

Figure 107: Linear regression residuals for the ratio γ/α.

The residuals shown here represent the sum of the residuals for each value in the datasets. It is possible to observe from Figure 106 and Figure 107 that the residuals for the ratios β/α and γ/α are very small, indicating a very good prediction for the linear behaviour of the aforementioned ratios with the spacecraft mass. When considering only the coefficient α, the values of the residuals are higher, indicating a less optimal linear relation between the coefficient and the spacecraft mass.

Nonetheless, for most of the linear regression analysis, the value of the sum of the residuals is still quite low (below 0.1), and only for a small area the residuals reach the maximum value of 0.175. Thanks to the overlying analysis, it was possible to first observe how to manipulate the weighting coefficients in order to obtain different expressions of the demisability index that more closely follow different aspects of the re-entry process (residual mass, casualty area, and demise altitude). It was then possible to observe that the selection of the weighting coefficients can be linked to the spacecraft class quite well through a linear relation and that such linear relation depends on the desired value of the evaluation functions. From the residuals analysis it is also possible to deduce that the ratio of the coefficients has a much more regular linear behaviour than the single coefficients itself. This indicates that the mutual relations between the coefficients are more important than the absolute value of the coefficients themselves.

7.5.5 Comparison between the new demisability index and the Liquid Mass Fraction

This final paragraph presents the comparison of the Pareto fronts obtained using the newly presented demisability index and the initially adopted LMF index. In order to compare the two formulations, the same test case of Section 7.4 has been used and the resulting Pareto fronts compared. As previously mentioned, the new index expression depends on the values adopted for the coefficients α, β, and γ. Consequently, exploiting the work carried out in Section 7.5.4 for the computation of the Pareto fronts relative to the different spacecraft classes, a series of coefficients were selected depending on the specific spacecraft class considered. The first comparison concerns a spacecraft belonging to the 2000 kg class; for this specific class, the coefficient selected for the comparison are summarised in Table 39. As it is possible to observe, case 1 tends to maximise the Spearman's rank relative to the residual mass (ρ_m), case 2 aims at giving the priority both to ρ_m and ρ_{Ac}, case 3 tends to prioritise ρ_{Ac} and ρ_{hd}, case 4 first maximises ρ_{hd} and then ρ_m, while case 5 first maximises ρ_{hd} and then ρ_{Ac}.

Table 39: Index coefficients used for the comparison with the LMF index for a 2000 kg spacecraft.

	α	β	γ	ρ_m	ρ_{hd}	ρ_{Ac}
Case 1	7.723	2.136	1.491	-0.9375	0.4500	-0.5875
Case 2	1.545	0.946	9.752	-0.7875	0.5625	-0.8875
Case 3	0.408	3.815	9.634	-0.5375	0.8375	-0.8375
Case 4	0.795	8.069	0.480	-0.4375	0.9875	-0.5375
Case 5	0.0252	7.745	3.867	-0.3375	0.9875	-0.5875

For the comparison, the specific case in exam is the one with a maximum number of 3 tank vessels for a 2000 kg spacecraft and a mission lifetime of 3 years, whose baseline Pareto front is represented by the one of Figure 74. Figure 108 to Figure 112 show the Pareto fronts obtained using the coefficients summarised in Table 39. Again, in each Pareto fronts the colour coding distinguishes between the materials, the shape of the markers identifies the number of tank vessels, and the style of the marker (solid or empty) distinguishes between spheres and cylinders. The first noticeable difference between all the Pareto fronts and the one of Figure 74 is the presence of more than just one *high-demisability* solution (on the upper left portion of the plot). This is because once a component has demised (null residual mass); the LMF index cannot distinguish between those solutions that demised earlier than others did. The same is not true for the new index because with the introduction of the term related to the demise altitude, even this aspect is taken into account and the solutions are differentiated. The second very noticeable difference is the value of the index itself, while the LMF index has a strictly limited value between 0 and 1 (0% and 100%), the boundaries of the new index are dependent upon the selection of the coefficients. Consequently, while the new index formulation can provide more insight into the actual re-entry process by merging into a single score three important elements of the re-entry, it is of less immediate interpretation with respect to the LMF index.

Considering now the different cases separately, it is possible to observe that the case number 1 (Figure 108) as a very similar behaviour to the original one of Figure 74. In fact, this case tends to maximise the index accordance with the residual mass distribution, which is closely related to the LMF index. Consequently, such behaviour was expected; however, some differences can be noticed. In particular, the relative difference between the different groups of solutions. For example, the relative distance between the cylindrical aluminium solutions and the spherical aluminium solutions has increased. This is a good behaviour as only the cylindrical solutions actually reach complete demise and they should be favoured by the index, as they do not contribute to the total casualty area.

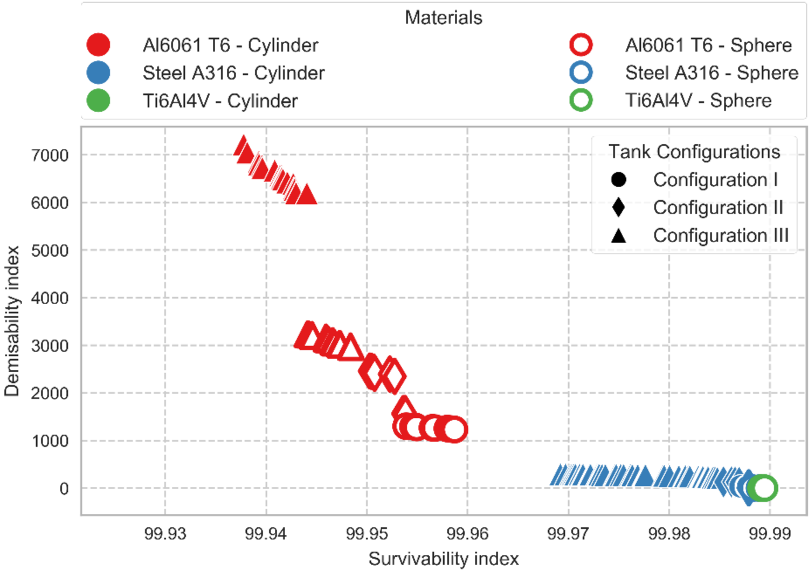

Figure 108: Pareto front plot for the case 1 of the new demisability index.

The group of low demisability solutions constituted by the stainless-steel solutions is even more penalised. This indicates that, despite the new index is oriented to have a behaviour like the LMF index; the inclusion of the contribution relative to the casualty area plays a significant role in penalising these solutions. More so, the casualty area contribution also introduces some new solutions (even though they are not clearly visible) at the very right end of the Pareto front. In fact, there are also present solutions with one and two spherical tanks and not just cylindrical stainless-steel tanks as it was the case in Figure 74.

The second case taken into account for the new index (Figure 109) has again a behaviour similar to the ones of Figure 74 and Figure 108, with only minor changes to the shape of the front but not on the solutions provided. Despite the importance of the casualty area, related term has increased and the one relative to the residual mass has decreased, still the behaviour tends to follow more closely the one of the residual mass. This indicates that the mass related term has a stronger relative variation with the change of the design parameter than the casualty area term. I also probably suggests that a further, wider study could be carried out with respect to the weighting coefficients, using wider boundaries than the ones used in Section 7.5.3.

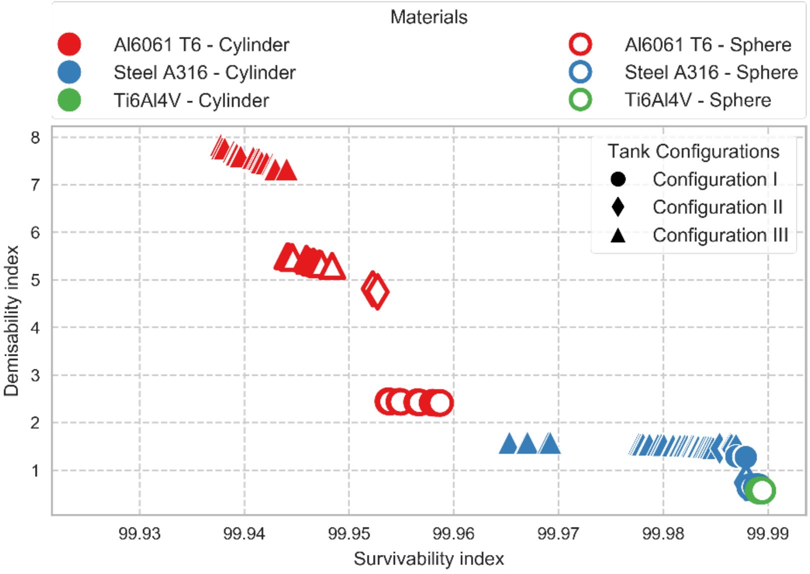

Figure 109: Pareto front plot for the case 2 of the new demisability index.

The case number three (Figure 110) presents a quite different behaviour with respect to the previous two cases. First, the relative difference of the index is values of the different groups is quite different: the solutions with three aluminium tanks are clearly the best ones in terms of demisability, while all the other solutions are more clustered in the bottom part of the Pareto front. The main difference resides in the stainless-steel solutions; in fact, only options with one single tanks have been found. This is clearly a consequence of the coefficient selected, which generates an index formulation that more closely follows the casualty risk contribution. In this case, in fact, the ratio between ρ_{Ac} and ρ_m is more important with respect to the case number two, and the result is that solutions with more than one tanks are less fit. However, the same behaviour is not repeated for the aluminium solutions despite the spherical aluminium solutions do not completely demise and reach the ground thus contributing to the casualty area. This is because for these solutions, the percentage mass loss increase still outweighs the term relative to the increase of the casualty area.

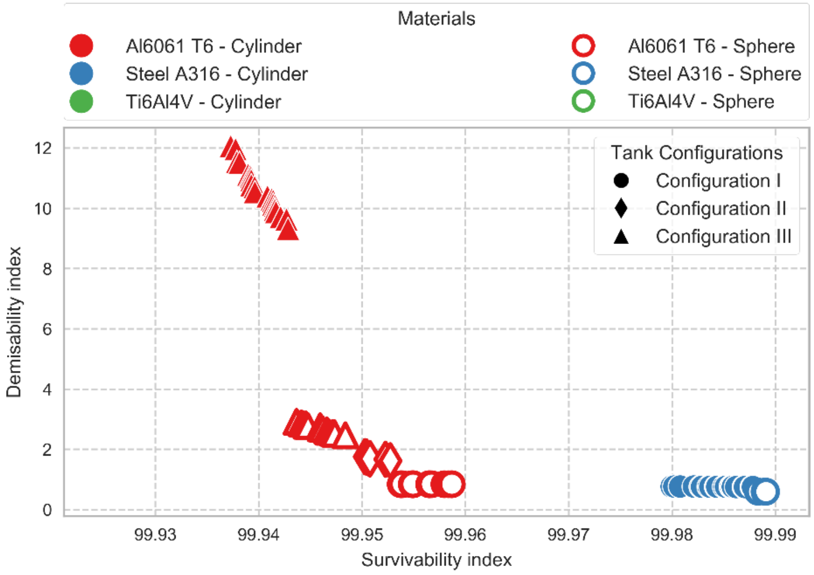

Figure 110: Pareto front plot for the case 3 of the new demisability index.

The case number four (Figure 111) is even more extreme with the solutions clearly separated between the demisable configuration of made of three cylindrical aluminium tanks and all the remaining non-demisable solutions , which are both made of aluminium and stainless steel and of different combinations of two and three vessels configurations. This behaviour is directly connected to the value selected for the coefficients, which prioritise the demise altitudes. In fact, all non-demisable solutions, which have low values of the demise altitude term, are clustered at the bottom of the Pareto front with very low values of the demisability index. At this point, it is interesting to compare this case with the case number five of Figure 112.

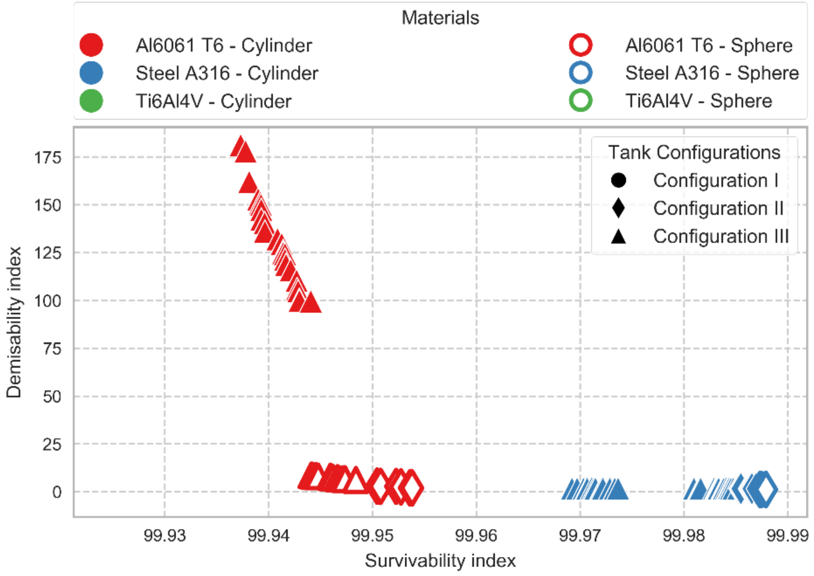

Figure 111: Pareto front plot for the case 4 of the new demisability index.

Both cases have the same high value of ρ_{hd}, while having a slightly different combinations of the two other fitness functions (ρ_m and ρ_{Ac}). Despite this difference is quite small, the results obtained with the two Pareto fronts for the low demisability solutions are very different. In fact, while in Figure 111 all such solutions are made of two and three vessels configurations, in Figure 112 they are all one-vessel solutions. Thus even slightly changing the combination of the desired evaluation functions can have a strong impact on the outcome of the Pareto front structure. This is also related to the fact that small variations of the fitness functions (especially at the *extremities* of the Pareto front) can be associated to large variations of the coefficients α, β, and γ.

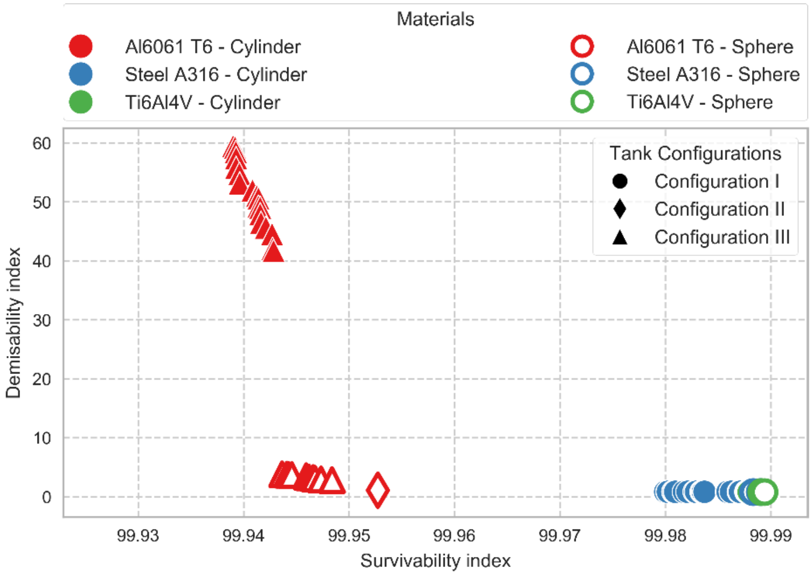

Figure 112: Pareto front plot for the case 5 of the new demisability index.

7.5.6 Summary and future development

This analysis has shown how it is possible to devise a demisability index formulation that can include different terms related to the major outcome of a re-entry simulation, and that it is possible to change the weights of the different contributions to tune the index towards a specific behaviour. Different *tunings* of the index can in fact lead to considerably different outcomes when different spacecraft configurations are compared based on how efficiently they demise. Despite the extensive analyses performed, there is still room for a better development and understanding of a comprehensive demisability index. It is in fact not an easy task to develop a consistent demisability index that is not limited to either computing the casualty risk (which is reductive when considering the concept of demisability in its entirety) or the mass loss during the re-entry. This effort goes towards this direct but it is important to outline that further studies may be needed. For example, we selected the index of Eq. (7.26), but the index of Eq. (7.27) had also similar performances and could be valuable to study it more in depth. In addition, a wider range for the weighting factors may be needed to better explore the relative combinations between them. In particular, the relation between the casualty risk term and the residual mass term as the latter has clearly a stronger contribution.

Chapter 8 Conclusions and future work

The work carried out during the PhD and described in the thesis is the result of the new exploration and investigation of two topics with a relatively recent history in the field of aerospace engineering. In fact, the main topics on which the present work is based are the capability of a specific spacecraft design to demise during the re-entry through the Earth's atmosphere, and the interaction with and the protection from space debris. It has been only in recent times that space debris has gained resonance as a possible threat to our capabilities to fully exploit space. Consequently, the protection of spacecrafts from an increasing number of high velocity particles polluting the space environment has gained interest. In fact, as the number of debris increases (especially in the most used and already populated region of space) the risks for spacecraft increase and the issues related to spacecraft protection become more and more relevant. As aforementioned, alongside space debris protection, the demise of spacecraft is the other main topic of this study. Despite studies concerning the re-entry of spacecrafts being of great relevance since the beginning of the space age, design-for-demise is a very new field. In fact, early studies were focusing on the methods to prevent the demise of spacecrafts, as the main interest was to design re-entry capsules for astronauts. Instead, design-for-demise aims at producing spacecraft design that favours the break-up and demise of the spacecraft such that it no longer poses threats for people on the ground. The new direction investigated by this PhD project is to study not just the advantages of the implementation of design-for-demise strategies but also their consequences on the overall design of a spacecraft configuration. In particular, we decided to focus on the effects that such design options have on the survivability of a spacecraft. As design-for-demise involves changes in the material, structure, and positioning of components and more in general involves changes in the design of the spacecraft, it is possible that is affects the resistance of the entire spacecraft and of specific critical components with respect to space debris impacts.

In order to explore this topic, two models have been developed, one for assessing the demisability of spacecraft configurations, and one for studying their survivability. These models have been developed to be completely compatible with each other and linked so that both the analyses could be carried out using a common definition of the spacecraft configuration. Both models have been developed throughout the entirety of the project and new features have been added continuously. Alongside the two models, two indices have also been devised in order to assess the level of demisability and survivability of spacecraft components and structure. These two indices allow for a fast and meaningful interpretation of the output of the demisability and survivability simulations.

The first set of results obtained concerns a fundamental analysis in order to understand the most influential parameters related to the design of a spacecraft and to the mission characteristics affecting the most the demisability and the survivability of spacecraft configurations. From the analysis it was found that the most relevant design parameters are the material, the dimension, and the thickness of a component. These parameters are important in influential the demisability and they should be prioritised over others when changing the design of a component. However, they are also the most influencing for the survivability. Consequently, a design also needs to be verified against the survivability requirements when the design-for-demise options are implemented. This means that trade-off solutions should be examined where the different design options generate different levels of demisability and survivability. Alongside the identification of the most important design parameters, the quantitative influence of the single design options on the survivability and demisability indices was investigated. Many of the design options, except for some changes in material, affect the demisability and the survivability in a contrasting way, i.e. while one of the two indices increases the other decreases. The different magnitude of this influence can also be observed, with the change of material and thickness being the most important. This is indeed an interesting result as it confirms the competing behaviour of the demisability and of the survivability and leads the way for the following analyses performed for the present work.

Following this first comprehensive analysis, the work focused on further developing the two models, adding new features and allowing more meaningful and complete analyses concerning simplified yet more realistic spacecraft configurations. The initial development block of the demisability model as described in Chapter 2 allows the user to simulate the re-entry trajectory and the demise of single elementary objects. This was a limiting approach; in fact, spacecrafts are composed of several components and subsystems. Consequently, additional features needed to be added in order to analyse more complex spacecraft architectures such as, for example, the modelling of break-up events. After the break-up event, all the components previously inside the spacecraft will be released and scattered. At that point, their trajectory is decoupled from the main structure and so is their demise. The updated version of the demisability model retains many of the initial characteristics, such as the object-oriented approach, the use of elementary shapes, and the averaged aerodynamics and aerothermodynamics. In the updated model, the spacecraft architecture can be more complex by defining the external structure and, separately, the internal components for a more complete destructive re-entry analysis. In addition, internal components can be attached to the external panels, which can also detach separately before the main spacecraft break-up. Moreover, external panels and flat plate structures in general can now be defined as both single sheets of material and as honeycomb structures with aluminium or composite cores. On the other hand, for the updated version of the survivability code, the main feature added is the possibility to evaluate the vulnerability of components contained inside the main spacecraft structure. In addition, the development of a novel methodology to compute the penetration probability of internal components is presented and compared with state-of-the-art software packages. The added capability of assessing the vulnerability of internal components now allows the user performing a full survivability analysis of preliminary spacecraft configurations; in fact, when considering internal components not only does the first impact with the external structure needs to be considered, but also the debris clouds that develop inside the spacecraft after the impact. The novelty introduced by the approach is the use of the concept of vulnerable zones, having thus the possibility to compute the survivability of a configuration in a fully probabilistic way, without relying on Monte Carlo simulations. In addition, to fully use the vulnerable zone while also considering the interaction between internal components, a novel methodology for the computation of the impact probability on internal components due to the secondary debris clouds has been developed.

As mentioned within the thesis, the aim of this work is to concurrently assess the effects of the demisability and of the survivability and search, where possible, for trade-off solutions as a function of the mission characteristics and requirements. This aim led to the development of a multi-objective optimisation framework where both the demisability and the survivability models are integrated to provide an effective tool to study the effects of preliminary design choices on the requirements arising from the demisability and from the survivability. The tool is able to evaluate a wide range of possible preliminary solutions against the demisability and the survivability, testing the search space using genetic algorithms, and then providing a family of optimised solutions. These solutions can be used as the starting point of more refined analyses by the design team. However, the early integration between the two requirements represent a considerable advantage in terms of efficiently design a spacecraft. Currently, in fact, these requirements are only considered in the latest stages of the mission design and usually imply the modification or the re-design of components. This is not an optimised procedure and can lead to delays or increased costs in order to meet the requirements. The proposed approach is aimed at reducing these limitations proposing an integrate approach since the early stages of the mission design.

Finally, the framework has been applied to relevant test cases and it proved able to explore the search space of feasible spacecraft configuration effectively. The test case of tank assemblies was considered of importance, given the high interest in the design-for-demise field for such components. The analysis was also extended to consider different types of spacecraft classes based on their mass, and mission lifetimes. The optimisation of the tank assembly considers several aspects of their design: the material, the thickness, the number of tanks, and the shape. In addition, the constraint on the feasibility of the solutions given the allowed maximum storage pressure of a certain tank design is also addressed. Considering all these aspects, a number of interesting observations could be made from the Pareto fronts obtained through the optimisation. First, it is important to observe that the optimiser was able to find trade-off solutions, actually confirming the competing behaviour existing between the demisability and the survivability. In addition, different types of solutions were found, varying in all the parameters considered, (material, shape, thickness, and number of tanks), meaning that all of them can make a difference when selecting a specific design considering the demisability and the survivability. Looking more closely at the resulting Pareto fronts, a first aspect is the difference in the output ranges for the two indices, with the demisability clearly having a wider range compared with the survivability. An important aspect also recognisable from the Pareto fronts is the importance of the mass of the spacecraft, especially for the demisability of a configuration. In particular, the interdependence between the mass of the spacecraft and the number of tanks in the assembly is very important. In fact, as the mass increases, only configurations with increasing number tanks produce fully demisable solutions. This also has an effect on the survivability because the *PNP* decreases with the increasing number of tanks. However, the gain in terms of demisability outweighs the survivability reduction as it is demonstrated by the optimiser always selecting the maximum number available of tanks for the most demisable solutions. Differently to the mission mass, the mission time does not influence the type of solutions in the Pareto front, but has the effect of shifting the solutions towards a lower survivability as the mission time increases

As an additional element to the design and as a demonstration that this research topic has still plenty to be explored, a further study on the possible *upgrade* of the demisability index initially adopted in the thesis was carried out. Section 7.5 provides the description of the procedure followed, which considered a set of possible expressions for the *new index* and analysis of them in order to select the most appropriate for our purposes. The new version of the index includes additional contributions to its computation so that in a single score it is also possible to take into account aspects relative not only to the mass loss during the re-entry but also relative to the casualty area of the surviving components and the demise altitude of the demised ones. This new index has then been analysed and studied as a function of the possible different weights that such terms can possess inside the expression. It resulted in the identification of Pareto fronts of weighting coefficients whose changes provide expressions of the index that can emphasise different aspects of the re-entry process still without neglecting the other terms. A further step pushed the analysis of the behaviour of the index as a function of the spacecraft class (i.e. the spacecraft mass), and identified that linear relationships can be found, with good confidence, between the weighting coefficients as a function of the spacecraft mass. Finally, examples of the new index, with different weighting factors, have been presented and compared with the initial version of the demisability index.

Overall, the presented study has explored a novel point of view to the design-for-demise philosophy: not only the positive effects should be analysed when implementing such solution, as they can affect other aspects of the design of the spacecraft. In this case, the capability of the spacecraft to withstand debris impacts has been considered. This work has created a methodology for concurrently analysing the demisability and the survivability of preliminary spacecraft configurations, introducing novelty in the methodology itself by integrating the two aspects into a multi-objective optimisation framework, and novelty in the development of the single models by carefully tailoring their features to the problem in exam. The demisability model started from an object-oriented methodology and has been included with new features such as the implementation of shielding techniques and the attachments of components to external panels. These features are of interest when even the survivability is considered. The survivability model has been equipped with a novel methodology to assess the damage on internal components that is based on the concept of vulnerable zones. In addition, a fully geometrical methodology, based on the shape of the particle ejecta, has been developed in order to consider the mutual shielding of internal components. In addition, a thorough sensitivity analysis identifying the most influential design parameter for both the demisability and the survivability has been carried out. Following this analysis, a set of preliminary maps has been developed for the quick evaluation of the level of demisability and survivability for the main types of components. Moreover, the multi-objective optimisation framework has been tested with a relevant test case, which considered spacecraft tank assemblies. It was demonstrated that the framework is able to deal with multiple components and component specific constraints and find trade-off solutions for many different types of mission scenarios. Finally, a preliminary analysis showed that the demisability index could be improved by including information concerning the casualty area and the demise altitude in order to increase its robustness.

8.1 Limitations of the work

The presented work focuses on the analysis of preliminary spacecraft design and as such, it is concentrated in examining the effects of more basic changes. Consequently, the models developed cannot consider more complicated design such as, for example, the use of external panels with cut-outs, which reduce the mass to be demised but can also increase the exposure of the internal components to the debris fluxes. In addition, currently, the model can only analyse simple-shaped objects so that even more complex shapes need to be reduced to an equivalent simplified geometry in order to be analysed. For what concerns the optimisation framework, it is important to underline that genetic algorithm are very well suited to effectively explore large search spaces such as the ones that have been taken into account; however, an additional, more refined local optimisation could be performed after the first genetic optimisation, to further refine selected solution from the Pareto front. Another aspect to be addressed is related to the uncertainties that are typical in these analyses, especially in the case of re-entries. At the moment, the uncertainties are not considered in the optimisation but could definitely have an influence on the optimisation analyses.

8.2 Future work

The analyses carried out throughout the PhD have encompassed a wide range of topics: the study of the re-entry dynamics and the relative techniques used to assess and predict the demise of spacecraft components and parts; the assessment of space debris impacts on spacecraft structures and components; the overview and implementation of design-for-demise techniques. Additionally, the devise of relevant indices to effectively express the level of demisability and survivability has been carried out as well as the development of a multi-objective optimisation framework that could exploit the characteristics of both models and allow the comparative study of the demisability and of the survivability of spacecraft configurations.

Despite the extensive work carried out on each one of these aspects, there is both the possibility to further develop the models and the frameworks and to perform other analyses concerning the duality between demisability and survivability. For what concerns the demisability model, improvements could be focused on the extension of the catalogue of the predefined component's shapes, by introducing shapes such as the cone, the truncated cone, the hollow cylinder, etc. Additionally, the material database could be extended and, the creation of multi-layer multi-material components could be introduced. These latest aspects could allow the demisability and survivability analysis of the behaviour of even the more complex shielding options, which have more intricate designs than the ones currently considered (i.e. single wall, double wall, and honeycomb sandwich panel). Finally, for what concerns the demisability model, the possibility of defining new break-up conditions in addition to the altitude-based one could be an interesting asset, so that even the influence of different modelling techniques could be evaluated when considering a combined demisability and survivability analysis.

For what concerns the survivability model, a first improvement could be to introduce the possibility of creating more complex shapes for the external structure of the spacecraft and the possibility to position components externally to the spacecraft and not only internally as it is the case at the moment. Another possible improvement is to consider debris impacts both during the nominal mission orbit and during the disposal/decay phase by considering the cumulative effects during the entire permanence in orbit of the spacecraft and not only for the operational lifetime as it is at the moment. A further area of development consists in continuing the development of the vulnerable zone methodology; in particular, the possibility to assess the impact probability on contained sub-components as only the first layer of internal components can be assessed at the moment.

The multi-objective optimisation framework could be improved by introducing the possibility to use different optimisation strategies in addition to the NSGA-II currently implemented. In addition, the possibility to consider model and initial conditions uncertainty in the optimisation could definitely improve the robustness of the optimisation. Furthermore, the capability of considering the relevant constraints for a larger number of components and subsystems could definitely be an asset.

For what concerns the analyses that can be performed regarding the effects of design-for-demise options on the demisability and survivability of spacecraft configuration, many aspects could be considered. For example, following the sensitivity analysis performed in Section 4, a similar, more in depth analysis, can be performed considering also the effect of the external structure, carefully studying how it affects the demisability and the survivability of internal components. Another dedicated analysis could study in what extent the attachment of the components to the external panels of the main spacecraft structure influences their demisability and their survivability. When does the increase in vulnerability of the component justify the increased demisability? Which are the main parameters influencing such phenomenon. In addition, specific studies concerning the demisability and the survivability of specific spacecraft components such as reaction wheels and tanks as a function of the mission characteristics (i.e. orbital and re-entry conditions) and considering the limitations introduced by the manufacturing constraints of such components could be extremely interesting. In fact, these types of analyses can lead to a set of preliminary design guidelines for each component as a function of the mission characteristics. Furthermore, more realistic test cases could be presented, including tests of complete spacecraft configurations.

Finally, the study about the improvement of the demisability and survivability indices could be extended. For example, the new devised demisability index could be further tested with different mission scenarios and types of configurations. For the survivability index, a weighting factor related to the criticality of each component could be devised.

Appendix A Material database

The material database used in the project is summarised in Table A-1. The majority of the data is from the Debris Assessment Software 2.0 (National Astronautics and Space Administration, 2015, Owens, 2014) database. When material properties such as the emissivity were not available in the DAS database, they were retrieved from the MatWeb database (MatWeb LLC, 2015) or from other publications (Beck J., 2015, Beck J., 2015b, Lips T., 2015, Lips T., 2005, Lips T., 2005a, Lips T., 2005b).

Table A-1: Material database data

Material	ρ_m	***HB***	T_m	h_f	C_m	ε	***C***	σ_y
	kg/m^3		*K*	*J/kg*	*J/kg-K*		*m/s*	*MPa*
Al 6061 T6	2713	95	867	386116	896	0.141	5100	276
Al 7075 T6	2787	150	830	376788	1012.35	0.141	5040	450
Titanium 6Al4V	4437	334	1943	393559	805.2	0.302	4987	880
AISI304	7900	123	1700	286098	545.1	0. 35	5790	215
AISI316	8026.85	149	1644	286098	460.6	0.35	5790	250
Inconel 601	8057.29	147	1659	311664	632.9	0.122	5700	450
Graphite-epoxy 1	1570	n/a	700	1.60E+07	1100	0.86	n/a	498.5
Graphite-epoxy 2	1550.5	n/a	700	236	879	0.9	n/a	498.5

For this work, all the material properties are assumed temperature independent (National Astronautics and Space Administration, 2015, Owens, 2014). The Brinell hardness (HB) measures the indentation hardness of materials through the scale of penetration of an indenter, loaded on a material test-piece. This parameter is only used in the vulnerability analysis. For this work, the ambient temperature *HB* hardness has been considered. As the BLEs correlations have been obtained with ambient temperature on-ground testing, this has been considered an applicable assumption. The melting temperature (T_m) and the heat of fusion (h_f) have all been retrieved from the DAS 2.0 database, except for the Graphite-epoxy 1, which has been gathered from Lips, T., 2015a. Both these quantities are only used in the demisability analysis. In the code, the melting temperature is the temperature after which the material starts to demise. After it has been reached the temperature is kept constant and the object starts to demise, loosing mass at a rate that is proportional to the heat flux and the heat of fusion. The heat of fusion (h_f) represents the amount of energy required to change the state of a substance from solid to liquid at constant pressure. The specific heat capacity (C_m) is again only used in the demisability analysis. It is the amount of energy required to raise the temperature of a substance per unit of mass. The specific heat capacity is a temperature dependent material. As we are using a database with constant quantities, the adopted value is the mean specific heat capacity between the reference and melting temperatures. These ranges are directly provided in the DAS 2.0 database. The emissivity (ε) of a material is its effectiveness in emitting energy as thermal radiation. This is an important parameter for the assessment of the demisability of an object. In fact, it regulates the amount of heat that the surface of an object emits as a function of its temperature. During re-entry, the surface of an object reaches high temperature, making the knowledge of the emissivity important for the correct analysis of the heat balance on the re-entering object. In general, the emissivity depends on the temperature and the state of the surface of an object. Given the harsh thermochemical environment of atmospheric re-entries, such state can be altered, for example, by the formation of oxides, which can strongly affect the emissivity of a material, usually increasing it (Pagan, A. S., 2016). In the present study, the emissivity is considered constant and relative to a surface that has not been altered by thermochemical reactions. In a future development of the tool we will consider these aspects and include temperature dependant relations for both the emissivity, given the recent efforts in the characterisation of common spaceflight materials for demisability application (Pagan A. S., 2016, Pagan A. S., 2015). The yield strength (σ_y) is defined as the stress at which a material begins to deform plastically. This parameter is only used in the vulnerability analysis for the computation of the critical impact diameter using the BLEs. Similarly, to the Brinell hardness, as the BLEs correlations have been obtained through ground-testing at ambient temperature, the ambient temperature value of the yield strength has been considered.

Appendix B Earth's atmosphere model

The re-entry analysis of a spacecraft requires the knowledge of the aerodynamic forces acting on it in order to correctly simulate its trajectory, as well as the aero-thermal heating the spacecraft experiences to predict its demise process. The knowledge of the main atmospheric properties and their derived quantities (i.e. Mach number, Knudsen number, etc) at any point during the descent is thus very important to adequately simulate the re-entry process. In this context, an atmospheric model must be able to represent the vertical variations of the main atmospheric properties such as density, pressure, and temperature. For our scope, the model used to describe the atmosphere is the 1976 U.S. Standard Atmosphere (National Oceanic and Atmospheric Administration, 1976), which is an idealised, steady state representation of the Earth's atmosphere from the surface up to an altitude of 1000 km, considered in a period of moderate solar activity and average weather conditions. The model does not consider daily and seasonal variations of the atmospheric characteristics, nor considers the influence of solar cycle variations; nonetheless, it provides a good compromise between complexity and accuracy. According to the 1976 Standard, the Earth's atmosphere can be broadly divided into two zones: the lower atmosphere, which extends from the surface to a geometric altitude of 86 km, and the upper atmosphere, from 86 km up to 1000 km. Each of the two zones is further divided into layers. Within each layer the temperature is represented with a predefined function of the altitude; pressure and density are then derived accordingly as functions of the altitude.

Lower atmosphere

The model adopted for the lower atmosphere divides it into seven layers (). Inside each layer, the molecular temperature is assumed to vary linearly with the geopotential altitude[4] (Figure B-1 (a)) following the relation

$$T_M\left(h\right)=T_{M,i}+LR_i\cdot\left(h-h_i\right) \tag{B.1}$$

where $T_M(h)$ is the molecular temperature at a specified geopotential altitude h, $T_{M,i}$ and h_i are the molecular temperature and the geopotential altitude at the base of the *i-th* layer respectively, and LR_i is the thermal lapse rate that is the gradient of the molecular temperature with respect to the geopotential altitude. Table B-1 shows the base values of the altitude, temperature, and pressure, together with the lapse rates for each of the layers into which the lower atmosphere is divided.

Table B-1: Layers characteristics for the lower atmosphere model.

Level	h_i	T_i	p_i	LR_i

---

[4] The *geopotential altitude* is a "gravity adjusted height" that is based on the assumption that the gravitational acceleration remains constant with the altitude.

0	0.000	288.150	1.0	-6.5
1	11.000	216.650	2.2233611×10-1	0.0
2	20.000	216.650	5.403295×10-2	+1.0
3	32.000	228.650	8.5666784×10-3	+2.8
4	47.000	270.650	1.0945601×10-3	0.0
5	51.000	270.650	6.6063531×10-4	-2.8
6	71.000	214.650	3.9046834×10-5	-2.0
7	84.852	186.946	3.68501×10-6	

Once the temperature profile is known, it is possible to express the variation of the pressure as a function of the geopotential altitude (Eq. (B.2)). The density can then be derived from the equation of state. The molecular weight of the air is obtained through a linear interpolation of tabulated data extrapolated from the 1976 U.S Standard Atmosphere document, corresponding to the boundaries of the seven layers.

$$p = \begin{cases} p_i \left[1 + \dfrac{LR_i \cdot (z - z_i)}{R \cdot T_{M,i}} \right]^{-\left\{ \frac{g_0}{R \cdot LR_i} \cdot \left[1 + \beta \left(\frac{T_{M,i}}{LR_i} - z_i \right) \right] \right\}} \cdot e^{\beta \cdot \frac{g_0}{R \cdot LR_i} \cdot (z - z_i)} & if \;\; LR_i \neq 0 \\ p_i \cdot e^{-\left[\frac{g_0 \cdot (z - z_i)}{R \cdot T_{M,i}} \right] \cdot \left[1 - \frac{\beta}{2} (z - z_i) \right]} & if \;\; LR_i = 0 \end{cases} \tag{B.2}$$

Where p_i is the base pressure relative to the *i-th* layer, g_0 is the sea-level gravitational acceleration, z is the geometric altitude, z_i is the geometric altitude of the i-th layer, and R is the air gas constant. *B=2/Re*. Figure B-1shows the variations of temperature, pressure, and density up to 86 km, obtained with the described model.

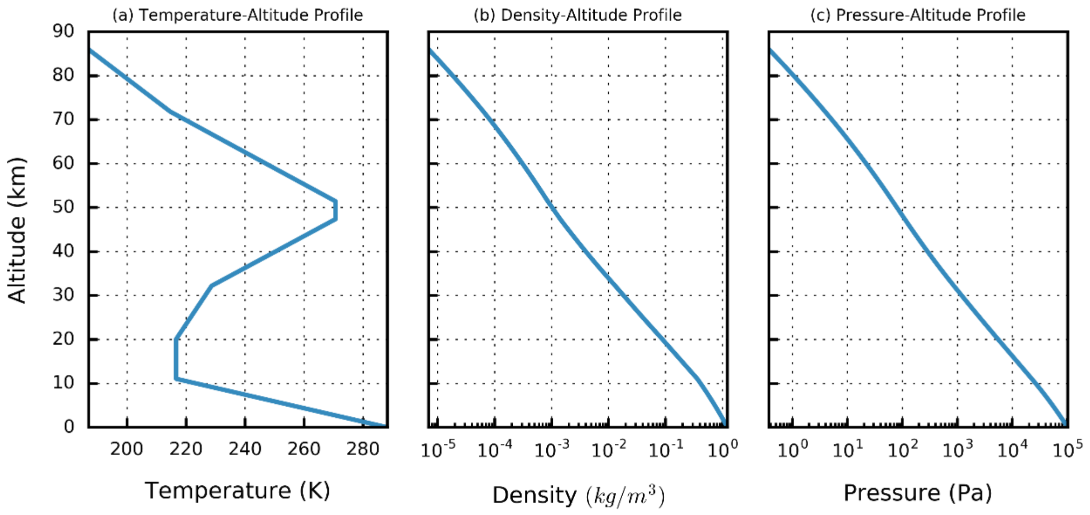

Figure B-1: Temperature, density and pressure profile as function of altitude for the lower atmosphere.

Upper atmosphere

For the upper atmosphere, a subdivision into layers is again used (Carmichael, 2014). Four layers are used for the temperature; in each layer the temperature profile is predefined (National Oceanic and Atmospheric Administration, 1976). The first layer is the isothermal layer, which spans from the top of the lower atmosphere at 86 km, up to 91 km. For this layer the temperature is constant and equal to 186.946 K. The following layer ranges from 91 km (Z_8) to 110 km (Z_9) and has an elliptical temperature profile described by the following expression:

$$T = T_C + C_1 \left[1 - \left(\frac{z - Z_8}{C_2} \right)^2 \right]^{1/2} \tag{B.3}$$

Where T_C = 263.1905 K, C_1 = -76.3232 K, and C_3 = -19.9429×10^3 km. The third profile is described with a linear relationship through the altitude range 110 km to 120km (Z_{10}) as follows:

$$T = T_9 + LR_9 \cdot \left(z - Z_9 \right) \tag{B.4}$$

with LR_9 = 12 K/km. In the last layer, the temperature profile is represented with an exponential profile encompassing the altitude range from 120 km to 1000 km (Z_∞) through the following equation:

$$T = T_\infty - \left(T_\infty - T_{10} \right) \cdot \exp\left(C_3 \cdot \xi \right) \tag{B.5}$$

where C_3 = 0.01875 *1/km*, T_∞ = 1000 km and ξ is defined as follows:

$$\xi = \left(z - Z_{10} \right) \cdot \left(\frac{R_e + Z_{10}}{R_e + z} \right) \tag{B.6}$$

where R_e is the Earth equatorial radius. For what concerns the variation of density and pressure with the altitude, following the procedure outlined in (Carmichael, 2014) leads to the definition of 22 layers (Table B-2). For each layer the base values of pressure, density and their derivatives are known, and the intermediate values are obtained through a cubic spline interpolation of tabular data. The cubic spline interpolation follows Eq.

$$p(y) = k_{00}(y) \cdot p_i + k_{10}(y) \cdot \Delta z \cdot m_i + k_{01}(y) \cdot p_{i+1} + k_{11}(y) \cdot \Delta z \cdot m_{i+1} \tag{B.7}$$

Where p_i and p_{i+1} are the values of the function at the bottom and top of the considered layer interval respectively, and m_i and m_{i+1} are the values of the derivatives of the function at the bottom and top of the considered layer interval respectively. Δz is the width of the layer interval (z_{i+1} - zi) and $y = (z-$

$z_i)/\Delta z$, with z being the point inside the interval at which the interpolated function has to be evaluated. h_{00}, h_{10}, h_{01}, h_{11} are the Hermite base functions, which are defined as

$$\begin{aligned} k_{00}(y) &= 2y^3 - 3y^2 + 1 \\ k_{10}(y) &= y^3 - 2y^2 + y \\ k_{01}(y) &= -2y^3 + 3y^2 \\ k_{11}(y) &= y^3 - y \end{aligned} \tag{B.8}$$

In the same way as for the lower atmosphere, the variation of the molecular weight of the gas mixture composing the atmosphere with the altitude is considered through a linear interpolation of tabular data

Table B-2: Reference levels for the layers of the upper atmosphere segment.

Altitude	***ln(p)***	$\frac{d}{dz}$***ln(p)***	***ln(ρ)***	$\frac{d}{dz}$***ln(ρ)***	***M***
86	-0.985159	-0.177196	-11.875633	-0.178126	28.95
93	-2.225531	-0.175466	-13.122514	-0.179926	28.77
100	-3.441676	-0.164802	-14.394597	-0.178522	28.21
107	-4.532756	-0.140984	-15.621816	-0.172973	27.39
114	-5.415458	-0.108912	-16.816216	-0.151242	26.58
121	-6.057519	-0.081631	-17.739201	-0.116653	25.92
128	-6.558296	-0.065477	-18.449358	-0.091833	25.38
135	-6.974194	-0.055406	-19.024864	-0.075897	24.88
142	-7.33398	-0.048383	-19.511921	-0.064855	24.44
150	-7.696929	-0.042767	-19.992968	-0.0561	23.85
160	-8.098581	-0.038071	-20.513653	-0.048839	23.26
170	-8.458359	-0.034413	-20.969742	-0.043231	22.62
180	-8.786839	-0.031634	-21.378269	-0.039026	22.05
190	-9.091047	-0.029452	-21.750265	-0.035753	21.51
200	-9.375888	-0.026543	-22.093332	-0.031466	20.99
250	-10.605998	-0.022682	-23.524549	-0.025849	18.84
300	-11.644128	-0.019374	-24.678196	-0.021147	17.37
400	-13.442706	-0.016838	-26.600296	-0.018018	15.56
500	-15.011647	-0.014361	-28.281895	-0.016025	13.24
600	-16.314962	-0.011244	-29.805302	-0.014163	9.22
700	-17.260408	-0.007865	-31.114578	-0.011516	5.75

800	-17.887938	-0.005184	-32.108589	-0.00787	4.3
1000	-18.706524	-0.004093	-33.268623	-0.0058	2.0

Figure B-2 shows the temperature, density, and pressure profiles as a function of the geometric altitude for the upper atmosphere.

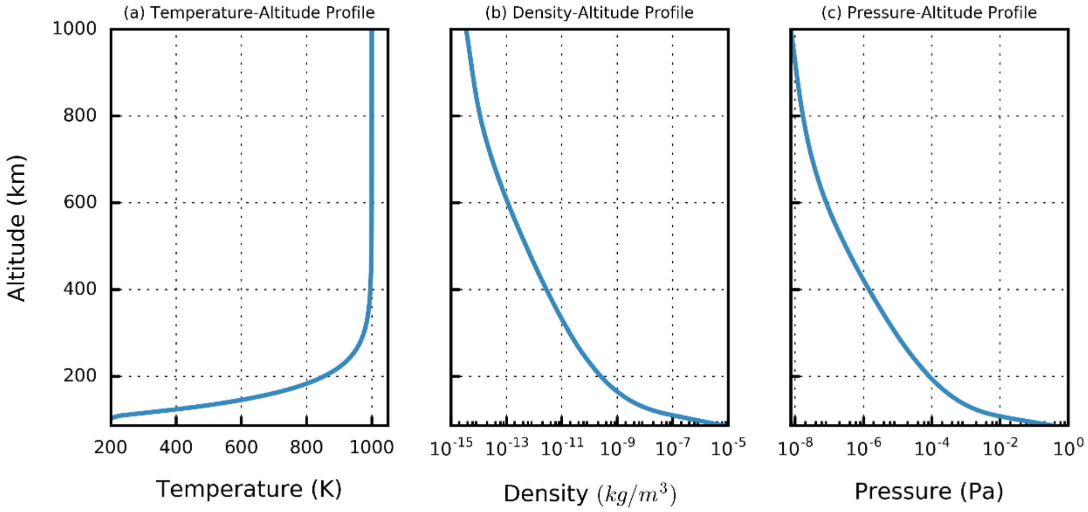

Figure B-2: Temperature, density and pressure profile as function of altitude for the upper atmosphere.

Appendix C Aerodynamics correlations for cylindrical shapes

The aerothermodynamics correlations used to assess the heat rate on cylinders (Klett, 1964) rely on a set of experimental data. For the free molecular case the expressions of the end and side shape factors are

$$\bar{F}_{q,\,fm}^{end} = 0.255 \tag{C.1}$$

$$\bar{F}_{q,\,fm}^{side} = 0.785 \cdot Y + 0.5 \cdot Z \tag{C.2}$$

Here Y represents the free-molecular flow ratio of the average heating on the sides of a rotating side-on cylinder to the heating on surfaces perpendicular to the flow. Z instead describes the free-molecular flow ratio of the heating on surfaces parallel to the flow to the heating on surfaces perpendicular to the flow. These curves comes from experimental data and are presented in Klett (1964). In order to have such data available in the code a curve-fit has been carried out in order to obtain analytic equations. In Figure C-1 are presented the Y and Z curve obtained with the curve-fit, and Eqs. (C.1) and (C.2) are the expressions obtained.

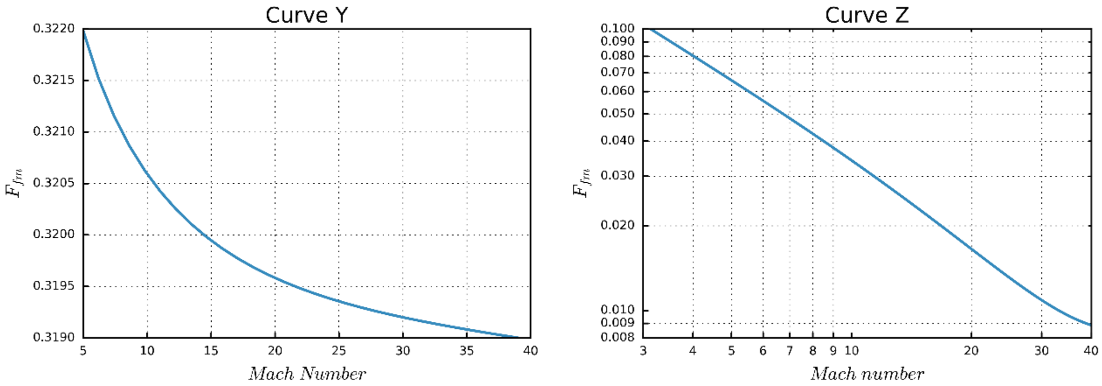

Figure C-1: Curve Y and curve Z for the computation of free-molecular shape factors for cylinders.

$$Y = 7.894 \times 10^{-7} \cdot M^2 - 0.00273 \cdot \ln\left(154.466 \cdot M\right) + 0.00011 \cdot M + 0.3396 \tag{C.3}$$

$$Z = -0.01385 \cdot \ln\left(2.7417 \cdot M\right) + 0.000395 \cdot M + 0.5211 + 0.2396 / M \tag{C.4}$$

For the continuum case the expressions for the side and end shape factors are:

$$\bar{F}_{q,c}^{end} = 0.323 \tag{C.5}$$

$$\bar{F}_{q,c}^{side} = 0.179 + 0.333 \cdot B \tag{C.6}$$

The term B represents the ratio of the average heating to the side of an end-on cylinder to the stagnation point heating of a sphere of the same radius. The curve B is represented in Figure C-2. Eq. (C.7) is instead the expression obtained from the curve fitting.

$$B = 1.5632\times10^{-5}\cdot\left(\frac{l}{d}\right)^2 - 0.0364\cdot\ln\left(6.829\times10^{-15}\cdot\frac{l}{d}\right) + 0.001307\cdot\frac{l}{d} - 1.0647 \quad \text{(C.7)}$$

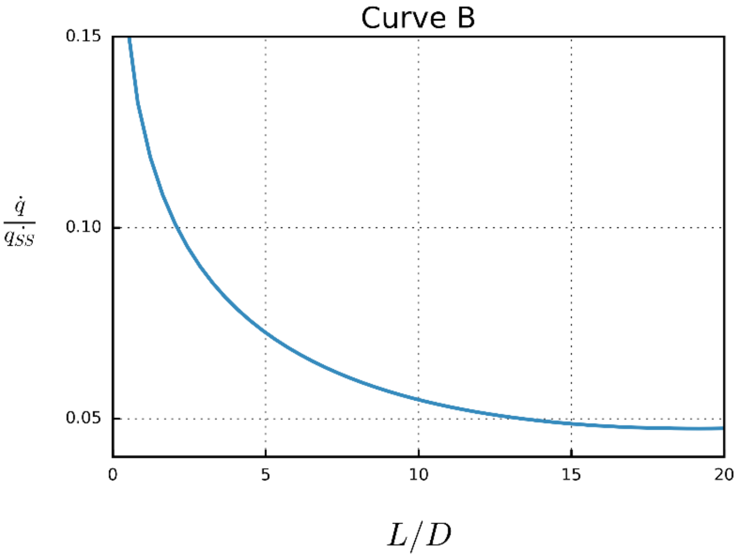

Figure C-2: Curve B for the computation of continuum flow shape factors for cylinders.

Appendix D Ballistic Limit Equations

Ballistic limit equations (BLEs) define the critical diameter that leads to the failure of a structure as a function of the velocity and impact angle, as well as the characteristics of the target such as the material, thickness, and configuration. Possible failure modality are perforation, detached spall and incipient spall and can be selected as a function of the particular component considered, whether it is a pressure vessel, a battery assembly or some other kind of components. BLEs are usually obtained through experimental studies in hypersonic impact facilities and through empirical correlations due to the very high complexity of the damage mechanism behind impacts at such high velocity regimes.

Single-wall BLEs

The BLEs for single wall structures adopted in the developed methodology are presented for completeness in the following. They are the reference equations for NASA's ballistic limit and debris impact analysis (Ryan and Christiansen, 2011, Christiansen et al., 2009). Different equations are used for structures of different materials. For single wall aluminium structures, the BLE corresponds to

$$d_c = \left[\frac{t_s}{k} \cdot \frac{HB^{1/4} \cdot \left(\rho_s / \rho_p \right)^{\alpha}}{5.24 \cdot \left(v_p \cdot \cos(\theta) / C \right)^{2/3}} \right]^{18/19} \tag{D.1}$$

with HB Brinell hardness of the material, ρ_S and ρ_p density of the shield and of the projectile respectively expressed in g/cm^3, v_p particle relative impact velocity in km/s, C speed of sound in the material considered in km/s, t_S thickness of the shield in cm, and θ impact angle. The value of the exponent α depends on the ratio between the particle density and the shield density (Eq. (D.2)) and the constant k depends on the type of failure mode considered: k = 3.0 for incipient spall, k = 2.2 for detached spall, and k = 1.8 for perforation.

$$\alpha = \begin{cases} 0.5 & \text{if } \rho_p / \rho_s < 1.5 \\ 2/3 & \text{if } \rho_p / \rho_s \geq 1.5 \end{cases} \tag{D.2}$$

Analogous equations can be derived for titanium (Eq. (D.3)), stainless steel (Eq. (D.4)), and CFRP (Eq. (D.5)) single wall structures as follows:

$$d_c = \frac{t_s}{k} \cdot \frac{HB^{1/4} \cdot \left(\rho_s / \rho_p \right)^{1/2}}{5.24 \cdot \left(v_p \cdot \cos(\theta) / C \right)^{2/3}} \tag{D.3}$$

$$d_c = \left[\frac{t_s}{0.621} \cdot \frac{\left(\rho_s / \rho_p \right)^{\alpha}}{\left(v_p \cdot \cos(\theta) / C \right)^{2/3}} \right]^{18/19} \tag{D.4}$$

$$d_c = \frac{t_s}{k} \cdot \frac{\left(\rho_s/\rho_p\right)^{\alpha}}{K_{CFRP} \cdot \left(v_p \cdot \cos(\theta)\right)^{2/3}} \tag{D.5}$$

In Eq. (D.4) for the stainless steel, the hardness of the material is included in the coefficient. In addition, no distinction is made between possible failure modes, as only perforation damage is considered. Eq. (D.5) was derived (Christiansen et al., 2009) for CFRP introducing the parameter K_{CFRP} that takes into account the effects of the material properties such as the hardness, the density and the speed of sound for non-isotropic materials. A value of 0.52 is adopted in the present work for the K_{CFRP} coefficient (Ryan and Christiansen, 2011).

Schafer-Ryan-Lambert BLE

The Schafer-Ryan-Lambert ballistic limit equation (Ryan and Christiansen, 2010) is an analytic expression used to describe the behaviour of multi-wall shielding technology against the impacts of space debris and meteoroids. The equation allows the user to compute the critical diameter for triple-wall structure (see Figure D-1), but can also be used for dual-wall and single-wall configurations.

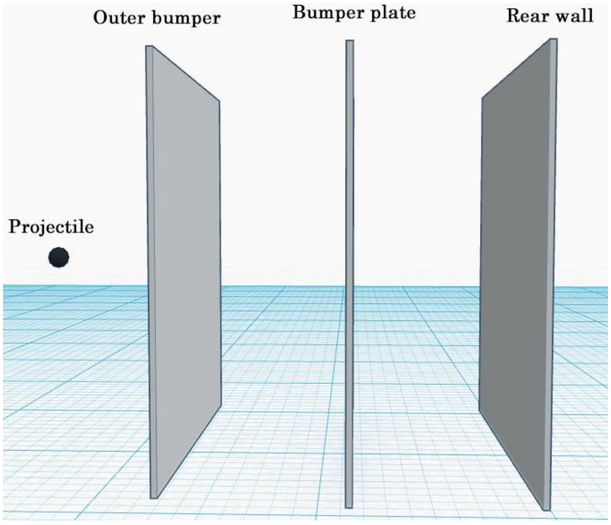

Figure D-1: Schematic configuration for the SRL BLE.

The critical diameter computation using the SRL BLE distinguishes between three different velocity regimes: the *ballistic regime*, the *shatter regime*, and the *hypervelocity regime*. In the ballistic regime ($V_p \leq V_{LV} \cdot \cos\theta$) the critical diameter is

$$d_c^{ball} = \left[\frac{\dfrac{\left(t_w^{0.5} + t_b\right)}{K_{3S}} \cdot \left(\dfrac{\sigma_y}{40}\right)^{0.5} + t_{ob}}{0.6 \cdot \left(\cos\theta\right)^{\delta} \cdot \rho_p^{0.5} \cdot v_p^{2/3}} \right]^{18/19} \tag{D.6}$$

where V_{LV} is the ballistic regime transition velocity, K_{3S} and δ are fitting factors whose values are shown in Table D-1. t_b is the bumper plate thickness, t_{ob} is the outer bumper thickness, and t_w is the rear wall thickness. In the hypervelocity regime ($V_p \geq V_{HV} \cdot \cos\theta$) instead we have:

$$d_c^{hyp} = \frac{1.155 \cdot \left[S_1^{1/3} \cdot \left(t_b + K_{tw} \cdot t_w\right)^{2/3} + K_{S2} \cdot S_2^{\beta} \cdot t_w^{\gamma} \cdot \left(\cos\theta\right)^{-\varepsilon} \right] \cdot \left(\frac{\sigma_y}{70} \right)^{1/3}}{K_{3D}^{2/3} \cdot \rho_p^{1/3} \cdot \rho_{ob}^{1/9} \cdot v_p^{2/3} \cdot \left(\cos\theta\right)^{\delta}} \tag{D.7}$$

where V_{HV} is the hypersonic regime transition velocity. K_{tw}, K_{S2}, K_{3D}, β, ε, and γ are fitting factors (see Table D-1); ρ_{ob} is the outer bumper density; S_1 and S_2 are the spacing between the outer bumper and the bumper plate, and the space between the bumper plate and the rear wall respectively. Finally, in the shatter regime ($V_{LV} \cdot \cos\theta \leq v_p \leq V_{HV} \cdot \cos\theta$) linear interpolation is used between the critical diameters obtained in the ballistic and in the hypervelocity regimes.

Table D-1: Summary of the coefficients for the SRL BLE.

Symbol	**Aluminium outer bumper**	**CFRP outer bumper**
V_{LV}	3 km/s	4.2 km/s
V_{HV}	7 km/s	8.4 km/s
K_{3S}	1.4	1.1
K_{3D}	0.4	0.4
K_{tw}	1.5	1
K_{S2}	0.1	1
β	2/3	1/3
δ	4/3 if $45 \geq \theta \geq 65^{\circ}$ 5/4 if $45 < \theta > 65^{\circ}$	4/3
ε	8/3 if $45 \geq \theta \geq 65^{\circ}$ 10/4 if $45 < \theta > 65^{\circ}$	0
γ	1/3	2/3

Appendix E Preliminary scaling relations for spacecraft configurations generation

During the work presented in the thesis, in several occasion it has been necessary to use preliminary spacecraft configurations to perform both the demisability and the survivability analyses. Whether it was required by the analysis of a single configuration, or by the optimisation of a spacecraft subsystem, or by a sensitivity analysis, the need for the generation of a sensible and feasible spacecraft configuration has presented itself several times. In addition, in several analyses performed, we were interested in the behaviour of the demisability and of the survivability with respect to the spacecraft mass. Therefore, it was important to have a set of relations to readily obtain a sensible spacecraft configuration for different values of the spacecraft mass. Consequently, a series of preliminary sizing relations for the main spacecraft structure, the solar arrays, and for some of the most common spacecraft components have been developed.

The main information required for the simulations concerns the overall size of the spacecraft, the solar array area, and mass. In addition, data needed for the sizing of some of the major spacecraft components was required, such as the amount of propellant for the mission, the amount of angular momentum, the amount of power needed by the spacecraft, etc. These data can then be combined with the sizing relations already presented in Section 7.4, to properly size the propellant tanks, the reactions wheels, and the batteries, as well as other components such as the magneto-torquers. The information required for the extrapolation of the trends related to these data with respect to the spacecraft mass have been gathered from the satellite database of the Union of Concerned Scientist (Union of Concerned Scientists, 2017). It is important here to specify that from the entire database, only LEO satellites (with apogee below 2000 km) have been considered, and only spacecraft with a mass larger than 250 kg. From these set of data relevant information has been extrapolated as a function of the spacecraft mass. First, the mission lifetime has been computed and it was possible to observe that the average mission lifetime is almost constant with the spacecraft mass and that the value is about 7.5 years. The majority of the missions have a mission lifetime concentrated around 7.5 years; however, a wide range of mission durations, and especially for spacecraft below 3000 kg is common, with mission lifetimes ranging from 1 year, up to 15 years. The second interesting information that can be extrapolated is the variation of the spacecraft power with the mass (). A linear interpolation of the database data led to the following relation:

$$\mathrm{W}_{S/C} = 0.6165 \cdot m_{S/C} + 201.14 \tag{E.1}$$

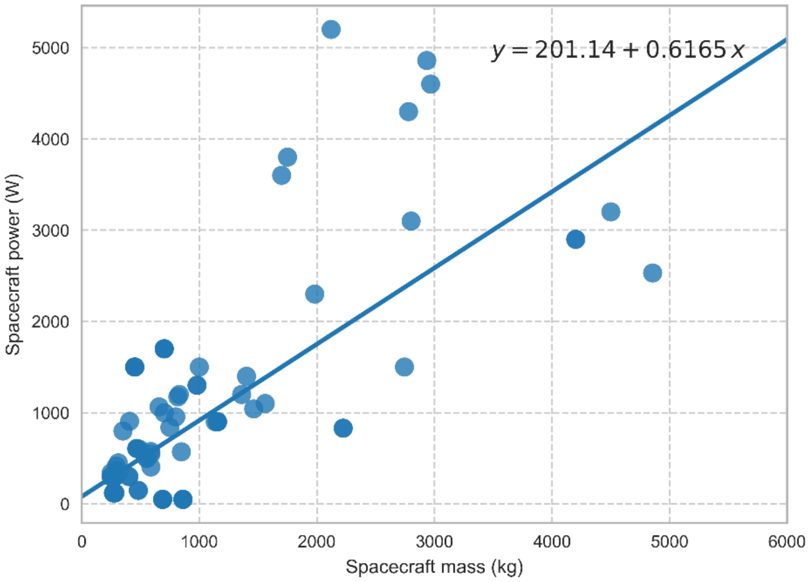

Figure E-1: Power vs mass relation for the satellite in the UCS database.

A third important information is the amount of propellant needed by the mission. Despite this quantity is highly mission dependant, in order to have the possibility for a quick estimate it was decided to perform a linear interpolation of the data in the database. The final relation obtained for the propellant mass (m_f) as a function of the spacecraft mass is as follows:

$$m_f = 67.563 + 0.0497 \cdot m_{S/C} \tag{E.2}$$

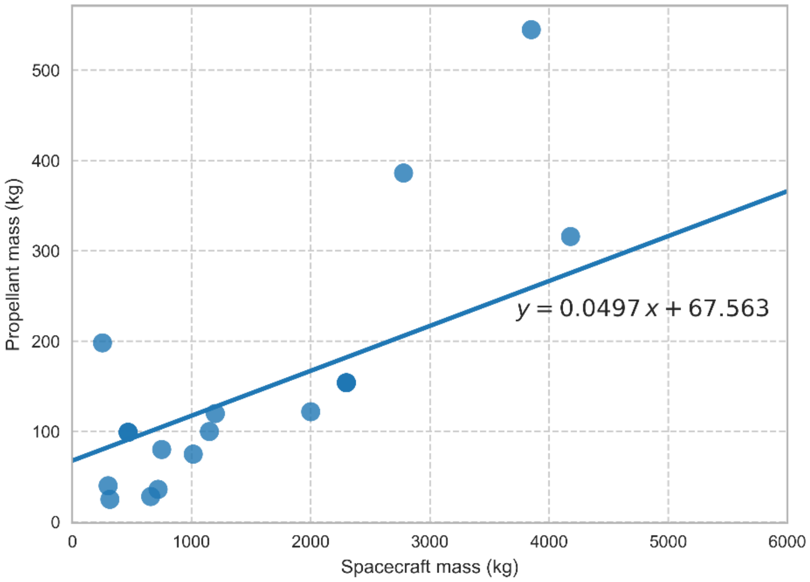

Figure E-2: Propellant mass vs spacecraft mass relation for the satellites in the UCS database.

In addition, it is useful to have an estimate of the solar panels area and mass. To do so, the average period and the average eclipse time for the spacecraft in the database have been computed. The resulting average period is 98.54 minutes and the average eclipse time is 35.4 minutes. Using these values and preliminary sizing relations (Wertz and Larson, 1999) it is possible to compute the approximate power the solar arrays are required to produce as a function of the spacecraft mass.

$$W_{sa} = \frac{\frac{W_e T_e}{X_e} + \frac{W_d T_d}{X_d}}{T_d} \tag{E.3}$$

where W_e and W_d are the power required during eclipse and daylight respectively; T_e and T_d are the times spent by the spacecraft in eclipse and daylight respectively. Finally, X_e and X_d are the path efficiencies in eclipse and daylight, and they are assumed to be equal to 0.65 and 0.85 respectively (Wertz and Larson, 1999). Using again a preliminary estimation it is also possible to compute the approximate solar panel area (Eq. (E.4)) and mass (Eq. (E.5)).

$$A_{sa} = \frac{W_{sa}}{I_d \cdot \eta \cdot L_d \cdot C_s \cdot \cos\theta} \tag{E.4}$$

$$m_{sa} = 0.04 \cdot W_{sa} \tag{E.5}$$

where I_d is the inherent degradation of the solar panels (assumed to have an average value of 0.77), η efficiency of the solar cells (assumed equal to 0.22), C_s is the solar constant equal to 1358 W/m^2, L_d is a term dependent on the yearly degradation of the solar arrays (assumed equal to 0.03). Finally, θ is the incidence angle between the solar arrays and the Sun (assumed equal to 45 degrees). The assumptions made in this phase for the computation of the solar arrays area and mass are all based on average mission values and have been considered compatible with the simplified and preliminary scaling relations developed.

For what concerns the angular momentum required by the spacecraft reaction wheels (H_{rw}), the data available was limited; nonetheless it was decided to linearly interpolate the available da to obtain a relation between the angular momentum and the spacecraft mass (Eq. (E.6)).

$$H_{rw} = 13.741 + 0.0231 \cdot m_{S/C} \tag{E.6}$$

For the sizing of some of the main spacecraft component as a function of the spacecraft mass, it is possible to use the relations of Section 7.3 (Eqs. (7.5), (7.6), and (7.10)) together with the scaling equations obtained here (Eqs. (E.2) and (E.6)). For the magneto-torquers, we used data from a catalogue (Cayuga Astronautics, 2018) to obtain the length, diameter, and mass of the components as a function of the dipole moment (Figure E-3 to Figure E-5).

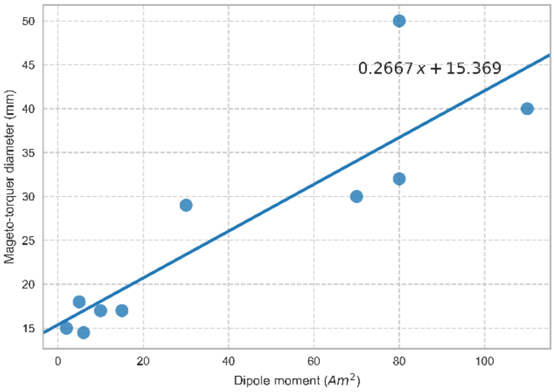

Figure E-3: Relation between the dipole moment and the diameter of a magneto-torquer.

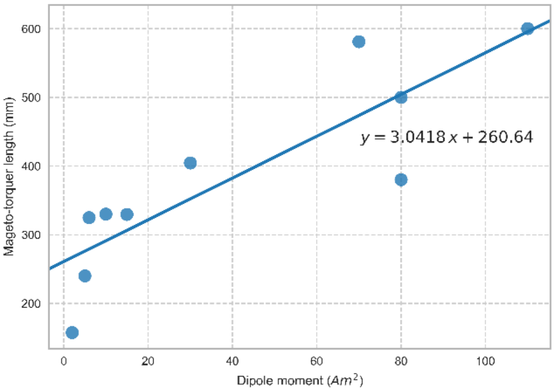

Figure E-4: Relation between the dipole moment and the length of a magneto-torquer.

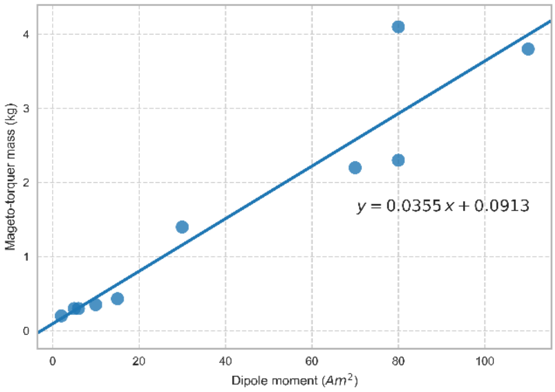

Figure E-5: Relation between the dipole moment and the mass of a magneto-torquer.

A relation between the dipole moment and the mass of the spacecraft (Eq. (E.7)) was then deduced from the available data of a set of missions (Table E-1).

$$B_d = 30.183 + 0.0356 \cdot m_{S/C} \tag{E.7}$$

Table E-1: Dipole moments values for some reference spacecrafts.

Spacecraft	**Mass (kg)**	**Dipole moment (Am^2)**
NovaSAR-S	430	30
Sentinel 2	1200	140
Aeolus	1400	100
Envisat	8000	315
DMC3	447	30
Swarm	468	10
MetOp	4185	160

An example of all the characteristics obtained for a set of spacecraft classes using the scaling relations just presented is summarised in Table E-2.

Table E-2: Summary of the spacecraft characteristics obtained with the scaling relations for a set of spacecraft classes.

S/C Mass	**Mission lifetime (yr)**	**m_f (kg)**	**$W_{S/C}$ (W)**	**H_{rw} (Nms)**	**W_{sa} (W)**	**A_{sa} (m2)**	**m_{sa} (kg)**
500	7.5	92	509	25	643	5	20
1000	7.5	117	818	37	1033	8	33
1500	7.5	142	1126	48	1422	11	45
2000	7.5	167	1434	60	1811	14	57
2500	7.5	192	1742	71	2201	17	70
3000	7.5	217	2051	83	2590	20	82
3500	7.5	242	2359	95	2979	23	94
4000	7.5	266	2667	106	3368	26	107
4500	7.5	291	2975	118	3758	29	119
5000	7.5	316	3284	129	4147	32	131
5500	7.5	341	3592	141	4536	35	144
6000	7.5	366	3900	152	4926	38	156

Bibliography

AILOR, W., HALLMAN, W., STECKEL, G. & WEAVER, M. Analysis of reentered debris and implications for survivability modeling. 4th European Conference on Space Debris, 2005. 539-545.

AIRBUS SAFRAN LAUNCHERS GMBH. 2003a. *Space Propulsion* [Online]. Bremen, Germany. Available: http://www.space-propulsion.com/index.html [Accessed July 2016].

AIRBUS SAFRAN LAUNCHERS GMBH. 2003b. *Space Propulsion* [Online]. Airbus Safran Launchers GmbH. Available: http://www.space-propulsion.com/spacecraft-propulsion/propellant-tanks/177-litre-hydrazine-propellant-tank.html [Accessed 2015].

ANDERSON, J. D. 2006. *Hypersonic and high temperature gas dynamics*, American Institute of Aeronautics and Astronautics.

ANNALORO, J., GALERA, S., KÄRRÄNG, P., PRIGENT, G., LIPS, T. & OMALY, P. 2017. Comparison between two spacecraft-oriented tools: PAMPERO & SCARAB. *Journal of Space Safety Engineering,* 4**,** 15-21.

ANNALORO, J., OMALY, P., RIVOLA, V. & SPEL, M. Elaboration of a New Spacecraft-oriented Tool: PAMPERO. Proceedings of the 8th European Symposium on Aerothermodynamics for Space Vehicle, 2015.

BATTIE, F., FOSSATI, T., GALLUCCI, S. & VOLPI, M. Vega launch vehicle upper stage re-entry survivability analysis. IEEE First AESS European Conference, 2012. 1-7.

BECK, J. May 5 2015. *RE: Personal Communication.*

BECK, J. & HOLBROUGH, I. 2014. *Belstead Research* [Online]. Available: http://www.belstead.com/ [Accessed January 2015].

BECK, J. & MERRIFIELD, J. 2015. A heat balance integral method for destructive re-entry codes. 8th European Symposium on Aerothermodynamics for Space Vehicles, 2-6 March 2015 Lisbon.

BECK, J., MERRIFIELD, J., HOLBROUGH, I., MARKELOV, G. & MOLINA, R. 2015. Application of the SAM Destructive Re-Entry Code to the Spacecraft Demise Integration Test Cases. 8th European Symposium on Aerothermodynamics of Space Vehicles, 2-6 March 2015a Lisbon.

BECK, J., MERRIFIELD, J., MARKELOV, G., HOLBROUGH, I. & MOLINA, R. 2015b. Verification and Application of the Sam Re-Entry Model. *Space Safety is No Accident.* Springer.

BJORKMAN, M. D., CHRISTIANSEN, E. L. & LEAR, D. M. 2014. Bumper 3 Software User Manual. NASA.

BLASCO, A., VAN DER LINDEN, J.GIL, B., JANSSEN, B., REYNIER, P., BECK, J., HERDRICH, G., MARYNOWSKI T. & HATTON, J. 2011. Overview of the results of ATV-1 Re-Entry Observation Campaign", *Proc. of 62nd International Astronautical Congress.*

BOYD, I. D., 1990, Rotational and vibrational nonequilibrium effects in rarefied hypersonic flow. Journal of thermophysics and heat transfer, 4(4), 478-484

BOYD, I. D., GOKCEN, T., 1994, Computation of axisymmetric and ionized hypersonic flows using particle and continuum methods. AIAA journal, 32(9), 1828-1835

BOYD, I. D., GOKCEN, T., 1993, Evaluation of thermochemical models for particle and continuum simulations of hypersonic flow. Journal of thermophysics and heat transfer, 7(3), 406-411

BRITISH STANDARDS 2014. Space systems - Assessment of survivability of unmanned spacecraft against space debris and meteoroid impacts to ensure successful post-mission disposal. Switzerland: BSI.

BUNTE, K., DESTEFANIS, R. & DROLSHAGEN, G. Spacecraft Shielding Layout and Optimisation Using ESABASE2/Debris. Proc. 5th European Conference on Space Debris, 2009.

CARMICHAEL, R. 2014. *Public Domain Aeronautical Software* [Online]. Available: http://www.pdas.com/atmosdownload.html [Accessed March 10 2015].

CAYUGA ASTRONAUTICS. 2018. *Magnetic torquer bars* [Online]. Available: http://www.cayugaastro.com/assets/products/MTBs/MTB.pdf [Accessed October 2017].

CHAN, K., SALTELLI, A. & TARANTOLA, S. Sensitivity analysis of model output: variance-based methods make the difference. Proceedings of the 29th conference on Winter simulation, 1997. IEEE Computer Society, 261-268.

CHRISTIANSEN, E., ARNOLD, J., CORSARO, B., DAVIS, A., GIOVANE, F., HYDE, J. & RATLIFF, M. 2009. Handbook for Designing MMOD Protection. Huston, Texas, USA: NASA Johnson Space Center.

COELLO, C. A. 2002. Theoretical and numerical constraint-handling techniques used with evolutionary algorithms: a survey of the state of the art. *Computer methods in applied mechanics and engineering,* 191**,** 1245-1287.

COLOMBO, C., LETIZIA, F., SOLDINI, S. & RENK, F. Disposal of libration point orbits on a heliocentric graveyard orbit: the Gaia mission. 25th International Symposium on Space Flight Dynamics, ISSFD, October 2015 Munich, Germany.

COLOMBO, C. & SWINERD, G. G. 2013. Astronautics Spacecraft Systems Notes. Southampton: University of Southampton.

COSTA, M. & MINISCI, E. MOPED: A multi-objective Parzen-based estimation of distribution algorithm for continuous problems. International Conference on Evolutionary Multi-Criterion Optimization, 2003 Berlin. Springer, 282-294.

D'ANGELO, S. & MINISCI, E. A. 2007. Multi-objective evolutionary optimization of subsonic airfoils by kriging approximation and evolution control. *Proceedings of the Institution of Mechanical Engineers,* 221**,** 805-814.

DEB, K. 2001. *Multi-objective optimization using evolutionary algorithms*, John Wiley & Sons.

DEB, K., PRATAP, A., AGARWAL, S. & MEYARIVAN, T. 2002. A fast and elitist multiobjective genetic algorithm: NSGA-II. *Evolutionary Computation, IEEE Transactions on,* 6**,** 182-197.

DEPCZUK, D. & SCHONBERG, W. 2003. Characterizing debris clouds created in oblique orbital debris particle impact. *Journal of Aerospace Engineering,* 16**,** 177-190.

EAGLEPICHER TECHNOLOGIES. 2016. *Nickel-Hydrogen Batteries and Cells* [Online]. EaglePicher Technologies LLC. Available: http://www.eaglepicher.com/technologies/battery-power/nickel-hydrogen-ni-h2 [Accessed January 2016].

ESTES, R. H. & MOORE, N. 2007. An Overview of Demise Calculations, Conceptual Design Studies, and Hydrazine Compatibility Testing for the GPM Core Spacecraft Propellant Tank. *54th JANNAF Propulsion Conference (CPIA).* Denver, CO, USA.

EUROPEAN SPACE AGENCY. 2008. *Requirements on Space Debris Mitigation for ESA Projects* [Online]. Available: http://emits.sso.esa.int/emits-doc/ESTEC/AD4RequirementsSpaceDebrisMitigationESA_Projects.pdf [Accessed].

EUROPEAN SPACE AGENCY. 2012. *Metop - meteorological missions* [Online]. European Space Agency. Available: http://www.esa.int/Our_Activities/Observing_the_Earth/The_Living_Planet_Programme/Meteorological_missions/MetOp/Overview14 [Accessed January 2016].

EUROPEAN SPACE AGENCY. 2016. *CryoSat-2 (Earth Explorer Opportunity Mission-2)* [Online]. eoPortal Directory. Available: https://eoportal.org/web/eoportal/satellite-missions/c-missions/cryosat-2 [Accessed July 2016].

FLEGEL, S. 2011. MASTER-2009 Software User Manual. Institute of Aerospace Systems (ILR).

FLEGEL, S., GELHAUS, J., WIEDEMANN, C., VORSMANN, P., OSWALD, M., STABROTH, S., KLINKRAD, H. & KRAG, H. 2009. The MASTER-2009 Space Debris Environment Model. *5th European Conference on Space Debris.* ESOC, Darmstadt, Germany.

FRITSCHE, B., KLINKRAD, H., KASHKOVSKY, A. & GRINBERG, E. 2000. Spacecraft disintegration during uncontrolled atmospheric re-entry. *Acta Astronautica,* 47**,** 513-522.

FRITSCHE, B. & KOPPENWALLNER, G. Computation of destructive satellite re-entries. Space Debris, 2001. 527-532.

FRITSCHE, B., LIPS, T. & KOPPENWALLNER, G. 2007. Analytical and numerical re-entry analysis of simple-shaped objects. *Acta Astronautica,* 60**,** 737-751.

FRITSCHE, B., ROBERTS, T., ROMAY, M., IVANOV, M., GRINBERG, E. & KLINKRAD, H. Spacecraft disintegration during uncontrolled atmospheric Re-entry. Second European Conference on Space Debris, 1997. 581.

GÄDE, A. & MILLER, A. 2013. ESABASE2/Debris Release 6.0 Technical Description European Space Agency.

GELHAUS, J., KEBSCHULL, C., BRAUN, V., SANCHEZ-ORTIZ, N., PARILLA ENDRINO, E., MORGADO CORREIA DE OLIVEIRA, R. & DOMINGUEZ-GONZALEZ, R. 2014. DRAMA Final Report - Upgrade of ESA's Space Debris Mitigation Analysis Tool Suite. European Space Agency.

GELHAUS, J., SANCHEZ-ORTIZ, N., BRAUN, V., KEBSCHULL, C., DE OLIVEIRA, J. C., DOMINGUEZ-GONZALEZ, R., WIEDEMANN, C., KRAG, H. & VORSMANN, P. Upgrade of DRAMA-ESA's Space Debris Mitigation Analysis Tool Suite. ESA Special Publication, 2013. 62.

GRASSI, L., BIANCHI, S., DESTEFANIS, R., KANZLER, R., BASSALER, P. & HEINRICH, S. 2017. Design for Demise techniques for medium/large LEO satellites reentry. *7th European Conference on Space Debris.* ESOC, Darmstadt, Germany.

GRASSI, L., TIBOLDO, F., DESTEFANIS, R., DONATH, T., WINTERBOER, A., EVANS, L., JANOVSKY, R., KEMPF, S., RUDOLPH, M., SCHÄFER, F. & GELHAUS, J. 2014. Satellite vulnerability to space debris – an improved 3D risk assessment methodology. *Acta Astronautica,* 99**,** 283-291.

HALLMAN, W. P. & MOODY, D. M. 2005. Trajectory Reconstruction and Heating Analysis of Columbia Composite Debris Pieces. Cambridge, MA, USA: The Aerospace Corporation.

INNOCENTI, L., SOARES, T. & DELAVAL, J. ESA Clean Space Initiative. ESA Special Publication, 2013. 4.

INTER-AGENCY SPACE DEBRIS COORDINATION COMMITTEE 2007. *IADC space debris mitigation guidelines*, Inter-Agency Space Debris Coordination Committee.

KELLEY, R., HILL, N., ROCHELLE, W., JOHNSON, N. L. & LIPS, T. Comparison of ORSAT and SCARAB reentry analysis tools for a generic satellite test case. 38th COSPAR Scientific Assembly, 2010. 3931.

KELLEY, R. L. Using the Design for Demise Philosophy to Reduce Casualty Risk Due to Reentering Spacecraft. 63rd International Astronautical Congress, 1-5 October 2012 Naples, Italy.

KLETT, R. D. 1964. Drag Coefficients and Heating Ratios for Right Circular Cylinder in Free-Molecular and Continuum Flow from Mach 10 to 30. Sandia Report, SC-RR-64-2141, Albuquerque.

KOPPENWALLNER, G., FRITSCHE, B., LIPS, T. & KLINKRAD, H. Scarab-a Multi-Disciplinary Code for Destruction Analysis of Space-Craft during Re-Entry. Fifth European Symposium on Aerothermodynamics for Space Vehicles, 2005. 281.

KUCHERENKO, S. 2005. Global sensitivity indices for nonlinear mathematical models. Review. *Wilmott Meg.*

KUIPER, W., DROLSHAGEN, G. & NOOMEN, R. 2010. Micro-meteoroids and space debris impact risk assessment for the ConeXpress satellite using ESABASE2/Debris. *Advances in Space Research,* 45**,** 683-689.

LANGTANGEN, H. P. & WANG, L. 2015. *Odespy Software Package* [Online]. Available: https://github.com/hplgit/odespy [Accessed].

LEWIS, H. G., RADTKE, J., BECK, J., BASTIDA VIRGILI, B. & KRAG, H. 2017a. Self-induced collision risk analysis for large constellations. *7th European Conference on Space Debris.* ESOC, Darmstadt, Germany.

LEWIS, H. G., RADTKE, J., ROSSI, A., BECK, J., OSWALD, M., ANDERSON, P., BASTIDA VIRGILI, B. & KRAG, H. 2017b. Sensitivity of the space debris environment to large constellations and small satellites. *7th European Conference on Space Debris.* ESOC, Darmstadt, Germany.

LEWIS, H. G., WHITE, A. E., CROWTHER, R. & STOKES, H. 2012. Synergy of debris mitigation and removal. *Acta Astronautica,* 81**,** 62-68.

LIOU, J. & JOHNSON, N. 2006. Planetary science - Risks in space from orbiting debris. *Science,* 311**,** 340-341.

LIPS, T. & FRITSCHE, B. 2005. A comparison of commonly used re-entry analysis tools. *Acta Astronautica,* 57**,** 312-323.

LIPS, T., FRITSCHE, B., KANZLER, R., SCHLEUTKER, T., GULAHAN, A., BONVOISIN, B., SOARES, T. & SINNEMA, G. 2015. About the demisability of propellant tanks during atmospheric re-entry from LEO. 8th International Association for the Advancement of Space Safety Conference, 18-20 May 2015 Melbourne, Florida. 475-482.

LIPS, T., FRITSCHE, B., KOPPENWALLNER, G. & KLINKRAD, H. 2004. Spacecraft destruction during re-entry–latest results and development of the SCARAB software system. *Advances in Space Research,* 34**,** 1055-1060.

LIPS, T., WARTEMANN, V., KOPPENWALLNER, G., KLINKRAD, H., ALWES, D., DOBARCO-OTERO, J., SMITH, R., DELAUNE, R. M., ROCHELLE, W. C. & JOHNSON, N. L. Comparison of ORSAT and SCARAB Reentry Survival Results. 4th European Conference on Space Debris, 18-20 April 2005a Darmstadt, Germany. 533.

LIPS, T., WARTEMANN, V., KOPPENWALLNER, G., KLINKRAD, H., ALWES, D., DOBARCO-OTERO, J., SMITH, R. N., DELAUNE, R. M., ROCHELLE, W. C. & JOHNSON, N. L. Comparison of ORSAT and scarab reentry survival results. 2005 / 08 / 01 / 2005b. 533-538.

LÖHLE, S., MARYNOWSKI, T., KNAPP, A., WERNITZ, R., & LIPS, T. 2011. Analysis Of The ATV1 Re-Entry Using Near-UV Spectroscopic Data From The ESA/NASA Multi-Instrument Aircraft Observation Campaign. In: *7th European Symposium on Aerothermodynamics*. Vol 692. pp. 133.

MARTIN, C., CHEESE, J., BRANDMUELLER, C., BUNTE, K., FRITSCHE, B., LIPS, T., KLINKRAD, H. & SANCHEZ, N. A debris risk assessment tool supporting mitigation guidelines. 4th European Conference on Space Debris, 1st August 2005a ESA/ESOC, Darmstadt, Germany. 345-352.

MARTIN, C., CHEESES, J., SANCHEZ-ORTIZ, N., KLINKRAD, H., BUNTE, K., HAUPTMANN, S., FRITSCHE, B. & LIPS, T. 2005b. Introducing the ESA DRAMA tool. *Science and Technology Series,* 110**,** 219-233.

MASSON, D. J., MORRIS, D. N. & BLOXSOM, D. E. 1960. Measurements of sphere drag from hypersonic continuum to free-molecule flow. Santa Monica, CA, USA: RAND Corporation.

MATWEB LLC. 2015. *MatWeb - Material Property Data* [Online]. Available: http://www.matweb.com/ [Accessed February 2015].

MERRIFIELD, J., BECK, J., MARKELOV, G., LEYLAND, P. & MOLINA, R. Aerothermal Heating Methodology in the Spacecraft Aerothermal Model (SAM). 7th IAASS Conference, 2014.

MERRIFIELD, J., BECK, J., MARKELOV, G. & MOLINA, R. Simplified Aerothermal Models for Destructive Entry Analysis. 8th European Symposium and Aerothermodynamics for Space Vehicles, 2015.

MINISCI, E. 2015a. Space Debris and Asteroids (Re)Entry Analysis Methods and Tools. Glasgow, UK: University of Strathclyde.

MINISCI, E. 2015b. *Space Debris and Asteroids (Re)Entry Analysis Methods and Tools* [Online]. Glasgow, UK: University of Strathclyde. Available: https://www.mat.uniroma2.it/Astro/slides/SSTS/SSTS-Minisci.pdf [Accessed].

MINISCI, E., AVANZINI, G., D'ANGELO, S. & DUTTO, M. 2008. Multi-objective design of robust flight control systems.

MITCHELL, M. 1995. Genetic algorithms: An overview. *Complexity,* 1**,** 31-39.

MOSHER, T. 1999. Conceptual spacecraft design using a genetic algorithm trade selection process. *Journal of Aircraft,* 36**,** 200-208.

NATIONAL ASTRONAUTICS AND SPACE ADMINISTRATION 1997. Rocket body components survive reentry. *The Orbital Debris Quarterly News.* Huston, Texas, U.S.A.: NASA.

NATIONAL ASTRONAUTICS AND SPACE ADMINISTRATION 2001. PAM-D Debris falls in Saudi Arabia. *The Orbital Debris Quarterly News.* Huston, Texas, U.S.A.: The Orbital Debris Program Office.

NATIONAL ASTRONAUTICS AND SPACE ADMINISTRATION. 2009. *ORSAT* [Online]. NASA Orbital Debris Program Office. Available: http://orbitaldebris.jsc.nasa.gov/reentry/orsat.html [Accessed July 14 2015].

NATIONAL ASTRONAUTICS AND SPACE ADMINISTRATION. 2011. *UARS Re-entry Overview* [Online]. Available: http://www.nasa.gov/mission_pages/uars/ [Accessed July 14 2015].

NATIONAL ASTRONAUTICS AND SPACE ADMINISTRATION 2012. Process for Limiting Orbital Debris. Washington, DC.

NATIONAL ASTRONAUTICS AND SPACE ADMINISTRATION. 2015. *Debris Assessment Software* [Online]. NASA Orbital Debris Program Office. Available: http://orbitaldebris.jsc.nasa.gov/mitigate/das.html [Accessed July 14 2015].

NATIONAL OCEANIC AND ATMOSPHERIC ADMINISTRATION 1976. U.S. Standard Atmosphere 1976. Washington, D.C.

O'CONNOR, B. 2008. Handbook for Limiting Orbital Debris. NASA Handbook 8719.14. *National Aeronautics and Space Administration, Washington, DC*.

OMALY, P. & SPEL, M. DEBRISK, a tool for re-entry risk analysis. ESA Special Publication, 2012. 70.

OWENS, T. M. 2014. *Aero-Thermal Demise of Reentry Debris: A Computational Model*. Master of Science, Florida Institute of Technology.

PARDINI, C. & ANSELMO, L. 2013. Re-entry predictions for uncontrolled satellites: results and challenges. *6th International Association for Space Safety Conference*. Montreal, Canada.

PAGAN, A., MASSUTI-BALLESTER, B., HERDRICH, G. 2016. Total and Spectral Emissivities of Demising Aerospace Materials. Frontier of Applied Plasma Technology. Vol 9. No. 1. pp. 7-12.

PAGAN A.S., MASSUTI-BALLESTER, B., HERDRICH, B., MERRIFIELD, J. A., BECK, J., LIEDTKE, V., & BONVOISIN, B. 2015. Experimental Demisability Investigation of Common Spaceflight Materials. *Proc. of ISTS*.

PERINI, L. L. 1972. Compilation and correlation of experimental hypersonic stagnation point convective heat rates. Silver Spring, Maryland: The Johns Hopkins University.

PLATNICK, S. 2016. *NASA's Earth Observing System* [Online]. National Aeronautics and Space Administration. Available: http://eospso.nasa.gov/mission-category/3 [Accessed January 2016].

PUTZAR, R. & SCHÄFER, F. 2006. Vulnerability of spacecraft equipment to space debris and meteoroids impacts. Germany: Ernst-Mach-Institute, Freiburg.

R.TECH. 2015. *Spacecraft Demise Workshop* [Online]. R.Tech, CNES, ESA. Available: http://scdw.rtech.fr/SCDW_WEB/UK/PAGE_Information.awp [Accessed April 2015].

RADTKE, J., STOLL, E., LEWIS, H. G. & BASTIDA VIRGILI, B. 2017. The impact of the increase in small satellite launch traffic on the long-term evolution of the space debris environment. *7th European Conference on Space Debris*. ESOC, Darmstadt, Germany.

READINGS, C. J. & REYNOLDS, M. L. 1996. Atmospheric Chemistry Mission. *Nine candidate Earth explorer missions-ESA SP*. Paris: European Space Agency.

REGAN, F. J. & ANANDAKRISHNAN, S. M. 1993. *Dynamics of atmospheric re-entry*, American Institute of Aeronautics and Astronautics.

REIMERDES, H.-G. & WOHLERS, W. Optimization of micrometeoroid and space debris protection systems. Space Debris, 2001. 655-660.

RILEY, D., PONTIJAS FUENTES, I., MEYER, J.-C., PROFFE, G. & LIPS, T. 2017. Design for Demise: System-level techniques to reduce re-entry casualty risk. *7th European Conference on Space Debris.* ESOC, Darmstadt, Germany.

ROCHELLE, W. C., MARICHALAR, J. J. & JOHNSON, N. L. 2004. Analysis of reentry survivability of UARS spacecraft. *Advances in Space Research,* 34**,** 1049-1054.

ROCKWELL COLLINS. 2016. *Satellite Stabilization Wheels* [Online]. Rockwell Collins. Available: https://www.rockwellcollins.com/Products_and_Systems/Controls/Satellite_Stabilization_Wheels.aspx [Accessed January 2016].

ROSSI, A., PARDINI, C., ANSELMO, L., CORDELLI, A. & FARINELLA, P. Effects of the RORSAT NaK drops on the long term evolution of the space debris population. 48th International Astronautical Congress, 1997.

RYAN, S. & CHRISTIANSEN, E. 2011. A ballistic limit analysis programme for shielding against micrometeoroids and orbital debris. *Acta Astronautica,* 69**,** 245-257.

RYAN, S. & CHRISTIANSEN, E. L. 2010. Micrometeoroid and orbital debris (MMOD) shield ballistic limit analysis program. Houston: NASA Johnson Space Center.

RYAN, S., SCHAEFER, F., DESTEFANIS, R. & LAMBERT, M. 2008. A ballistic limit equation for hypervelocity impacts on composite honeycomb sandwich panel satellite structures. *Advances in Space Research,* 41**,** 1152-1166.

SALTELLI, A. 2002. Making best use of model evaluations to compute sensitivity indices. *Computer Physics Communications,* 145**,** 280-297.

SALTELLI, A., ANNONI, P., AZZINI, I., CAMPOLONGO, F., RATTO, M. & TARANTOLA, S. 2010. Variance based sensitivity analysis of model output. Design and estimator for the total sensitivity index. *Computer Physics Communications,* 181**,** 259-270.

SALTELLI, A., TARANTOLA, S. & CHAN, K.-S. 1999. A quantitative model-independent method for global sensitivity analysis of model output. *Technometrics,* 41**,** 39-56.

SANCHEZ, P., COLOMBO, C., VASILE, M. & RADICE, G. 2009. Multicriteria comparison among several mitigation strategies for dangerous near-earth objects. *Journal of Guidance, Control, and Dynamics,* 32**,** 121-142.

SCHÄFER, F., LAMBERT, M., CHRISTIANSEN, E., KIBE, S., STOKES, H., REIMERDES, H.-G., MESHCHERYAKOV, S., ANGRILLI, F. & ZENGYAO, H. The inter-agency space debris coordination committee (IADC) protection manual. 4th European Conference on Space Debris, 2005a.

SCHÄFER, F., LAMBERT, M., CHRISTIANSEN, E., KIBE, S., STOKES, H., REIMERDES, H. G. & ZENGYAO, H. The inter-agency space debris coordination committee (IADC) protection manual. 4th European Conference on Space Debris, 2005b ESA/ESOC, Darmstadt, Germany. 39.

SCHÄFER, F., RYAN, S., LAMBERT, M. & PUTZAR, R. 2008. Ballistic limit equation for equipment placed behind satellite structure walls. *International Journal of Impact Engineering,* 35**,** 1784-1791.

SCHAUB, H., JASPER, L. E., ANDERSON, P. V. & MCKNIGHT, D. S. 2015. Cost and risk assessment for spacecraft operation decisions caused by the space debris environment. *Acta Astronautica,* 113**,** 66-79.

SCHONBERG, W. P. 2001. Characterizing secondary debris impact ejecta. *International Journal of Impact Engineering,* 26**,** 713-724.

SHANNON, R. & CHRISTIANSEN, E. 2009. Micrometeoroid and Orbital Debris (MMOD) Shield Ballistic Limit Analysis Program. Huston, Texas, USA: NASA Johnson Space Center.

SNIVELY, J. B., TAYLOR, M. J. & JENNISKENS, P. 2011. Airborne imaging and NIR spectroscopy of the ESA ATV spacecraft re-entry: instrument design and preliminary data description. *International journal of remote sensing*, Vol. 32. Issue 11. pp. 3019-3027.

SOBOL, I. M. 2001. Global sensitivity indices for nonlinear mathematical models and their Monte Carlo estimates. *Mathematics and computers in simulation*, 55**,** 271-280.

SPACE DEBRIS OFFICE. 2017. *Space Debris by the Numbers* [Online]. Darmstadt, Germany: European Space Agency. Available: http://www.esa.int/Our_Activities/Operations/Space_Debris/Space_debris_by_the_numbers [Accessed October 2017].

SREEKANTH, A. K., RESEARCH, D. & ORGANISATION, D. 2003. *Aerodynamic Predictive Methods and Their Validation in Hypersonic Flows*, Defence Research & Development Organisation, Ministry of Defence.

STANSBERY, E. G. 2014. NASA Orbital Debris Engineering Model. *In:* KRISKO, P. H., ANZ-MEADOR, P. D., HORSTMAN, M. F., OPIELA, J. N., HILLARY, E., HILL, N. M., KELLEY, R. L., VAVRIN, A. B. & JARKEY, D. R. (eds.) *ORDEM 3.0 - User's Manual.* Huston, Texas, United States: NASA.

STOKES, H., COUGNET, C., GELHAUS, J., OSWALD, M., SCHAEFER, U. & THEROUDE, C. 2012. A Detailed Impact Risk Assessment of Two Low Earth Orbiting Satellites. *International Astronautical Congress.* Naples, Italy.

STOKES, H., SWINERD, G., WALKER, R. & WILKINSON, J. 2000. Achieving cost effective debris protection of unmanned spacecraft using SHIELD. *51st International Astronautical Federation Congress.* Rio de Janeiro, Brasil.

STOKES, P. & SWINERD, G. Debris protection optimisation of a realistic unmanned spacecraft using SHIELD. 4th European Conference on Space Debris, 2005. 515.

TEWARI, A. 2007. *Atmospheric and Space Flight Dynamics: Modeling and Simulation with MATLAB® and Simulink®*, Birkhäuser.

THE AEROSPACE CORPORATION. 2016. *Center of Orbital and Reentry Debris Studies* [Online]. The Aerospace Corporation. Available: http://www.aerospace.org/cords/ [Accessed 29 Jun 2015].

TRISOLINI, M., LEWIS, H. G. & COLOMBO, C. Survivability and Demise Criteria for Sustainable Spacecraft Design. 66th International Astronautical Conference, 2015 Jerusalem.

TRISOLINI, M., LEWIS, H. G. & COLOMBO, C. Demise and Survivability Criteria for Spacecraft Design Optimisation. International Association for the Avancement of Space Safety Conference, 18-20 May 2016a Melbourne, Florida.

TRISOLINI, M., LEWIS, H. G. & COLOMBO, C. 2016b. Demise and survivability criteria for spacecraft design optimization. *Journal of Space Safety Engineering*, 3**,** 83-93.

TRISOLINI, M., LEWIS, H. G. & COLOMBO, C. Multi-objective optimisation for spacecraft design for demise and survivability. Final Stardust Conference, 31 October - 4 November 2016c ESTEC, Noordwijk, The Netherlands.

TRISOLINI, M., LEWIS, H. G. & COLOMBO, C. Spacecraft design optimisation for demise and survivability. 67th International Astronautical Congress, October 2016d Guadalajara, Mexico. International Astronautical Federation.

TRISOLINI, M., LEWIS, H. G. & COLOMBO, C. Demisability and survivability multi-objective optimisation for preliminary spacecraft design. 68th International Astronautical Congress, 25-30 September 2017a Adelaide, Australia.

TRISOLINI, M., LEWIS, H. G. & COLOMBO, C. 2017b. On the demisability and survivability of modern spacecraft. *8th European Conference on Space Debris.* Darmstadt, Germany.

TRISOLINI, M., LEWIS, H. G. & COLOMBO, C. 2018a. Demisability and survivability sensitivity to design-for-demise techniques. *Acta Astronautica,* 145**,** 357-384.

TRISOLINI, M., LEWIS, H. G. & COLOMBO, C. 2018b. Spacecraft design optimisation for demise and survivability. *Aerospace Science and Technology,* 77**,** 20.

UNION OF CONCERNED SCIENTISTS 2017. UCS Satellite Database. 2 Brattle Square, Cambridge MA: Union of Concerned Scientists.

VASILE, M. & COLOMBO, C. 2008. Optimal impact strategies for asteroid deflection. *Journal of guidance, control, and dynamics,* 31**,** 858-872.

VASILE, M. & ZUIANI, F. J. P. O. T. I. O. M. E., PART G: JOURNAL OF AEROSPACE ENGINEERING 2011. Multi-agent collaborative search: an agent-based memetic multi-objective optimization algorithm applied to space trajectory design. 225**,** 1211-1227.

VECTRONIC AEROSPACE. 2014. *Space Applications* [Online]. VECTRONIC Aerospace GmbH. Available: http://www.vectronic-aerospace.com/space.php [Accessed January 2016].

WASWA, P. M. & HOFFMAN, J. A. 2012. Illustrative NASA Low Earth Orbit spacecraft subsystems design-for-demise trade-offs, analyses and limitations. *International Journal of Design Engineering,* 5**,** 21-40.

WASWA, P. M. B., ELLIOT, M. & HOFFMAN, J. A. 2013. Spacecraft Design-for-Demise implementation strategy & decision-making methodology for low earth orbit missions. *Advances in Space Research,* 51**,** 1627-1637.

WELTY, N., RUDOLPH, M., SCHÄFER, F., APELDOORN, J. & JANOVSKY, R. 2013. Computational methodology to predict satellite system-level effects from impacts of untrackable space debris. *Acta Astronautica,* 88**,** 35-43.

WERTZ, J. R. & LARSON, W. J. 1999. *Space Mission Analysis and Design*, Springer Netherlands.

ZOBY, E. V., MOSS, J. N. & SUTTON, K. 1981. APPROXIMATE CONVECTIVE-HEATING EQUATIONS FOR HYPERSONIC FLOWS. *Journal of Spacecraft and Rockets,* 18**,** 64-70.

ZOTES, F. A. & PEÑAS, M. S. J. E. A. O. A. I. 2012. Particle swarm optimisation of interplanetary trajectories from Earth to Jupiter and Saturn. 25**,** 189-199.

ZUPPARDI, G. & ESPOSITO, A. 2000. Recasting the Fay-Riddell formulae for computing the stagnation point heat flux. *Proceedings of the Institution of Mechanical Engineers, Part G: Journal of Aerospace Engineering,* 214**,** 115-120.